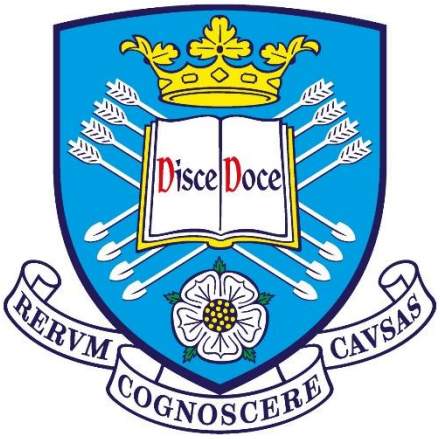

Applications of 3D Inkjet Bioprinting with Silk as Biomaterial

PIYUSH KUMAR

Department of Chemical and Biological Engineering

The University of Sheffield

A thesis submitted to the University of Sheffield in accordance with the requirements of the degree of Doctor of Philosophy

SUPERVISORS:

DR XIUBO ZHAO, DR STEPHEN EBBENS

June 2021 (Revised: November 2021)

Abstract

This work explores the novel applications of 3D inkjet bioprinting technology in the areas of biomedical sciences and environmental sciences. The versatility of inkjet bioprinting was reviewed and explored by experimenting with silk fibroin as the biomaterial ink for fabricating millimetre-sized 3D fibroin structures and investigating them through three different projects.

In the first project, the feasibility of fibroin structures for use as 3D carriers for on-carrier culture of neuronal cells was explored. 3D cell culture is a solution to the limitations, such as flattening and loss of physiological relevance of cells, observed in the conventional 2D culture. The results in this study demonstrated proliferation of cells and the ability of cells to differentiate under specific conditions while adhering to the fibroin structures. This study, thus, promises a new and robust platform for 3D culture of neuronal and other cells for applications in such techniques as guided neuronal growth, 3D cell-patterning and *in vitro* cell proliferation for adoptive cell transfer.

In the second project, 3D fibroin structures were utilised as self-propelled motors (SPMs) for their potential use in inducing fluid flow in microwells for the enhancement of diffusion-rate limited biomedical assays by rapid agitation of the analytes. The SPMs were fabricated in four different geometric shapes, propelled with two physical mechanisms and their propulsion data were analyzed to deduce the most favourable geometric shape and propulsion mechanism among the samples. It was concluded that among the four designs and two propulsion mechanisms tested, the line-shaped 1-armed surface tension driven SPMs showed the most reliable and predictable propulsion behaviour with maximum rotations throughout the observation time period and, therefore, could be used in the future for further investigations with different assays.

In the third project, 3D fibroin structures were utilised as surface tension driven self-propelled sensors for the approximate determination of surface tension of an unknown water sample and thereby indicate the level of dissolved contaminants in the sample.

The results showed significant differences in the propulsion velocity decay over time or deceleration, with sensors showing propulsion for much longer periods of time in water samples containing low level of contaminants and having higher surface tension compared to those propelling in relatively more contaminated water samples which had lower surface tension. This study put forward a simple to use technique for on-the-site detection of dissolved contaminant levels in a water sample.

Together, the experiments conducted and the results obtained across the three projects in this work demonstrate the flexible and multi-faceted applicability of 3D inkjet bioprinting technology in biomedical and environmental areas of research. This work will thus inspire and lay the foundations of numerous future research and investigations involving inkjet bioprinting.

Acknowledgements

I would like to thank everyone who has helped me during my PhD.

Publications

[1] David Gregory, Piyush Kumar, Ana Jimenez-Franco, Yi Zhang, Yu Zhang, Stephen Ebbens, Xiubo Zhao; Reactive Inkjet Printing and Propulsion Analysis of Silk-based Self-propelled Micro-stirrers; Journal of Visualised Experiments; (146); e59030; 2019; https://doi.org/10.3791/59030

[2] Yi Zhang, Piyush Kumar, Songwei Lv, Di Xiong, Hongbin Zhao, Zhiqiang Cai, Xiubo Zhao; Recent Advances in 3D Bioprinting of Vascularized Tissues; Materials & Design; Volume 199; 2021; 109398; ISSN 0264-1275; https://doi.org/10.1016/j.matdes.2020.109398

[3] Piyush Kumar, Stephen Ebbens, Xiubo Zhao; Inkjet Printing of Mammalian Cells – Theory and Applications; Bioprinting; Volume 23; e00157; 2021; https://doi.org/10.1016/j.bprint.2021.e00157

[4] Piyush Kumar, Abigail Legge, David Gregory, Andy Nichols, Henriette Jensen, Stephen Ebbens, Xiubo Zhao; 3D Printable Self-Propelling Sensors for Detection of Water Quality via Surface Tension; 2021
Submitted to JCIS Open (Under Review)

[5] Piyush Kumar, Yi Zhang, Stephen Ebbens, Xiubo Zhao; 3D Inkjet Printed Self-Propelled Motors for Biomedical Micro-Stirring Applications.
Due to be submitted soon

[6] Piyush Kumar, Ana Jimenez Franco, Xiubo Zhao; 3D Neuronal Cell Culture on Fibroin Cell Carriers Fabricated by 3D Inkjet Bioprinting.
Due to be submitted soon

Extra-Doctoral Achievements

Fellowship of the Higher Education Academy (FHEA)

Graduate Teaching Assistant (GTA)

1. CPE130 Autodesk AutoCAD.
2. CPE150 Computing Basics- Microsoft Excel.
3. MAT408 Bioengineering Lab- SEM and FTIR.
4. CPE6116 Bioengineering Lab- Gel Electrophoresis.
5. FCE6100 Professional Behaviour and Ethical Conduct.
6. CPE402 / CPE6020 Ansys Computational Fluid Dynamics Training.
7. Project Supervision and Thesis Writing Support to MEng and MSc students.
8. Correction / Marking of assignments and project dissertations of MEng and MSc students.

Doctoral Development Programme (DDP)

1. FCE6100 Professional Behaviour and Ethical Conduct.
2. MEC6008 Graphical Programming with LabView.
3. CPE6023 Synthetic Biology.
4. BMS6007 Mass-spectrometry-based Proteomics and Metabolomics.
5. PHY248 Physics with LabVIEW.
6. MEC6408 Industrial Marketing- Basics and Cases.
7. MEC6013 An Introduction to Solidworks.
8. MGT388 Finance and Law for Engineers.
9. Introduction to Programming- CIC6001 HPC Computing, CIC6005 FORTRAN, CIC6006 C and C++, CIC6007 MATLAB, CIC6010 Python.

Contents

Abstract I

Acknowledgements III

Publications IV

Extra-Doctoral Achievements V

Fellowship of the Higher Education Academy (FHEA) V

Graduate Teaching Assistant (GTA) V

Doctoral Development Programme (DDP) V

Contents VI

List of Figures XI

Chapter 1 XI

Chapter 2 XI

Chapter 3 XII

Chapter 4 XIII

Chapter 5 XIII

Chapter 1: INTRODUCTION 1

1.1 3D Bioprinting 1

1.2 3D Inkjet Bioprinting 3

1.2.1 Thermal Actuation and Piezoelectric Actuation 5

1.2.2 Continuous Inkjet (CIJ) and Drop-On-Demand (DOD) 7

1.2.3 Non-Reactive and Reactive 7

1.3 Printability of Biomaterial Inks and Bioinks 9

1.4 Applications of 3D Inkjet Bioprinting 10

1.4.1 Cell Microarrays & Cell Micropatterning 10

1.4.2 Tissue Engineering 19

1.4.3 *in vivo* Bioprinting 25

1.4.4 Biomolecule Printing & Patterning 29

1.4.5 Drug Loading 33

1.4.6 Fabrication of Self-Propelled Biodevices 37
1.5 Biomaterials 38
1.5.1 Natural 39
1.5.2 Synthetic 40
1.6 Silk Fibroin 40
1.7 Applications of Silk Fibroin as Biomaterial 43
1.8 Objectives and Scope of Thesis 45
Chapter 2: EXPERIMENTAL METHODS 47
2.1 Materials 47
2.2 Extraction of Fibroin 47
2.3 Drying of Fibroin 48
2.4 Dissolution of Fibroin 49
2.5 Dialysis of Fibroin Solution 50
2.6 Fibroin Concentration Measurement & Storage 52
2.7 Preparation of Fibroin Biomaterial Ink 54
2.8 Characterization of Fibroin Biomaterial Ink 54
2.8.1 Surface Tension Measurement 54
2.8.2 Viscosity Measurement 58
2.8.3 UV-Visible Absorbance Spectrophotometry 60
2.9 3D Inkjet Printer 63
2.10 LabVIEW Programme to Run the Printer 65
2.11 Computer Aided Designs of Fibroin Structures 67
2.12 3D Reactive Inkjet Bioprinting Process 68
2.13 Characterization of Printed Fibroin Structures 70
2.13.1 Microscopy 70
2.13.2 Optical Microscopy 70
2.13.3 Fluorescence Microscopy 72
2.13.4 Scanning Electron Microscopy 73
2.14 Statistics 75

Chapter 3: 3D NEURONAL CELL CULTURE ON FIBROIN CELL CARRIERS FABRICATED BY 3D INKJET BIOPRINTING 76
3.1 Abstract 77
3.2 Introduction 78
3.2.1 Scaffold-Free Models 81
3.2.2 Scaffold-Based Models 82
3.2.3 Applications of 3D Cell Cultures 83
3.2.4 Current Study 84
3.3 Experimental Methods 84
3.3.1 Materials 84
3.3.2 Fibroin Scaffold Design and Fabrication by Printing 84
3.3.3 Scaffold Surface Functionalization 85
3.3.4 Culture of PC12 and SH-SY5Y Cells 85
3.3.5 Cell Seeding on Fibroin Cell Carriers 85
3.3.6 Imaging of Cell-Scaffold Constructs 86
3.3.7 Live / Dead Cytotoxicity Assay 86
3.3.8 Resazurin–Resorufin Cell Proliferation Assay 87
3.3.9 Statistical Analysis 87
3.4 Results 87
3.4.1 Cell Seeding Density 87
3.4.2 Characterization of Cells on 3D Fibroin Carriers 88
3.4.3 Live/Dead Assay 91
3.4.4 Cell Metabolic Activity Assay 92
3.4.5 Culture with Nerve Growth Factor 94
3.4.6 Characterization with SEM 95
3.5 Discussion 96
3.6 Conclusion and Future Prospects 98
Chapter 4: 3D INKJET PRINTED SELF-PROPELLED MOTORS FOR BIOMEDICAL MICRO-STIRRING APPLICATIONS 99
4.1 Abstract 100

4.2 Introduction 101
4.2.1 Physical Self-Propelled Systems 101
4.2.2 Chemical Self-Propelled Systems 102
4.2.3 Biological Self-Propelled Systems 103
4.2.4 Applications and Current Study 104
4.3 Experimental Methods 108
4.3.1 Materials 108
4.3.2 Preparation of Fibroin Ink for Printing 108
4.3.3 3D Inkjet Printing Process 108
4.3.4 Characterization of SPMs 110
4.3.5 SPM Propulsion 111
4.3.6 Propulsion Data Acquisition 112
4.3.7 Tracking & Trajectory Analysis 112
4.3.8 RPM Counter 113
4.3.9 Statistics 114
4.4 Results 115
4.5 Discussion 128
4.5.1 Effect of Geometry 128
4.5.2 Effect of Propulsion Mechanism 129
4.6 Conclusion 130
Chapter 5: 3D PRINTABLE SELF-PROPELLING SENSORS FOR DETECTION OF WATER QUALITY VIA SURFACE TENSION 131
5.1 Abstract 132
5.2 Introduction 133
5.3 Experimental Methods 136
5.3.1 Materials 136
5.3.2 Collection of Wastewater 136
5.3.3 Wastewater Sample Preparation 137
5.3.4 Characterization of Wastewater: Chemical Oxygen Demand 137

5.3.5 Characterization of Wastewater: Surface Tension 137
5.3.6 Sensor Fabrication by 3D Inkjet Printing 138
5.3.7 Sensor Propulsion in Wastewater 139
5.3.8 Propulsion Trajectory Tracking and Analysis 140
5.3.9 Statistics 140
5.4 Results 141
5.5 Discussion 147
5.6 Conclusion 149
Chapter 6: CONCLUSION AND FUTURE PROSPECTS 150
Chapter 7: REFERENCES 153

List of Figures

Chapter 1

Figure 1.1: Applications of 3D Bioprinting

Figure 1.2: Piezoelectric vs. Thermal Inkjet Printing

Figure 1.3: Non-reactive vs. Reactive Inkjet Printing

Figure 1.4: Parameters for Printability of a Fluid

Figure 1.5: Inkjet Printed Cell Microarray

Figure 1.6: Inkjet Printed Cell Micropatterning

Figure 1.7: Inkjet Printing for Tissue Engineering

Figure 1.8: Inkjet Printing for *in vivo* Bioprinting

Figure 1.9: Inkjet Printing of Biomolecules

Figure 1.10: Inkjet Printing of Pharmaceuticals

Figure 1.11: Inkjet Printed Self-Propelling Motors

Figure 1.12: Structure of Silk Fibroin

Figure 1.13: Various Forms and Applications of Silk Fibroin

Chapter 2

Figure 2.1: Extraction of Fibroin

Figure 2.2: Preparation of Silk Cocoon and Extraction of Fibroin

Figure 2.3: Dissolution of Fibroin

Figure 2.4: Dialysis of Fibroin Solution

Figure 2.5: Dissolution and Dialysis of Fibroin Solution

Figure 2.6: Fibroin Solution Comparison Before and After Prolonged Storage

Figure 2.7: Tensiometer

Figure 2.8: Principle of Wilhelmy Plate Method of Tensiometry

Figure 2.9: Tensiometry Data of Fibroin Solution

Figure 2.10: Viscometer

Figure 2.11: Viscometry Data of Fibroin Solution

Figure 2.12: UV/Vis Spectrophotometer

Figure 2.13: Spectrometry Data of Fibroin Solution

Figure 2.14: 3D Inkjet Printer

Figure 2.15: Jetting Device and Printer Stage

Figure 2.16: Structure of the Jetting Device

Figure 2.17: LabVIEW Programme for Printer Operation

Figure 2.18: Parameters of Voltage Pulse Waveform

Figure 2.19: Computer Aided Design for Printing

Figure 2.20: Time Lapse of Jetting Droplets

Figure 2.21: Printed 3D Fibroin Structure

Figure 2.22: Light Microscopy

Figure 2.23: Fluorescence Microscopy

Figure 2.24: Scanning Electron Microscopy

Chapter 3

Figure 3.1: Visual Comparison between 2D and 3D Cell Cultures

Figure 3.2: Fluorescence Micrographs of PC12 Cells in 3D Culture

Figure 3.3: Fluorescence Micrographs of SH-SY5Y Cells in 3D Culture

Figure 3.4: Live/Dead Assay of PC12 and SH-SY5Y Cells in 3D Culture

Figure 3.5: Metabolic Activities of PC12 and SH-SY5Y Cells in Scaffold Containing Wells

Figure 3.6: Metabolic Activities of PC12 and SH-SY5Y Cells only on Scaffolds

Figure 3.7: Fluorescence Images of PC12 Cells with Nerve Growth Factor in 3D Culture

Figure 3.8: SEM Images of PC12 Cells with Nerve Growth Factor in 3D Culture

Figure 3.9: Simplified Illustration of Neuronal Growth Pattern on 3D Fibroin Scaffolds

Chapter 4

Figure 4.1: Ribbon Diagram of Structure of Catalase

Figure 4.2: Computer Aided Design of Self-Propelled Motors

Figure 4.3: LabVIEW Programme for SPM Propulsion Tracking

Figure 4.4: LabVIEW Programme for RPM Calculation from Propulsion Data

Figure 4.5: Catalytic Self-Propelled Motors

Figure 4.6: Marangoni Self-Propelled Motors

Figure 4.7: Catalytic and Surface Tension Driven Propulsion Mechanisms

Figure 4.8: SEM Images of Self-Propelled Motors

Figure 4.9: Illustration of SPM Propulsion Tracking

Figure 4.10: Video Frames of Propulsion of Catalytic SPMs with Different Layers

Figure 4.11: Angle of Orientation of Catalytic SPMs with Different Layers

Figure 4.12: Video Frames of Propulsion of Catalytic SPMs with Different Shapes

Figure 4.13: Video Frames of Propulsion of Marangoni SPMs with Different Shapes

Figure 4.14: Instantaneous Velocity Deceleration of Representative SPMs

Figure 4.15: Angle of Orientation of Representative Catalytic SPMs

Figure 4.16: Angle of Orientation of Representative Marangoni SPMs

Figure 4.17: Mean RPM of SPMs

Figure 4.18: Fluctuation of RPM over time of Representative SPMs

Chapter 5

Figure 5.1: 3D Inkjet Printing Process of Fibroin Self-Propelled Sensors

Figure 5.2: Chemical Oxygen Demand and Surface Tension Values of Water Samples

Figure 5.3: Video Frames and Illustration of Sensor Propulsion and SEM Images

Figure 5.4: Instantaneous Velocity Mean Decay Time and Representative Decay Rate

Chapter 1: INTRODUCTION

In this chapter, first, the 3D bioprinting technology is introduced. Afterwards, 3D inkjet bioprinting and its multitudinous applications are discussed. Here, I also discuss 3D reactive inkjet bioprinting as a feasible tool for fabricating various structures using inks made from the desired biomaterials. Second, I give a brief description on biomaterials. Later, I discuss the silk fibroin, its applications and its feasibility to be used as a biocompatible and environmentally friendly biomaterial ink for fabricating 3D structures through bioprinting.

1.1 3D Bioprinting

3D printing technology is an amalgamation of mechanical engineering, computer science and materials science. 3D printing was first introduced by Hideo Kodama in the form of laser assisted printing in 1981 [1] and by Charles Hull in 1983 in the form of stereolithography [2]. Since then, it has been extensively explored to fabricate a variety of structures for a variety of applications. With the assistance of digital computer aided design (CAD), which are developed within sophisticated 3D modelling softwares, the predesigned 3D structures can be precisely fabricated in a bottom-up and layer-by-layer manner at the desired size scale. 3D printing relies on 3D CAD for creating and controlling all the dimensions of the product. CAD is the virtual three-dimensional representation of the product and it is tested using real world parameters for precise refinement before product fabrication. As 3D printing offers high geometric accuracy up to as small as a few hundred microns, it has found extensive applications in the fabrication of 3D structures with complex internal architecture and equally complicated external topography without employing excessive tooling or machining, such as turning, milling, drilling, planing, broaching, and sawing, which can incur high manufacturing costs, wastage of valuable time and inefficiency of human resources. The diverse

applications of 3D printing include a wide range of areas, such as aerospace engineering [3, 4], automotive industries [5, 6], soft electronics [7-9], self-propelled micromotors [10-12], tissue engineering [13-22], regenerative medicine [23-25], food industries [26-28], drug delivery [29-32], cancer research [33-37], high-throughput screening tests and assays [38-40], joint replacement implants [41-43], prosthetic implants [44, 45] and biological robots or biobots [46].

When 3D printing technology is complemented with biology and medicine, it is called 3D bioprinting. 3D bioprinting is the process of patterning, assembling, and building-up living and non-living biomaterials or biological components, such as cells and biomolecules, in accordance to a 3D structural organization based on the computer aided design and ink deposition with the help of a 3D bioprinter [47-49]. Because of its higher precision and faster production rates than conventional 'top-down' approaches of manufacturing, and scope for easy design manipulation, 3D bioprinting has been explored for fabricating a variety of structures, such as cell-free as well as cell-laden scaffolds for tissue engineering and for achieving the ultimate goal of *in vitro* solid organ bioprinting for solid organ transplantation [50-58].

Currently, 3D bioprinting has applications in diverse markets including medical and pharmaceutical industries alongside more areas under investigation as broadly exemplified in **Figure 1.1**. Integration of research, design and manufacturing is key to realise the full advantages of 3D bioprinting in these sectors. The advantages of 3D bioprinting for large-scale biomedical production depends on its significance in the development or fabrication of the right products where it clearly gives the best solution in comparison to other manufacturing practices. Specific advantages of 3D bioprinting include, but are by no means limited to, reduction or even elimination of assembling several hundreds of individual parts to build up a structure, promotion of tool-less production, fabrication of structures with complex and anatomically accurate inner geometry, easy product design diversification through CAD, reduction in wastage of raw materials, time and labour costs, easy digitisation of the workflow and excellent

repeatability. 3D bioprinting integrates digital design, such as, CAD, in its core, which allows accuracy in designs, shapes, and sizes of the parts with real-world practical applications in consideration. 3D bioprinting enables the production of high performance and specialised structures with a diverse variety of materials, from natural biomaterials, such as extra-cellular matrices (ECMs) to synthetic biomaterials, such as polymers and hydrogels. However, a deep understanding of the biomaterial properties, the final design and different 3D bioprinting techniques is required for successful results.

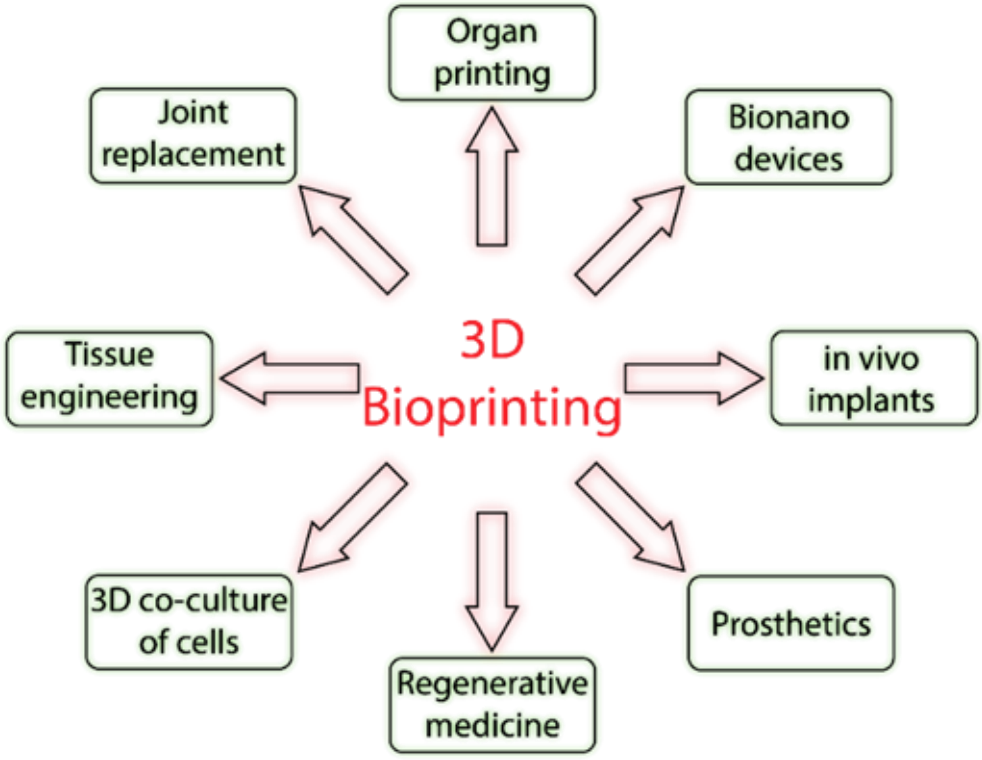

Figure 1.1: *Various current and potential future biomedical applications of 3D Bioprinting.*

1.2 3D Inkjet Bioprinting

While inkjet printers have been ubiquitously used in offices and homes to print texts and images on paper in 2D, researchers are exploring further potential functionalities of inkjet printing technology to fabricate 3D biological constructs which require a repeated and precise deposition of biomaterials as droplets in high-resolution patterns on a specific substrate. Inkjet printing is a type of printing technique that physically recreates a digital

image or a computer-aided design (CAD) by jetting a series of ink droplets on a flat substrate, such as, paper, plastic, glass or silicon. Such a printer uses micro-dispensing devices for jetting the ink droplets. Inkjet printing can work either using a single-ink system or a multiple-ink system with both the approaches capable of precisely printing single or multiple materials at micrometre resolution with essentially very minimal restrictions in the achievable geometric complexity of the 2D or 3D spatial arrangement. Therefore, this technique has the potential to create biologically relevant constructs, such as cell scaffolds, with complex external and internal architecture.

The advantage of using inkjet printing for 3D bioprinting is that it is a non-contact process of material deposition for fabricating 2D or 3D structures of any shape and size. This allows as little as pico-litre volumes of a liquid ink to be deposited in each jetting. This dramatically saves the costs of biomaterials and other ink components, such as growth factors, hormones and enzymes, which are usually very expensive [52]. Additionally, the non-contact deposition method of inkjet printing minimises the risk of contamination of the final product with minimal wastage of ink materials. The non-contact method also helps in achieving both precision and accuracy in localization and design by ensuring precise control over deposition of droplets thereby allowing a high micrometre-scale resolution [59]. The small volume per layer also allows faster drying of the deposited ink which makes it easy to print the ink layer-by-layer repeatedly at the same location on the substrate. Such layer-by-layer deposition of the ink, a process also known as additive manufacturing, helps in obtaining three dimensional structures exactly as modelled in computer aided design softwares. Through inkjet printing, it is easy to allow introduction of gradients in concentration of biomaterials or number of cells by altering the droplet deposition spacing and droplet size and frequency [60]. Inkjet printing offers flexibility in substrate choices and is not limited to any specific substrate, for example, microtiter plates and membranes, which various other techniques might be limited to. The micro-dispensing or the jetting devices have an annular layer of a piezoelectric or heating material that mechanically compresses the ink fluid in response to the CAD's electric

current pulses. The more viscous the ink material is, the higher the pulsating voltage needs to be in order to ensure proper droplet formation and jetting from these devices [61, 62]. Overall, inkjet bioprinting is suitable for use with a wide range of materials and for an even wider range of applications.

Irrespective of its many advantages, inkjet printing also suffers from a few limitations which are: (1) limit in the choices of printable materials, for example, due to the specific ink's viscosity and surface tension; (2) the mechanical stress and heat during the jetting process may affect the activity of sensitive biomaterials and cells [52]; (3) the nozzle geometry, such as its length and diameter, may affect printing patterns at very high resolutions [59]; (4) clogging of the nozzle which leads to irregular droplet sizes and directionality [52]; (5) difficulty in achieving large scale constructs due to the slow fabrication speeds in a few cases; (6) cell aggregation and sedimentation in ink reservoir during printing. Nonetheless, the advantages of inkjet printing overshadows its drawbacks and offer the ability to fabricate multi-material and multi-scale constructs with complex designs at a high printing resolution, as its building block, i.e., the jetted droplet, has a very small volume in the picolitre range [63].

1.2.1 Thermal Actuation and Piezoelectric Actuation

On the basis of the actuation technique or the mode of jetting, inkjet bioprinting can be classified into two main variants, namely, thermal and piezoelectric [52, 64, 65], as illustrated in **Figure 1.2**. In thermal inkjet bioprinting, a heating device (thin film heater/resistor) is placed inside the jetting device chamber which holds the fluid ink. When the CAD signal is received from a computer, the heating device rapidly heats up (~ 300 °C/µs), causing a sudden vaporisation and expansion of fluid volume, which is in immediate contact with the heater, and formation of a vapour bubble which in turn causes fluid displacement and the jetting of ink droplets [52, 64, 65]. In piezoelectric inkjet bioprinting, on the other hand, a piezoelectric material surrounds the fluid cavity of the

jetting device containing the ink. Piezoelectricity is the electric charge that accumulates in certain solid materials in response to applied mechanical stress. This occurs due to the presence of electric dipole moments in such solids which re-orient of molecular dipole moments under the influence of the external stress. Piezoelectric materials also show the opposite effect, called the converse piezoelectric effect, where the application of an electrical field creates mechanical deformation in the crystal. Thus, by definition, piezoelectric materials are certain solid materials which undergo mechanical deformations in response to an applied electric field and vice versa [52, 65]. As a result, when the electrical CAD signal is received, the piezoelectric material contracts in a pre-defined manner and causes ejection of the fluid out of the nozzle and the subsequent formation of droplets [52, 65, 66]. Other actuation techniques are electrostatic, electrohydrodynamic, solenoid-valve and acoustic inkjet printing [67]. These, however, are much less commonly used owing to their major limitations, which are, the necessity to have a conductive ink in the case of electrostatic and electrohydrodynamic inkjet printing; large droplet sizes at 500 µm or more causing low resolution printing in the case of solenoid-valve inkjet printing; and the necessity for upside down substrate placement in case of acoustic printing [67-69].

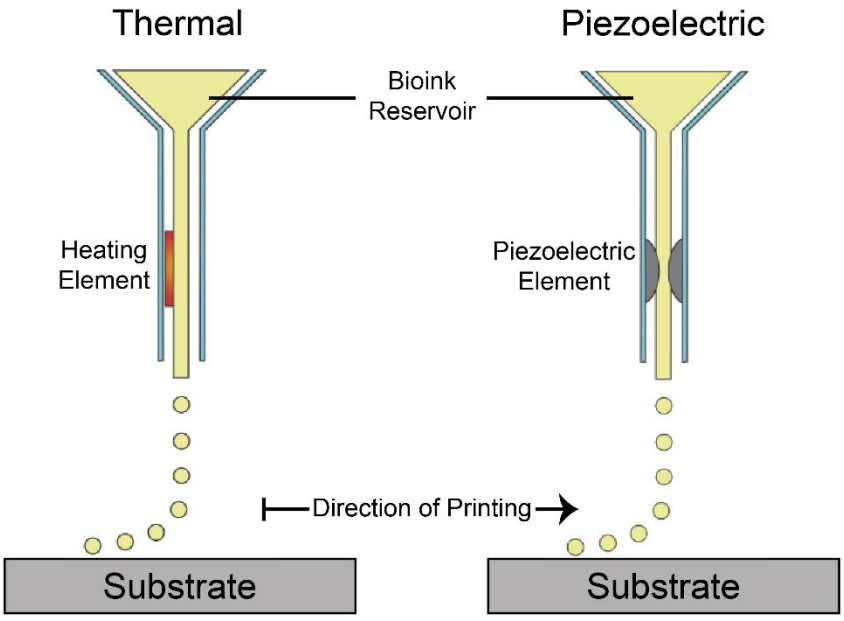

Figure 1.2: *Schematic illustration of thermal and piezoelectric inkjet printing processes. [image adapted from ref. [70] Copyright © 2016 IOP Publishing Ltd].*

1.2.2 Continuous Inkjet (CIJ) and Drop-On-Demand (DOD)

On the basis of the mode of deposition of the ink, inkjet bioprinting can be classified as either continuous or drop-on-demand [64, 71, 72]. In continuous inkjet (CIJ) bioprinting, a conductive fluid ink is jetted very fast, almost in the form of a continuous stream. After jetting, the ink is electrically charged and passed through an electrical field, which deflects the ink droplets towards the substrate in accordance to the CAD signal received from the computer. The non-deflected droplets are recycled and sent to the reservoir in the printhead so that they can be used for printing again [64, 71, 72]. In drop-on-demand (DOD) inkjet bioprinting, the jetting device actuates and jets out the ink droplets by propagating a pressure pulse in the ink fluid filled chamber only when the electrical signal is received on the basis of the CAD. For the correct placement of the deposited ink material, either the printhead or the substrate moves in X-Y-Z Cartesian coordinates [64, 71, 72]. From the perspective of bioprinting, CIJ has a few disadvantages, such as the risk of contamination in the biologically sensitive ink reservoir due to continuous ink recycling, the obligation to use electrically conductive inks, and relatively lower printing resolution. Therefore, DOD has become the most common inkjet bioprinting technique. In DOD, as droplets are ejected only when required, the biomaterial wastage is minimal compared to CIJ. There is also close to zero risk of contamination in the biologically sensitive ink because a recycling system is not needed, which means that the ink used is always fresh.

1.2.3 Non-Reactive and Reactive

On the basis of mode of formation of the final 3D structure, inkjet bioprinting can be categorised as either non-reactive inkjet bioprinting, which is simply called inkjet bioprinting, or reactive inkjet bioprinting as illustrated in **Figure 1.3**. In the non-reactive

technique, a single ink is simply deposited on the substrate after which the 3D structure forms either through physical changes, such as evaporation of water content, or through chemical changes, such as time-dependent self-assembly of peptides or hydrogels. In the reactive technique, two or more mutually reactive inks are used which react after jetting to form the required 'printed' product. Apart from the main ink, a supplementary biological / non-biological ink is dispensed layer-by-layer at the same location on the substrate as the main ink or through mid-air collision with the droplets of the main ink using tilted jetting devices, after which it reacts with the main ink and forms rigid 3D structures through irreversible, or in some cases, reversible, chemical changes, such as cross-linking and polymerization of the precursor fluid in the main ink. Thus, the dispensing of the supplementary ink can be either alternating [10-12] or simultaneous through mid-air collision [73, 74] with the dispensing of the main ink. The reactive technique is particularly helpful in those situations where the end product is incompatible with the jetting devices or for fabricating structures composed of those materials which are not printable themselves, such as solid end-product materials and materials which are insoluble or barely soluble to form printable liquid inks but can be formed through reaction with different liquid reactant materials [61]. This approach opens a new window for printing a much wider variety of materials and exploring different solidification mechanisms.

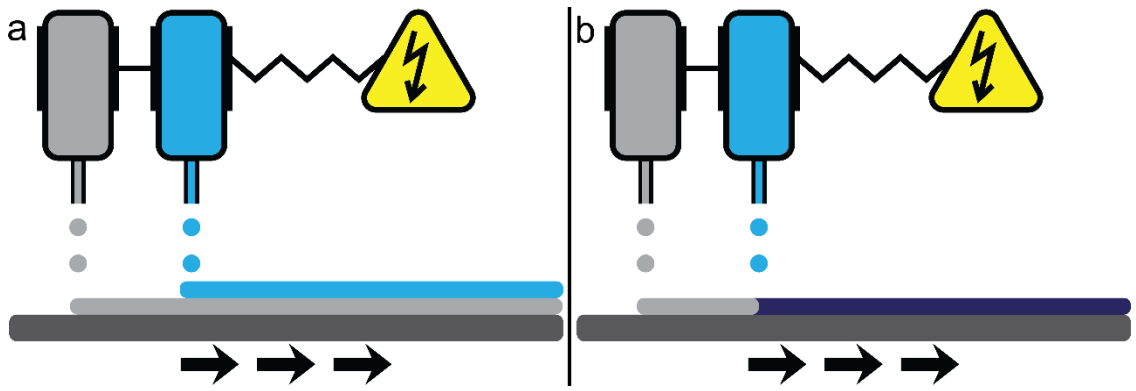

Figure 1.3: *Schematic illustrations of* ***(a)*** *non-reactive and* ***(b)*** *reactive inkjet printing processes. Different non-reacting inks form different consecutive layers on the substrate, whereas, different reacting inks form a layer of product on the substrate.*

1.3 Printability of Biomaterial Inks and Bioinks

Depending on the purpose, 3D inkjet bioprinting can be carried out using either cell-free biological inks or cell-laden biological inks. According to the widely accepted definition [48, 49, 75], a cell-free ink formulation containing only biomaterials and/or biologically active molecules, such as growth factors, is called 'biomaterial ink'. On the other hand, a 'bioink' is a formulation of cells that may also contain biologically active molecules for cell growth and biomaterials for mechanical support. The applications of 3D inkjet bioprinting can, thus, be categorised as those utilising biomaterial inks and those utilising bioinks.

The printability of an ink by inkjet technology depends on the surface tension, viscosity and inertia of the fluid which forms the bulk of the ink. These physical characteristics are determined by the Weber number (W) and Reynolds number (R), the two dimensionless physical constants, and the Ohnesorge number ($Oh = \sqrt{W} / R$). If the Z number, which is the inverse of Ohnesorge number ($Z = R / \sqrt{W}$) is too low (< 1), the viscous forces prevent detachment of droplet at the nozzle, whereas if the Z number is too high (> 10), the inertial forces, that is, the inertia imparted to the droplets from actuation, cause formation of several small ‘satellite’ droplets after the main droplet has already detached [71].

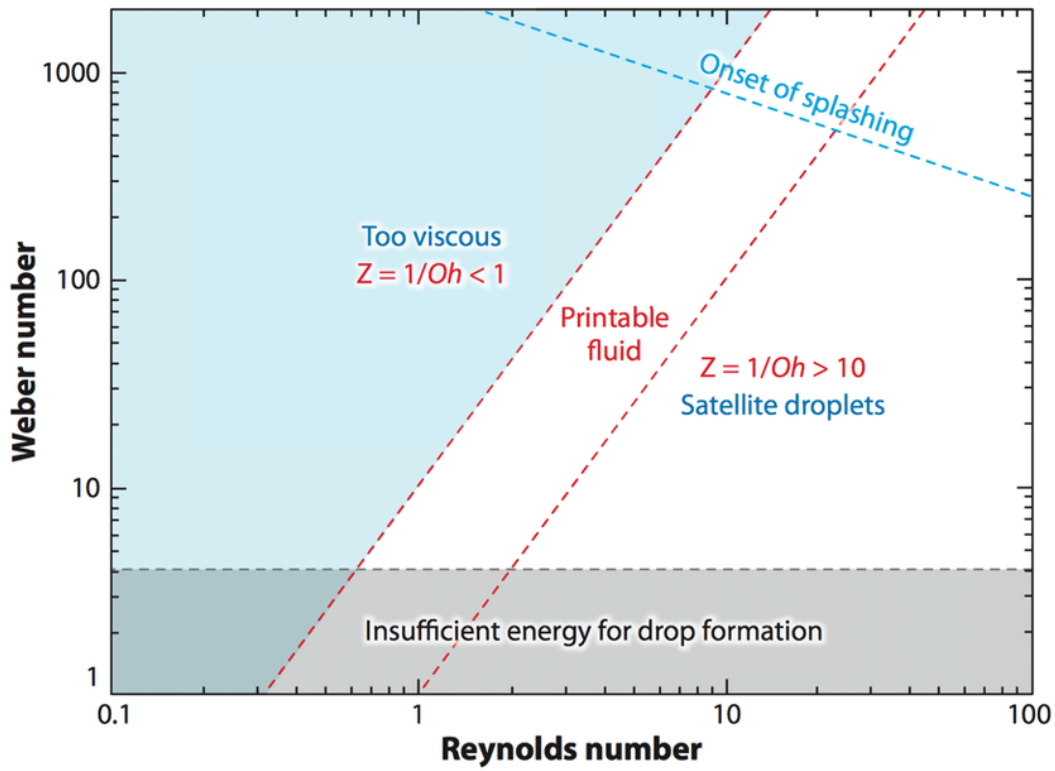

Figure 1.4: *Illustration to show the range of Weber number and Reynolds number of a printable fluid. The Weber number is the ratio of drag force to cohesion force or inertia to surface tension, whereas the Reynolds number is the ratio of inertia to viscosity. [image taken from ref. [71] Copyright © 2010 Annual Reviews].*

1.4 Applications of 3D Inkjet Bioprinting

Owing to its versatility, 3D inkjet bioprinting has been applied in wide variety of research and in diverse disciplines. Some of the important applications in biomedical research areas which have been discussed here are cell microarray and micropatterning, tissue engineering, *in vivo* bioprinting, biomolecule printing and patterning, drug formulation and fabrication of self-propelled biodevices.

1.4.1 Cell Microarrays & Cell Micropatterning

A cell microarray is an analytical tool having several different types of cells deposited in well-organized rows on a substrate, often called as a chip or lab-on-a-chip, for performing high-throughput and multiplexed biomedical assays or biosensing [76]. The advantage

of cell microarrays is that several different analytes, such as therapeutics, antibodies, lipids, peptides, enzymes, and other molecules, can be analysed on a wide phenotype of cells at once [76, 77]. Another important significance of cell microarrays is the effective miniaturisation of conventional assay methodologies for medical diagnostics of various diseases [78]. This not only helps minimise sample size of scarce analytes and expensive reagents but also makes the diagnosis process faster, efficient and portable [77, 79]. Additionally, in cell biology, cell microarrays can be applied to study cell-cell interactions, cell interactions with their microenvironment and cellular mechanics and physiology under different conditions and stimuli [80]. As inkjet bioprinting is establishing itself as a prominent tool for direct and non-contact cell printing and single cell sorting, it helps in very fast and easy fabrication of cell microarray based lab-on-a-chip devices and bioMEMS [78, 81, 82]. However, one important issue with cell microarray is the quick drying up of the freshly printed culture medium dots, containing the cells, owing to their picolitre volume [77, 83]. This necessitates the printed array to be used for analytical studies within minutes or else risk obtaining either misleading data or no data at all. Another challenge is the spreading out of the dots or cell migration from one location to another leading, again, to false assay or biosensing results [77, 83]. In order to overcome these challenges, Liberski et al. [83] adopted a new approach to fabricating cell microarray with dual liquid phase system as shown in **Figure 1.5**. The authors first printed dots of culture medium at specific locations on a substrate and simultaneously spread a thin layer of an oxygen-permeable mineral oil, in their case paraffin, evenly all over the substrate. Afterwards, mouse L929 immortalized fibroblast cells were printed on top of the culture medium dots already submerged under a thin layer of the oil. The cells traversed through the oil layer and sank at the bottom of the dots where they remained alive for several hours, as indicated by the >90% cell viability 7 hours post-printing. The non-volatile oil in this biphasic system prevented the culture medium from drying out. This approach makes the cell microarray chips more practicable for such biosensing or assay applications which require prolonged experimentation of up to a few hours before

the required results can be obtained. Additionally, the hydrophobicity of oil assures that the dots with cells in them do not spread out, thus maintaining the integrity of the microarray design.

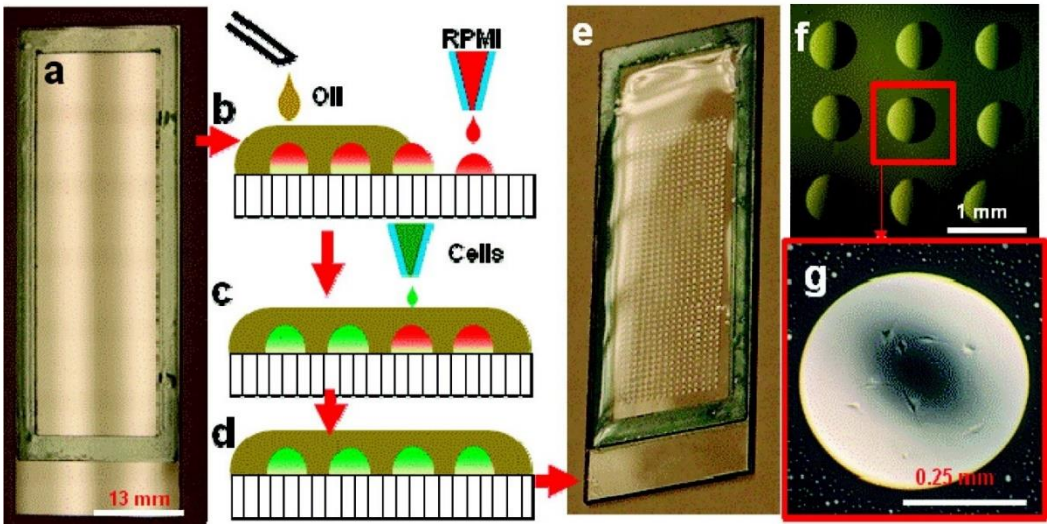

Figure 1.5: *Stages of cell microarray fabrication.* ***(a)*** *glass slide substrate with sealing frame along the edges to prevent oil spillage,* ***(b – d)*** *printing of culture medium, spreading of paraffin oil and printing of L929 cells,* ***(e)*** *substrate with fully printed microarray,* ***(f)*** *a micrograph of microarray units (scale bar: 1 mm),* ***(g)*** *a micrograph of a printed dot containing cells after 7 hours of incubation (scale bar: 0.25 mm). [image taken from ref. [83] Copyright © 2010 American Chemical Society].*

With ongoing design and operational advancements, inkjet bioprinting is now capable of printing not only one cell per droplet but also a fixed number of more than one cell per droplet, as per the requirement. To demonstrate the feasibility of inkjet bioprinting in building a live cell microarray with very high precision in cell number per printed dot, Jonczyk et al. [79] used a commercial piezoelectric inkjet cell printer (Nano-Plotter NP2.1) to fabricate a microarray of A-549 human lung cancer cells, suspended in DMEM with 10% FCS before printing. Around 1200 cells per dot were printed in an array with a very low average spot-to-spot variation of ±8.6 in cell number. After printing and culturing the cells for 3 days in a humidified environment, the authors observed a high cell viability of up to 88%. Elsewhere, Park et al. [84] developed a cancer microtissue co-culture array by piezoelectric inkjet printing cancer cells on nanofibrous membrane with embedded

fibroblasts. Firstly, CCD-1112SK fibroblasts were grown on top of nanofiber membranes which were fabricated by electrospinning polycaprolactone solution and placed in 96-well plates to act as substrate for cancer cell printing. Then, HPV18-positive HeLa cervical cancer cells, suspended in DMEM with 0.5% collagen, were printed in the wells, with 150 droplets in each well, achieving an almost 100% cell viability as observed immediately after printing. The deposited cancer cell aggregates increased in size due to cell proliferation, while maintaining their shape, similar to *in vivo* tumours, for up to 7 days post-printing. Also, the matrix metalloproteinases MMP2 and MMP9, which are the hallmarks of invasive cancers, were found to be upregulated in all the microtissues. These results showed the robustness of the method in developing an inkjet bioprinted *in vitro* cancer model.

An even more precise and smaller scale microarray was fabricated by Mi et al. [85] who developed a novel piezoelectric cell printing system with a high printing position accuracy of 10 μm which ensured printability in tiny microwells, and a low droplet volume of 0.1 nL which ensured single cell dispensing ability. Single GFP-transfected MDA-MB-231 human breast cancer cells and single RFP-transfected human umbilical vein endothelial cells (HUVECs), suspended in different culture media, were printed on a microfluidic chip 22 x 22 mm in size and consisting of an array of 400 microwells, each measuring 200 μm in depth and 300 μm in diameter. Up to 70% of droplets contained single cells on performing the printing at 90 V with 75 μm diameter nozzle and 1 x 10^6 cells/mL bioink concentration. The whole microfluidic chip platform was kept in an ice tank, without submerging the top printing area, to prevent the droplets in the microwells from drying out. The printed cells showed normal growth and migration such as surface adherence, migration to the sides of the wells and spindle formation and more than 87% viability 7 days post-printing. Additionally, incubating the cancer cells with paclitaxel caused inhibition of cell growth and migration and hindrance of normal cellular shape and morphology. The authors, thus, developed a new inkjet bioprinting based platform for multicellular printing and high throughput single cell analysis and drug screening.

In these research studies, the accurate drug screening results with known drugs show promise of mitigating the high failure rates of human clinical trials of those new under-trial drugs which have successful preclinical testing results in conventional assays and animal models but do not accurately represent human *in vivo* conditions.

Cell micropatterning is the deposition of cells in a pre-determined 2D or 3D pattern on a substrate or scaffold to mimic the complex *in vivo* tissue architecture with micrometre scale resolution for various purposes, such as drug screening and tissue engineering. Alongside cell microarray models, micropatterned cells are applied to establish the foundation of cell-based biomedical micro-electro-mechanical systems (bioMEMS), organ-on-a-chip models and point-of-care (PoC) devices for personalized medicine [86]. Additionally, in cell biology, cell micropatterning is applied to investigate multi-cell interactions, cytoskeleton mechanics, cell axis and symmetry during division and differentiation, cell migration and the effects of environment and stimuli [87, 88]. Cell micropatterning, thus, is the miniaturised deposition of more than one type of cells on a substrate based on a pre-determined 2D or 3D geometry. The concept of utilizing inkjet printing for cell micropatterning, albeit indirectly, was developed in the 1980s when cell adhesion molecules and monoclonal antibodies were inkjet printed in pre-defined patterns on a substrate, upon which, culturing of cells resulted in growth of specific cells only on those specific patterned locations due to specific cell adhesion [89]. This method was called as cytoscribing and the cellular patterns thus obtained as cytoscripts. Cytoscribing was one of the most important steps towards the development of the first direct inkjet printing of cells. Deposition of different cells in required configuration is a step forward to generate organoids *in vitro*, called as organ-on-a-chip, for mimicking *in vivo* organs [86]. The resulting structures act as disease models for drug screening and has the potential to lay the foundation for *in vitro* organ biofabrication for organ transplantation [90]. In one of the first such studies, Xu et al. printed rat primary embryonic motor neurons [56], hippocampal neurons [91] and cortical neurons [91], all suspended in DPBS solution, with a modified commercial thermal inkjet printer. The cells

were patterned as separate circles on the substrates, which were carefully incubated with culture medium for cell proliferation and differentiation. The circular pattern facilitated the motor neurons in forming a neural ring within 2 days of culture and forming dendritic extensions by the 7th day. The hippocampal and cortical neurons also started showing differentiation and neuronal ring formation within a day of seeding and developed extensive processes by the 13th and the 9th day, respectively. Such printed neuronal models have the potential to be used to study brain diseases, such as epilepsy [92]. In another research, Park et al. [93] have demonstrated the printing and patterning of mammalian cells onto a liquid-filled substrate, a culture dish filled with culture medium. The researchers used a piezoelectric inkjet printer to print NIH3T3 mouse fibroblasts and HEK293A human kidney cells, suspended in culture medium, first as dots to determine positional accuracy in a liquid environment and then as different patterns for co-culturing the printed cells, as shown in **Figure 1.6 (a)**. As the droplet containing the cells plunges into the culture medium in the dish as illustrated in **Figure 1.6 (b)**, the impact force causes the cells to deviate from their pre-defined positions as they sink in the medium and adhere to the bottom of the dish. For solving this issue, the authors adjusted the printing parameters and obtained a minimum best positional error of ±66 μm. For this, the optimal printing parameters, as used by the authors, were the stage movement speed of 5 mm/s, the nozzle-substrate distance of 1 mm and the culture medium volume of 3 mL in the dish. This bioprinting strategy is also one of the approaches to eliminating the risk of quick drying up of the printed dots and can, thus, be beneficial not only for cell micropatterning but also for cell sorting and cell microarray fabrication. Afterwards, the cells were printed in various geometric shapes with fine edges for co-culturing. The authors were also able to print the cells in complex patterns with cell concentration gradients rather than hard boundaries as shown in **Figure 1.6 (c)**, thus resulting in a 2D architecture of co-cultured *in vitro* cells that mimics natural tissues even more closely.

Research has also furthered into 3D cell micropatterning, which either requires separate layers of a gel-like support material to be printed alternately with the directly printed cells

[91, 94], or requires printing of cells suspended in a liquid cross-linker onto a crosslinkable scaffold precursor [95, 96]. One early example [91] of alternate printing of cells and scaffold is for the fabrication of multi-layered neural sheets by thermal inkjet printing. NT2 neuronal precursor cells suspended in DPBS were printed layer-by-layer alternating with a layer of fibrinogen and thrombin which yielded a fibrin gel layer. The sandwiched cells showed even distribution, anchorage to scaffold fibres with filopodia, and development of neurites within 12 days of *in vitro* culture, thus, forming neural sheets which measured 25 x 5 x 1 mm in dimensions. Such neural constructs provide a vital tool for the clinical study of treatment of neural injuries and degenerative diseases. Similarly, an early example [95] of co-printing of cells with a scaffold precursor is for the fabrication blood vessel like tubular structures using a modified commercial thermal inkjet printer. Human microvascular endothelial cells (HMVEC) suspended in thrombin and DPBS were printed on a fibrinogen containing substrate to form a rectangular grid of fibrin tubes around 100 μm in diameter with embedded cells. The cells showed alignment, proliferation and confluence on the inner lining of the micron-sized 3D fibrin channels, thus, mimicking angiogenesis and forming blood capillaries during the 21 days of *in vitro* culture.

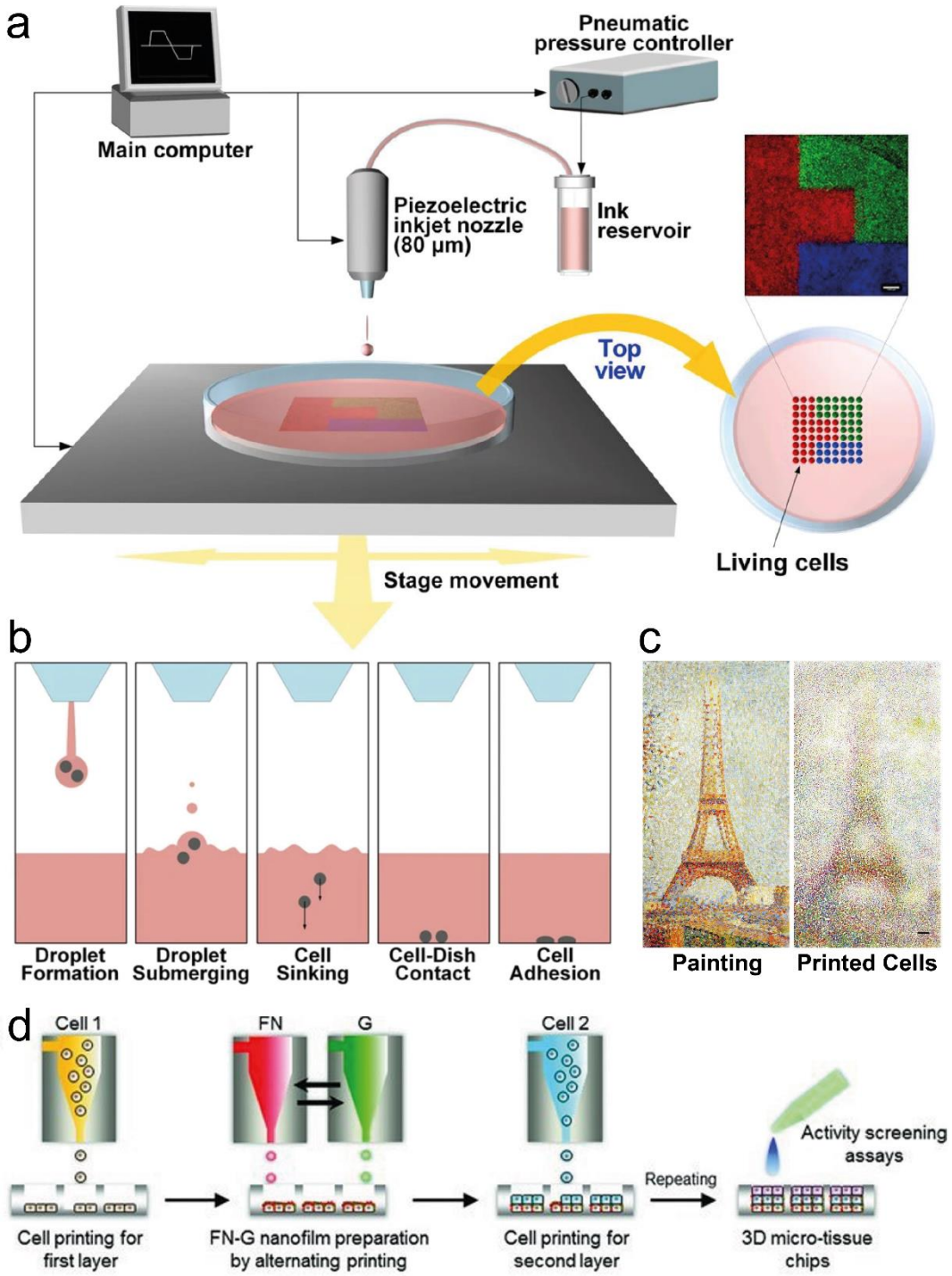

Figure 1.6: *Schematic illustrations of* ***(a)*** *cell printing in a liquid substrate to create cellular micropatterns, and* ***(b)*** *the cellular voyage from the inkjet nozzle to the bottom of the culture dish after traversing through the liquid culture media.* ***(c)*** *Cell density controlled printing, based on an Eiffel Tower painting as design source, to create micropatterns with cellular gradient, as imaged with the help of three different fluorophores (scale bar: 1 mm). [image taken from ref. [93] Copyright © 2017 Springer Nature].* ***(d)*** *Schematic illustration of step-wise construction of a liver-on-a-chip model by 3D cell micropatterning and subsequent testing of effect of different drugs, cosmetics and chemicals.* ***Cell 1:*** *Endothelial cells (HUVEC);* ***FN:*** *Fibronectin;* ***G:*** *Gelatin;* ***Cell 2:***

Hepatocytes (HepG2). [image taken from ref. [94] Copyright © 2013 WILEY-VCH Verlag GmbH & Co. KGaA, Weinheim].

More recent examples of 3D cell micropatterning involve co-printing and subsequent co-culture of multiple cell types, thus forming more complex constructs. Matsusaki et al. [94] developed a 3D liver-on-a-chip with different layers of hepatocytes and endothelial cells, the two most abundant cells in liver, as a model for drug and cosmetics screening and evaluation assays and an alternative to the use of animal models. Human hepatocellular carcinoma cells (HepG2) and human umbilical vein endothelial cells (HUVEC) were printed as single (HepG2), double (HUVEC/HepG2), and triple (HUVEC/HepG2/HUVEC) layers in 440-microwell plates, as shown in **Figure 1.6 (d)**, by a commercial piezoelectric inkjet printer (DeskViewer) for high throughput evaluations and to investigate the effect of cell-cell interactions. Fibronectin and gelatin layers were printed in between the cell layers to mimic the extra cellular matrix. The liver microtissues, thus formed, were incubated for 2 days and evaluated by liver function tests which revealed CYP3A4 and albumin secretions as confirmed by fluorescently labelled antibodies. Normal liver function was also confirmed by degradation of Vivid red enzyme to resorufin by CYP3A4 enzyme. For hepatotoxicity assay, the microtissue was incubated with troglitazone for 2 days, after which, the 3-layered microtissues showed higher cytotoxicity than single and double layered ones. Overall, with increasing the number of layers, the fluorescence intensities indicating albumin secretion, CYP3A4 secretion and CYP3A4 activity also increased successively. As liver plays a central role in metabolism, liver-on-a-chip based devices are going to become essential clinical and industrial tools and in such a scenario, inkjet bioprinting offers a very easy and fast route to construction of such devices.

A more complex, hybrid and multi-layered patterning of different mammalian cells was shown by Xu et al. [96] who fabricated a three cell composite hydrogel structure using a modified thermal inkjet printer. Human amniotic fluid-derived stem cells (hAFSCs), canine smooth muscle cells (dSMCs), and bovine aortic endothelial cells (bECs) were

suspended in calcium chloride in three separate cartridges and printed simultaneously on separate pre-determined locations on a sodium alginate and collagen composite solution. Several layers of printing and alginate cross-linking resulted in formation of hybrid 3D hydrogel with three cell types, thus, resembling a cross-species or chimeric tissue model. The circular hydrogel measured just under 1 cm in diameter with a half of the area covered by bECs, a quarter of the area covered by dSMCs and the remaining quarter of the area covered by hAFSCs. On 7-day *in vitro* culture, the cells showed anchorage to the scaffold, high viability of >90%, normal proliferation, and normal physiology and phenotypic expression. After 3-day *in vitro* culture, the construct was implanted subcutaneously in athymic mice for 2 weeks, after which the cells showed high viability and remained at their original locations within the hydrogel. Also, owing to their different functions, the hAFSCs, dSMCs and bECs were tested for differentiation, electrophysiology, and vascularization, respectively, immediately after printing, after 7 days of *in vitro* culture and after 4 weeks of *in vivo* implantation. The hAFSC implants were incubated in osteogenic culture medium *in vitro* for 1 week and then implanted for 18 weeks, after which, bone tissue formation was observed. All the dSMCs showed similar mean potassium current and voltage values as non-printed control cell sample. After 8 weeks of implantation, the scaffolds with bECs showed abundantly and significantly more vascularization than scaffold-only implants. Thus, the authors showed the feasibility of inkjet bioprinting for *in vitro* fabrication of 3D heterogeneous tissues.

Apart from developing lab-on-a-chip devices, a big proportion of the 2D and 3D cell micropatterning research is focussed on tissue engineering and, therefore, some of its examples have been discussed in the next section.

1.4.2 Tissue Engineering

Tissue engineering is one of the most important areas of application of 3D inkjet bioprinting. The multi-nozzle and layer-by-layer fabrication approach of inkjet bioprinting

helps converge and assimilate multiple steps of tissue engineering into a single broad step. As inkjet bioprinting is a drop-by-drop dispensing method, its application in tissue engineering has largely been limited to smaller scale tissue fabrication in comparison to other methods, such as extrusion bioprinting. However, it gains advantage in achieving a relatively higher, micron-scale printing resolution on tissue engineering substrates and scaffolds. For relatively simpler fabrication of small-sized structures resembling cartilage, bones, and straight tubular blood vessels, the use of conventional inkjet bioprinting with cell laden bioink is optimal, as has been shown in a number of previous research. For example, Gao et al. [51] printed a bioink consisting of acrylated peptides, acrylated polyethylene glycol (PEGDMA), I-2959 photoinitiator, and bone marrow derived human mesenchymal stem cells (hMSCs) with simultaneous photopolymerization to form cell-laden hydrogel structures measuring 4 mm in diameter and 4 mm in height using a thermal inkjet printer. The cells showed even distribution throughout the hydrogel, 80–90% viability 24 hours post-printing and, upon culture in chondrogenesis-specific and osteogenesis-specific media, proliferated and differentiated into cartilage-like and bone-like tissues through chondrogenesis and osteogenesis, respectively, as indicated by the increase in hydrogel compressive modulus, and secretion and deposition throughout the hydrogel of proteoglycans in chondrogenic differentiation and calcium in osteogenic differentiation. To fabricate blood vessel like tubular structures, Hewes et al. [97] used a piezoelectric inkjet printer with a single jetting device of 80 μm nozzle diameter. Human umbilical vein endothelial cells, HUVEC-turboGFP, were suspended in a mixture of alginate and fibrinogen and printed in a bath of calcium chloride and thrombin in the shape of a hollow cylinder. Free-standing tubular cell-laden hydrogel structures corresponding to blood microvessels and measuring 300 μm in diameter and 1–2 mm in height were, thus, obtained after just 2 minutes of printing for each structure. After 14 days of incubation in culture medium, majority of the cells were noted to have migrated towards the inner side of the scaffold and form a confluent monolayer similar to blood vessels, a process which shows similarities with angiogenesis.

While early research in tissue engineering remained limited to proof-of-concept studies and improving inkjet bioprinting technology by fabricating basic and small-scale cell-laden hydrogel structures, more sophisticated and tissue-specific inkjet bioprinting is being carried out in current research by adopting novel and more robust printing approach and developing hybrid inkjet bioprinting platforms. A novel approach of harnessing *in vivo* like cell-ECM interaction for cellular self-organization based tissue fabrication was shown by Park et al. [98] who patterned Detroit 551 and Hs68 human dermal fibroblasts with precisely controlled cell density on collagen hydrogel substrate through a piezoelectric inkjet printer. Post-printing cell-ECM interaction caused self-organization in the printed cells leading to formation of 3D cell-collagen microtissues. Also, precise and custom control over cell reorganization and 3D microtissue formation was achieved by controlled bioprinting with different cell densities, pattern size, and pattern shape, as confirmed by different sizes and shapes of the growing microtissues. The cells in the growing 3D microtissues showed elongated and stretched morphology with an even cell surface distribution of integrin α5β1, which is a marker for cell adhesion to ECM, and fibronectin, which is a marker for cell-cell and cell-ECM focal adhesions. Thus, the inkjet bioprinted microtissue was shown to be an accurate mimicry of *in vivo* tissues. Afterwards, a human skin model was constructed by inkjet bioprinting human epidermal keratinocytes on the patterned microtissue grown from Detroit 551 fibroblasts after 7-day culture. The bilayered skin model, thus produced, consisted of the upper epidermis and the lower papillary dermis microstructures at the dermo-epidermal junction. This research shows the potential of inkjet bioprinting to fabricate more complex and dynamic microenvironments of the human body. In an attempt to significantly increase the size of inkjet bioprinted tissue engineering scaffolds without increasing their fabrication time, Yoon et al. [99] developed an inkjet-spray printing method in which cell-laden bioink layers were printed with alternating fine spray of a cross-linking agent deposited by spray-coating technique as shown in **Figure 1.7 (a)**. To test their printing platform, NIH3T3 mouse fibroblasts and 293A human embryonic kidney cells were

separately suspended in sodium alginate and printed with alternating spraying of calcium chloride to form hydrogels, as shown in **Figure 1.7 (b – c)**, with excellent post-printing viability of the embedded cells. This method allowed free-form, high-resolution and multi-layered printing of cell laden hydrogel structures, ranging at a large scale from <1 mm to >10 cm in size for the first time, and at relatively faster printing speeds of up to 75 mm/s which is much faster than in most previous studies. Afterwards, Hs68 human dermal fibroblasts, suspended in alginate-GelMA blend bioink, were printed to form hydrogel and cultured for 2 weeks during which the hydrogels maintained their shape and the cells showed normal cell spreading morphology and physiological functioning as confirmed by staining nuclei, f-actin, and collagen type I secreted by the fibroblasts. This novel technique holds the potential to be extended to multi-nozzle inkjet printers to build even larger scale hydrogel structures.

In another novel approach, Kim et al. [100] combined inkjet bioprinting with extrusion bioprinting to build a novel Integrated Composite tissue/organ Building System (ICBS). The ICBS possessed the capacity to separately and simultaneously dispense four and five biomaterials from its inkjet and extrusion modules, respectively, and consisted of a printing platform with high positional accuracy of 2.5 μm, 1 μm and 10 μm in x, y and z coordinates, respectively. To test its utility and efficacy, the authors built a human skin model with a functional transwell system in a broad single step as illustrated in **Figure 1.7 (d)**. The transwell system, which helps in culture, growth and maturation of the cells, is fabricated with a sacrificial gelatin bottom layer and polycaprolactone (PCL) as the supportive mesh for dermis using the extrusion module. Human primary dermal fibroblasts (HDFs) were suspended in collagen hydrogel and printed with the pneumatic extrusion printing module to form the dermis. Human primary epidermal keratinocytes (HEKs) were suspended in keratinocyte growth medium and printed with the piezoelectric inkjet printing module to form the epidermis. After 14 days of culture, a mature *in vitro* skin model with stretched dermis and stratified epidermis and a very high spatial resolution and uniform cell distribution is obtained alongside high cell viability and

proliferation rates. Additionally, the keratinocytes showed a more widespread distribution of E-cadherin cell junction markers compared to the manually seeded control, representing that the printed cells in the skin model show tighter cell junctions and an enhanced and more functional cell to cell interaction. It can, therefore, be said that the recent trend in the application of inkjet bioprinting in tissue engineering is to actualize the *in vitro* inkjet bioprinting based fabrication of truly implantable tissues, such as skin, skeletal muscles, cardiac muscles, blood vessels, cartilage and bones, with favourable *in vivo* results.

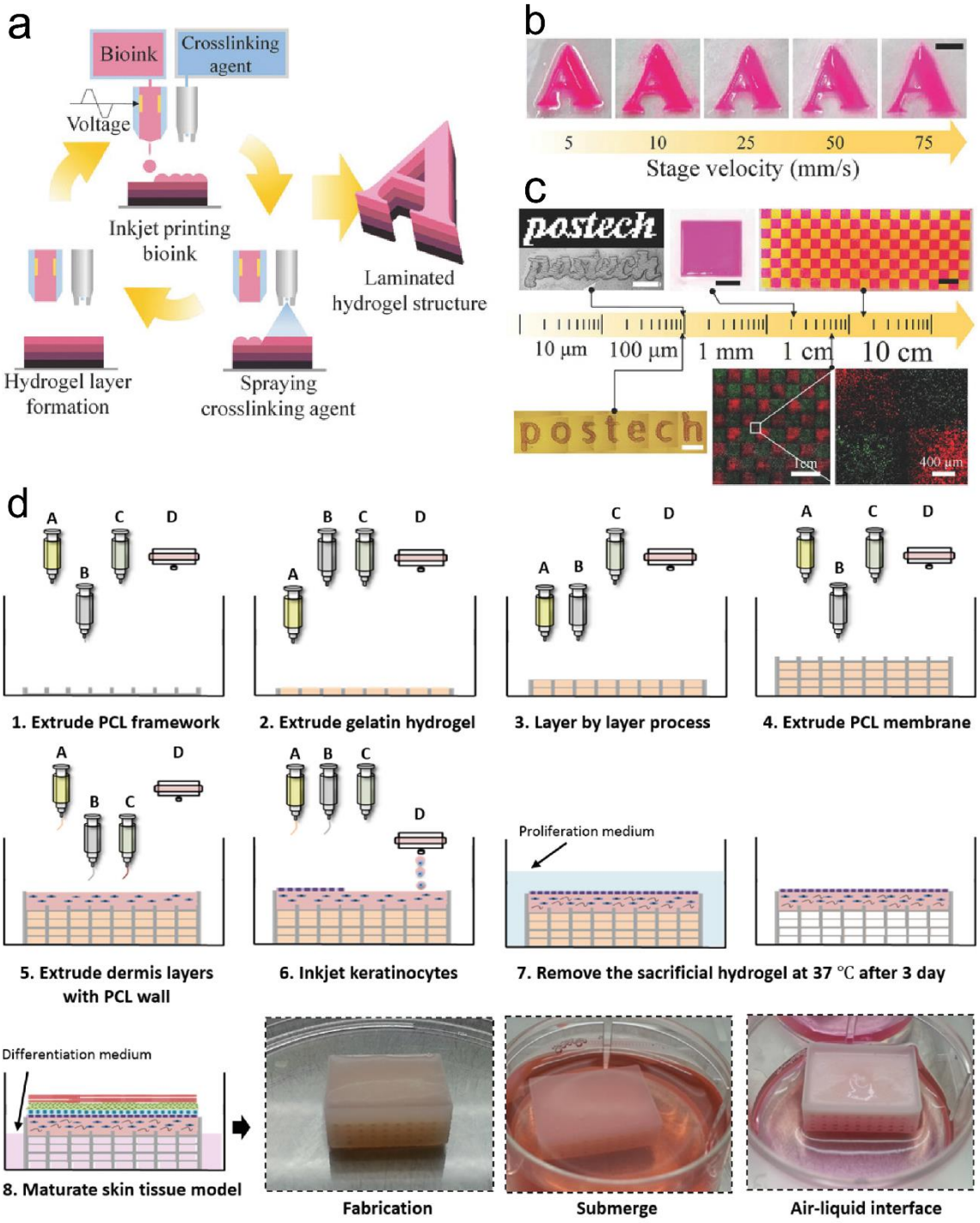

Figure 1.7:* (a)** *Schematic illustration of the inkjet printing – spray coating method for rapid fabrication of large cell-laden hydrogel scaffolds for applications in tissue engineering;* ***(b) *images of hydrogel letter-shape structures built at different printing speeds, showing minimal effect of speed and possibility of a rapid fabrication through inkjet bioprinting (scale bar: 5 mm);* ***(c)*** *images and light micrographs showing the range of scalability and high cell viability of the described method (scale bar: 1 cm in black, 1 mm in white unless otherwise mentioned). [image taken from ref. [99] Copyright © 2018 WILEY-VCH Verlag GmbH & Co. KGaA, Weinheim].* ***(d)*** *Schematic illustration of the step-wise fabrication of human skin model with functional transwell system using*

a novel Integrated Composite tissue/organ Building System. ***Nozzle A:*** *Sacrificial gelatin (extrusion);* ***Nozzle B:*** *supportive PCL (extrusion);* ***Nozzle C:*** *HDFs in collagen (extrusion);* ***Nozzle D:*** *HEKs in culture medium (inkjet). [image taken from ref. [100] Copyright © 2017 IOP Publishing Ltd].*

As larger and larger 3D tissues are fabricated, diffusion limitations begin to pose an increasingly bigger challenge in successful exchange of gases, uptake of nutrients, removal of wastes, and thus, the long-term survival of cells. In an attempt to solve the perfusion limitation problem in 3D tissue models, Negro et al. [101] printed a mixture of sodium alginate and PEG with crosslinkable active transglutaminase factor XIII to resemble the extracellular matrix (ECM), and simultaneously printed C2C12 muscle progenitor cells, suspended in sacrificial sodium alginate, inside the ECM layers using a piezoelectric inkjet printing based commercial Microdrop Autodrop system. On selective digestion of alginate with alginate lyase enzyme in pre-determined 3D pattern, microfluidic or perfusion networks resembling simple *in vivo* vascular networks were formed. The cells left in the space after the removal of sacrificial alginate showed normal proliferation while leaving enough space for easy perfusion of culture medium and gases. Afterwards, the authors also printed NIH 3T3 fibroblasts suspended in sodium alginate to show formation of hydrogel structures in various shapes, with high precision of 100 µm, with large size range of up to several centimetres, and with high cell viability of >90% at 4 hours post-printing. This work, thus, shows a high potential of inkjet bioprinting to solve one of the key challenges of *in vitro* tissue engineering and organ fabrication which is the inability of the current bioprinting techniques to integrate an intricate network of vasculature throughout the volume of the *in vitro* fabricated 3D tissues [102].

1.4.3 *in vivo* Bioprinting

When inkjet bioprinting is used to deposit cells directly at a desired site, such as a wound, in a living organism, the procedure is called *in vivo* cell printing and it holds substantial potential for improving the treatment of large burns, chronic wounds, and even deep

tissue injuries. Fast and aseptic healing of acute or chronic skin wounds is essential to prevent further infections or hypertrophic scarring. It is especially important if the wound has a large surface area and/or is deep such as those in the case of ulcers, burns and diabetic wounds. In such wounds, the conventional treatment strategies using bandages and ointments often fail or result in delayed healing. The application of natural or artificial skin grafts provide relatively better results, but such a clinical practice is often limited by the unavailability of such grafts or allergy and graft rejection [103]. For sorting out such limitations, Albanna et al. [104] applied the inkjet bioprinting technique to directly print living skin cells on skin wounds, as illustrated in **Figure 1.8 (a – d)**, and assess the wound healing capability. Skin wounds were created by surgical excision and removal of a small part of dorsal skin in murine and porcine models. A handheld laser scanner was then used to scan the wounds for creating their 3D maps to be converted to CAD for cell printing. For printing on the murine model, human cells were used as a proof-of-concept study to show the capability of inkjet bioprinting of constructing a human skin mimic and the printability of human skin cells and their post-printing potency of forming a functional skin. Human dermal fibroblasts and epidermal keratinocytes, both suspended in a mixture of fibrinogen and collagen, were filled in two separate cartridges and a third cartridge was filled with thrombin. First, the fibroblasts were printed on the wound, followed by printing of thrombin to cross-link the fibrinogen and form a stable matrix. After allowing cross-linking for 15 minutes, the keratinocytes were printed, again followed by printing of thrombin. The wounds showed epithelium formation by week 1 and complete wound closure by week 3. In comparison, the untreated wounds and wounds printed with cell-less fibrinogen-collagen-thrombin matrix showed open wound areas up to week 4 due to slow and poor epithelialization. Immunohistochemistry assay with anti-human nuclear antigen showed the post-printing presence of human fibroblasts and keratinocytes in the healing wounds up to week 3 and week 6, respectively. For the porcine models, allogeneic and autologous cells were used, with the same printing procedure, as autologous and allogeneic testing done on porcine models better mimic

the human skin healing in comparison to the murine model which has different skin healing rates and mechanisms. The wounds printed with autologous fibroblasts and keratinocytes showed faster closure, lesser contraction at the edges, higher re-epithelialization, and much intense network of blood vessels throughout epidermis and dermis by week 4 to week 8, thus, resulting in least scarring in comparison to the wounds printed with allogeneic cells, cell-less matrix and untreated wounds. On comparing the results to the manual cell spraying technique which is applied in current clinical practice, this bioprinting technique provided similar results. On the other hand, one advantage of this technique was that the cells could be deposited separately in an accurate and custom layer-by-layer pattern rather than depositing an unorganized mixture of both cell types which leads to failures or sub-optimal results as in the manual method.

All the previously mentioned inkjet printing technologies possess two (X, Y) or three (X, Y, Z) degrees of freedom while printing. In addition to forward-backward (X), left-right (Y) and up-down (Z) movements, a conventional robotic arm with remote centre of motion (RCM), as illustrated in **Figure 1.8 (e)**, can perform roll, pitch and yaw forms of movement. Printing with an inkjet bioink dispenser attached at the end of a robotic arm, however, can provide six degrees of freedom instead of the conventional maximum of the three Cartesian directions of movement [105]. Such a technique can enable cell printing in 3D space for fabricating complex *in vivo* mimics with precise cell/tissue localization, and in those medical cases which require direct cell application therapies, such as printing *in vivo* directly at the site of injury for faster healing of musculoskeletal injuries, chronic wounds and burnt skin. Robotic arm based 3D bioprinting, thus, has a high potential of solving the current challenges of healing critical tissue defects and developing minimally invasive surgery procedures as illustrated in **Figure 1.8 (f)**. Inkjet bioprinting can, thus, not only print the 2D patterns of cells in several layers to form a 3D tissue *in vivo*, but it will also have the capability to move around in 3D space with no restriction in the choice of printing location. Furthermore, with all the bioprinting technologies, *in vitro* biofabrication of vascularized soft organs, purposed for organ

transplantation, remains a challenge [90]. As described earlier, inkjet bioprinting can print one cell at time in any desired pattern. Combining it with the robotic six degrees of freedom of movement and the inherent capacity of cells to differentiate, organize and exhibit controlled growth, as seen during developmental morphogenesis [106], holds the potential, at least in theory, to revolutionize *in vitro* tissue and organ fabrication.

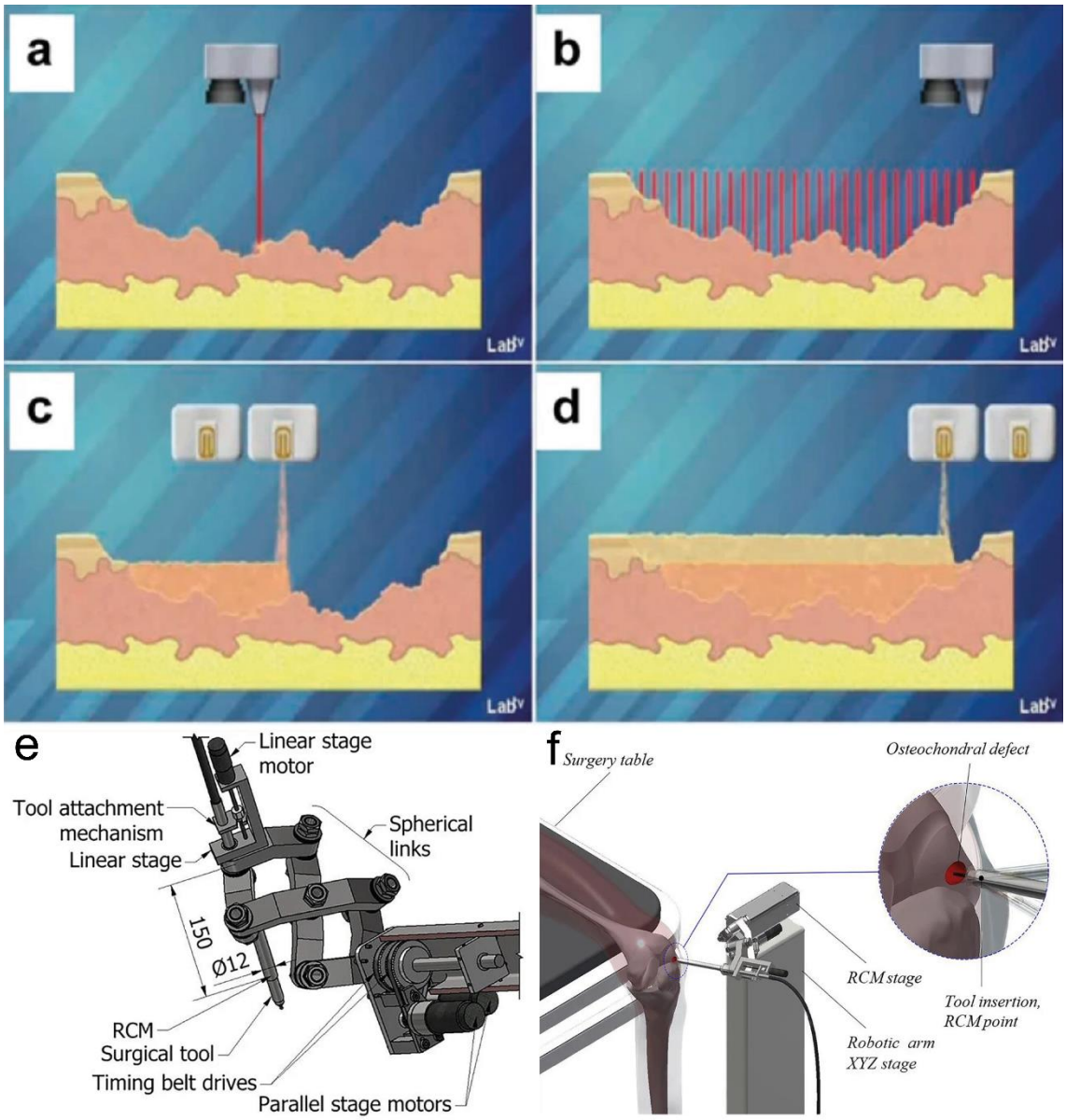

Figure 1.8 *Schematic illustration of in vivo inkjet printing of skin cells on an open wound for faster and scar-free healing.* ***(a)*** *A laser scans the contour of the wound in 3D;* ***(b)*** *the computer makes a 3D map of the volume to be printed and calculates the specific amount and type of the cells to be printed on the different sites of the wound;* ***(c)*** *the inner dermal cells are printed first;* ***(d)*** *the outer epidermal cells are printed on top of the dermal layer. [images a – d taken from ref. [104]*

*Copyright © 2019 Springer Nature]. **(e)** Schematic illustration of the design of a robotic arm with remote centre of motion (RCM) which confers six degrees of freedom (x, y, z, yaw, pitch and roll). The end of the arm can be fitted with an inkjet printing device as per the need. **(f)** Schematic illustration of a proposed set-up in which surgery and cell printing is being conducted in vivo on a diseased or wounded knee joint. [images e – f taken from ref. [105] Copyright © 2019 Springer Nature].*

An advanced application of *in vivo* cell printing, by combining it with gene transfection of the printing cells, was investigated by Xu et al. [107] by direct inkjet co-printing of porcine aortic endothelial (PAE) cells mixed with pmaxGFP plasmids into the subcutaneous tissues of athymic or nude mice. Before printing cells, fibrinogen and thrombin were printed in alternate layers *in vivo* into the subcutaneous tissue in order to form an implanted cuboid fibrin structure or scaffold, that could allow easy retrieval of cells later for analysis. After cell printing on it, the structure was left implanted for 7 days after which it was surgically removed, washed and analysed. The structure was found to retain its initial cuboid shape and the printed cells embedded in the fibrin structure showed high viability along with GFP expression, indicating successful gene transfection. Conducting such simultaneous procedures may help in the future in medical cases requiring cell transplantation, where any genetic or metabolic defect in the cells is corrected through appropriate gene transfection and the transfected cells are printed at the required location *in vivo*.

1.4.4 Biomolecule Printing & Patterning

Similar to cells and biomaterials, biomolecules, such as DNA and proteins, can be deposited and patterned using inkjet bioprinting either as 2D arrays and patterns or in multiple layers / droplets.

The use of inkjet printing to develop DNA microarray was first tried more than two decades ago. Goldmann and Gonzalez [108] used a commercial thermal inkjet paper printer to transfer DNA molecules on a solid support with very high resolution of 300 dpi

and high throughput, which turned out to be much superior to then existing robotic pipetting or blotting techniques of creating gene arrays. Specifically, the authors printed three different DNAs, which were plasmid Bluescript II KS^+, a 600 bp fragment of mouse glyceraldehyde 3-phosphate dehydrogenase (GAPDH), and 200 bp fragment of the catalytic domain of the human epidermal growth factor-receptor (EGFR). All the DNA solutions were diluted to 1 µg/µL and mixed with Pelikan 4001 blue ink for visual analysis of print output quality. The printing was done on nitro-cellulose membranes and nylon membranes. The printed samples on the membranes were baked and stored according to the established DNA hybridization protocol and then hybridized with radiolabelled probes. The authors were able to detect probe signals from the inkjet-printed DNA hybridized with cDNA probes with high sensitivity and after short exposure times of around 12 minutes. This research was a successful attempt for increasing the resolution and speed of DNA hybridization based gene analysis and also establishing inkjet printing as a promising method for DNA and other biomolecule deposition.

For an interesting non-biological application of developing transistors for bioelectronic devices, salmon DNA complexed with cetyltrimethyl ammonium chloride (DNA-CTMA) was inkjet printed to produce an electron blocking layer which could act as semiconducting layer and help develop bio-based organic light emitting diodes (OLEDs) and field effect transistors (FETs) [109]. Spatially controlled, high throughput, high resolution and picolitre scale deposition capabilities of inkjet printing allowed the development of such a bioelectronic device based on films DNA-complexes. In this research, the authors also used different organic solvents and deposition substrates to ascertain the best combination to make sure minimal or no coffee ring effect, which was made possible due to the versatility of inkjet printing technology in the choice of solvents to act as the base of the ink.

In case of proteins, such as enzymes, inkjet printing can help develop microarrays for applications such as enzyme based biomedical assays. However, inkjet printing has been found to affect the normal protein function, such as enzymatic activity, in some

research. Nishioka et al. [110] printed the enzyme horseradish peroxidase using a piezoelectric inkjet printer and observed decrease in enzymatic activity with increasing actuation voltage which in turn increased compression rates inside the jetting device. The authors thus concluded their results to be a caveat in the wider acceptance of inkjet printing technology as a tool to fabricate microarrays of biomolecules. In another research, however, Setti et al. [111] found no effect of a modified thermal inkjet printer on the activity of the enzyme glucose oxidase. Such differences in results among different research can be safely attributed to the fact that proteins and other biomolecules are highly diverse and heterogeneous and their stabilities are affected by a variety of factors. One method of eliminating protein damage or damage to any biomolecule in the ink from the jetting process is to modify the physical properties of the ink fluid, such as its surface tension, viscosity and rheological properties, so that it becomes easily printable at low actuation energies and thus suffering lower mechanical and thermal stresses. Di Risio and Yan [112] used a commercial piezoelectric laboratory inkjet printer and explored a range of different physical properties of the fluid ink containing the enzyme horseradish peroxidase by adding surfactants, such as Triton X-100, and viscosity modifiers, such as ethylene glycol, poly ethylene glycol and glycerol. The authors were able to show that once the ink was optimized for printing, the enzyme didn't get denatured significantly. To summarise, addition of appropriate entities, such as chaperones and small sugar molecules, to protect proteins from shear damage, and the modification of physical properties of carrier fluid and inkjet actuation to minimise mechanical and thermal damage would help in safely carrying out inkjet printing of any protein [113].

A rather unique application of inkjet printing of polypeptides and DNA was reported by Li et al. [114] who fabricated 3D polypeptide-DNA hydrogel structures for use as tissue engineering scaffolds. The authors prepared polypeptide-DNA conjugate for inkjet bioprinting of structures in various three-dimensional shapes. A polypeptide-DNA conjugate, containing several single-stranded DNAs (ssDNAs) grafted onto a

polypeptide backbone, was deposited layer-by-layer alternating with a DNA linker, containing double stranded DNAs (dsDNAs) with sticky ends complimentary to the ssDNA. The mixing of the two inks led to the *in situ* formation of an interlinked network of hydrogel by the hybridization between ssDNA and dsDNA sticky ends. Such a DNA-based hydrogel has several advantages, such as permeability to nutrients, biodegradability, and controllable responsiveness to pH, temperature, enzymes and light, when used as 3D cell-culture scaffolds for tissue engineering

Apart from DNA and protein, biomolecules, such as growth factors, have also been micropatterned using inkjet printing to open up newer possibilities, such as directed cell growth and differentiation for applications in understanding cell behaviour and in regenerative medicine. Ilkhanizadeh et al. [115] printed fibroblast growth factor-2 (FGF2), ciliary neurotrophic factor (CNTF) and foetal bovine serum (FBS) using a modified commercial thermal inkjet paper printer for the controlled or patterned steering of differentiation of rat embryo neural stem cells (NSC) on poly acrylamide based hydrogels. The authors were able to obtain expected and accurate results, part of which is shown in **Figure 1.9**, with the cells remaining undifferentiated in the areas printed with FGF2, cells showing markers for astrocytic differentiation (glial fibrillary acidic protein, GFAP) in areas printed with CNTF, and cells showing markers for smooth muscle differentiation (smooth muscle actin, SMA) in areas printed with FBS. The results further showed an increase or decrease in the number of differentiating cells upon increasing or decreasing the growth factor concentration, thereby showing the ability to control functional gradient of biomolecules by inkjet printing based deposition. In another similar research, Phillippi et al. [60] used piezoelectric inkjet printing to pattern and immobilize the growth factor bone morphogenetic protein 2 (BMP2) on fibrin films and showed controlled differentiation of mouse primary muscle-derived stem cells (MDSCs) cultured on the films. On culturing the cells under myogenic conditions, the authors observed development of osteogenic lineage in cells growing on the BMP2 printed areas and development of myogenic lineage in cells growing on the non-treated areas. The authors

thus were able to grow different subpopulations of cells on the same substrate or chip in a controlled pattern. Both of the above mentioned and other similar research have opened up exciting new opportunities for experimental studies on stem cells.

The research thus far has therefore shown that inkjet printing technology can be widely adopted to develop microarrays and micropatterns of genes, proteins, growth factors and other biomolecules wherever suitable and beneficial to do so for applications in a wide variety of areas of research.

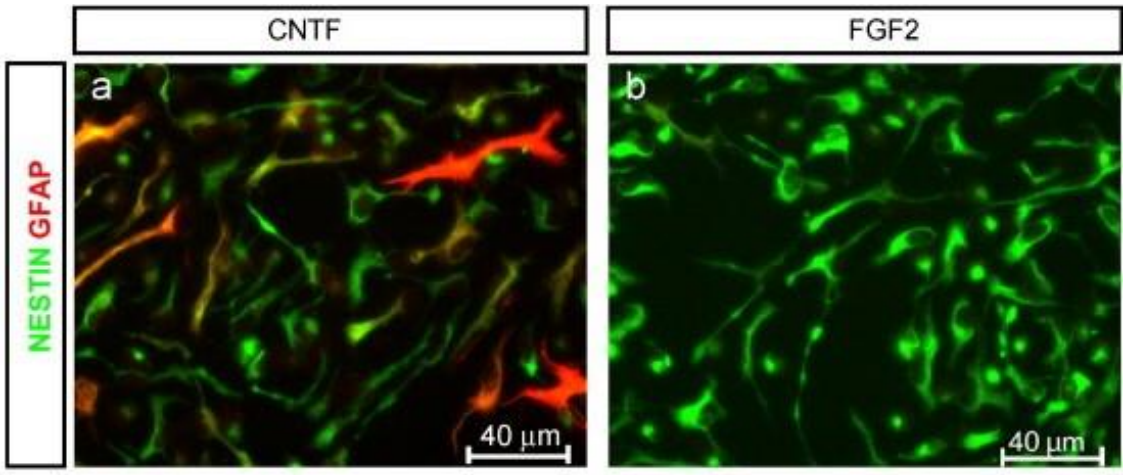

Figure 1.9: *Fluorescence images of rat embryo neural stem cells (NSCs) cultured on poly acrylamide hydrogel coated slides printed with growth factors CNTF and FGF2 on different areas of the slide using a modified commercial thermal inkjet paper printer.* ***(a)*** *Cells undergo astrocytic differentiation, characterised by their expression of glial fibrillary acidic protein (GFAP), only on CNTF printed areas and take up the red colour after immunocytochemistry.* ***(b)*** *On the contrary, cells not undergoing any differentiation remain as NSCs, characterised by their expression of nestin, and take up the green colour after immunocytochemistry. Such cells are found on both CNTF and FGF2 printed areas, but are the only cells found on the FGF2 printed areas. [image taken from ref. [115] Copyright © 2007 Elsevier].*

1.4.5 Drug Loading

Several drugs, therapeutics and biopharmaceuticals which require a special or more efficient mode or route of administration can benefit from inkjet printing technology as has been shown in numerous research. Loading precisely controlled amount of drugs into polymeric matrix, such as polycaprolactone and polyethylene oxide, through inkjet

printing has been shown to allow better control over the drug release profile [116]. Another interesting application was shown by Rowe et al. [117] who inkjet-printed tablets with four different kinds of complex oral drug delivery profiles. First, the immediate-extended-release tablets consisting of the drug chlorpheniramine maleate in two sections, a fast release section eroding within 10 minutes and an extended-release section eroding over 7 hours. Second, the breakaway tablets consisting of a middle fast eroding section which separated two drug releasing and slow eroding outer sections. Third, the enteric dual pulsatory tablets in which the drug diclofenac was printed with a separation in two areas within one continuous excipient phase causing the drug to release in pulses with lag time of 4 hours. Fourth, the dual pulsatory tablets which consisted of two diclofenac containing different excipient sections which dissolved in opposite pH, first immediately in low pH environments, and then after 5 hours in high pH environments. This research thus showcased inkjet printing as an all-in-one tool for formulating drugs with a variety of release profiles.

The capability of inkjet printing to load very tiny volumes of drugs on suitable carriers is particularly beneficial if the drugs have very low solubility in aqueous phase which in turn greatly diminishes their bioavailability. An early example [118] in this regard is the use of piezoelectric inkjet printing for the fabrication of tiny 60 µm diameter microspheres of the biocompatible copolymer poly (lactic-co-glycolic) acid loaded with the anti-cancer drug paclitaxel, which is poorly soluble in water. Such small volume packaging of drug molecules greatly enhances their bulk surface area to volume ratio and hence their bioavailability. Similarly, Boehm et al. [119] used a piezoelectric inkjet printer to load the anti-fungal miconazole on polymeric microneedles as shown in **Figure 1.10 a** and which can be used as topical patches for treating skin infections. Miconazole, which is an imidazole class of anti-fungal drugs, is poorly soluble in polar solvents, such as water, and therefore loading them directly on microneedles is an optimum mode of topical administration. The antifungal potency of the microneedle-loaded miconazole was tested against *Candida albicans*, which is associated with skin fungal infections. Swabs of *C.*

albicans were applied on Sabouraud dextrose agar plate, followed by the placement of miconazole loaded microneedle patch on the agar in direct contact with the fungus. Following an incubation of 24 hours, zones of fungal growth inhibition were clearly observed indicating high efficacy of the microneedle loaded drug and of the inkjet printing based drug formulation technique.

Apart from making drug formulations for better control over drug release or for better bioavailability of drugs, inkjet printing has also been used for loading medical devices with drugs or pharmacological agents. A prominent example of this application are drug eluting stents, which keep the blocked blood vessels open as intended and also release necessary drugs locally and slowly over extended periods of time for preventing blood clots and cell proliferation which could lead to fibrosis around the stent. In this regard, Tarcha et al. [120] inkjet-printed fenofibrate and a rapamycin derivative called ABT-578 on stainless steel stents coated with phoshorylcholine-linked methacrylate tetra-copolymer as shown in **Figure 1.10 b**. These stents possessed complex geometry in 3D space and inkjet printing proved to be a very suitable methodology for functionalizing them with the required therapeutic agents with 100% loading efficiency and 0% loss of drug functionality compared to the non-printed control. Additionally, an artificial *in vitro* drug elution test to observe drug release profile over a period of 24 hours showed no significant difference between the drug loaded by inkjet printing and the drug loaded by the conventional method of spray atomization. In a similar research, Wu et al. [121] fabricated a bone implant loaded with multiple drugs using a commercial laboratory inkjet printer for management and treatment of bone tuberculosis. The authors used poly (DL-lactic acid) or PDLLA as the base material of the implant as well as the excipient for the anti-TB drugs. The PDLLA implants were fabricated as circular discs of approximately 8 mm in diameter with four concentric layers consisting of two anti-TB drugs in the sequence of isoniazid–rifampicin–isoniazid–rifampicin. The drug release assays, conducted both *in vitro* and *in vivo* in the rabbit model, showed expected sequential release of isoniazid and rifampicin from outside to inside with the peak drug

concentrations detected from days 8 to 12, showing the capability of inkjet-printed implant to undergo controlled erosion for extended slow drug release.

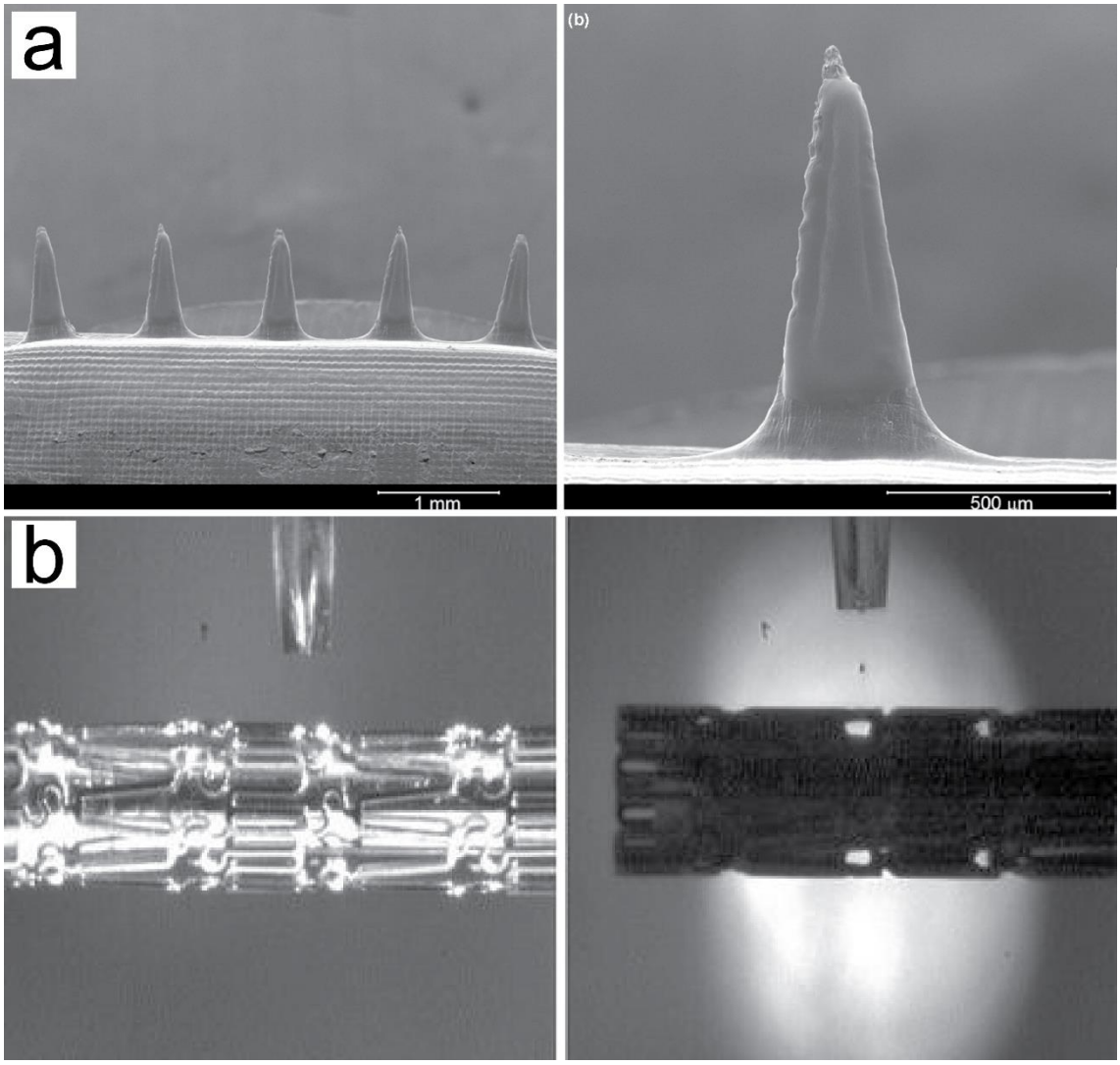

Figure 1.10: *Examples of drug loading using inkjet printing technology.* ***(a)*** *SEM image of an array of five polymeric microneedles (left) and a magnified SEM image of one microneedle (right) loaded with the drug miconazole on its top. [image taken from ref. [119] Copyright © 2014 Elsevier, Creative Commons License].* ***(b)*** *Close up lighted image (left) and strobed image with visible jetting droplet (right) of the nozzle of a jetting device depositing the rapamycin derivative drug ABT-578 on the stent. [image taken from ref. [120] Copyright © 2007 Springer Nature].*

The interestingly wide and innovative variety of utilization of inkjet printing for drug loading to achieve different pharmacological objectives has shown the versatility and adaptability of inkjet printing technology in this area and shows strong promise for inkjet

printing to become a mainstream tool for drug formulation and loading in the pharmaceutical industry.

1.4.6 Fabrication of Self-Propelled Biodevices

A relatively less common utilization of 3D inkjet printing technology is to fabricate self-propelling particles using any compatible material of choice. Self-propelled particles (SPPs) are entities which can utilize a variety of propulsion mechanisms by interacting with their surrounding environment, drawing energy from it and converting this energy from one form into another to initialize and maintain constant motion and propel in space and time. The concept of such self-driven particles is an area of active research in order to engineer and produce artificial SPPs with desired qualities and controllability. When their intended application is for biomedical and environmental research, the SPPs can be referred to as self-propelled biodevices (SPBs). Depending on the intended application, the SPB size can lie in the nanometre-scale [122, 123], or the micrometre-scale [124, 125], or the millimetre-scale [11, 12]. Inkjet bioprinting is suitable for fabricating SPBs in the size range of hundreds of micrometres to a few millimetres. Previous studies have investigated the applications of several SPBs, such as, silk fibroin Janus micro-rockets with catalase embedded within the SPB matrices for controlled propulsion in biological and non-biological liquid media [10]. These silk SPBs utilised chemical and physical mechanisms to propel in the liquid medium, such as human serum solution containing hydrogen peroxide. For chemical propulsion, for example, the catalytic reaction between catalase and hydrogen peroxide has been utilised, whereas, for physical propulsion, for example, poly (ethylene glycol) (PEG) has been used to create surface tension gradient to propel the SPBs at the air-liquid interface, a phenomenon which is also called Marangoni effect [10-12]. The effect of different parameters, i.e., hydrogen peroxide concentration, distribution of catalase enzyme within an individual silk fibroin SPB and number of layers deposited in 3D to create SPBs, on

the propulsion speed and orientation were also investigated [10, 11]. Promising results were observed when the SPBs displayed very rapid mixing of millilitre-scale volume of ink in water in a proof-of-concept experimentation as shown in **Figure 1.11** [12]. These SPBs thus have the potential to be used as micro-mixing devices in small fluid volumes for enhancing biomedical assays.

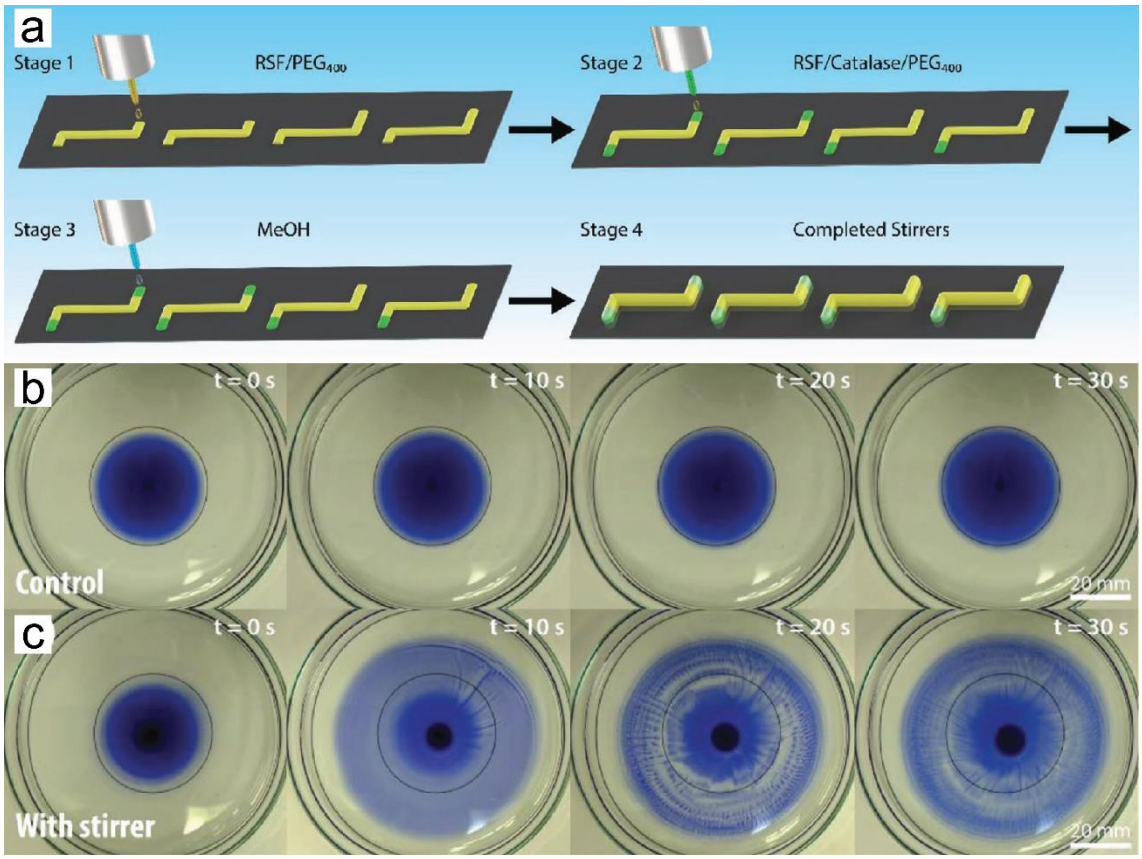

Figure 1.11:* (a)** *Schematic illustration of inkjet printing of self-propelled silk microstirrers.* ***(b and c) *The millimetre scale 3D silk fibroin microstirrers shows stirring capability with ink as sample and demonstrates a potential for use in biological assays. [image taken from ref. [12] Copyright © 2019 Wiley-VCH GmbH, Weinheim]*

1.5 Biomaterials

Biomaterials are biologically compatible (and environmentally friendly) materials which can be used for various purposes in biomedical science, for example, to build scaffolds for 3D cell and tissue culture and to build artificial skin grafts for burn victims. They are

the main ingredient used in bioprinting. The ideal biomaterials used for formulating bioinks or biomaterial inks should be capable of forming self-supporting 3D structures with high resolution and appropriate mechanical robustness. They should also possess good biocompatibility, biodegradability, and low cytotoxicity to facilitate cell growth either *in vitro* or *in vivo*. Based on the source of origin, biomaterials can be categorised as natural and synthetic. While natural biomaterials are sourced from living organisms, the synthetic ones are manufactured artificially. The natural and synthetic biomaterials are also combined to form composite biomaterials in an attempt to create biomaterials possessing only the advantageous features of its constituents, but none of their disadvantages or limitations.

1.5.1 Natural

Natural polymers such as fibroin, fibrin, collagen, cellulose, gelatin and alginate possess such characteristics which allow them to be commonly formulated with or without cells to form inks for 3D bioprinting. Besides, they are also capable of mimicking the extracellular matrix (ECM), which helps achieve optimum cellular growth and function and hence resulting in effective tissue regeneration. As the name suggests, natural biomaterials are obtained or derived from natural sources, such as natural proteins and extra-cellular matrices (ECMs). The micron scale architectural resolution of natural biomaterials makes them useful for a wide array of biomedical applications including in 3D bioprinting. An example of natural biomaterial is collagen which is derived from animal skin, tendon and placenta and has advantages such as the ability to be printed into membranes [126]. Another common natural biomaterial is gelatin which is derived from animal bones and can be printed as well [127]. Being of animal origin, natural biomaterials suffer from a few disadvantages, such as batch to batch variation in the precise molecular composition. This causes variability in results such as rheological parameters, which affects printability during bioprinting.

1.5.2 Synthetic

Synthetic biomaterials are artificially manufactured and are biologically compatible materials used in biomedical and environmental applications among others. Alongside natural polymers, synthetic polymers have been increasingly used to fabricate 3D structures. Common FDA approved examples include poly (ethylene glycol) (PEG), poly (lactic-co-glycolic acid) (PLGA), poly (lactic acid) (PLA), poly (caprolactone) (PCL), and poly (2 hydroxy ethyl meth-acrylate) (pHEMA). The advantage of synthetic biomaterials is that they are easy to mass produce without any batch-to-batch variation. As the synthetic biomaterials are biologically inert, they can easily be modified or functionalized with bioactive molecules for desired purposes, such as surface functionalization with cell adherence molecules for support in 3D cell culture. Moreover, synthetic polymers have tailorable processability, that is, viscoelastic flexibility by virtue of which the stress to strain ratio can be adjusted for different printing requirements and which is beneficial for high resolution of 3D bioprinting [128].

1.6 Silk Fibroin

Silk is a generic term used for several naturally occurring fibrous proteins, of which, the most commonly known is the one made by the larvae of silk moth *Bombyx mori* before its pupation. These cocoons are made of fibroin, a fibrous protein, stuck together with another protein called sericin as illustrated in **Figure 1.12 (a)**. Silk fibroin (SF) has been found to have excellent mechanical properties, biocompatibility and biodegradability [129], which makes it an ideal choice for fabricating 3D structures for biomedical and environmental applications. SF exists in three polymorphic forms, namely, silk I, II and III. Silk I is a water-soluble metastable form containing mainly helixes and random coils; silk II is a water-insoluble form containing mainly antiparallel β sheets of crystallized silk; and silk III is a threefold or triple helix polyglycine II helical structure that is very rare and exists at the water-air interface of silk solution. Similar to other fibrous proteins, SF has

repeating units of amino acid sequences as illustrated in **Figure 1.12 (b – c)**. The naturally occurring SF on a cocoon consists of three main hexapeptide domains of such repeating units, a crystalline domain (GAGAGS), an amorphous domain (GAGAGY) and a GAGAGA domain [130, 131]. Through hydrogen binding, the (GA)n motifs from antiparallel β sheet structures further stack through van der Waals forces and form hydrophobic nano crystallizations [130, 132]. In this study, the water-soluble silk I is used as the ink for 3D reactive inkjet printing alongside methanol, which turns it into the water-insoluble silk II structure. Fibroin can be extracted from cocoons by a process known as degumming in which it is boiled in sodium carbonate solution to dissolve and remove sericin, leaving behind the insoluble fibroin. Fibroin is dissolved by boiling it in calcium chloride or lithium bromide solution after which the solution is purified by dialysis in pure water. This fibroin solution is also referred to as regenerated fibroin because it is brought back to its natural liquid state as it exists inside the larvae. The fibroin in the solution is in the amorphous state, called as Silk I, which consists of water-soluble random peptide coils. Under different types of treatment, such as heating, mechanical shear, exposure to methanol, etc., the silk I converts to Silk II, which consists of water-insoluble and crystalline beta-sheets. This ability of chemical and structural transition has been utilised for controlled fabrication of 3D structures for applications ranging from scaffolds for tissue culture to vectors for drug payload delivery.

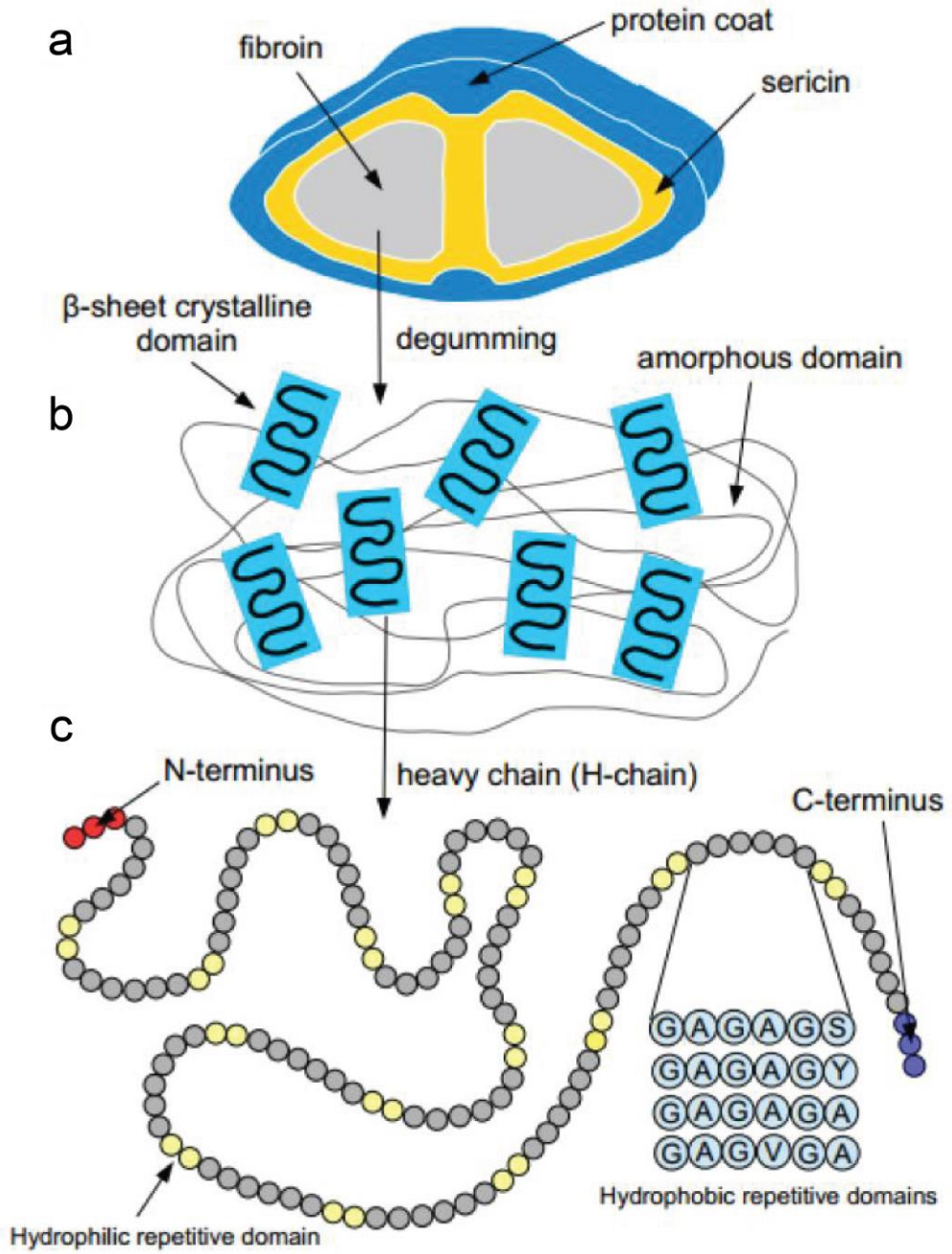

Figure 1.12: (a) *Schematic illustration of transverse section of raw silk fibre as found on the cocoon to show its internal structure. It consists of two fibroin fibres held together by sericin and covered with a protein coat.* ***(b)*** *Illustration of the fibroin b-sheets embedded across the amorphous fibroin matrix.* ***(c)*** *Illustration of the molecular structure of fibroin heavy chain (H chain) peptide consisting of repetitive hydrophilic and hydrophobic domains. The hydrophobic sub-domain is made up of different repeating units of hexapeptides. Here, the different amino acids mentioned are glycine (G), alanine (A), serine (S), and tyrosine (Y). [image taken from ref. [133] Copyright © 2016 MDPI].*

1.7 Applications of Silk Fibroin as Biomaterial

The *Bombyx mori* silk fibroin is a well-researched biomaterial with a variety of current and promising applications. Apart from conventional usage for manufacturing textiles, fibroin has been finding extensive applications in a wide variety of areas. It has been utilised extensively both in research, such as in cell culture scaffolds as well as in industry, such as in cosmetic products. For use as a biomaterial, fibroin from *Bombyx mori* silkworm features excellent mechanical properties [134], biocompatibility [135], biodegradability [136], ease of processing [137], and long term *in vivo* stability [138]. It has already been in use for a variety of biomedical applications, such as sutures for closing wounds, wound dressing, vascular prosthesis and structural implant, tissue engineering scaffolds, drug immobilisation matrix and drug delivery [137, 139-141]. This diversity in applications is possible because silk fibroin can be processed into different physical forms, such as gel, film or membrane, beads, needles and porous sponges. Fibroin and its modified derivatives are used as substrate coatings or films for 2D cell culture to study the effect on cell attachment, growth and differentiation. For example, substrate-coating with fibroin conjugated to poly (D, L-lactic acid) results in increased osteoblast attachment and proliferation [142]. On the other hand, substrate-coating with fibroin mixed with poly (ethylene glycol) causes decrease in L929 fibroblast cell attachment [143]. Tissue engineering is a major application area for silk fibroin and its modified forms. Fibroin based 3D scaffolds have demonstrated good cell attachment and proliferation of cartilage [144], ligament [145], bone [146] and vascular cells [147] in different studies. For better results, the 3D fibroin scaffolds also need to be functionalized with cell adhesion molecules, such as, BMP-2 (bone morphogenic protein) [148], and RGD peptide (Arginylglycylaspartic acid) [149], which is found in the extracellular matrices of most animal species. The relatively slower rate of biodegradation *in vivo* makes fibroin desirable for several drug delivery studies, which require slow and constant rates of therapeutic release. Small molecular drugs can be encapsulated non-specifically

in fibroin microspheres [150] or films [151] for release by passive diffusion. It has also been tested in several research for *in vivo* bone and soft tissue engineering in which it has shown little to no inflammatory or immune response in animals [138, 152, 153]. The drugs are usually loaded into porous fibrous biomaterials by adsorption, and as several drugs have good affinity for silk fibroin, the drug delivery systems based on silk fibroin have been extensively explored, such as porous silk fibroin hydrogels made by lyophilization which provide a sustained release delivery system for antibodies [138, 154]. Particles of silk fibroin containing different protein payloads have also been fabricated to release bone morphogenetic proteins with very favourable drug release profile [155]. Forms like needles made by silk fibroin conjugated with drugs or peptides are also have the potential use in the drug delivery system [156]. Silk fibroin is often mixed with other polymers such as chitosan [157], collagen [158] and gelatin [159] to form porous three-dimensional structures like matrix, gel and sponges to seed cells for the engineering in different types of tissues, such as bone, cartilage, skin and vascular tissue. Because the silk fibroin has the ability to retain moisture, it is widely used as wound dressing for burn victims.

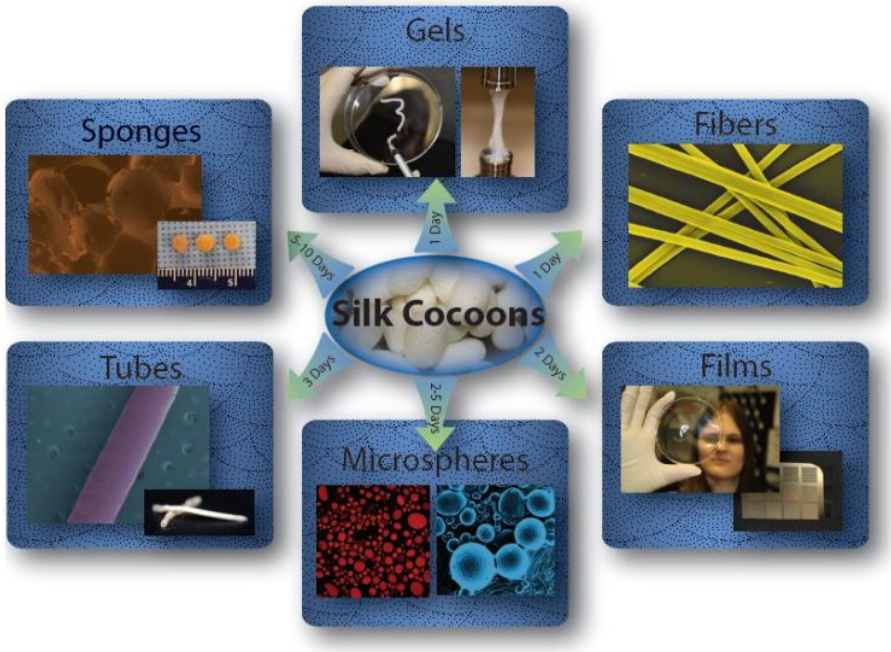

Figure 1.13: *Various forms of biomaterials fabricated from silk fibroin using different processing approaches. [image taken from ref. [137] Copyright © 2011 Nature America Inc.]*

1.8 Objectives and Scope of Thesis

In this thesis, I have explored the width and depth of novel applications of 3D inkjet bioprinting and put forward my own innovative applications based on my experiments and resultant findings. Consequently, I have shown the versatility of 3D inkjet bioprinting by utilising 3D bioprinted fibroin structures for three different applications. The first objective of this study is to use 3D fibroin structures as cell carriers for culturing nerve PC12 and SH-SY5Y cells. Afterwards, the live/dead assay and alamar blue cell proliferation assay are conducted to determine cell health and growth. Such 3D cell culture models provide a physiologically more relevant platform for *in vitro* cell culture. With respect to neuronal cells, the 3D fibroin structures also provide a platform as an *in vitro* as well as an *in vivo* nerve guidance conduit for treatment of nerve damage through degeneration or injuries. The second objective is to use 3D fibroin structures as self-propelled motors which are catalytically driven and surface tension driven in a liquid environment. One type of particles self-propels in aqueous hydrogen peroxide solution through the catalytic decomposition of the hydrogen peroxide fuel by catalase enzyme, which is contained in the catalytic regions of the particles. The other type of particles self-propels in pure water through surface tension gradient generated by a surfactant contained in and leaching from the particles themselves. Afterwards, the SPM propulsions are recorded through video capture, tracked for determining propulsion trajectory, and analysed. The data on propulsion behaviour and trajectory patterns of the different SPMs are compared to determine the best SPM geometry and propulsion mechanism for their future applications as micro-mixing devices for biological assays, such as ELISA, which could lead to significant enhancement in assay sensitivities. The third objective is to apply 3D fibroin structures as self-propelling sensors for generic detection of soluble contaminants in wastewater samples by exploiting the surface tension driven propulsion mechanism of the SPMs as the marker for estimating the surface tension values and their corresponding expected soluble contaminant levels.

This study can help in development of easy to use and fast acting sensors for on-site or in-the-field detection of contaminant levels in the absence of sophisticated laboratory equipment.

The scope of this thesis is in widening the applicability of 3D printing in biomedical and environmental research and to help the scientific community in acknowledging its versatility, ease of use and advantage over conventional fabrication approaches. The novelty of this thesis is in the demonstration of usability of 3D inkjet printing technology for minute adjustments and refinement in the parameters of printing of fibroin structures depending on their intended application. Examples of such adjustability include easy manoeuvrability for printing any desired geometric shape, precise deposition of enzyme or surfactant at designated locations, and very high accuracy in the volume of material deposited for fabricating the 3D structures which in turn guarantees reproducibility or minimal variations across different batches of fabricated samples. Another equally important novelty of this thesis is the demonstration of the already versatile silk fibroin as a biomaterial with even further multifaceted potential in future applications. While the rigid and insoluble silk II structure of fibroin makes it a suitable self-propelling particle and a compatible cell carrier, its porosity helps carry payload, such as an enzyme or a surfactant, as required. Additionally, its rough surface also assists cells in anchoring and adhering strongly, thereby making it optimum for use as a cell carrying scaffold. Thus, the overall scope of this thesis is to find newer biomedical and allied applications of 3D inkjet bioprinting using silk fibroin as the printed biomaterial structure at millimetre scale.

Chapter 2: EXPERIMENTAL METHODS

2.1 Materials

Bombyx mori silkworm cocoons were obtained from State Key Laboratory of Silkworm Genome Biology and Biological Science Research Centre, Southwest University, China. Silicon wafer substrates for printing 3D structures were purchased from Compact Technology Ltd, UK. Ultrapure high quality deionized water (DI water), filtered with a 0.2 µm filter, was used in all experiments. All other chemicals were commercially obtained and were of analytical grade. Sodium carbonate (Na_2CO_3) was purchased from Alfa Aesar. Calcium chloride ($CaCl_2$) was purchased from Fluka Analytical. Ethanol (C_2H_5OH) was purchased from Fisher Scientific. Cellulose derived dialysis tubes with molecular weight cut-off of 12,000–14,000 Daltons were purchased from Sigma Aldrich. PEG_{400} was purchased from Sigma Chemistry. Methanol (CH_3OH) was purchased from Acros Organics. The equipment used were hotplates, thermometers, beakers, Petri dishes, Eppendorf tubes, etc. as available in the laboratory.

2.2 Extraction of Fibroin

For the extraction of fibroin, which is also called degumming of silk, 5 g of silk cocoons were cut into ~0.25 cm^2 small pieces and rinsed and cleaned in de-ionized water. 2 litres of de-ionized water was taken in a large beaker and heated on a stirring hotplate to bring it to boil. 4.24 g of sodium carbonate was then added carefully to the boiling water to make a 0.02 M solution and allowed to dissolve with the help of a continuously rotating magnetic stir bar placed in the beaker. The thoroughly rinsed pieces of silk cocoon were then added into the solution and kept under constant boiling and stirring at 100–110 °C for 90 minutes, during which the sericin gradually got dissolved in water and fibroin fibre was left behind floating in water in the beaker. During boiling, the beaker was covered partially with an aluminium foil to prevent excessive loss of water as water vapour. Care

was also taken to keep the water level at 2 litres by occasionally adding pre-heated water into the beaker to compensate for the loss of water due to constant boiling.

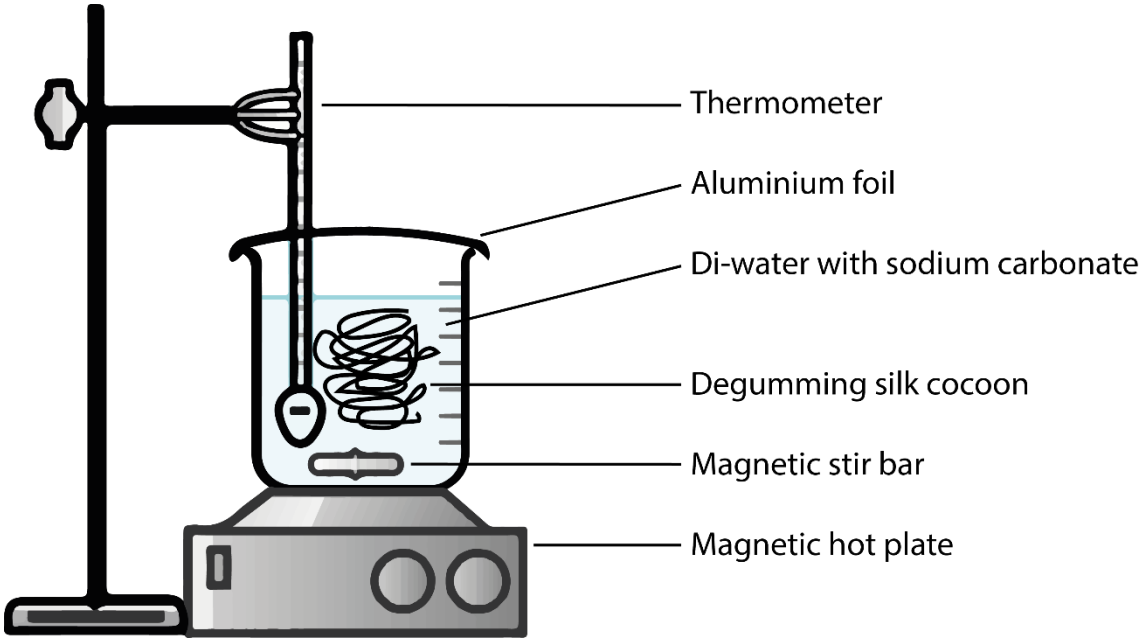

Figure 2.1: *Schematic illustration of extraction of fibroin by the removal of sericin or "degumming" of silk cocoon.*

2.3 Drying of Fibroin

The extracted fibroin was removed from the hot sodium carbonate solution carefully with the help of a glass rod or spatula. If the fibres were not tangled together then a Buchner funnel with filter paper was used to recover small fibroin pieces by pouring out the solution. Fibroin fibres were then washed thoroughly 3–4 times with de-ionized water to ensure total removal of sericin, spread out on a crystallization dish and kept in a drying oven at 60 °C and left overnight for drying.

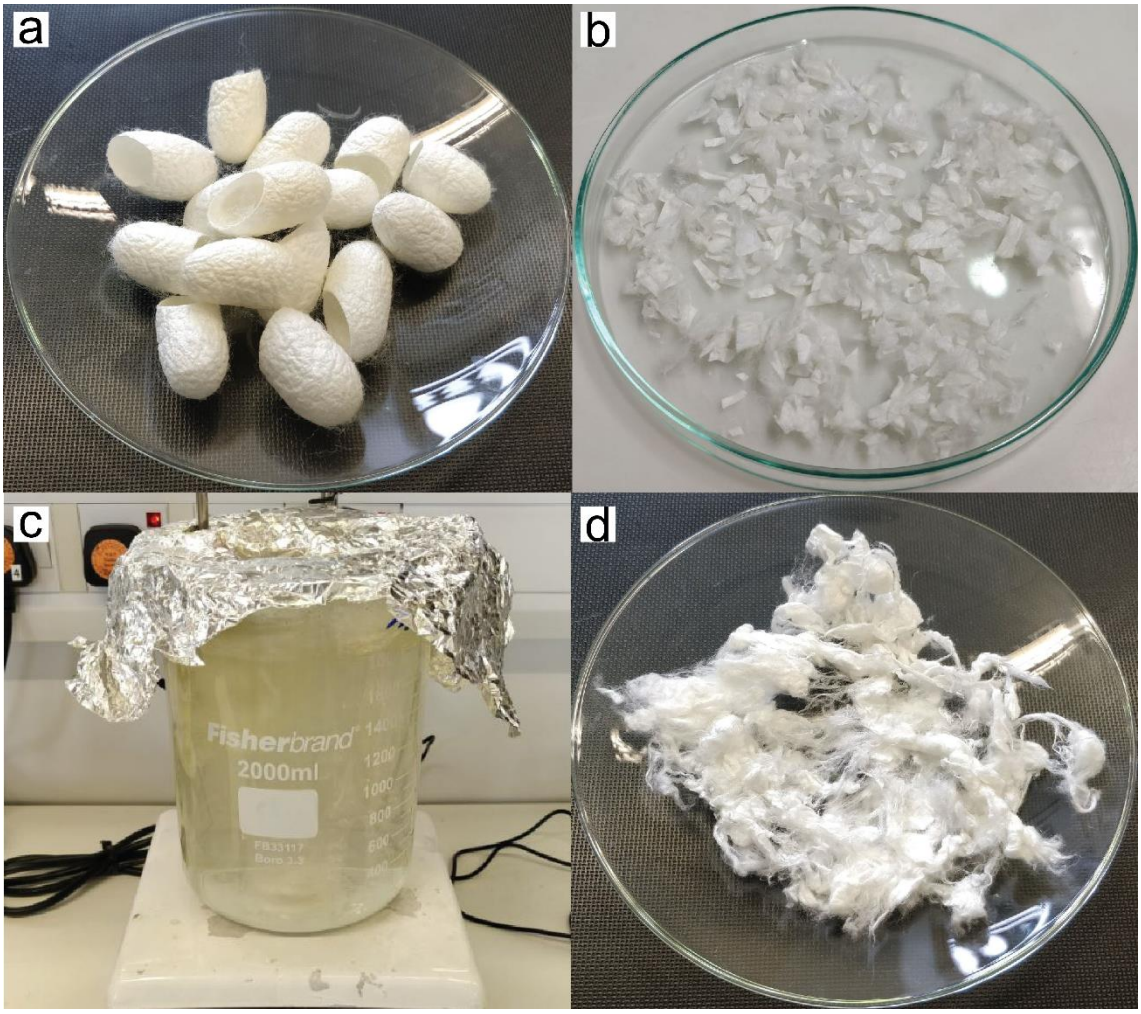

***Figure 2.2:* (a)** *Bombyx mori silk cocoons;* **(b)** *Cocoon cut into small pieces;* **(c)** *Fibroin extraction or degumming of silk;* **(d)** *Extracted and dried fibroin.*

2.4 Dissolution of Fibroin

For dissolving silk fibroin, a ternary solvent system containing 3.1 g of calcium chloride, 3.7 g of filtered ethanol and 4.8 g of filtered de-ionized water was prepared. This solution is also called Ajisawa's Reagent and has the molar ratio of $CaCl_2$:ethanol:water = 1:2:8 [160]. A small glass bottle was taken and a small magnetic stir bar was put inside it. Water and calcium chloride were then mixed in the bottle and the lid was closed to avoid loss of water from the exothermic reaction that ensued. The mixture was then stirred on a magnetic plate until all of the calcium chloride granules were dissolved. A few seconds of ultra-sonication treatment helped in faster dissolution. The solution, thus obtained,

was filtered into a small beaker with the help of a 0.7 µm filter and a 10 mL syringe. Ethanol was then poured into the calcium chloride solution and the beaker was moved gently to mix the contents well. The Ajisawa solution thus prepared was then poured into the two-neck round-bottom-flask and heated to 80 °C. A thermometer was placed in one of the necks, making sure that its bulb remained dipped inside the solution, to measure the solution temperature accurately. The other neck was blocked with a stopper to prevent evaporation. 1 g of extracted and dried silk fibroin was added to this solution as soon as the temperature reached and stabilised precisely at 80 °C. A small magnetic stir bar kept the solution mixed during dissolution. The fibroin was then left for dissolution for 90 minutes.

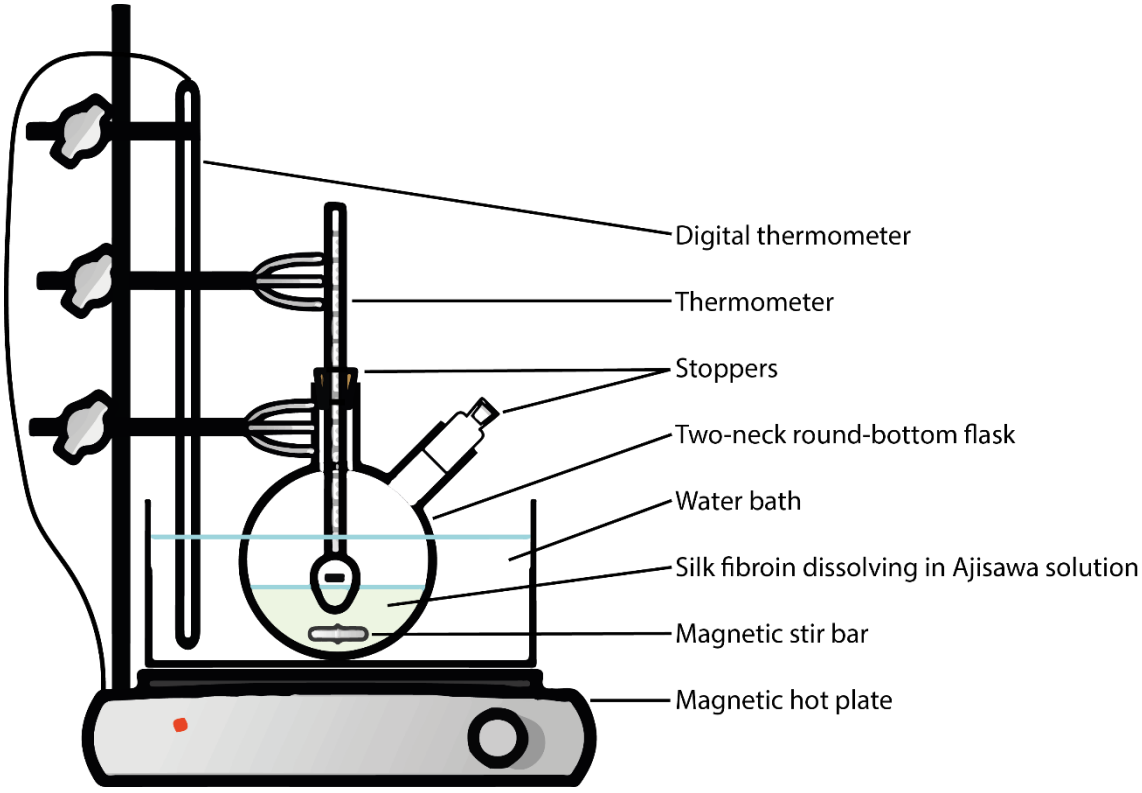

Figure 2.3: *Schematic illustration of dissolution of silk fibroin using Ajisawa solution.*

2.5 Dialysis of Fibroin Solution

After 90 minutes of dissolution, the round-bottom-flask was taken out of the hot water bath and the viscous solution of dissolved fibroin inside it was left to cool down to 40 °C.

The cooled fibroin solution was dialysed to make it free from ethanol and calcium chloride. For this, the fibroin solution was poured into a dialysis tube with one ligated end (molecular weight cut-off = 12,000–14,000). The open end of the tube was then carefully tied as well. The tube with fibroin solution inside was now kept in deionized water in a 2-litre beaker for the removal of calcium chloride and ethanol through osmosis. The water was changed at 1 hour, 2 hours, 3 hours since initiation and then left in fresh water overnight. The dialysing fluid or deionized water was changed again and kept for 1 hour the next morning. Conductivity measurement was taken at the beginning and before changing water each time. Water was changed further until its conductivity had got below < 3 μS). The whole process took around 12–15 hours. After dialysis, the fibroin solution inside the dialysis tube is less viscous with all the calcium chloride and ethanol removed and is slightly cream in colour. After dialysis, the dialysis tube was carefully cut and the fibroin solution was poured out into a beaker. The solution was then poured into Eppendorf tubes and centrifuged twice at 10,000 rpm for 5 minutes to remove undissolved fibroin and other particulate matter. The supernatant fibroin solution, called regenerated silk fibroin (RSF), was then poured into a 30 mL tube and stored in refrigerator at 4 °C. In RSF, the word ‘regenerated’ means that the fibroin fibres from silk cocoons are dissolved and regenerated into liquid state as found inside the silkworms.

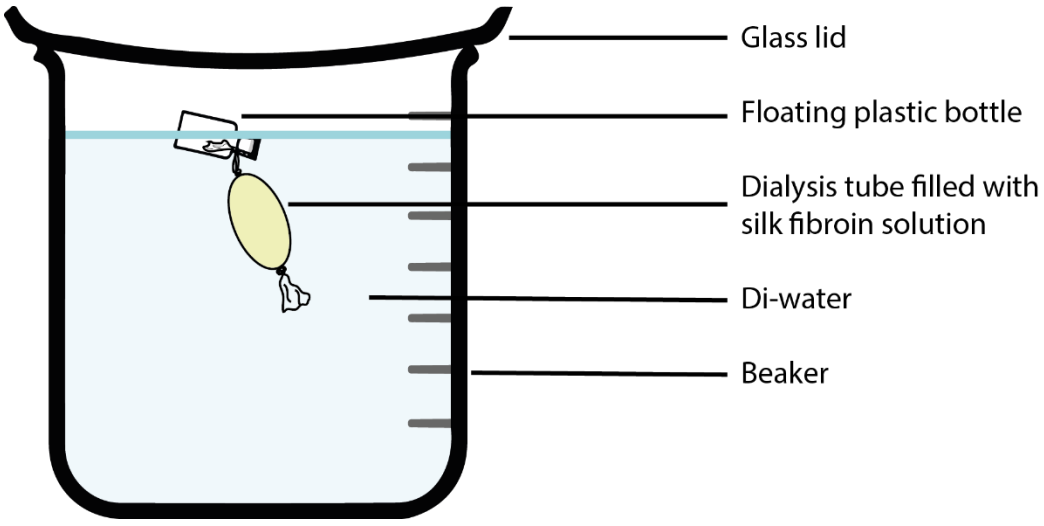

Figure 2.4: *Schematic illustration of dialysis of silk fibroin solution.*

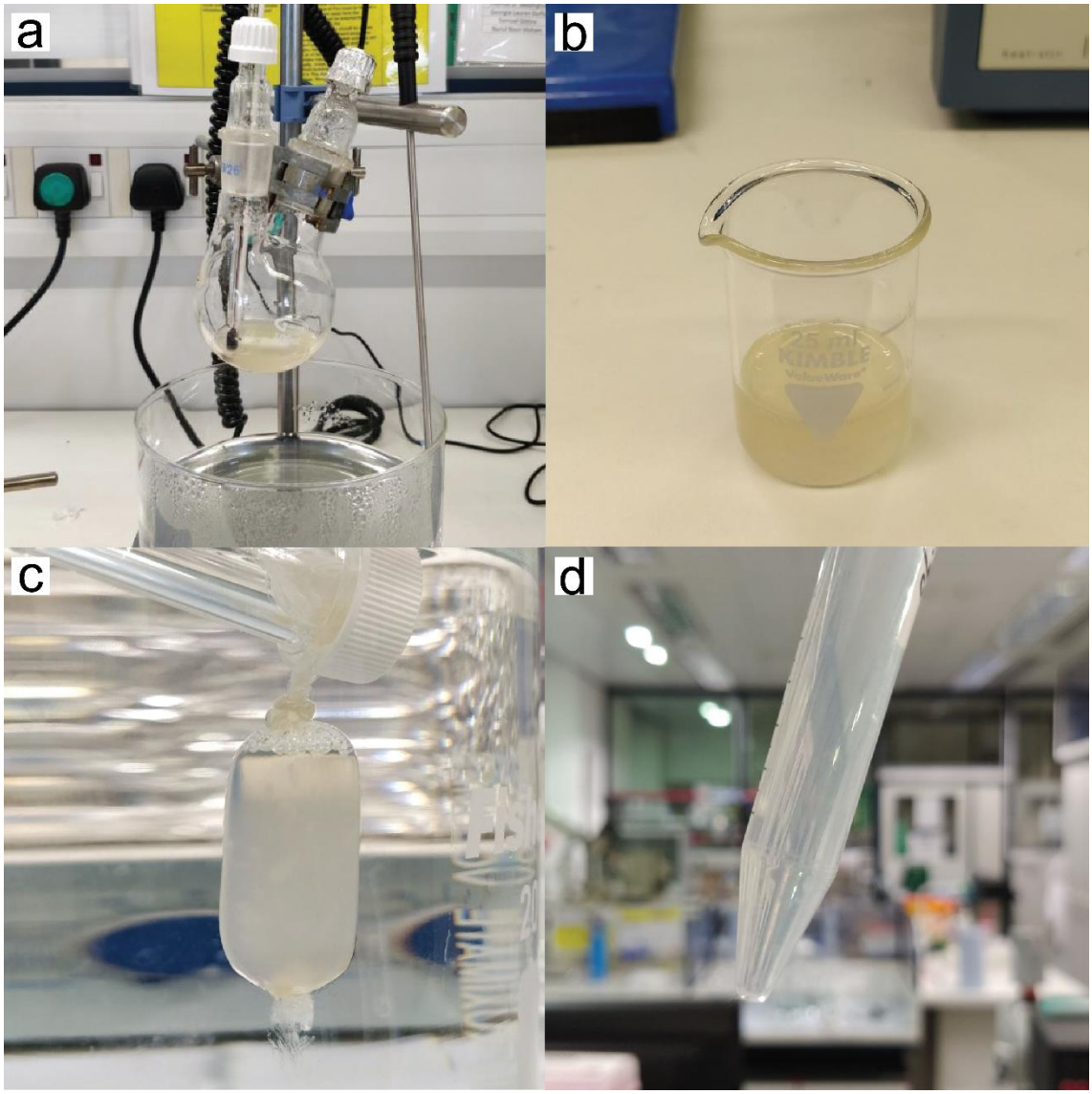

Figure 2.5:* (a)** *Fibroin dissolution setup;* ***(b) *Fibroin solution after dissolution;* ***(c)*** *Fibroin solution during dialysis;* ***(d)*** *Fibroin solution after dialysis and centrifugation.*

2.6 Fibroin Concentration Measurement & Storage

The fibroin solution concentration was determined by weighing small samples of known volume of solution before and after drying on microscope slides. Three clean glass slides were taken, numbered and their weights measured. 200 µL of dialysed fibroin solution was pipetted out on each one of these slides. Care was taken not to spill the solution off of the glass slide edge. The slides were then kept in a drying oven at 60 °C to let the water in the solution evaporate away. The slides were taken out after 1 hour and allowed to cool down for around 20–30 seconds. Their weights were measured again. The initial

weights of glass slides were subtracted from the final weights of glass slides having the dried fibroin solution on them. The difference in weight was the weight of silk fibroin per 200 µL of solution. Multiplying this value with 5 gave the concentration of silk fibroin in terms of mg/mL. Stock fibroin solutions of 40 mg/mL were made by adding DI-water to the original solution and stored at 4 °C prior to use. Following is the equation to calculate fibroin concentration:

$$\text{Silk Fibroin (w / v)} = \frac{W2 - W1}{V1}$$

Weight of clean glass slide = W2

Weight of slide with fibroin = W1

200 µL of fibroin solution = V1

Concentration of fibroin = w/v

Degumming of silk cocoons consistently revealed that they are composed of around 67 % fibroin by mass.

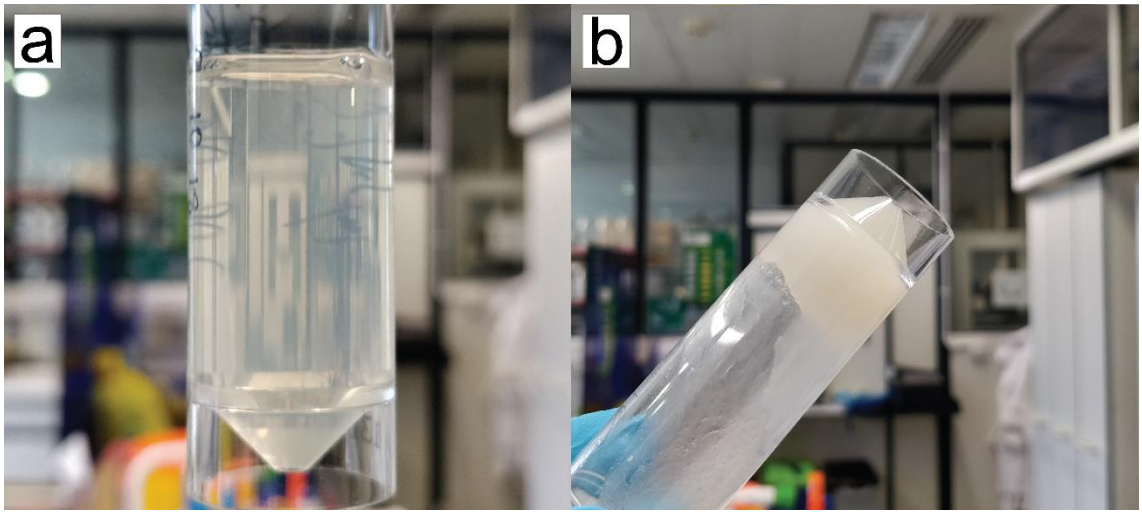

Figure 2.6: *Fibroin solution remains in liquid for almost a month before undergoing gelation. Camera pictures of fibroin solution* ***(a)*** *on day 0, and* ***(b)*** *after more than 1 month.*

2.7 Preparation of Fibroin Biomaterial Ink

The fibroin solution is mixed with PEG_{400} to prepare the primary biomaterial ink with their concentrations maintained at 40 mg/mL and 14 mg/mL, respectively, in the ink for printing the 3D fibroin structures. The addition of PEG_{400} to fibroin has been found to aid in better and firmer droplet formation and deposition during inkjet printing [10]. For the curing ink, 0.05 mg/mL of Coomassie brilliant blue is added to 100% methanol to impart a contrasting light blue colour. Methanol converts the fibroin random coils to rigid beta sheets and Coomassie brilliant blue helps in making the 3D structures better visible during various applications. The volumes of fibroin solution, PEG_{400} and DI water are taken proportionately as per the concentrations mentioned above to make a final volume of 1.5 mL ink per batch to store in the reservoir vials for printing.

2.8 Characterization of Fibroin Biomaterial Ink

2.8.1 Surface Tension Measurement

Surface tension is the elastic tendency of a fluid surface to attain minimum surface area at an interface. It is denoted by the Greek letter γ (gamma). Surface tension originates from the cohesive force between the molecules of the liquid. It is measured as the elastic stretching force (F) per unit length (l), as depicted in the following equation:

$$\gamma = \frac{F}{l}$$

Similar to several other physical characteristics of a material, the surface tension of a liquid is affected by temperature and presence of impurities. In case of water, for example, surface tension decreases with increasing temperature and on increasing the amount of dissolved solutes in most cases.

The surface tension of the fibroin ink was measured by a tensiometer (model number K11 MK4 manufactured by KRÜSS GmbH, Germany) using a standard Wilhelmy platinum plate probe measuring 19.9 x 10 x 0.2 mm in dimensions and having an immersion depth of 2 mm in the sample as shown in **Figure 2.7**. The tensiometer consists of a mobile stage with vertical freedom of movement to provide ample space for placing the probe and the sample and to allow precision in the immersion of probe in the sample. In the Wilhelmy plate method, the plate is vertically suspended from an electronic balance with the help of a thin metal rod. The plate is then slowly immersed just below the liquid surface while being kept perpendicular to the interface to form the meniscus. The force exerted on the plate by the liquid at the interface is measured as the surface tension of the liquid. As shown in **Figure 2.8**, a complete wetting or 0° contact angle prevents the need to include any correction factors, unlike the du Noüy ring method, in the calculation of surface tension. The surface tension is calculated by the following equation:

$$\gamma = \frac{F}{l \bullet cos\theta}$$

Here, γ denotes surface tension, F denotes force applied on liquid surface, l denotes length over which force is measured, and θ denotes angle of contact between the liquid surface and plate.

The tensiometer is connected to a touchscreen display panel running on Microsoft Windows platform for controlling the tensiometer, running the measurements and observing the results. For the measurement, 10 mL of fibroin ink was taken for each measurement conducted at an ambient temperature of around 20 °C. Each measurement was run for 50 minutes generating 3000 readings, of which, the last 10 readings were averaged automatically by the tensiometer to give the final reading of the surface tension of the sample. Five measurements were taken from different fibroin

samples to obtain the mean value. The measurements were taken on days 0, 7, 14, 21 and 28 since the preparation of fibroin ink and its storage at 4 °C. All the data were noted down and plotted in Origin™ to generate graphs to analyze the relationship between time and any potential changes in surface tension in the fibroin ink. The fibroin solution did not show any significant changes in its surface tension over the 28-day observation time period as shown in **Figure 2.9**. After more than a month, however, the fibroin ink converted from the usual liquid state into gel at random as shown in **Figure 2.6** with the total conversion taking 3 – 4 days.

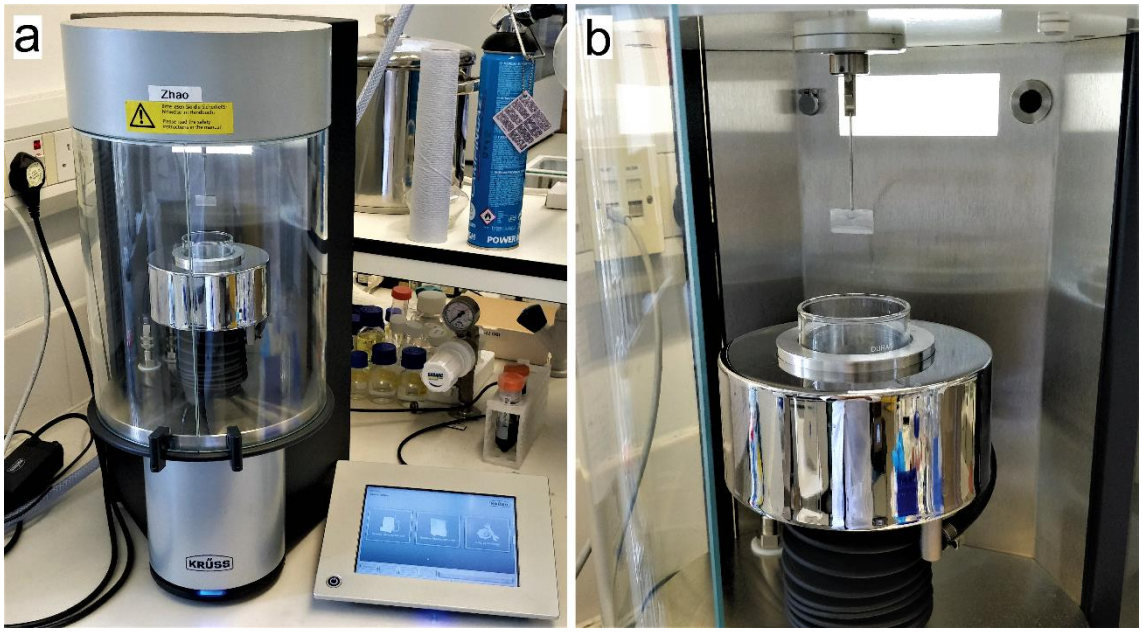

Figure 2.7: (a) *Tensiometer.* ***(b)*** *Close up image of stage showing the sample container and the Wilhelmy plate hanging from the micro-balance.*

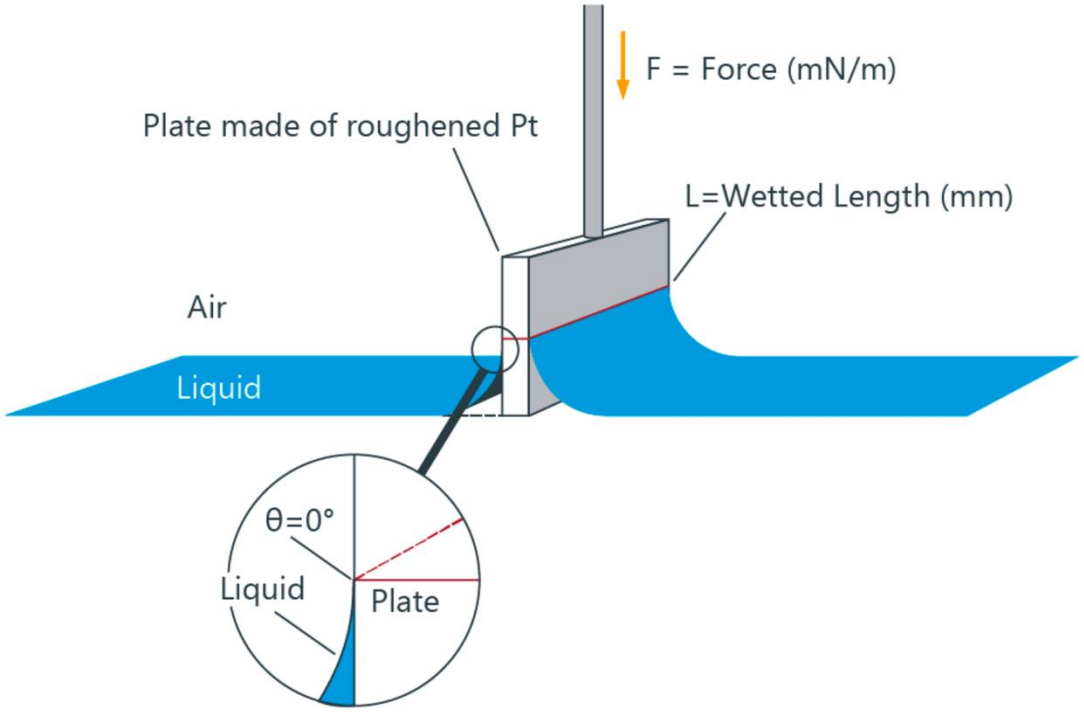

Figure 2.8: *Wilhelmy plate method showing an immersed plate with 0° contact angle owing to complete wettability of the plate. [image taken from ref. [161] Copyright © 2013 KRÜSS GmbH, Germany].*

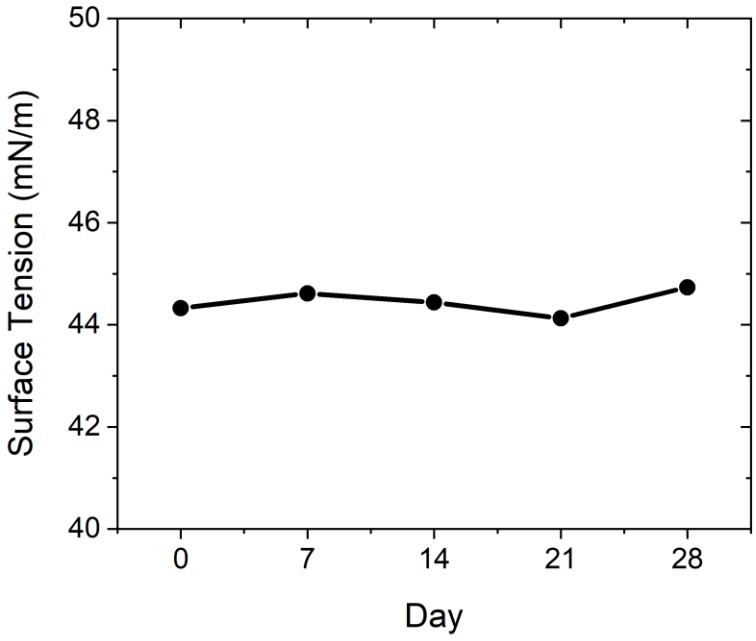

Figure 2.9: *Tensiometry data of fibroin solution taken once a week for 4 weeks. Surface tension were measured on days 0, 7, 14, 21 and 28 from the day of sample preparation. No significant difference was observed over the measurement time period, which indicates that no gelation or conformational changes of the molecular bonds had occurred at least within a month.*

2.8.2 Viscosity Measurement

Viscosity is the resistance of a fluid against deformation or flow caused by an external applied force. It is denoted by the Greek letter μ (mu). Like surface tension, viscosity originates from the cohesive force between the molecules of the liquid.

The viscosity of fibroin ink was measured once a week for 1 month to determine the effect of time on the chemistry or physical characteristics of the ink, which could be observed as changes in its viscosity. For this, a vibrating viscometer (SV-1A vibro-viscometer manufactured by A&D, Japan) was used as shown in **Figure 2.10**. The concept behind vibrating viscometer is that viscosity is calculated from the energy lost to the shear force applied by the vibration of the sensor plates. The more viscous the liquid, the more will be the energy lost for same amount of vibration. First, both the polycarbonate sample holding cup and the viscometer probe were rinsed with deionized water and dried with a clean tissue paper. Viscometer was then calibrated with deionized water, which has a known viscosity of 8.9×10^{-4} Pa.S or 0.89 mPa.S at 25 °C. For this, 2 mL of de-ionized water was pipetted into the sample holding cup and then the probe was carefully lowered just enough to submerge it into the water sample. The viscometer probe was then switched on to take the reading. After calibration, the viscosities of fibroin ink samples were measured following a similar procedure. Between each measurement, both, the probe and the sample cup, were rinsed and dried properly to remove the residue of the previous sample. The measurements were taken on days 0, 7, 14, 21 and 28 since the preparation of fibroin ink and its storage at 4 °C. As the viscometer calculates sample viscosity by comparing the sample data with the actual viscosity of water, care is taken to calibrate the viscometer on each day before taking the measurements. All the data were written down and plotted in Origin™ to generate graphs to analyze the relationship between time and any potential changes in viscosity in the fibroin ink. The fibroin solution did not show any significant changes in its viscosity over the 28-day observation time period as shown in **Figure 2.11**. After more than a month,

however, the fibroin ink converted from the usual liquid state into gel at random as shown in **Figure 2.6** with the total conversion taking 3 – 4 days.

Figure 2.10: *Viscometer.*

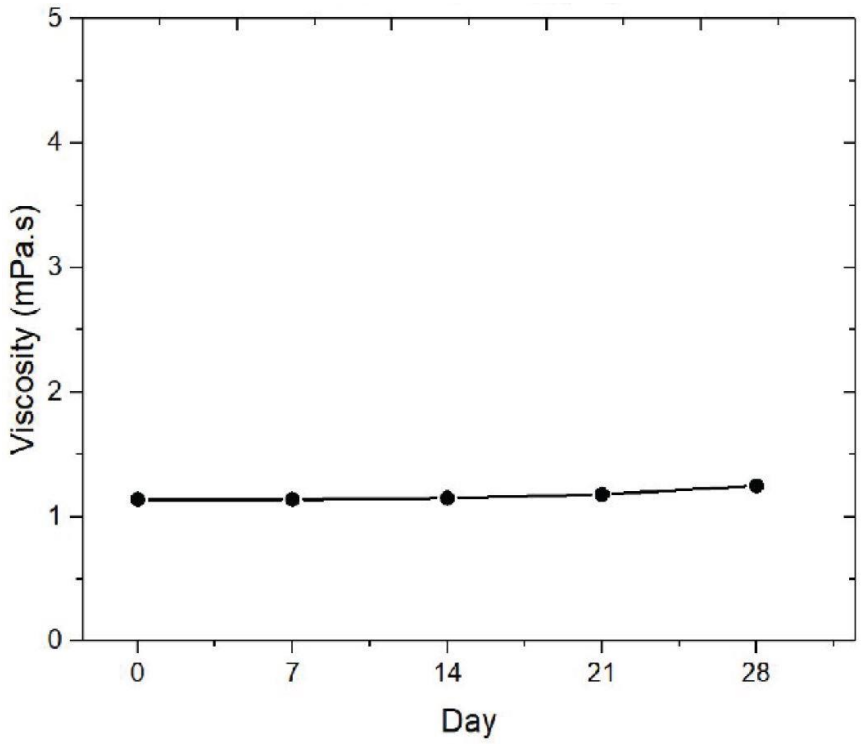

Figure 2.11: *Viscometry data of fibroin solution taken once a week for 4 weeks. Viscosity was measured on days 0, 7, 14, 21 and 28 from the day of sample preparation. No significant*

difference was observed over the measurement time period, which indicates that no gelation or conformational changes of the molecular bonds had occurred at least within a month.

2.8.3 UV-Visible Absorbance Spectrophotometry

Spectrophotometry is a branch of spectroscopy which quantitatively measures the absorbance or reflection or transmission of electromagnetic waves by a material as a function of wavelength. This technique is useful in the identification of unknown materials in a given sample.

The absorbance spectra of fibroin ink were measured once a week for 1 month to determine the effect of time on the chemistry of the inks, which could be observed as changes in its absorbance spectra. For this, a UV/Vis spectrophotometer (model number 6715 manufactured by JENWAY, UK) was used as shown in **Figure 2.12**. Spectrophotometry is a laboratory technique utilized for the quantitative analyses of different compounds present in a sample. Its working principle is based on the fact that different compounds absorb incident energy or electromagnetic radiation at different wavelengths. This absorption of specific wavelengths is determined by the natural vibrational energy of the chemical bonds of different compounds present in the sample. During the measurement, a beam of light with the wavelength range of 200 nm to 600 nm passes through a cuvette which has a path length of 10 mm and is holding 500 µL of the sample. The intensity of the transmitted light is measured to generate the absorbance spectra graph depicting absorbance intensity (in arbitrary units) against wavelength (in nm).

$$\text{Absorbance (A)} = -\log_{10}\frac{\text{Intensity of Transmitted Light}}{\text{Intensity of Incident Ligtht}}$$

$$\text{or, A} = -\log_{10}\frac{I(\lambda)}{Io(\lambda)}$$

First, the quartz cuvette was rinsed with de-ionized water and dried with a clean tissue paper and dry air. A baseline was then generated in the spectrophotometer with deionized water because all the samples to be tested contained water as solvent. For this, the cuvette was filled with 500 µL of deionized water and placed into the cuvette holding chamber in the spectrophotometer. The spectrophotometer was then made to take the baseline reading. After this, the samples' absorbance readings were taken following a similar procedure. Before each measurement, the cuvette was rinsed and dried properly to remove the residue of the previous sample. The measurements were taken on days 0, 7, 14, 21 and 28. As the spectrophotometer generates sample absorbance spectra by comparing the sample data with the baseline data, care was taken to generate water baseline on each day before starting measurements. All the data stored in the spectrophotometer were transferred to the computer using the JENWAY 67-series software and copied into the Microsoft Excel sheet. The data were then imported and plotted in Origin™ to generate graphs to analyze the relationship between time and any potential changes in chemical bonds in the fibroin ink. The fibroin solution did not show any significant changes in its UV-visible absorbance spectra over the 28-day observation time period as shown in **Figure 2.13**.

Figure 2.12: *UV/Vis Spectrophotometer.*

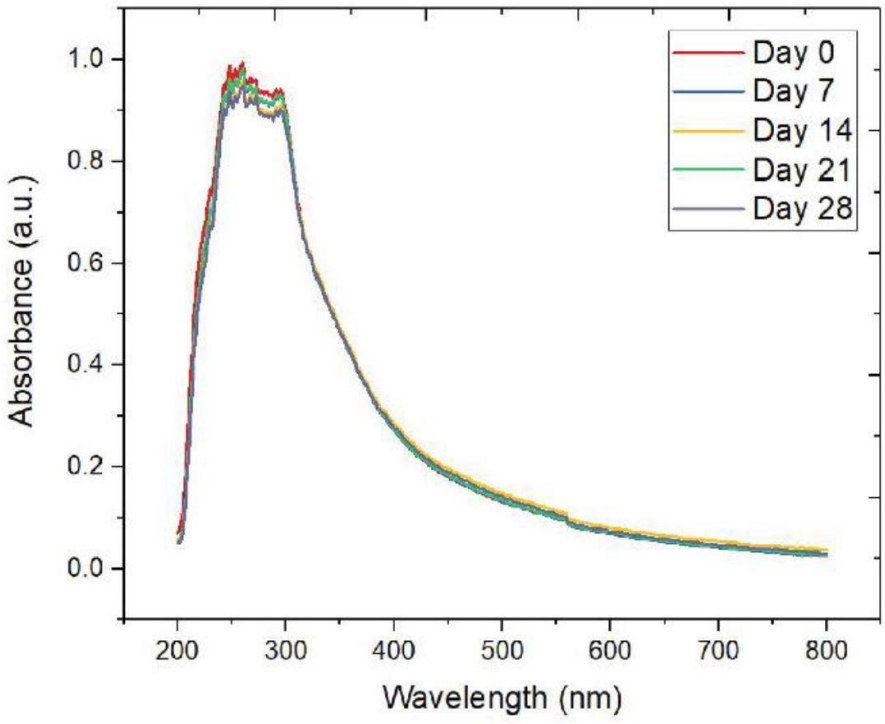

Figure 2.13: *UV-Visible spectrometry data of fibroin solution taken once a week for 4 weeks. No significant difference is found across the observation period. UV-Vis absorbance spectra of fibroin solution measured on days 0, 7, 14, 21 and 28 from the day of ink sample preparation. No*

significant difference is observed over the measurement time period, which indicates that no gelation or conformational changes of the molecular bonds have occurred at least within a month.

2.9 3D Inkjet Printer

A custom-built 3D inkjet printer was used for drop-on-demand (DoD) printing of fibroin biomaterial ink to fabricate millimetre-scale fibroin structures in different geometrical shapes. The jetting devices used in the printer were manufactured by and purchased from MicroFab Technologies Inc. These devices have piezoelectric material inside them which generates pressure pulses in response to controlled electrical signals received by the software programme. They have a glass nozzle with 60 µm inner diameter for jetting out the ink. The programme used for digitally controlling and manoeuvring the printer was built with on the LabVIEW platform (National Instruments Corporation, USA). Besides controlling the printer, the programme also controlled the amount and spatial position for the ejection of droplets. The spatial position was pre-determined by designing the geometrical shapes of the SPPs in Microsoft Excel, in which, the droplets are recognised as coordinates in X–Y plane when read by the programme. Silicon wafer, which is relatively more hydrophobic than a glass slide, is used as the substrate on which the fibroin structures were printed. Hydrophobicity helps in giving the structures accurate 3D shape by reducing the spreading of droplets after they have fallen on the substrate.

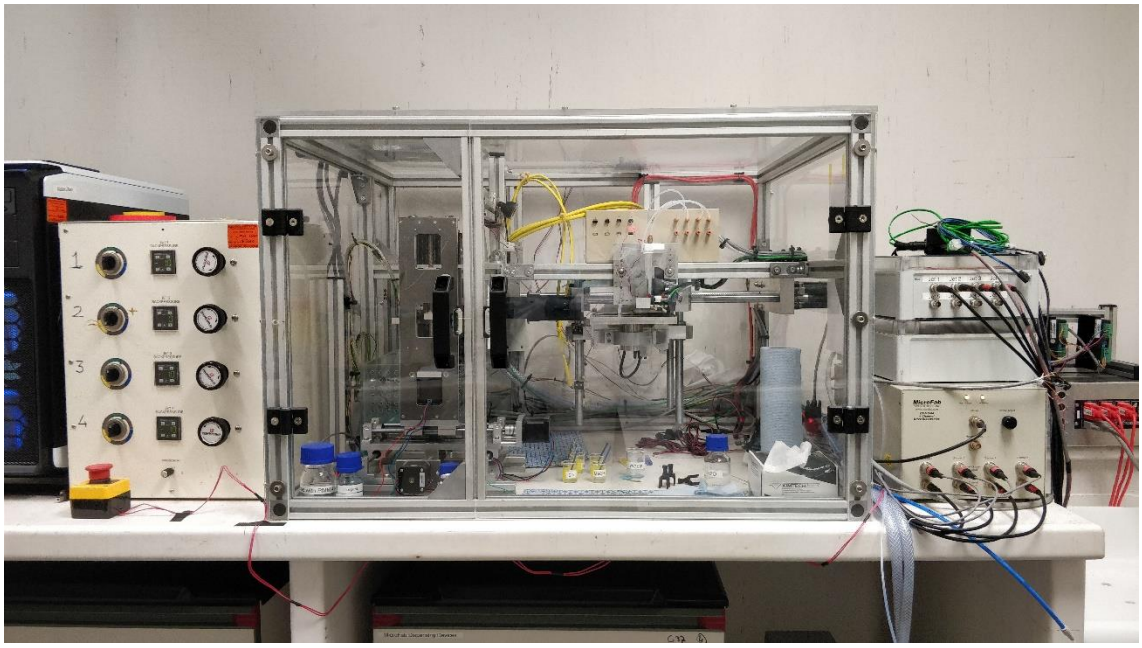

Figure 2.14: *The custom-built 3D inkjet printer.*

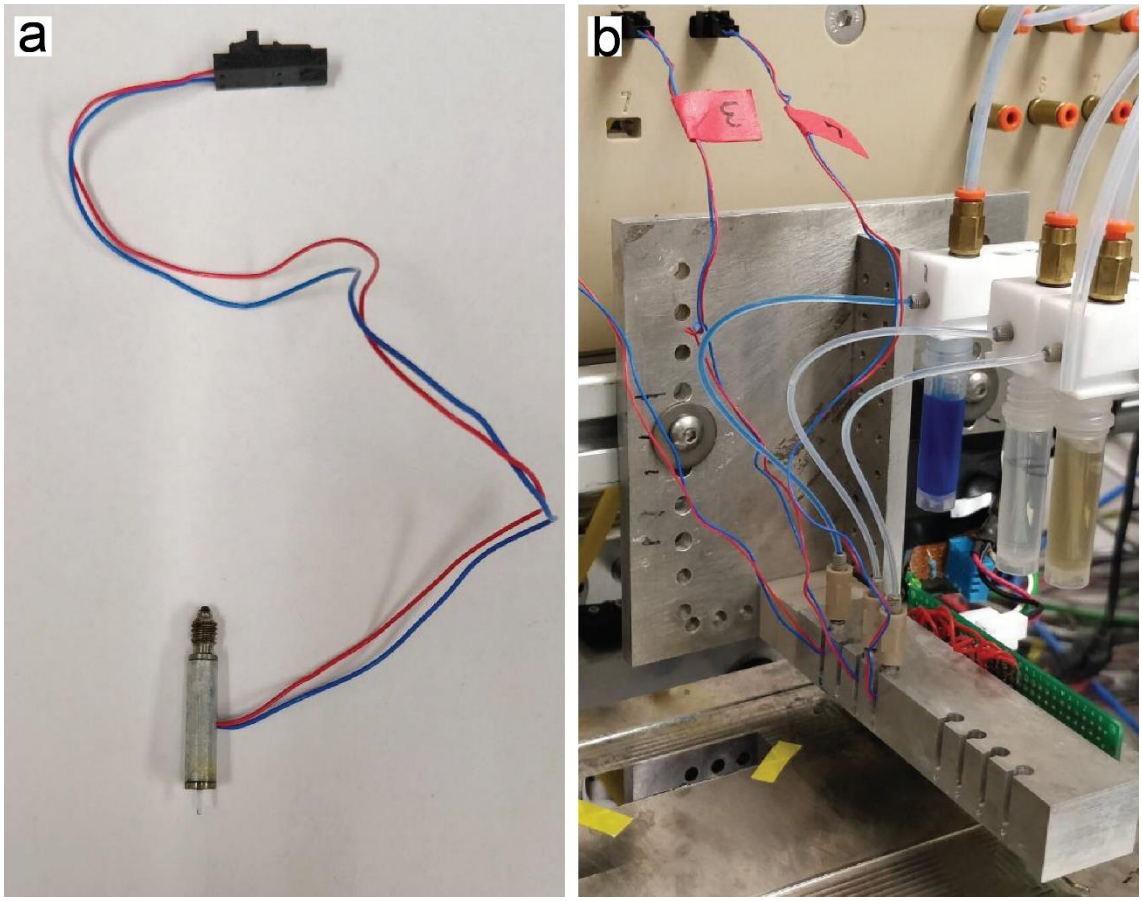

Figure 2.15: (a) *A jetting device used in the printer;* ***(b)*** *The printer stage with the inks and their respective jetting devices plugged in their separate channels and a silicon wafer substrate which is carefully stuck in place with adhesive tapes.*

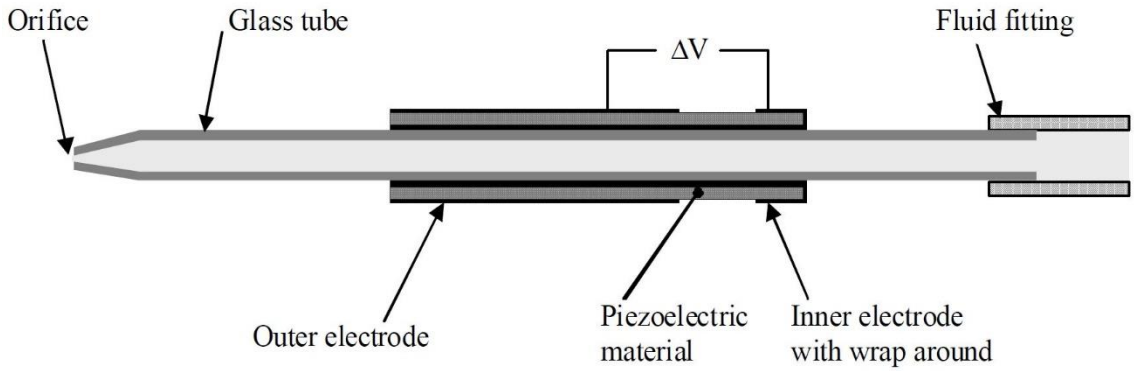

Figure 2.16: *Schematic illustration of the longitudinal section of a jetting device. [image taken from ref. [162] Copyright © 2012 MicroFab Technologies, Inc., USA].*

2.10 LabVIEW Programme to Run the Printer

A custom programme built on the LabVIEW platform was used to control and run the printer as shown in **Figure 2.17**. The programme also allowed dynamic manipulation of voltage parameters for precise control over the jetting behaviour of the jetting devices throughout the printing runtime as illustrated in **Figure 2.18**. The number of droplets per jetting could be controlled by changing the frequency of the voltage pulses, a technique characteristic of the drop-on-demand printers. In this study, 2 drops of each ink were jetted together per jetting for each dot in the design, as it gave optimum thickness to the 3D structures. As each droplet was kept a fixed distance away from another droplet, the voltage impulse frequency was adjusted depending on the speed at which the printer stage moved step-wise during printing. The voltage parameters were continuously monitored and modified if required to affect ink droplets.

Figure 2.17: *A screen capture of the Front Panel of the LabVIEW programme which is the GUI used to control and run the in-house built printer.*

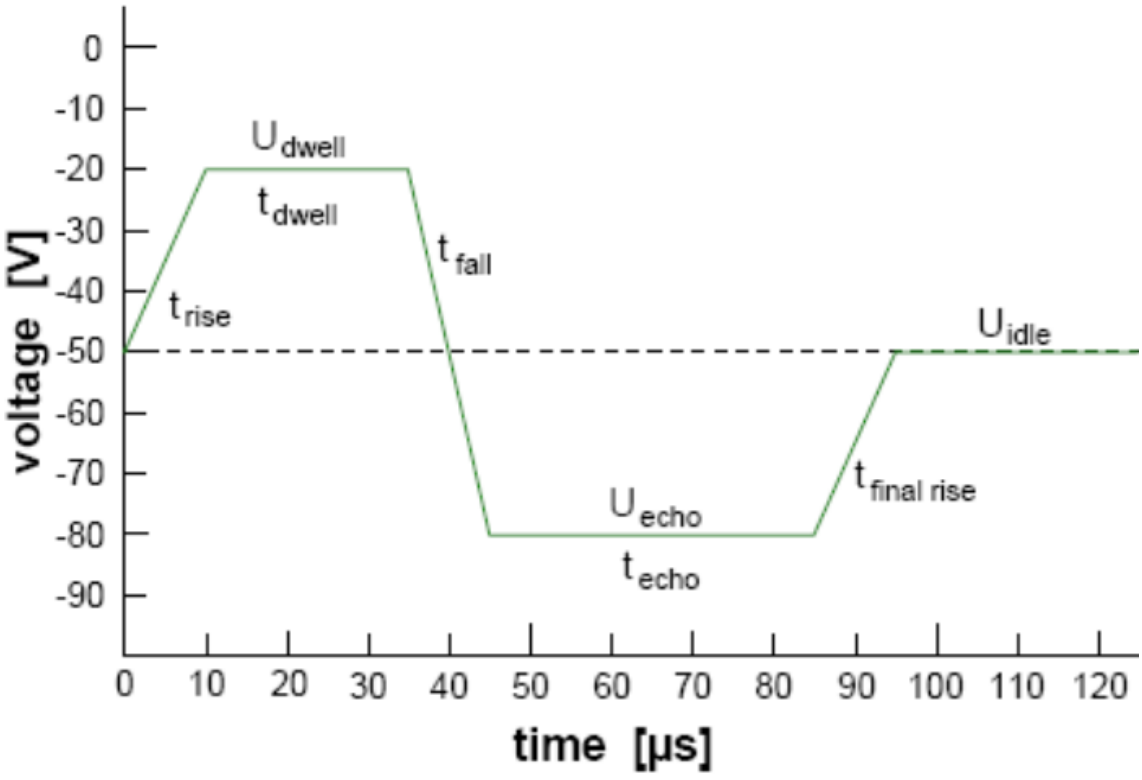

Figure 2.18: *A model illustration of the voltage pulse parameters utilised to control the printing. Here, t-fall represents the voltage which compresses the piezoelectric material inside the jetting device, resulting in the fall of droplet. Negative voltage means excess of electrons. [image taken from ref. [163] Copyright © 2012 MicroFab Technologies, Inc., USA].*

2.11 Computer Aided Designs of Fibroin Structures

The geometric shapes of the 3D structures were designed in the form of groups of points in the 2-dimensional X–Y coordinates in a Microsoft Excel file as shown in **Figure 2.19**. Several X and Y coordinate points were defined in serial order in an Excel sheet in such a systematic manner that plotting and visualising these coordinates on a graph gave the desired shape of the structure in 2D. The LabVIEW programme read the coordinates serially and ran the printer accordingly. Each coordinate point made the printer jet once through the jetting device. The calibration value was kept such that 500 points in Excel sheet meant 1 mm length during real printing. For printing, the distance between two successive coordinate dots was kept at 70 points or 0.14 mm as this gave optimum printing results, owing to the resolution limit of the particular printer used in this study. Separate columns in Excel sheets were created for fibroin solution (main ink) and methanol (curing ink) for getting alternate prints. Below given are the Excel sheet designs of the main body of the 3-armed structure as an example.

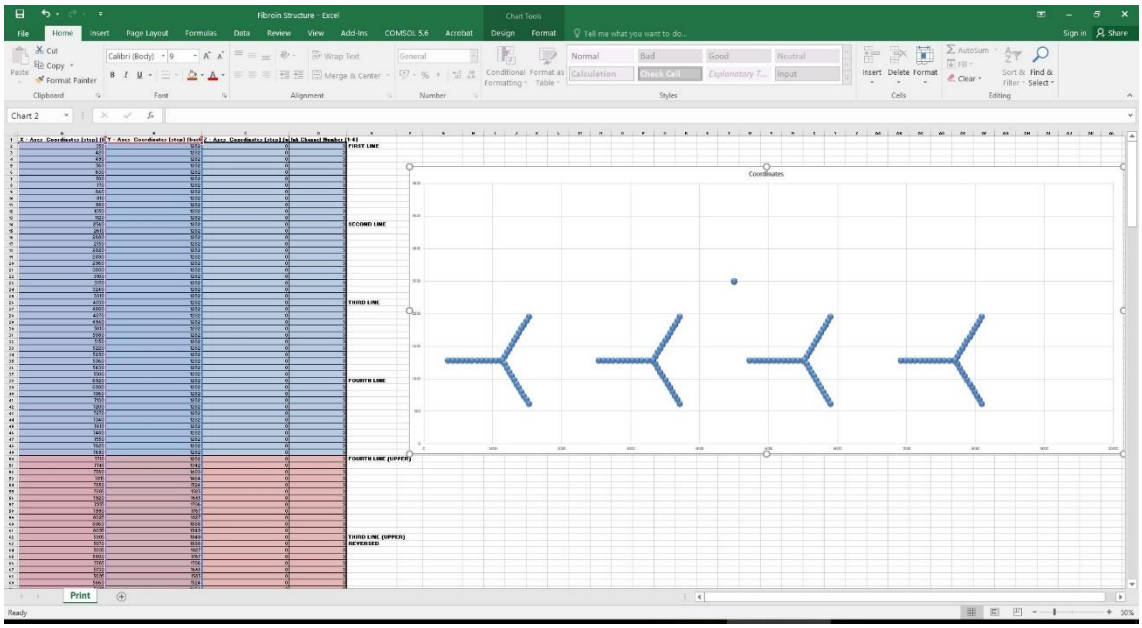

Figure 2.19: *An example of the 2D Computer Aided Design (CAD) of the fibroin structures in Microsoft Excel. Printing several layers on top of each other in accordance to the 2D CAD gives the final 3D structures.*

2.12 3D Reactive Inkjet Bioprinting Process

Printing was done on clean polished silicon wafer substrates placed on printer stage and stuck securely with sticky tapes. The inks were loaded into separate reservoirs and then the backpressure was adjusted to ensure the inks were not dropping passively from the jetting devices. Before printing, all the channels were calibrated for accurate positioning on the substrate. For this, a dot array was printed at the same coordinate location with all the printing channels. Any deviations in the droplet positioning were then corrected by shifting the channel position. Printing was done through the alternate layer-by-layer deposition of the primary ink and the curing ink. The inks were printed one layer at a time and each successive layer alternated with a layer of curing / crosslinking ink or methanol. Methanol converts the silk I in the preceding primary ink layer into silk II [164]. This was done to obtain the non-soluble and stable beta-sheets to form the 3D structures. Methanol was preferred over ethanol as cross-linking agent as it is more volatile than ethanol. The 70-point dot distance value for droplet jetting was kept constant across all the shapes. The arms of the structures were approximately 1.25 mm long. A total of 100 layers per structure were printed and 6 structures were printed per batch on one silicon wafer. The consequential total printing runtime turned out to be around 5–7 hours for different shapes. During the printing process, the room temperature remained in the range of 20–24 °C and the relative humidity level in the room remained in the range of 60–70 %. During printing of fibroin 3D structures, the ink 1 and ink 3 were printed layer by layer alternately for consecutive depositing of fibroin and its curing on the substrate. This also helped in keeping the fibroin deposition accurate by preventing excessive spreading on the substrate until the solvent water in fibroin fully dried up. After printing, the printed 3D fibroin structures were removed from the substrate by either soaking in DI water and gently agitating or in a dry state very carefully with a fine needle, depending on the intended application.

An in-house built drop-on-demand (DOD) inkjet printer, equipped with commercial piezoelectric jetting devices (80 μm nozzle diameter, MicroFab Technologies Inc., USA), was used to print the scaffolds on a silicon wafer substrate. The silicon wafer was cleaned with 5% Decon-90 solution followed by 70% ethanol and DI water, after which it was carefully wiped dry and placed firmly on the printing stage. The jetting device actuation voltage (70–90 V), actuation frequency (~300 Hz) and bioink channel pressure (-10 to -15) were adjusted for optimum droplet formation and dispensing. The distance between the jetting device nozzle and substrate was kept at approximately 10 mm. The fibroin solution (40 mg/mL) was mixed with PEG_{400} (14 mg/mL) to help generate stable droplets. Each layer of fibroin-PEG_{400} bioink was deposited alternating with a layer of methanol, which is dispensed from a second jetting device (40 μm nozzle). Methanol converts the soluble α-helix chains of fibroin into the insoluble β-sheets, thus giving the deposited ink a rigid structure and shape as per the required design. This process of printing is called 3D reactive inkjet printing. A total of 150 layers each of fibroin and methanol were printed for each batch of scaffolds. After printing is over, the scaffolds, measuring ~2.5 mm in length, were dipped in DI water and gently removed from the silicon wafer surface and stored in DI water at room temperature prior to use.

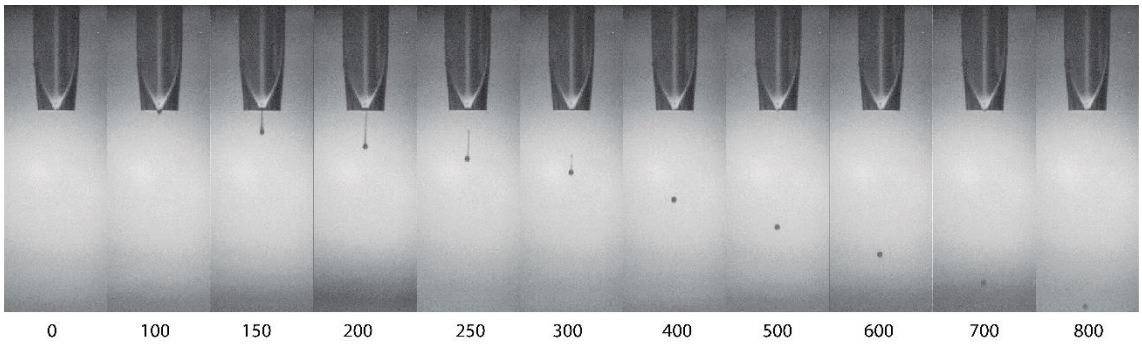

Figure 2.20: *The time lapse images of the 80 μm diameter nozzle of a jetting device captured during printing using a macro-lens camera. The ejecting ink droplet is clearly visible. The numbers below the images represent the time elapsed, in microseconds (μS), since the initiation of jetting of the fibroin ink droplet. For capturing the frame at a particular elapsed-time, the strobe light is adjusted using the LabView programme to light up only at that elapsed-time.*

Figure 2.21: *Freshly printed sample of a 3-arm star shaped 3D fibroin structure. Each arm of the structure is approximately 1.5 mm long.*

2.13 Characterization of Printed Fibroin Structures

2.13.1 Microscopy

Microscopy is a laboratory technique of using microscopes to virtually magnify and view objects or features of an object which are too small to be within the resolution range and thus not visible to the human eyes. In my study, I have used optical fluorescence and scanning electron microscopy to observe the detailed features of the 3D printed fibroin structures and its samples during and after the different experiments.

2.13.2 Optical Microscopy

An optical or light microscope uses the visible spectrum of the electromagnetic radiation or light and a system of optically transparent lenses to produce magnified images of minute objects of a large size range. The Nikon ECLIPSE LV150 (Nikon Corporation, Japan) compound optical microscope, as illustrated in **Figure 2.22**, was used during my research.

There are two types of optical or light microscopes, namely, simple and compound. A simple light microscope consists of a single double convex lens, e.g., a hand-held

magnifying lens. On the other hand, a compound light microscope consists of at least two double convex lenses, namely, an objective and an ocular or eyepiece. As the name suggests, the objective lens is the one aimed at the sample, whereas the ocular lens is the one through which the eye observes the sample's image. The total final magnification of produced by a microscope is calculated by multiplying the magnifying powers of the objective and ocular lenses. Current advanced compound microscopes, such as the Nikon ECLIPSE LV150, consist of several lenses as both objective and ocular lenses are themselves made up of a system of lenses, thus, allowing much higher magnitudes of magnification. These microscopes are also equipped with a CCD camera sensor, which is connected to a computer, for capturing and saving digital images.

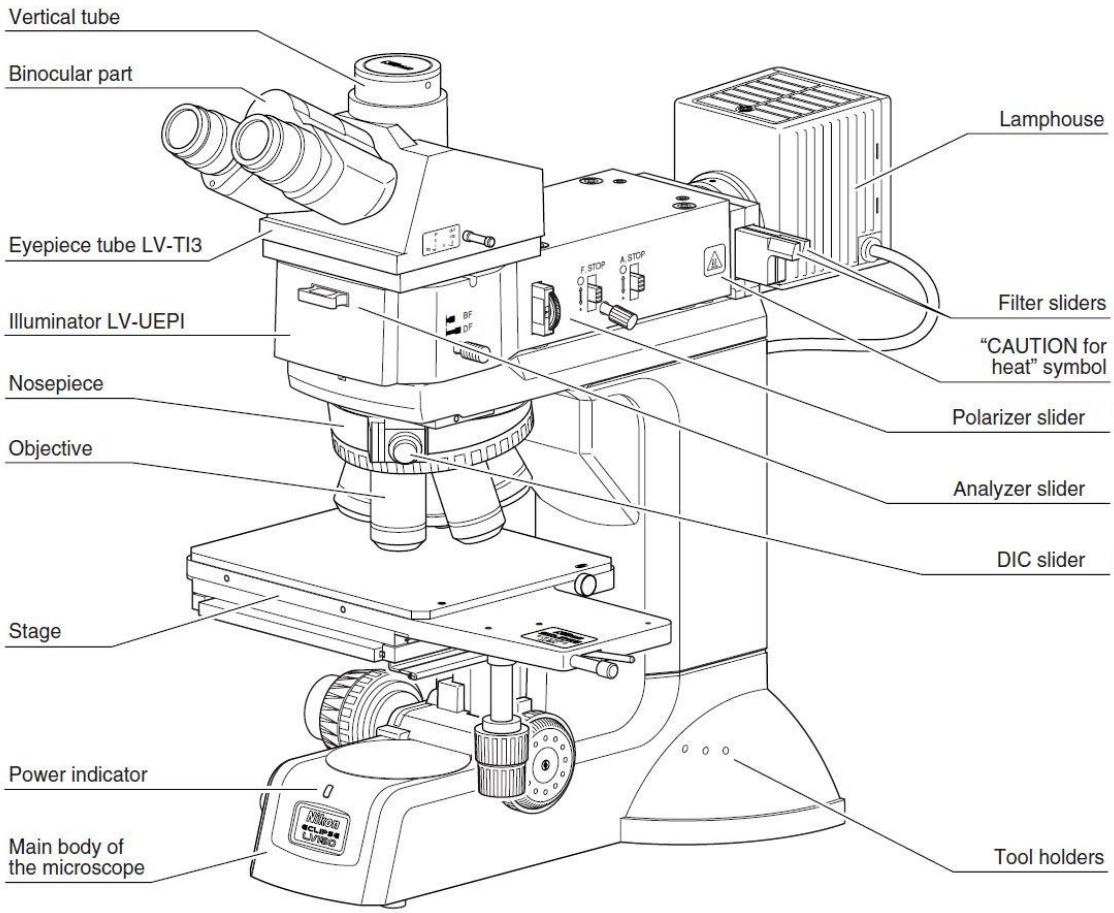

Figure 2.22: *Schematic illustration of Nikon ECLIPSE LV150 microscope with the digital eclipse camera system. [image courtesy: Nikon Corporation, Japan].*

2.13.3 Fluorescence Microscopy

Fluorescence microscopy is a technique in which fluorescence is used as the source of illumination for producing the magnified image of the specimen. Fluorescence is a form of luminescence in which a substance absorbs electromagnetic radiation at a particular wavelength and concurrently emits it at another wavelength. The emitted radiation is usually lower in energy, and therefore, has lower wavelength. If the emitted wavelength of a fluorescent substance is within the visible spectrum, then it can be used as a fluorophore for staining non-fluorescent specimen that need to be observed under a fluorescence microscope.

For imaging, the specimen is stained with fluorophores specifically and at desired locations and then illuminated / excited with laser at that specific wavelength which is absorbed by the fluorophore and, which in turn, emits light at longer wavelengths. An emission filter separates the incident excitation laser from the emitted weaker light. This filter is a wavelength-specific dichroic beam splitter and it lets the emitted light pass through it and reach the objective, but stops and reflects back any excitation laser light. A type of fluorescence microscopy, which is widely used in biomedical sciences, is epifluorescence microscopy in which an illumination light is passed through the specimen and focussed at the objective and camera sensor alongside the emitted fluorescent light. This gives a much higher signal-to-noise ratio and thus more detailed visibility of the specimen.

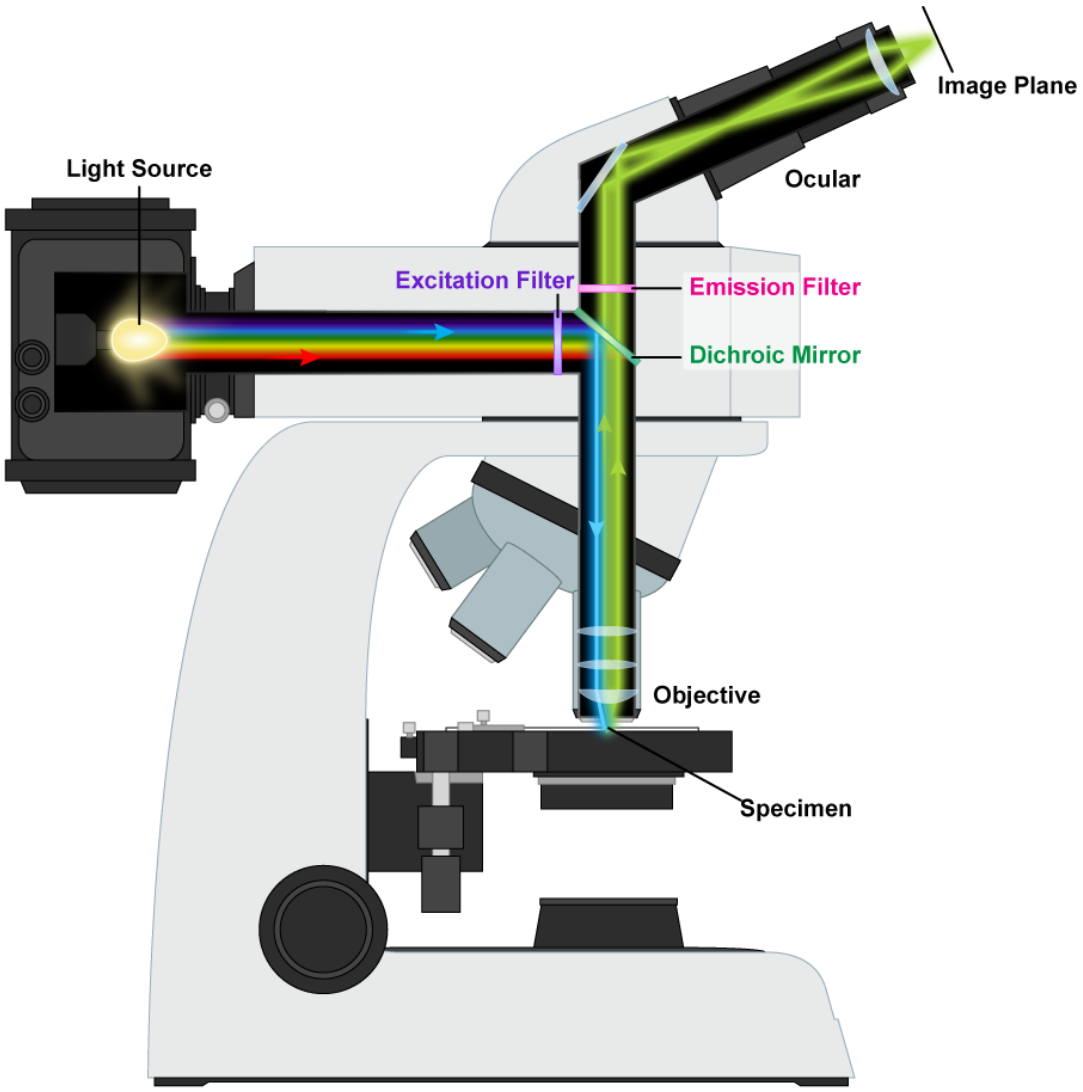

Figure 2.23: *Schematic illustration of working principle of a wide-field fluorescence microscope. [image taken from ref. [165] Creative Commons License].*

2.13.4 Scanning Electron Microscopy

Scanning electron microscopy is the technique of using a focussed beam of electrons to scan the surface of a specimen and produce topographical images with magnification at several orders of magnitude. The electrons are produced in electron gun, which consists of a heating cathode filament, and passed through a series of hollow cylindrical ‘lenses’ to focus the beam at the specimen. The electron beam is first passed through an anode, which accelerates the electrons, and then through an aperture which blocks the off-axis electrons from proceeding further. A system of condenser lenses then applies magnetic

field to the beam for focussing it into a narrow beam. Afterwards, the beam passes through an electromagnetic objective lens, which focuses the beam on the sample, and deflection coils, which move the narrow beam over the sample to create the raster image of the sample. On hitting the specimen, the electrons interact with the specimen matter by getting absorbed or scattered and produce secondary electrons alongside backscattered electrons, transmitted electrons, Auger electrons, cathodoluminescence and X-rays. The low energy secondary electrons are collected at two detectors which consequently produce greyscale images of the specimen. As the wavelengths of electrons at various energy levels are much shorter than that of the visible light spectrum, electron microscopy can produce ultra-high resolution images at a very high magnification (> 100,000x) in comparison to other microscopy techniques.

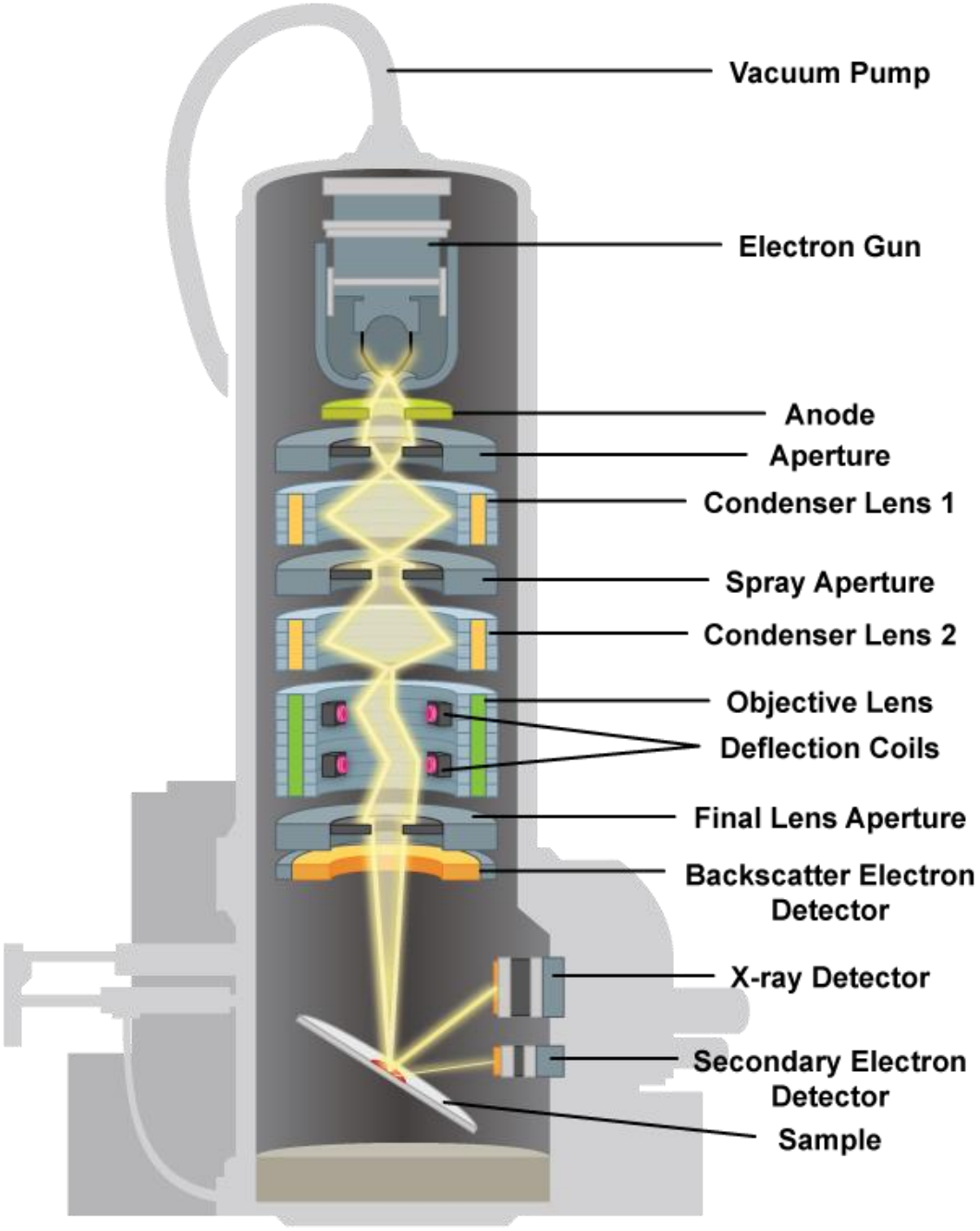

Figure 2.24: *Schematic illustration of working principle of a scanning electron microscope. [image taken from ref. [165] Creative Commons License].*

2.14 Statistics

Origin™ 2020 was used to generate all the graphs. Specific statistical analyses methodologies used for different experiments are mentioned in their respective chapters.

Chapter 3: 3D NEURONAL CELL CULTURE ON FIBROIN CELL CARRIERS FABRICATED BY 3D INKJET BIOPRINTING

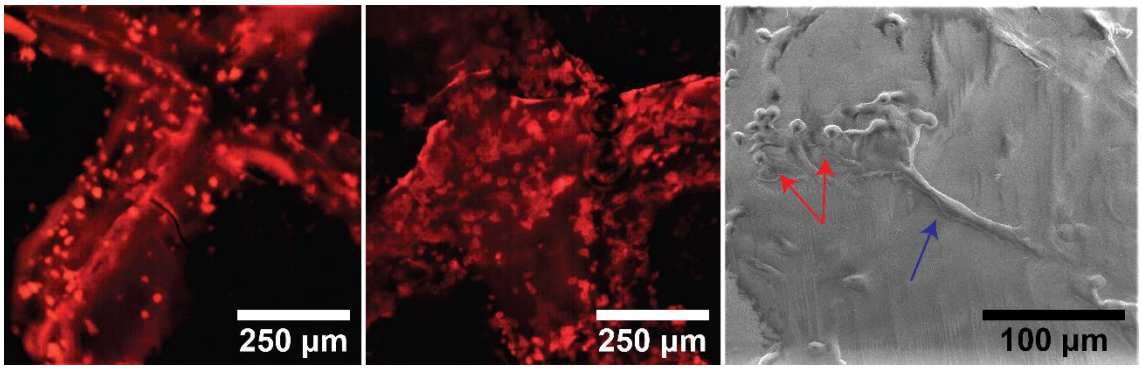

3.1 Abstract

3D cell culture represents a relatively more accurate picture of *in vivo* environment in comparison to the conventional plate based 2D culture. However, emulating a cell's physiologically relevant natural habitat *in vitro* has been challenging. Numerous models have been developed for cultivating cells in 3D so that they do not lose their native spherical shape. In this work, cross- or plus-shaped 3D silk fibroin structures fabricated using 3D inkjet bioprinting were used as cell carriers or scaffolds to culture and proliferate neuronal PC12 and SH-SY5Y cells. Fibroin is an excellent biomaterial for cell and tissue engineering. To aid cellular adherence on the fibroin carrier, the cell adherence molecule poly-l-lysine (PLL) was used to functionalize the fibroin carrier surface by simply incubating the fibroin carriers in PLL for 12 hours. The live / dead assay after 24 hours of culture confirmed that fibroin and the cell adherence molecules have no cytotoxic effects on the cells. Scanning electron imaging after 72 hours of culture showed that the PC12 cells were able to retain their shape and position on the fibroin carrier for prolonged periods of time, measured up to 7 days of culture, and also differentiate under nerve growth factor, both of which were excellent results. As it is important to fabricate the cell carriers in any shape and size depending on the required growth pattern, 3D inkjet bioprinting was used to print plus shape as a model at millimetre-scale for cultivating the cells and analyse cell growth rates and patterns. The results demonstrated inkjet bioprinted scaffolds, functionalized with cell adherence molecules can very effectively work as cell carriers to provide native ecosystem for 3D cell culture.

3.2 Introduction

Cell culture is the removal of living cells from their natural environment and their subsequent growth under controlled laboratory conditions. It has been a fundamentally important tool in biological research for more than a hundred years and is conducted in two conventional ways, namely, as a cell suspension and on a flat surface of an agar plate or a culture flask. Cell suspension and agar plates are mostly used for culturing eukaryotes, such as algae, and prokaryotes, such as bacteria. For culturing the cells and tissues of higher organisms, such as mammals, cell-culture flasks are used because the mammalian cells, such as mouse fibroblast cells and human mesenchymal stem cells, are adherent cells, that is, they require a substrate to attach to for growth and replication. This is because of the complex *in vivo* environment of higher organisms within which all the cells reside naturally.

However, even though it has become a standard in cell research, the flat two-dimensional surface of a culture flask only provides a substratum for cell adherence and does not replicate the real *in vivo* conditions. Multicellular living organisms are composed of a variety of cells residing in a three-dimensional (3D) and physiologically active environment which also consists of the extracellular matrices (ECMs). The ECMs provide surface to the cells for attachment, migration and maintenance of natural polarity. The *in vivo* environment consists of extra cellular matrices (ECM) and different categories of neighbouring or niche cells with which the cells constantly interact physiologically through a variety of cell signalling molecules, other chemical cues, and mechanical cues [166]. When the cells of multicellular organisms, such as mammals, are cultivated *in vitro*, they lose their native environment as the culture plates cannot provide multidirectional cell adhesion platforms. As a result, the cells become flattened, thus losing their native spherical shape, on the surface of the culture flasks. This leads to physiological anomalies in cellular functions and any intricate research conducted on such cells possesses the risk of yielding inaccurate results. This has far-fetched negative

implications because cell culture is a basic laboratory tool, which is applied in numerous fields beyond cell biology research, such as drug discovery, cancer research, cosmetic industry, stem cell therapy and gene editing. Limitations of conventional 2D cultures occasionally lead to inaccurate results in drug testing research, cell-based assays and other cell biology research. This in turn leads to over-dependence on animal trials for accuracy and may cause unexpected results in human trials. As a result, the past two decades has seen and emergence in a variety of 3D cell culture models.

Therefore, for an accurate and effective emulation of the *in vivo* environment, ideally, the cells need to be cultured on extra cellular matrix alongside neighbouring or niche cells and in the presence of all the necessary chemical cues, such as cell signalling molecules, and hormones. The first step towards achieving such an ideal *in vitro* cell culture model is three dimensional or 3D cell culture in which the cells do not get flattened, do not proliferate irregularly and do not lose their natural phenotypic characteristics [167, 168]. Another vital attribute is cell polarity, which is easier to be maintained in a 3D cell culture where cells are relatively relaxed, not bound by gravity, and free to move or migrate and explore their microenvironment. For such cells as epithelial glandular cells and neuronal cells for example, maintenance of cell polarization is essential for directional secretion of biologically active molecules, as has been shown, as an example, in the 3D *in vitro* organoid model of endometrial glands [169]. In addition, gene expression and mRNA splicing patterns can vary considerably between 2D and 3D cultures of the same cells [170, 171], as shown, for example, in the melanoma cell lines cultured as 3D spheroids [172]. In 2D culture, the cell to cell interaction is also restricted to communication with adjacent cells in single plane only, whereas in 3D, the cells can interact with adjacent cells from other planes [173].

On a flat 2D surface, cell attachment and spread occurs within minutes, which, in contrast, may take a few to several hours to occur on a 3D scaffold or cell carrier as the cells explore the adherence surfaces around them [174]. The morphological differences between the cells growing in 2D and in 3D is illustrated alongside real cell fluorescence

images in **Figure 3.1**. Cells lose their spherical shape in the vertical Z axis under the influence of gravity and become flattened. Therefore, while there is no difference in the X and Y axes between 2D and 3D cultures, the cells in 2D lose physiological relevance in the Z axis.

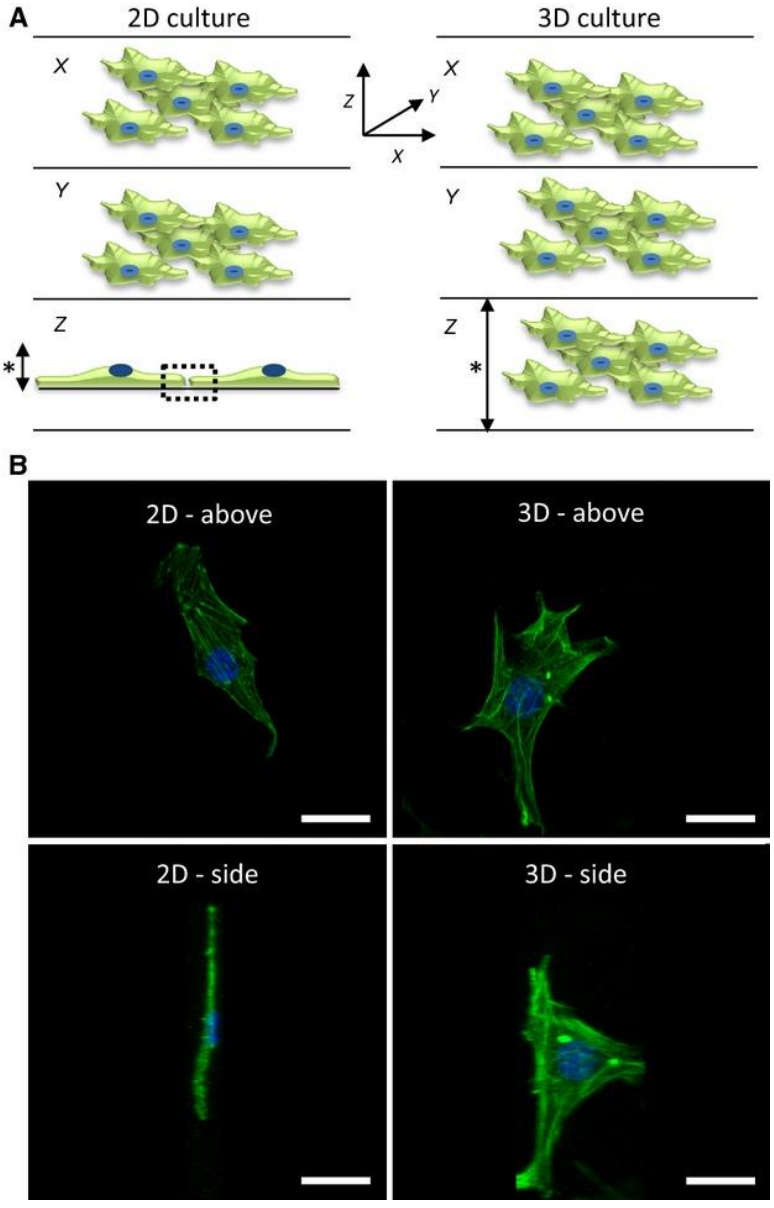

Figure 3.1: *Visualization of the impact of physical culture environment on cell structure.* ***(A)*** *Schematic and* ***(B)*** *Live cell comparison between the morphology of cells grown on a 2D surface and in a 3D environment (scale bar: 10 µm). The cells lose thickness in the z-axis or height under the influence of gravity in 2D culture. In comparison, 3D culture allows versatility in the cell shape and size in all the three dimensions. [image taken from ref. [173] Copyright © 2015 Creative Commons CC BY].*

In order to address the issue of physiological irrelevance, several 3D culture models have been put forward in the past two decades. These models can be categorised as scaffold-free models and scaffold-based models. Scaffold-free 3D cell culture is conducted by developing a ball of cells through hanging drop model or through magnetic levitation in suspension using magnetic nanoparticles. Such models are suitable for short term research only, as the cell mass has a small critical upper limit of diameter ranging from a few hundred microns to a few millimetres depending on the cell type, after which the core cells begin to undergo necrosis due to the lack of nutrients and oxygen arising from diffusion limitation. Major focus is, therefore, on the scaffold-based 3D cell culture models which can be grown to much larger scales and house millions of cells at once. Among these, there are two major types, in-scaffold 3D cell culture and on-scaffold 3D cell culture. While in-scaffold culture is good for growing multiple cell types for tissue engineering and organoid culture, the on-scaffold culture is excellent for growing a single cell type for drug discovery and for cultivating cells at fast pace for obtaining biomolecules, or for stem cell therapy and gene editing.

3.2.1 Scaffold-Free Models

Scaffold-free 3D cell cultures are essentially a mass of cells clumped together with the number of cells proliferating up to a few hundred micrometres. Such models can be developed through hanging drop cell culture and in suspension cultures. In hanging drop, a small number of cells are seeded in the wells of a hanging drop culture plate, such as a Terasaki plate, and kept inverted during incubation. Inverting the plate causes the cells to clump together due to gravity within the culture medium drop which doesn't fall due to the adhesive capillary force between the water in culture medium and plastic of the culture plate. The buoyancy of cells in the medium cancels the gravitational force causing weightlessness in the cell mass and optimum freedom of growth in any direction. In suspension cultures, the method usually adopted is to get magnetic nanoparticles

internalized inside the cells which are then kept afloat against gravity using a strong neodymium magnet placed above the suspension. In either method, the cell spheroids grow up to several hundred micrometres after which the diffusion limit causes the cells in the spheroid core to undergo necrosis, thereby limiting the maximum achievable size of the 3D cell culture model [175]. Nonetheless, scaffold-free spheroids are better than 2D cultures in emulating avascular or minimally vascular 3D masses of cells *in vivo*, such as, tumours, which have a heterogeneous population of oxygen and nutrient rich surface cells and the deep-seated hypoxic and nutrient deficient core cells [176]. Another example is 3D spheroids of pluripotent stem cells which can be differentiated to form spherical embryoid bodies. Scaffold-free *in vitro* 3D spheroids are, thus, excellent representatives of *in vivo* tumourigenesis and stem cell differentiation for applications in cell biology and drug discovery research.

3.2.2 Scaffold-Based Models

Scaffold-based 3D cell cultures comprise of cells adhering to and growing on a cell carrying scaffold made of either natural, synthetic or hybrid biomaterials. The cell carrier or scaffold provide a platform *in vitro* for cells to maintain their three-dimensional physiologically relevant shape and polarities. High water content scaffolds or hydrogels are highly diffusible to nutrients and gases and thus help grow cells inside them and such cultures are called in-scaffold models. In comparison, the hard scaffolds, such as silk and various synthetic polymers, allow the cells to attach and grow on their surface, usually with the help of cell attachment molecules, such as fibronectin, vitronectin and laminin, adsorbed on the scaffold surface. These cell carrying scaffolds or ‘cell carriers’ can be fabricated in any geometric shape and in a wide range of size using a variety of sophisticated equipment such as, 3D bioprinters and electrospinners. When compared to the scaffold-free models, the scaffold-based models can support a large number of cells and cultured for several days. In addition, multiple different cell types can be

supported in the same culture which helps develop more complex *in vitro* 3D tissue and organoid models.

3.2.3 Applications of 3D Cell Cultures

Virtually any field of research that requires cell-based experiments benefits from 3D cell cultures owing to their superior and more accurate replication of *in vivo* physiology. One major area is drug discovery in which new chemical candidates are studied for potential use as drugs or therapeutics for the treatment of diseases. Studying the effect of novel drug-candidate chemicals on the physiologically accurate cell populations can provide data almost similar to animal or human trial results, thus, saving crucial resources and time and easily maintaining research ethics. Cancer and tumour modelling is another major area of research which can benefit from 3D cell cultures, such as for analysing the effects of amount of nutrient and oxygen supply and wastage and carbon dioxide removal on the core cells and surface cells of an *in vitro* grown cancer cell spheroid in comparison to normal and healthy cells. It can also help in accurately testing and evaluating new anti-cancer drugs before conducting any human trials. One relatively rarer but very important area of application is the ability of rapid *in vitro* multiplication of pluripotent stem cells for stem cell transplantation in terminally ill patients suffering from genetic diseases. In this practice, the bone marrow stem cells are extracted, their genetic defect corrected and the corrected cells are then proliferated *in vitro* for transplantation back into the patient. But a conventional 2D culture causes a slower than required rate of cell growth and also holds a potential risk of the cells losing their potency and normal phenotypic expression. In this case, therefore, 3D cultures offer much better promise of improving and fastening the process of stem cell transplantation. Important applications include, but are not limited to: (1) To grow cells in physiologically more relevant conditions; (2) drug discovery, gene editing, stem cell therapy; (3) potential to develop printed grafts for regenerative medicine; (4) patterned differentiation of nerve cells.

3.2.4 Current Study

In this study, I have cultured neuronal mouse PC12 cells and neuronal human SH-SY5Y cells on the millimetre scale 3D fibroin structures fabricated by 3D reactive inkjet printing and acting as cell carriers for 3D culture and potentially for nerve guidance. The cell carriers are biocompatible, stable, homogeneous in size and take a few minutes to a few hours to be fabricated depending on their quantity per batch. The flexibility in shape and size and the rigidity of the cell carriers make them a good choice for nerve guidance and patterning in 3D space. Such patterning help facilitate growth of nerve cells for treatment of nerve injuries or nerve degeneration. For convenience, only the cross or plus shaped 3D structure was imaged for all the results. Growing neuronal cells with 3D support enables to generate a large population of cells *in vitro*. This can be used as a model for cultivation and differentiation of brain tissue or ganglions for the study of neuronal diseases, drug discovery and for potential adoptive cell transfer for the treatment of nervous degenerative diseases.

3.3 Experimental Methods

3.3.1 Materials

The materials required for fibroin scaffold fabrication are described in **Chapter 2, section 2.1**. Poly-l-lysine was purchased from Thermo Fisher Scientific, UK. The neuron-like rat tumour PC12 cell line was obtained from American Type Culture Collection (ATCC). The neuroblast-like human SH-SY5Y cell line was obtained from ATCC. Unless otherwise stated, chemicals and reagents were purchased from Sigma Aldrich, UK.

3.3.2 Fibroin Scaffold Design and Fabrication by Printing

The fibroin biomaterial ink was prepared using the method described in **Chapter 2, Sections 2.2 to 2.7**. Afterwards, a ‘plus’ shaped was designed in CAD for fabricating scaffolds. The size of the scaffolds was ~2.5 mm in length in both X and Y dimensions

and ~0.5 mm in breadth. The 3D printing was carried out as explained in **Chapter 2, Section 2.12**.

3.3.3 Scaffold Surface Functionalization

The scaffolds were gently taken out of storage and submerged in 70% ethanol for sterilization. Meanwhile, poly-l-lysine (PLL) (MW = 70k – 150k) was diluted to 0.01% (w/v), as recommended in the product manual, prior to use. The scaffolds were carefully taken out of the ethanol, air-dried under sterile environment, submerged in the cell adhesion molecule PLL and left for 12 hours or overnight to allow the molecules coat the entire surface of the scaffolds before cell seeding to help in cell adherence. The scaffolds were thus ready for cell seeding.

3.3.4 Culture of PC12 and SH-SY5Y Cells

The PC12 and SH-SY5Y cells were cultured in medium-sized culture flasks (75 cm^2) in Dulbecco's Modified Eagle Medium (DMEM) with high glucose supplemented with 10% foetal calf serum (FCS), 1% penicillin-streptomycin, 1% glutamine, and 0.5% Amphotericin B (Fungizone™) in an incubator maintained at 37 °C and 5% CO_2. The cells were found to be confluent in 3 days. On confluence, the cells were detached with 0.25% (w/v) trypsin–EDTA (Ethylenediaminetetraacetic acid) and resuspended in culture medium. For cell seeding, the cells were counted manually using a haemocytometer slide and diluted to 1 x 10^4 cells/mL as a standard or to the required concentration.

3.3.5 Cell Seeding on Fibroin Cell Carriers

One piece of scaffold is placed in one well of the V-bottom 96-well plates and added with ~1000 cells from the cell suspension (= 100 µL of cell suspension). The remainder of well is filled with culture medium. Other wells are similarly filled with scaffold and cells as replicates.

3.3.6 Imaging of Cell-Scaffold Constructs

The scaffolds with adherent cells were imaged after 24, 48 and 72 hours of incubation under a fluorescence microscope. Following incubation for the different time periods, the medium was carefully removed and the cell-scaffold constructs in the well plates were gently washed twice with PBS. The cells on the scaffolds were then fixed in 3.7% paraformaldehyde, which cross-links and 'glues' the cellular components irreversibly, for 20 minutes at room temperature, followed by washing twice with PBS solution and then incubated for a further 10 minutes in 0.1% Triton X-100, which is a detergent and it increases the membrane permeability for enhancing fluorophore uptake. Afterwards, the cells on scaffolds were washed twice with PBS solution and stained for 60 minutes with phalloidin-TRITC to visualise the cytoplasm and with DAPI to visualise nucleus. The fluorophores were removed, the stained cells on scaffolds were washed twice with PBS and finally fresh PBS was added before imaging. Several micrographs were taken by focussing different parts of the 3D construct lying at different focal planes in the Z axis, and stacked together to form a single Z-stacked image using the Zerene Stacker software (Zerene Systems LLC, USA). For the SEM images, the cell on scaffolds were fixed as described, carefully retrieved from the well plates, placed on the carbon tabs and then air dried before imaging.

3.3.7 Live / Dead Cytotoxicity Assay

For qualitative live / dead assay, the culture medium in the wells was removed and a serum-free medium containing 0.001% (v/v) SYTO 9™ (Invitrogen) and 0.0015% (v/v) propidium iodide (PI) were added into the wells. The well plates are then incubated for 30 min at 37 °C and 5% CO_2. Afterwards, the medium was removed and the wells were washed twice and filled up with PBS solution. The cell-scaffold constructs in the wells were then imaged using a fluorescence microscope with a UV illumination source and appropriate filters for different fluorophores.

3.3.8 Resazurin–Resorufin Cell Proliferation Assay

Qualitative cell proliferation or metabolic activity assay was assessed at 0 hours and after 24, 48 and 72 hours in culture. Culture medium was removed from the wells containing the cell-scaffold constructs and 100 µM resazurin dissolved in PBS was added along with assay-dependent culture medium. The cells were then incubated for 4 hours at 37 °C and 5% CO_2. The reduced resorufin from the wells were then transferred into black 96-well plates and the fluorescence intensity was measured in a FLx800 fluorescence plate reader (Biotek Instruments Inc.) at 540/635 nm. Background fluorescence was measured and subtracted from the results. In case of cells on scaffolds, the fluorescence values of the cells growing in V-bottom wells without scaffolds as a control were averaged and subtracted from the fluorescence data of the sample wells to obtain the approximate values of metabolic activities of cells growing only on the scaffolds.

3.3.9 Statistical Analysis

The resazurin-resorufin assay fluorescence data were plotted in Origin™ 2020. P values of < 0.05 were taken as significant.

3.4 Results

3.4.1 Cell Seeding Density

Using ImageJ, the dimensions of a plus-shaped scaffold were measured to be approximately 0.25 cm in length, 0.05 cm in breadth and ~100 microns in thickness (as measured from SEM images) for each of the two perpendicular lines of the plus-shape. This gave a total surface area available for culture to be 0.05 cm^2 (length x breadth x 2 x two sides). Placing one scaffold in one well of a V-bottom well plate, 10,000 cells were seeded per well.

3.4.2 Characterization of Cells on 3D Fibroin Carriers

The cells were seeded and incubated with fibroin cell carriers and imaged at 24h, 48h and 72h post seeding with fluorophores phalloidin-TRITC (red) and DAPI (blue). While phalloidin binds to the F-actin molecules, TRITC fluoresces as red and DAPI binds to the genetic material and fluoresces as blue. The fibroin cell carriers inadvertently showed absorption of the fluorophores resulting in significant background noise. Z-stacked light micrographs of cell-scaffold constructs are shown in **Figure 3.2** for PC12 cells and in **Figure 3.3** for SH-SY5Y cells. The PC12 cells showed prominent adherence and visually evident proliferation in number. The SH-SY5Y cells, on the other hand, showed weak adherence and fell off the scaffolds in significant quantities during the staining process.

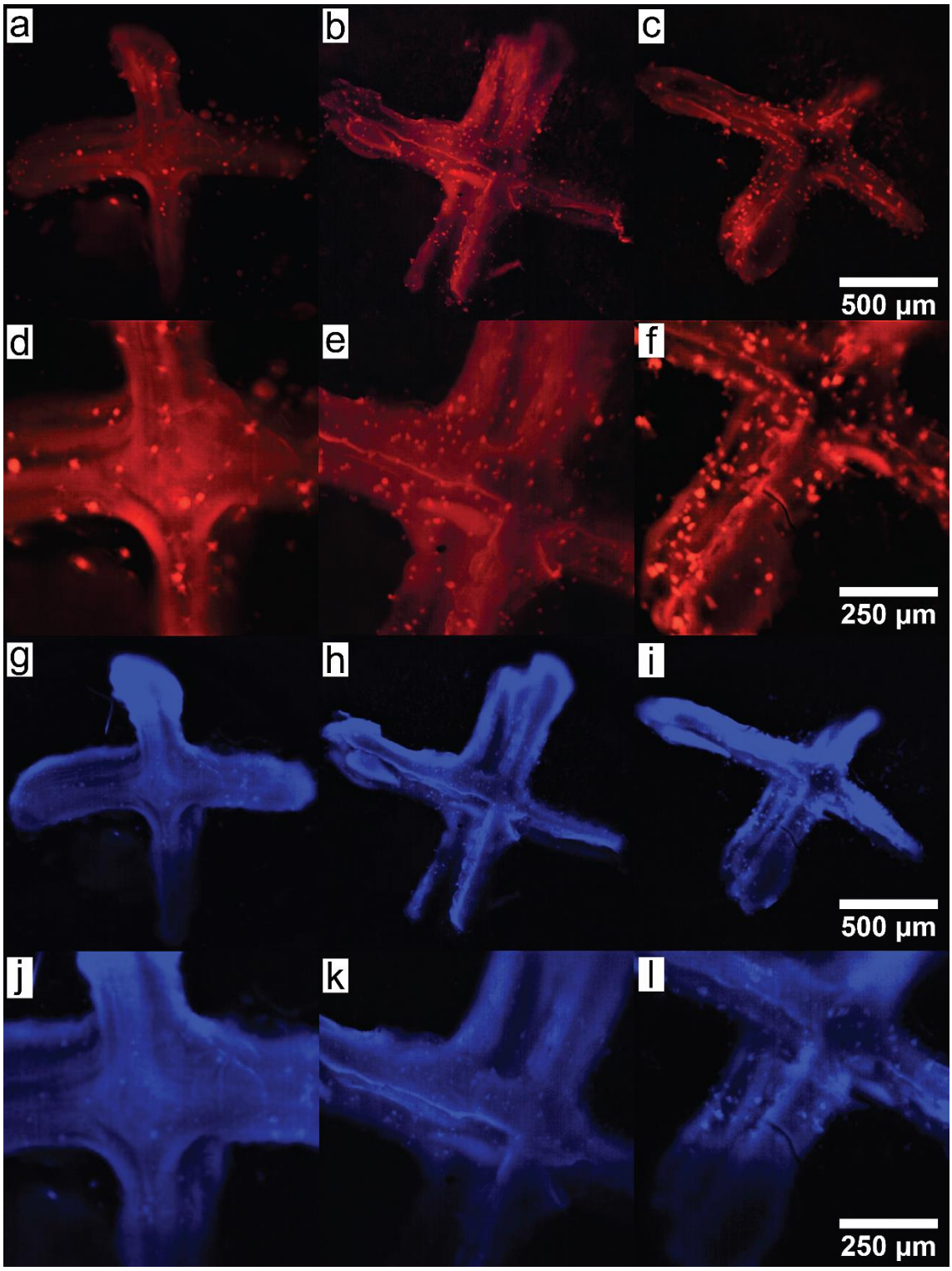

Figure 3.2: *Z-stacked fluorescence micrographs of PC12 cells growing on 3D fibroin carriers and imaged at two magnification levels after 24 hours (a, d, g, j), 48 hours (b, e, h, k) and 72 hours (c, f, i, l). The cells were stained with phalloidin-TRITC (red) and DAPI (blue) and imaged separately for the two fluorophores to avoid colour noise. The fibroin absorbed significant amounts of fluorophores and caused background noise in fluorescence. The cells can be seen as small spherical dots adhering and growing on the carriers. The images were taken with a wide-field fluorescence microscope using UV lamp and filters for different wavelengths of incident light.*

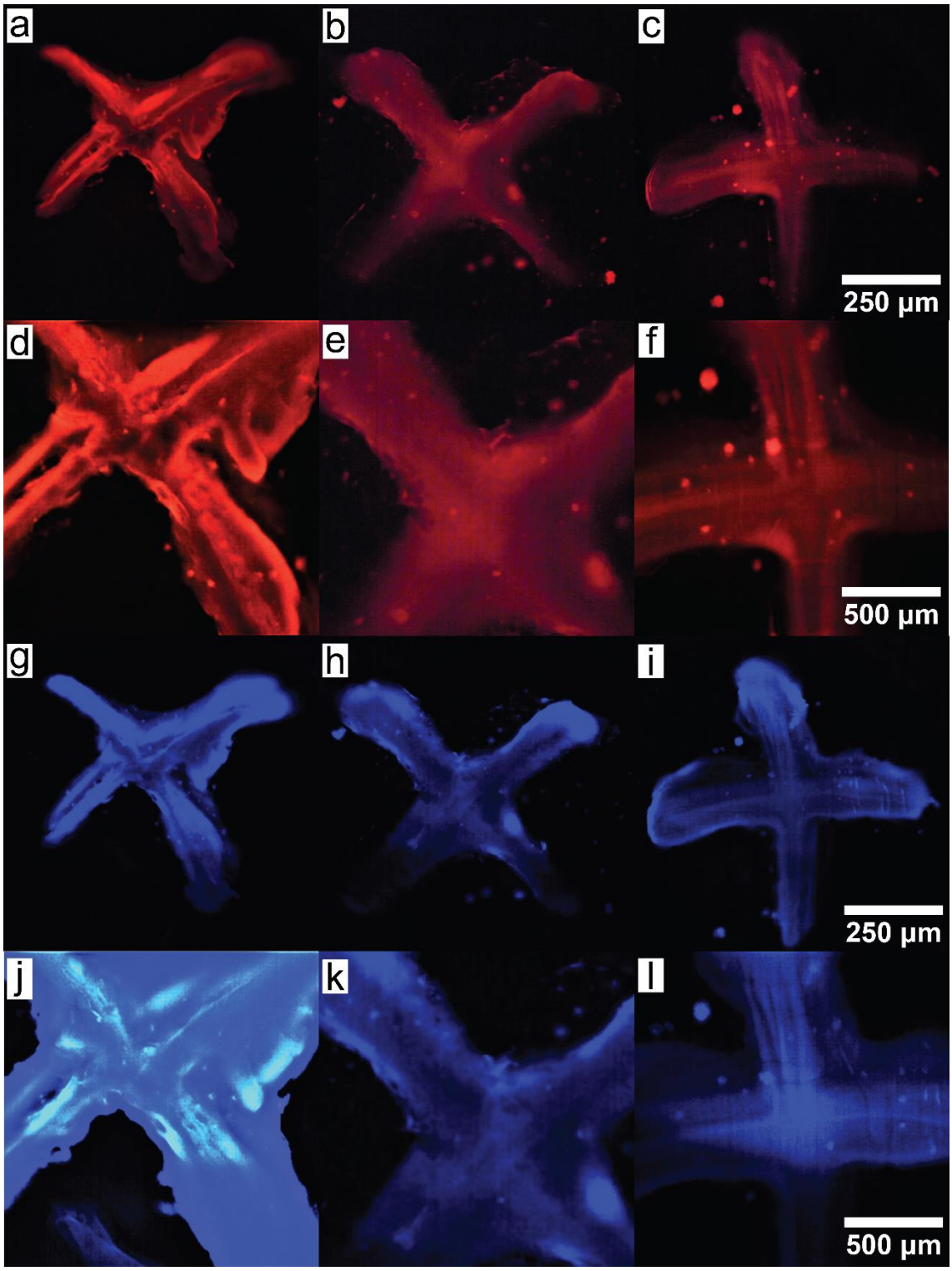

Figure 3.3: *Z-stacked fluorescence micrographs of SH-SY5Y cells growing on 3D fibroin carriers and imaged at two magnification levels after 24 hours (a, d, g, j), 48 hours (b, e, h, k) and 72 hours (c, f, i, l). The cells were stained with phalloidin-TRITC (red) and DAPI (blue) and imaged separately for the two fluorophores to avoid colour noise. The fibroin absorbed significant amounts of fluorophores and caused background noise in fluorescence. The cells can be seen as small spherical dots. The images were taken with a wide-field fluorescence microscope using UV lamp and filters for different wavelengths of incident light.*

3.4.3 Live/Dead Assay

For the live/dead assay to assess the potential toxicity of fibroin scaffolds, the cells were seeded and incubated with fibroin scaffolds and imaged at 72h post seeding with fluorophores SYTO 9 (live- green) and propidium iodide (dead- red). The fibroin cell carriers inadvertently showed absorption of the fluorophores resulting in significant background noise. Z-stacked light micrographs of cell-scaffold constructs are shown in **Figure 3.4 a – b** for PC12 cells and in **Figure 3.4 c – d** for SH-SY5Y cells. Both PC12 and SH-SY5Y cells took up the membrane permeable SYTO 9 and showed its green fluorescence while the red fluorescence of impermeable was not observable inside the cells, suggesting that very few or no cells became non-viable while adhering to the scaffolds. Similar to the previous staining procedure, the PC12 cells showed prominent adherence while the SH-SY5Y cells showed weak adherence and fell off the scaffolds in significant quantities during the live/dead assay staining process.

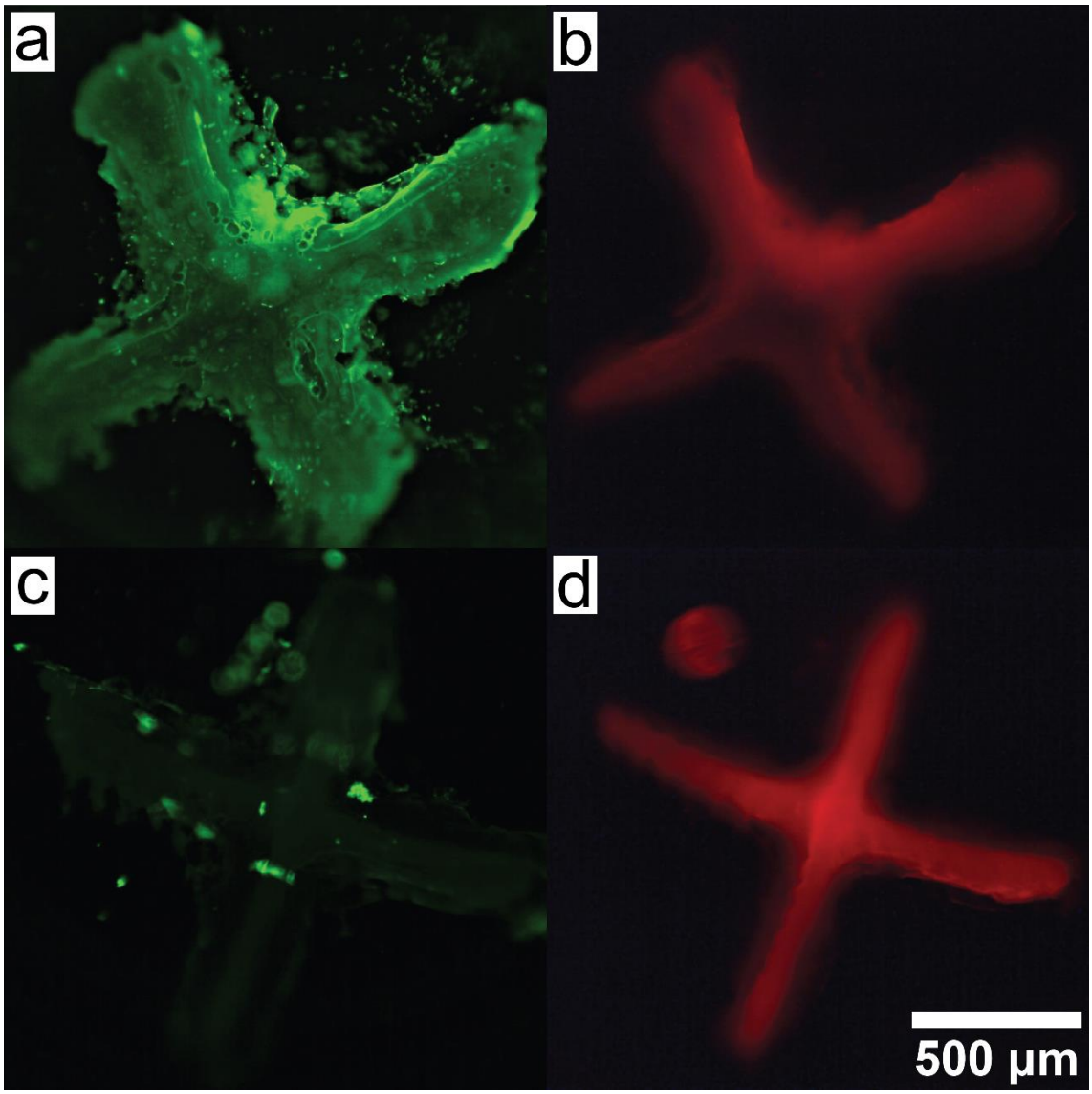

Figure 3.4: *Live/Dead assay of PC12 and SH-SY5Y cells after 72 hours of incubation. Very few cells are seen as the majority of the cells have been inadvertently sloughed off and washed away during the staining process. The cells also seemed to fall off easily during the staining procedure as they were not fixed in this live cell assay. The fibroin also inadvertently absorbed the fluorophores, causing background noise. The images were taken with a wide-field fluorescence microscope using UV lamp and filters for different wavelengths of incident light.*

3.4.4 Cell Metabolic Activity Assay

Resazurin-resorufin (Alamar Blue) assay showed significant growth of PC12 cells in 3D environment. The SH-SY5Y cells failed to adhere, as seen in images previously, and grow significantly on 3D scaffolds.

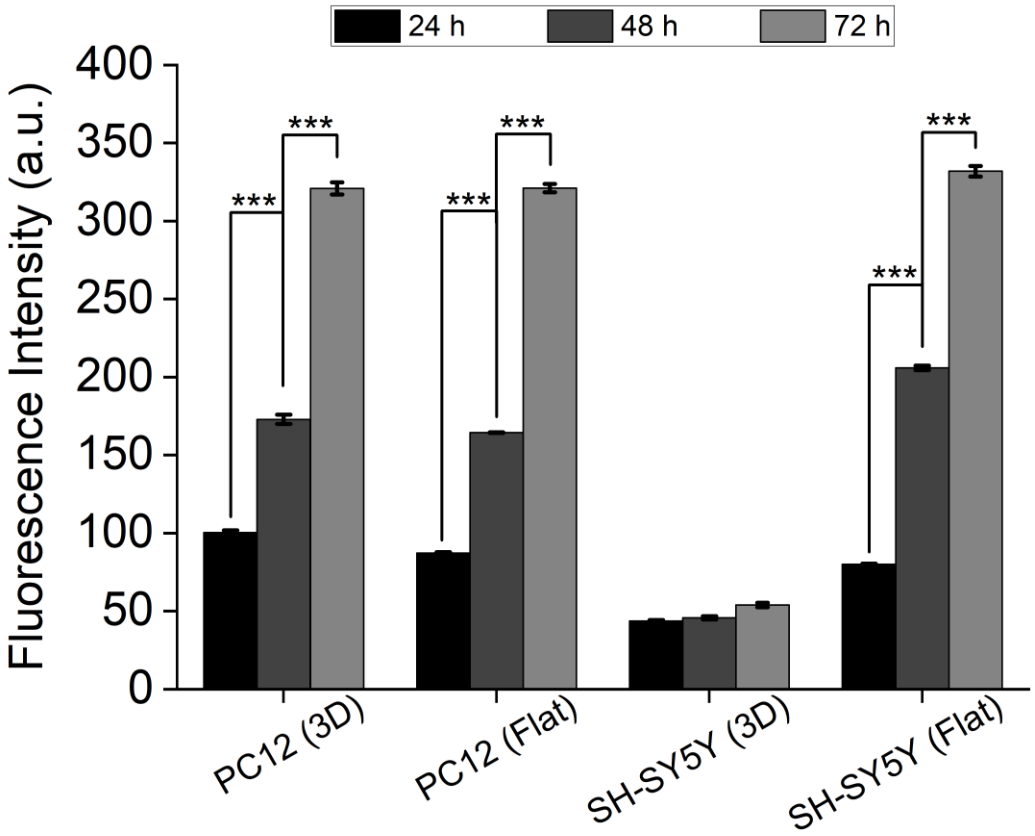

Figure 3.5: *Metabolic Activities of PC12 and SH-SY5Y cells obtained by the resazurin-resorufin or alamar blue assay. The SH-SY5Y cells are known to form clumps especially in the absence of growth factor, such as retinoic acid, and consequently showed lack of adherence and significant growth on 3D carriers. (*** p <= 0.05).*

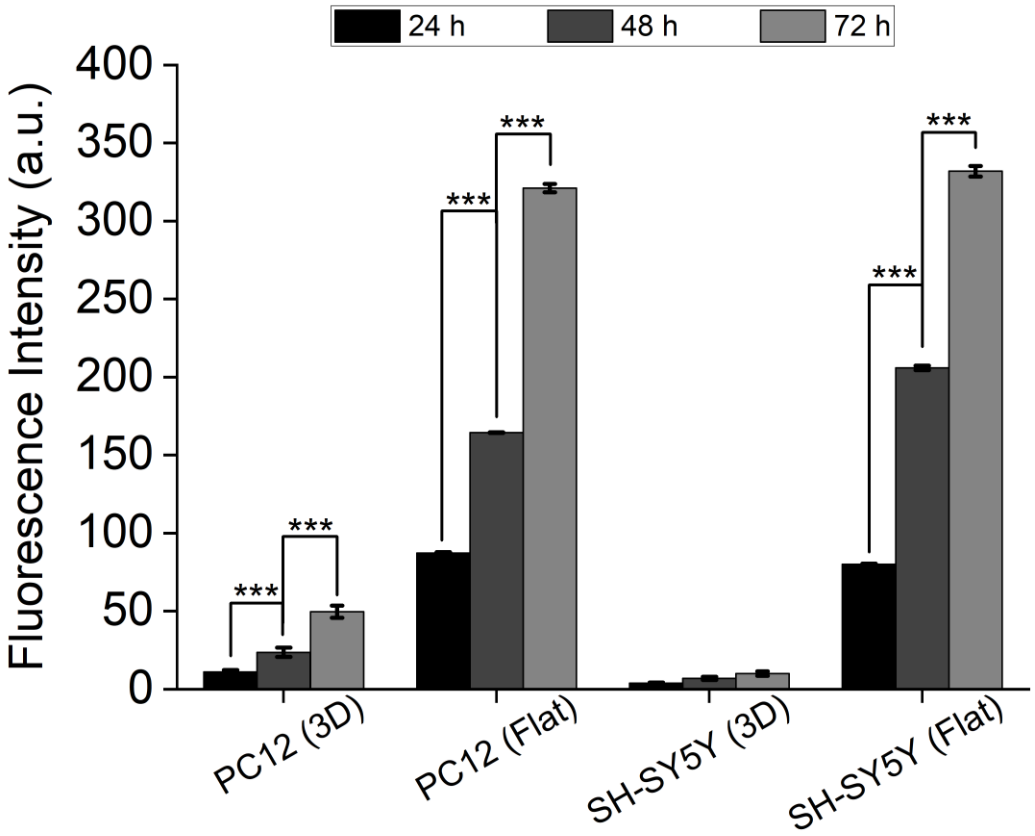

Figure 3.6: *Metabolic Activities of PC12 and SH-SY5Y cells obtained by the resazurin-resorufin or alamar blue assay after subtracting the I fluorescence intensities of metabolic activities of cells growing in V-bottom plates in absence of any cell carrier from the 3D culture fluorescence intensity data. Thus, this graph shows the absolute fluorescence intensities of cells growing only on the carriers. (*** p <= 0.05).*

3.4.5 Culture with Nerve Growth Factor

Culturing the PC12 cells with nerve growth factor (NGF) mixed in the medium showed a higher proliferation rate and onset of differentiation as shown in the fluorescence images taken 72h post seeding in **Figure 3.7**. The scanning electron images of cells on scaffold is shown in **Figure 3.8**. Some of the cells clearly show onset of differentiation marked by the distinctive growth of dendrites. A differentiation experiment with SH-SY5Y cells could not be conducted due to their failure in adhering to the 3D scaffolds.

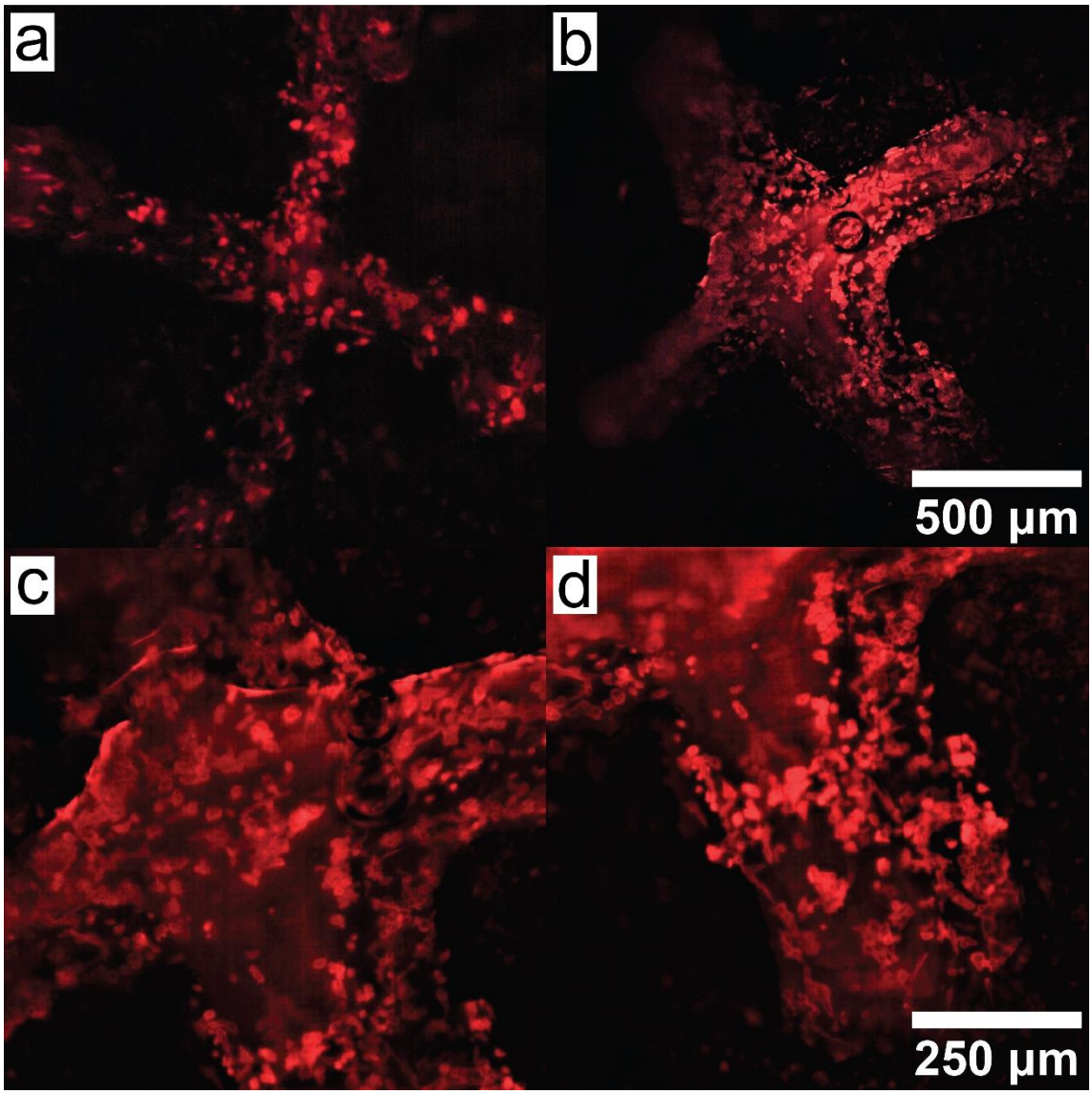

Figure 3.7: *Z-stacked fluorescence images of PC12 cells obtained after 72 hours of culture in medium containing nerve growth factor (NGF). The cells showed greater adherence and spreading as the NGF aids in growth of protoplasmic extension marking the onset of dendritic growth. The images were taken with a wide-field fluorescence microscope using UV lamp and filters for different wavelengths of incident light.*

3.4.6 Characterization with SEM

Differentiating PC12 cells on fibroin scaffolds were imaged with scanning electron microscope (FEI Inspect F). Some of the cells showed cytoplasmic extensions indicated by red arrows while a few showed dendritic growths indicated by blue arrows in the **Figure 3.8**.

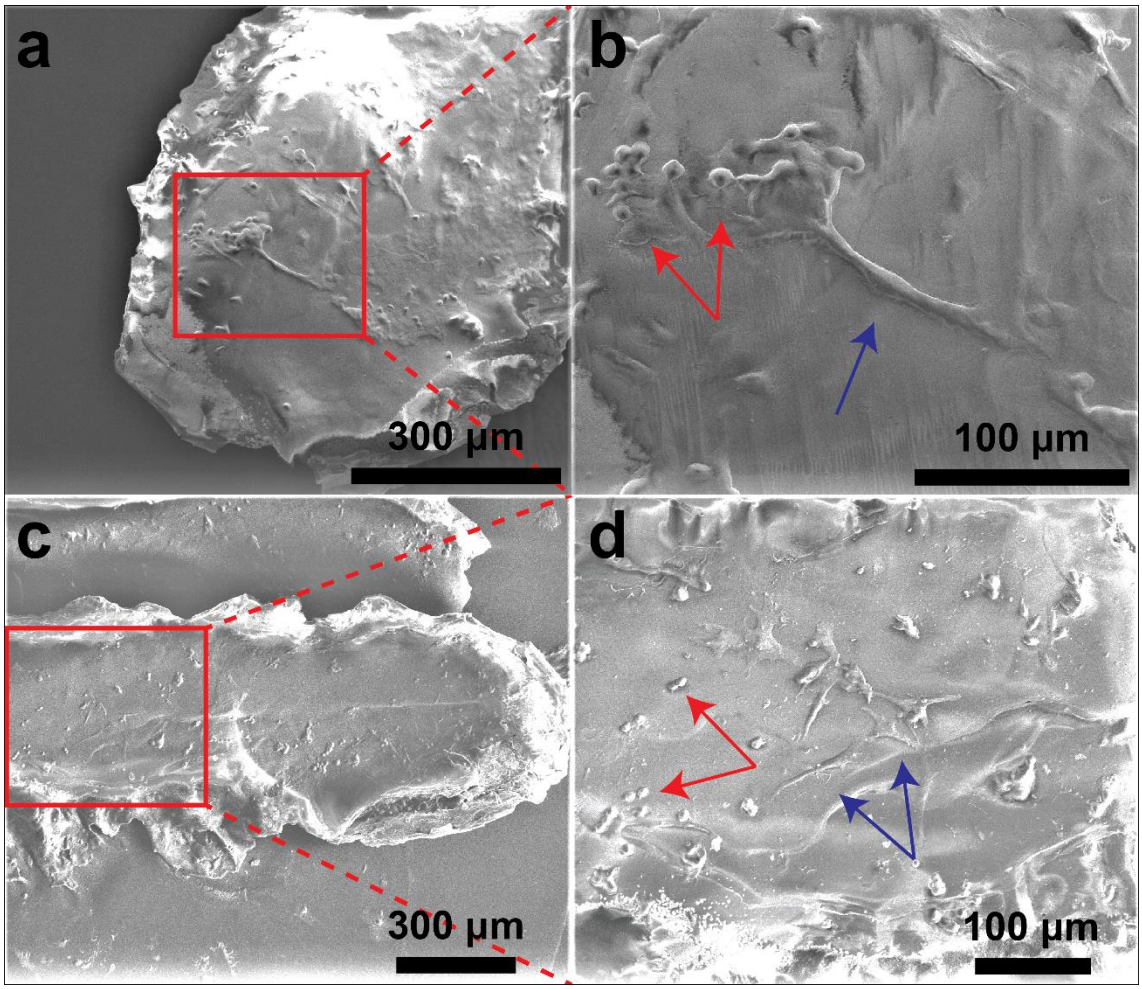

Figure 3.8: *SEM images of the PC12 cells grown on silk fibroin cell carrier in media containing NGF and imaged after 72 hours of culture. The red arrows indicate undifferentiated cells, while the blue arrows indicate differentiating cells along with cytoplasmic extensions and dendrite growth. The sample preparation for SEM caused a significant number of cells to slough off.*

3.5 Discussion

3D culture of cells is an advancement over the conventional plate-based culture of adherent cells. Among the innumerable areas of cell-based research, *in vitro* brain tissue and ganglion models are an important area for understanding neurodegenerative diseases. In that regard, a 3D neuronal cell culture platform using fibroin scaffolds or cell carriers was developed in this study. Rat pheochromocytoma PC12 cells and human neuroblastoma SH-SY5Y cells were used in the study and cultured on fibroin scaffolds fabricated using 3D reactive inkjet printing. The PC12 cells adhered on the scaffolds as

observed in the fluorescence images and showed significant proliferation as observed in the resazurin-resorufin assay for assessing cellular metabolic activity. The SH-SY5Y cells, in contrast, failed to adhere strongly and did not show significant proliferation. The undifferentiated SH-SY5Y cells are known to form mounds or clumps of cells and appeared similarly clumped in the images obtained in this study. This caused poor adhesion of SH-SY5Y cells on the scaffolds resulting in their frequent sloughing off the scaffold surface. The nerve growth factor (NGF) helped initiate differentiation in PC12 cells as evident by the cytoplasmic extensions and growing dendrites at different stages in the SEM images. Additionally, the NGF also helped the cells adhere more strongly to the scaffold surface as observed in the fluorescence images.

The work in this chapter is expected to inspire further research in the area of cell patterning in 3D and achieving guided and directional neuronal growth in 3D. An example of expected pattern of growth of neuronal cells in 3D, while maintaining their native shape without getting affected by gravity, is illustrated in **Figure 3.9**. This model gives flexibility in the development of both 3D culture carrier or scaffold as well as 3D nerve guidance carriers to facilitate axon and dendrite growth in the required pattern in 3D.

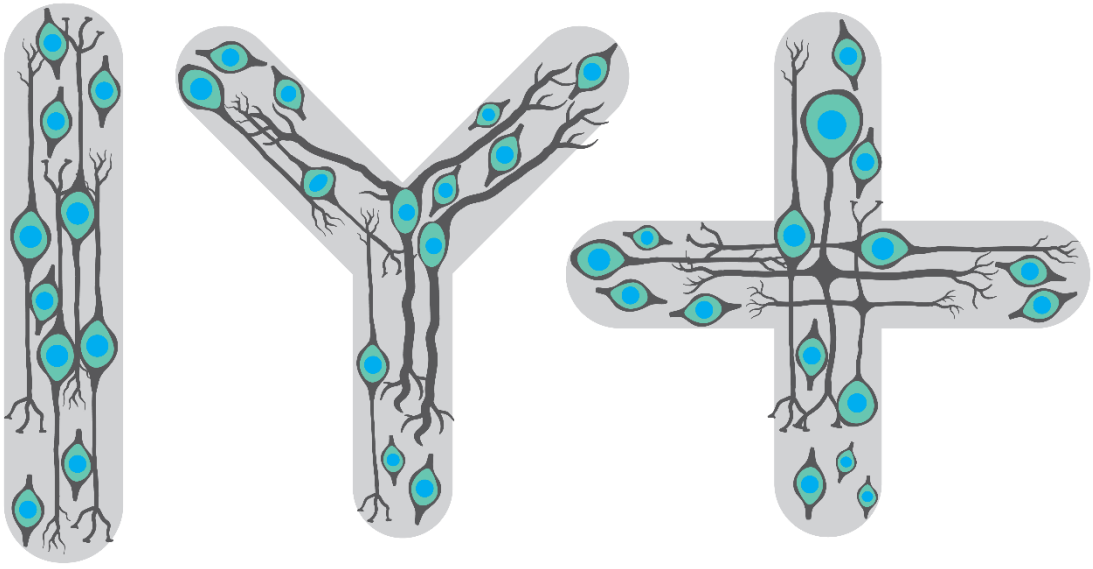

Figure 3.9: *Simplified schematic and exemplary illustration of nerve cells after differentiation while adhering to 3D cell carriers of desired shape which is determined by the desired growth pattern.*

3.6 Conclusion and Future Prospects

This study shows the applicability of developing 3D cell cultures by using an inkjet bioprinter to fabricate 3D cell carriers in any desired geometric shape. In this study, PC12 and SH-SY5Y cells were grown on millimetre-sized 3D fibroin cell carriers. Neuronal cell PC12 growing on differently-shaped fibroin cell carriers, which are fabricated by 3D inkjet bioprinting, can be shown to divide and proliferate. The PC12 cells adhered to the cell carriers, maintained their native spherical shape and showed increase in cell number over the 72 hours of observation period. Additionally, the PC12 cells also showed differentiation in the form of dendrite growth on culturing them in nerve growth factor. In the future, this technique is supposed to be applied for 3D cell micropatterning of the nerve cells. It differently shaped fibroin scaffolds can also be used as *in vitro* or *in vivo* nerve guidance conduits for treating nerve degeneration and repairing nerve damage. Additionally, this 3D culture can be used as a model and a template for growing and differentiating stem cells in 3D culture for applications in adoptive cell transfer based therapies.

Chapter 4: 3D INKJET PRINTED SELF-PROPELLED MOTORS FOR BIOMEDICAL MICRO-STIRRING APPLICATIONS

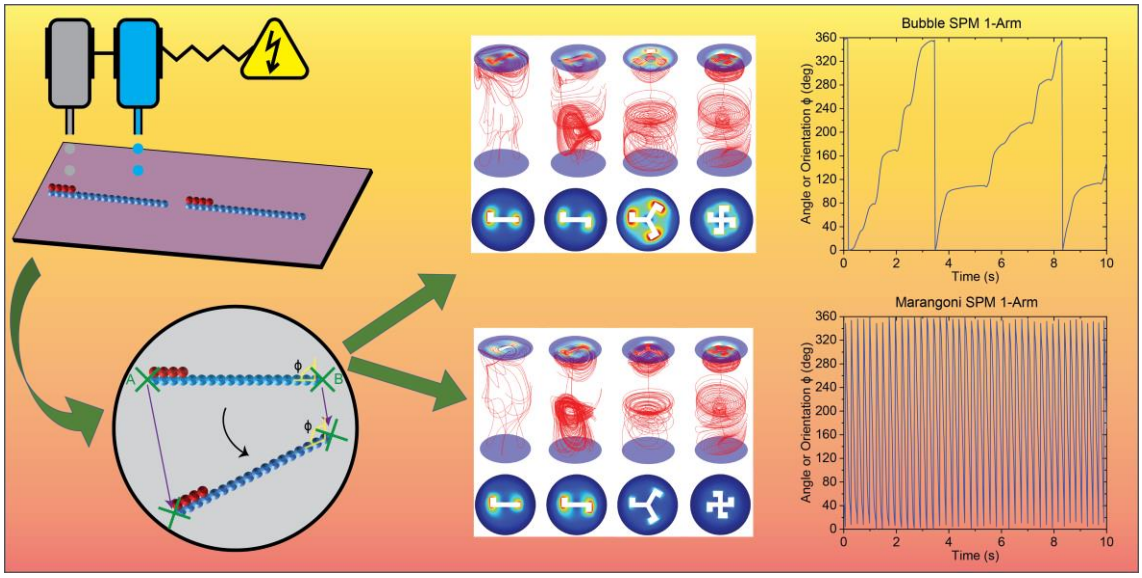

4.1 Abstract

In this study, the application of 3D reactive inkjet printing technology to precisely fabricate millimetre-sized self-propelled motors (SPMs) from regenerated silk fibroin and with well-defined shapes is reported. The resulting 3D structures are an example of self-propelled particles (SPPs) capable of generating motion without external actuation and have potential applications in medicine and environmental sciences for a variety of purposes ranging from micro-stirring biological assays and sensing water quality. 3D inkjet printing generated well-defined solid silk structures at millimetre-scale by converting water soluble regenerated silk fibroin (silk I) to insoluble silk fibroin (silk II). SPMs in four different geometric shapes, each utilising two different propulsion mechanisms, were analysed and compared in terms of their propulsion behaviour, such as instantaneous velocity decay, RPM fluctuations over time and overall propulsion trajectory. The two propulsion mechanisms were bubble propulsion through catalysis and surface tension gradient through surfactant leaching. For catalytic propulsion, the structures were selectively doped in specific regions with the enzyme catalase in order to produce motion via bubble generation and bursting in hydrogen peroxide solution. For surface tension propulsion, non-doped structures were propelled through surface tension gradient caused by leaching of PEG_{400} surfactant in DI water. The results demonstrated the ability to tune the motion by varying the dimensions or geometric shapes of the printed structures and by varying the propulsion mechanism. It was observed and concluded that the simple 1-arm geometric shape propelling with surface tension gradient caused by the leaching of surfactant leads to faster propulsion velocities with smooth deceleration. In comparison, bubble propulsion was observed to be slower and jerky and uneven in deceleration.

4.2 Introduction

Self-propulsion is the ability of an object or particle to generate its own movement in a fluid medium. Such self-propelled objects or particles can employ a variety of propulsion mechanisms which could be categorised as physical, chemical and biological propulsions. Taking inspiration from natural self-propelling systems, a wide variety of artificial self-propelled motors (SPMs) have been developed for applications in an equally diverse variety of fields. Such artificial SPMs employ a variety of propulsion mechanisms to produce motion, which can be categorized as either physical propulsion or chemical propulsion [10, 124, 125, 177-179].

4.2.1 Physical Self-Propelled Systems

Physical propulsion mechanisms include various physical forces that can induce self-propulsion are surface tension gradient, temperature gradient, light energy [180], acoustic energy [181], magnetic field [122, 123], and electric field. Surface tension driven camphor boats, exemplifying self-propelled particles (SPPs), are an old historical example [182, 183]. First scientifically documented in the 17th century, it took nearly two centuries to fully understand that the phenomenon of self-propulsion of camphor particles on water surface occurs due to surface tension gradient, a phenomenon which is also called Marangoni effect. Surface tension is a physical property of fluid surfaces to acquire the least possible surface area. It resists distortion and thus can also be defined as energy required to increase surface area of a liquid by a given amount [184]. Marangoni effect occurs due to non-equilibrium in surface tension, that is, different parts of the fluid surface momentarily have different tensions thus resulting in a gradient in the stress force [185]. Within such a gradient, heat and matter on a fluid surface always show the tendency to travel to regions of higher surface tension [186]. In optical or light-dependent systems, near infra-red illumination is used to cause a temperature gradient which propels the particles, a phenomenon called as thermophoresis [180, 187]. Sound waves

in the ultrasonic range have enough sound pressure gradient to drive nano- to micro-meter sized particles [181]. In magnetism-dependent systems, particles made of magnetic materials, such as ferromagnetic and superparamagnetic materials, can be oriented and set into motion under an external magnetic field [188]. Electrical mechanisms cause propulsion in two ways, namely, electrophoresis which drives charged particles under a direct current (DC) electric field gradient, and dielectrophoresis which drives neutral particles under an alternating current (AC) electric field gradient [189]. Catalysis induced bubble production and burst leading to thrust is another category of physical propulsion mechanism. A common technique of bubble propulsion in research is catalase induced decomposition of hydrogen peroxide into water and oxygen. Another example is a dual-catalyst system embedded on carbon nanotubes in which glucose oxidase decomposes glucose into hydrogen peroxide, which is then quickly decomposed by catalase, producing oxygen bubbles, which cause propulsion of the nanotubes. It is a system that does not require hydrogen peroxide as fuel in the surrounding media and can, thus, be applied in a wider variety of liquid media [190].

4.2.2 Chemical Self-Propelled Systems

A common chemical propulsion mechanism is to use catalytic or enzymatic activity to either generate motion producing gradients or generate bubbles that impart momentum to the object when they detach. Chemical reactions can lead to a variety of changes in a particle or in the surrounding environment in a fluid or at an interface that set the particles in motion. Catalysis is a common form of chemical mechanism causing self-propulsion. Several catalysis-induced reactions form such products which occupy much larger volume than the reactants. For utilizing this mechanism, in a study, the enzyme urease was trapped inside carbon nanotubes, which is then propelled in a liquid medium containing urea as fuel. Urease decomposes urea into ammonia and dissolved carbon dioxide, which expands in volume and is released out as liquid nanojet, providing

propulsion to the nanotubes [191]. Previous studies have investigated several catalytic and chemical SPMs, including polystyrene beads with platinum nanoparticles and chromium adsorbed on the surface [177], gold-platinum bimetallic Janus nano-rods [178], magnesium Janus micro-stirrers or motors [124], micro-stirrers or motors made of a magnesium core and titanium dioxide shell with embedded gold nanoparticles [125], and silk fibroin Janus micro-rockets with catalase embedded within the scaffold [10]. Enzymes, however, are not the only source of catalytic reactions. Platinum, deposited on micron-sized polystyrene beads, acts as a catalyst inducing the breakdown of hydrogen peroxide into water and oxygen. The second mechanism which provides propulsion to the beads is self-diffusiophoresis, in which, a sudden increase in local dissolved oxygen concentration drives the beads into motion [177, 192]. The third mechanism of chemical propulsion is catalysis-induced self-electrophoresis in asymmetrically designed particles. In a study, electron movement within the gold-platinum Janus particles caused self-propulsion in the particles. Electrons move from platinum to gold because both catalyse hydrogen peroxide decomposition, but in different ways [193]. A non-catalytic chemical reaction can also provide gradients strong enough for propelling colloidal particles. In a study, magnesium-core titanium-dioxide-shell particles propel in water as magnesium reacts vigorously with water, producing hydrogen bubbles. The propulsion lasted for as long as 18 minutes until the whole magnesium core dissolves away leaving behind hollow shell [125]. In light-dependent systems, photocatalytic reactions from high energy UV-light lead to chemical changes, such as, ion concentration gradient, which propel the particles. One example is aggregation and dissociation of Ag_3PO_4 microparticles in response to UV light [194].

4.2.3 Biological Self-Propelled Systems

In theory, individual living organisms are considered as self-propelled systems with several magnitudes of size range. These biological ‘SPSs’ utilize the same physical and

chemical propulsion mechanisms, as described above, but in a more complicated and ordered manner. They obtain energy from their surroundings through biological processes, such as, nutrition, photosynthesis and respiration, and utilize it for movement (phototaxis, chemotaxis, etc.) and locomotion (flight or fight behaviour, flying, running, etc.) in response to a variety of stimuli, such as, light, temperature, pH, sight, sound, smell, etc. Micro-organisms, such as, bacteria and protozoans, display more observable similarities to self-propelled particle systems. Colony forming micro-organisms, such as, *Staphylococcus* and *Volvox*, and swarming organisms, such as, ants, honey bees, fishes and birds, display ordered collective motion similar to active matter systems. At the fundamental level, the living organisms 'propel' with the help of biological molecular motors, which exhibit well-orchestrated self-propulsion behaviours. The F_OF_1 ATP synthase molecules are rotating machines that drive ATP synthesis by creating an electrochemical gradient of protons across the inner membrane of mitochondria. Other molecular motors include cilia and flagella, which are locomotory cellular organelles. The natural occurrence of SPP systems inspire the design and fabrication of artificial SPP systems.

4.2.4 Applications and Current Study

Self-propulsion is an area of active research in order to engineer and produce SPMs with desired qualities and controllability for a variety of applications. Depending on the intended application, SPM size can range from a few nanometres to a few centimetres. Such custom-made SPMs have multitudinous potential applications in biomedical sciences, biomedical research and environmental science research. Examples include medical diagnosis of diseases with lab-on-a-chip devices [188], loading and *in vivo* targeted delivery of therapeutics [195], environmental remediation, e.g., cleaning of oil spills [124], and photocatalytic degradation of chemical and biological warfare agents, such as *Bacillus anthracis* and nerve agents [125]. In hydrodynamics, different

propulsions of SPMs in different fluids help in determining unknown parameters, such as surface tension, viscosity and Marangoni force. [196].

It is therefore desirable to be able to produce SPMs that undergo specific trajectories, such as long linear trajectories for transport or rotational trajectories for micro-mixing applications. The focus in this study is on rotational motion for micro-mixing or stirring of biomedical assays and finding out which geometric shape and propulsion mechanism offers the best results out of the alternatives tested in this study. Owing to its diverse applications, there is no single established method to fabricate SPMs, but for biomedical and environmental applications, it is essential to use a material which is biocompatible, biodegradable, eco-friendly, readily available, cheap and allows easy fabrication of complex SPMs. Regenerated silk fibroin (RSF) is one such biomaterial that fulfils all these parameters along with being also approved by the Food and Drug Administration (FDA).

In this study, millimetre-size self-propelled motors made of regenerated silk fibroin using 3D reactive inkjet printing were made to propel in liquid medium through catalysis and surface tension gradient. Catalyst-substrate reaction and surface-tension gradient were utilised as energy sources for demonstrating two different SPM propulsion mechanisms. The enzyme catalase and its substrate hydrogen peroxide were used for driving SPMs through catalytic reaction (herein called “catalytic SPMs”). The surfactant poly (ethylene glycol) or PEG (MW = 400) was used for driving SPMs through surface tension gradient, a phenomenon which is also known as the Marangoni effect (herein called “Marangoni SPMs”). Within both propulsion mechanisms, the SPMs were printed in four different geometric shapes, as shown in **Figure 4.2**, in order to analyse the effect of geometry on the propulsion behaviour and trajectories.

In catalytic SPMs, the enzyme catalase was used as the "engine” to generate propulsion with hydrogen peroxide solution being used as the aqueous fuel medium. Catalase is an enzyme found in the peroxisome organelles of almost all the cells of most living organisms, from bacteria to humans. It catalyses the conversion of hydrogen peroxide

(H_2O_2), a source of reactive oxygen species (ROS) into the harmless products, namely, water and oxygen [197]. It thus protects the cells from oxidative damage caused by ROS. In cells, the product oxygen readily dissolves into the surrounding aqueous medium. At a larger scale, however, a larger quantity of oxygen is produced, assembling together in the form of bubbles and providing propulsion to the particles. Catalase is one of the fastest known enzymes clocking at 800,000 catalytic events per second and is limited only by diffusion rate [197]. It can thus generate enough amount of oxygen bubbles and resulting force in order to propel millimetre-sized particles. The release of oxygen bubbles from the enzyme sites of the SPMs generates a force onto the particle causing it to undergo propulsion in the opposite direction of the bubble release [10] as shown in **Figure 4.7 a**. The H_2O_2 decomposition reaction is a first order reaction with respect to both catalase and H_2O_2 and therefore, it is a second order reaction overall. It means that the rate of reaction increases linearly with an increase in the concentration of either of the two reactants. The catalase found in humans has a tetrameric structure, consisting of four subunits as shown in the ribbon diagram in **Figure 4.1**. Each subunit is made up of a polypeptide chain (~500 amino acids), a haeme group and an NADPH molecule [198]. Catalase breaks down two molecules of hydrogen peroxide at a time into two molecules of water and one molecule of oxygen. This break down is a two-step process. In the first step, the haeme (Fe^{3+}) reduces an H_2O_2 molecule to water and generates a covalent oxyferryl species (Fe^{4+}=O). In the second step, oxyferryl oxidizes a second H_2O_2 molecule to molecular oxygen (O_2) and releases the ferryl oxygen species as water [198]. The pH of a 5% solution of commercially available H_2O_2 usually varies between 5 and 7 [199]. Catalase has been found to be stable at this pH range without any significant loss in its enzymatic activity [200]. Encapsulation of catalase inside the porous fibroin scaffold ensures further enzyme stability for extended periods of time as has been shown previously [10, 201]. On the body of a catalytically driven SPMs, different positioning of the catalytic engine sites as shown in **Figure 4.2 a–d** resulted in different propulsion behaviour and trajectories [177].

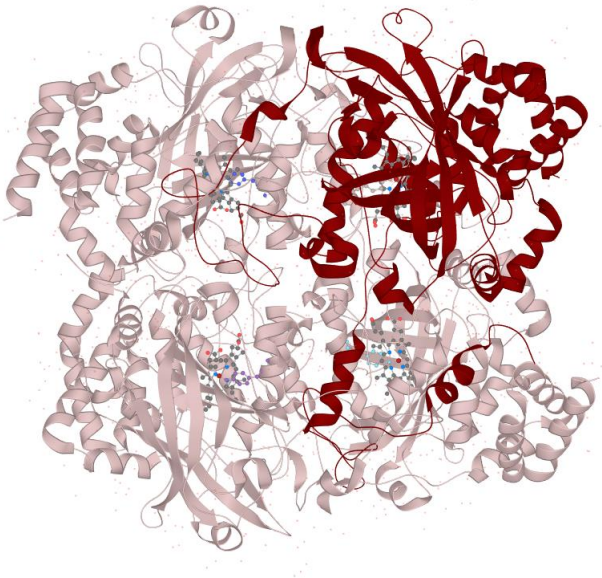

Figure 4.1: *Ribbon diagram of the structure of bovine liver catalase (image obtained from Protein Data Bank. PDB ID: 1tgu).*

Marangoni effect is the name given to the tendency of matter and energy to flow from a region of low surface tension towards a region of high surface tension along the interface of two fluids, such as the air and water interface [186, 202, 203]. Marangoni effect can be visualised if an object floating on water surface gets propelled owing to a sudden change in the surface tension in the object's vicinity. Substances capable of causing such sudden changes in surface tension are called as surface-active agents or surfactants. Poly (ethylene glycol) or PEG is one such substance. As a solute-solvent mixture has a lower surface tension than the pure solvent, any substance, which is soluble in water can act as an agent to cause Marangoni effect on water surface. In Marangoni SPMs, the design is kept consistent and similar to the catalytic SPMs by keeping the engine-equivalent regions devoid of any catalase as shown in **Figure 4.2 e–h**. The continuous leaching of PEG_{400} from the SPMs with asymmetry in weight distribution causes the rotational propulsion as shown in **Figure 4.7 b**.

In pursuit of generating efficient micro-stirring motors, it is necessary to fabricate SPMs with well-defined geometric shapes and engine positions and compare the different geometric shapes and powers of the engine. SPMs printed with engine or engine-

equivalent sites off centre gave the SPMs an asymmetry that resulted in rotational motion rather than random or predominantly linear motion. This approach also made it simple to manufacture SPMs in a variety of shapes and design configurations defined by computer-aided design (CAD), thus allowing easier and more accurate controllability on the desired movement during practical applications. This study provides a blueprint for the manufacturing SPMs with RSF at millimetre scale. The use of inkjet printing for manufacturing RSF micro-stirring motors opens the door for the highly versatile production of SPMs from materials, such as fibroin, which are not otherwise able to be deposited or fabricated through other means, such as evaporation. The motivation for this study is also to evaluate a possible application for these microstirring devices to overcome current diffusive transport limitations observed in biological assays [204].

4.3 Experimental Methods

4.3.1 Materials

The list of materials is described in **Chapter 2, Section 2.1**. Additionally, catalase enzyme derived from bovine liver (>20,000 units/mg) was purchased from Sigma Life Science and hydrogen peroxide was purchased from Sigma Aldrich.

4.3.2 Preparation of Fibroin Ink for Printing

The process of preparation of fibroin ink for 3D reactive inkjet printing is described in **Chapter 2, Section 2.2 – 2.7**.

4.3.3 3D Inkjet Printing Process

The process of 3D reactive inkjet printing is described in **Chapter 2, Section 2.11 – 2.12**. Additionally, for printing the catalytic engine sites of the catalytic SPMs, fibroin solution at 40 mg/mL was mixed with PEG_{400} at 14 mg/mL and catalase at 5 mg/mL (with catalytic activity of >20,000 units/mg) to formulate a second primary ink (ink 2). As mentioned

previously, the contrasting blue colour of the SPMs imparted by Coomassie brilliant blue mixed in the curing methanol (ink 3) helped in their easy recognition and automated tracking after propulsion. Additionally, in this study, the three inks and their separate channels required the use of three jetting devices during printing. Each channel needed to have its unique jetting parameters adjusted to ensure that each ink gave a good and stable droplet formation as shown in **Figure 2.19**. These parameters are dependent on specific jetting device and ink and, therefore, need to be adjusted accordingly. Following is the serial order of stage-wise printing of the different inks:

Stage 1: printing of Ink 1 (main body)

Stage 2: printing of Ink 3 (curing ink)

Stage 3: printing of Ink 2 (catalytic ink for engine sites) or Ink 1 (Marangoni SPMs)

Stage 4: printing of Ink 3 (curing ink)

Stage 5: repeat Stages 1–4 as required for the desired number of layers (e.g., 100).

Four simple geometric shapes of SPMs were designed for comparing the effect of geometry on propulsion behaviour as shown in **Figure 4.2**. The 1-engine and 2-engine SPMs were straight lines. In 1-engine catalytic SPM, the enzyme is positioned on the side of one end. In 2-engine catalytic SPM, the enzyme is located on the alternate sides of the two ends. In 3-engine and 4-engine catalytic SPMs, the enzyme was positioned on the same side of the ends of all the arms in order to give directionality during propulsion. The length and width of the printed SPMs were approximately 1.25 x 0.3 mm for each arm as measured from the light micrographs using ImageJ.

For Marangoni SPMs, same geometry was used except that the composition at the bulging tip of the arms or the engine-equivalent regions was kept the same as the rest of the body.

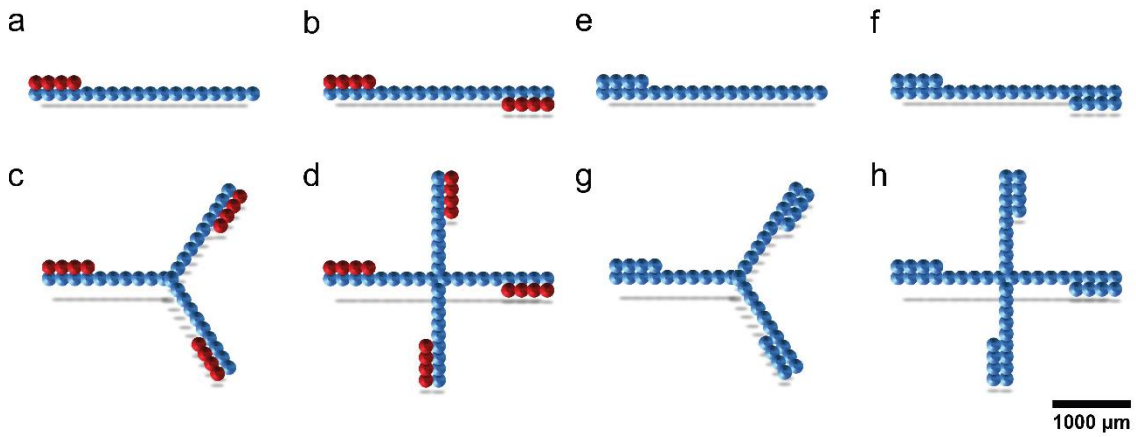

Figure 4.2: *Computer generated illustration of the four geometrical designs of the catalytically driven and surface tension driven SPMs as observed through the Microsoft Excel spreadsheet graph plots. The blue and red colours represent the main body and the catalase positions of the SPMs named as* ***(a)*** *1-engine,* ***(b)*** *2-engine,* ***(c)*** *3-engine, and* ***(d)*** *4-engine. In the Marangoni SPMs, the whole body of SPMs is uniform in composition and named as* ***(e)*** *1-engine equivalent,* ***(f)*** *2-engine equivalent,* ***(g)*** *3-engine equivalent, and* ***(h)*** *4-engine equivalent. The bulging design of the engine and engine-equivalent parts at the tip of the SPM arm also provides asymmetry to the mass distribution and thus favouring rotational motion by imparting differential drag when propulsion force is generated.*

4.3.4 Characterization of SPMs

The SPMs were characterized using light microscopy and scanning electron microscopy, whose working principles are described in detail in **Chapter 2, Section 2.13**. For acquiring light micrographs, freshly fabricated SPMs were imaged as shown in **Figures 4.2 and 4.3**. For SEM, images were taken separately with both unused (pre-propulsion) and used (post-propulsion) SPM samples. Unused and used SPMs were removed from the silicon wafer and bulk solution, respectively, and transferred onto 10 mm wide carbon sticky pads mounted on aluminium scanning electron microscopy (SEM) stubs. The samples were dried in a drying oven for 10 min at 60 °C. The sample stubs were then loaded onto the sputter coater stage and 50–100 nm of gold is sputter coated (argon plasma at 0.05 Torrs) onto the samples, ensuring a homogeneous gold surface coverage of the sample. Afterwards, the sample stubs were removed from the sputter coater, loaded onto the SEM stage and imaged under vacuum at 5.0 kV. Care was taken not to

use very high acceleration voltages, which can burn the silk and give rise to false features in the images.

4.3.5 SPM Propulsion

The SPMs were propelled under room temperature (~ 20 °C) at a fluid interface, which means the boundary between two fluid phases (liquid or gas). For catalytic SPM propulsion, the silicon wafer slide with imprinted SPMs was dipped in water for a few minutes to remove the SPMs off the wafer surface and to wash away PEG_{400}. A glass Petri dish was cleaned with deionised water and wiped clean ensuring that the surface remained dust free. 10 mL of 5 % w/v H_2O_2 solution was then dispensed into the Petri dish and left to equilibrate. A washed SPM was then transferred carefully on the tip of a syringe needle and placed in the centre of the Petri dish on H_2O_2 solution. At this stage, the catalase in the SPM instantly started to catalyse the breakdown of hydrogen peroxide into water and oxygen with bubble formation around the engine part of the SPM. The oxygen bubbles provided force to the SPM which started propelling with circular or rotating motion. The Marangoni SPMs, on the other hand, were taken off the silicon wafer directly with the help of a sharp needle and placed on deionised water for carrying out the surface tension driven propulsion. The 12-well plates, with 23 mm well diameter, were selected for propelling Marangoni SPMs owing to their extremely fast initial velocities which caused them to run out of the camera frame. In case of catalytic SPMs, 90 mm Petri dish was chosen to make sure that enough H_2O_2 was present so that it didn't become a reaction-rate limiting factor. Additionally, as catalytic SPM propulsion was much slower than Marangoni SPM propulsion, no catalytic SPM propelled out of the video frame.

4.3.6 Propulsion Data Acquisition

The bottom of the Petri dish or 12-well plate was lit up with a cool-white LED light-source (AGPtek Lightpad) and a high speed PixeLink™ CCD colour camera (model: PL-D732CU-T), fitted with Navitar™ macro zoom lens (1-60135 zoom tube lens with 1-6010 camera coupler attachment), was used to capture and record the SPM propulsions, which were saved as AVI files. A total of 12,000 frames were captured per video per SPM at the rate of 100 frames per second, giving a total length of 120 seconds per video. Each video was then analysed for tracking the trajectory of the moving SPM using a custom-built developed programme built in the LabVIEW platform (National Instrument Corporation, USA). After recording, ImageJ was used to generate image sequence from the video frames for all the sensors.

4.3.7 Tracking & Trajectory Analysis

Automatic tracking was done by importing the video of a propelling SPM into the custom-built LabVIEW tracking programme as shown in **Figure 4.3**. In this programme, the coordinates of each SPM were tracked on its two ends frame by frame by calculating the linear displacement of the tracking points between two consecutive frames as shown in **Figure 4.6**. The LabVIEW algorithm then analysed the tracking data, reporting the mean instantaneous velocities of both ends of the SPMs together with the calculated centre of mass velocity. The tracking programme calculated instantaneous velocities in each frame by locating an SPM's spatial positions in two consecutive frames, calculating the SPM's spatial displacement between the frames, and then dividing the displacement by the time difference between the two frames (frame rate). Together with this, the trajectory direction angle and orientation angles over time were calculated indicating the rotational velocities of the SPMs. After tracking was finished, the data was automatically compiled and exported in a Microsoft Excel file.

The instantaneous velocity was calculated as SPM displacement divided by the time taken for displacement between two consecutive video frames by the programme using the following equation:

$$V_{inst} = \frac{\sqrt{(x_2-x_1)^2+(y_2-y_1)^2}}{t_2-t_1}$$

Here, x_2 and y_2 are the position coordinates in second frame, while x_1 and y_1 are the position coordinates in the first frame. Likewise, $t_2 - t_1$ is the time between the two consecutive frames (Δt_{frame}). The values obtained for each frame were then used for determining the velocity decay of SPMs over time.

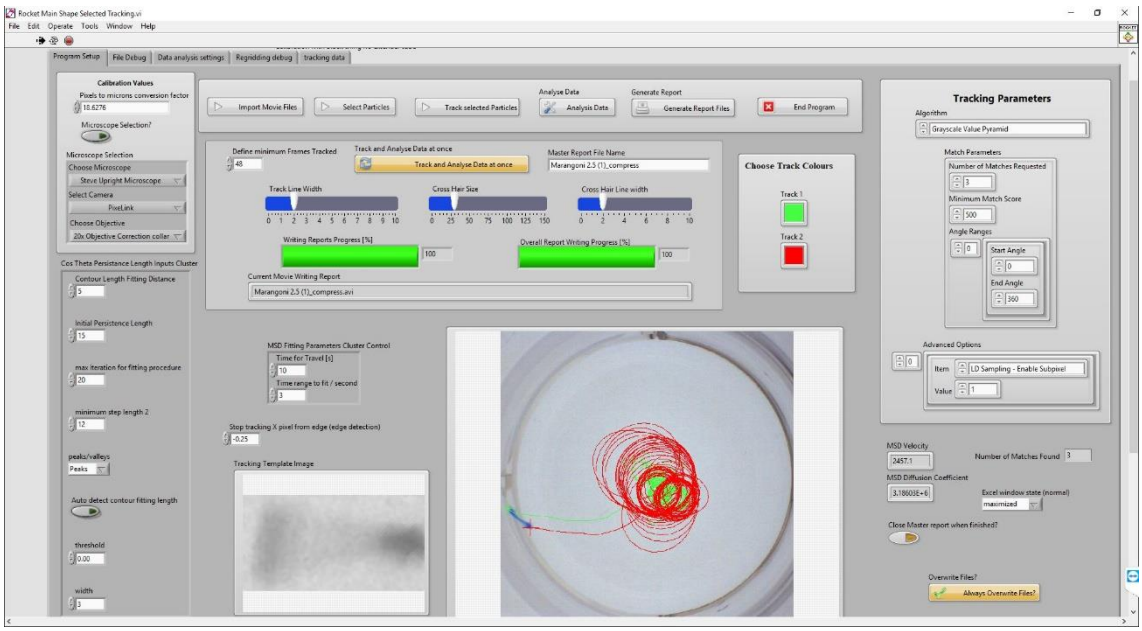

Figure 4.3: *Image of the Front Panel of the LabVIEW programme which is the GUI for conducting tracking of SPM propulsion.*

4.3.8 RPM Counter

In order to accurately count the number of rotations and calculating RPM, I wrote a compact programme in the LabVIEW platform which imports and reads the excel file

consisting of the instantaneous angles of orientation obtained from the tracking data and then outputs the RPM. The GUI of the programme is shown in **Figure 4.4** with the left half showing the Front Panel and the right half showing the Block Diagram. The rate of change of RPM was calculated by finding the times taken by angles of orientation to complete the consecutive cycles of 360° and then plotting the obtained values over the 120 seconds of observation time period.

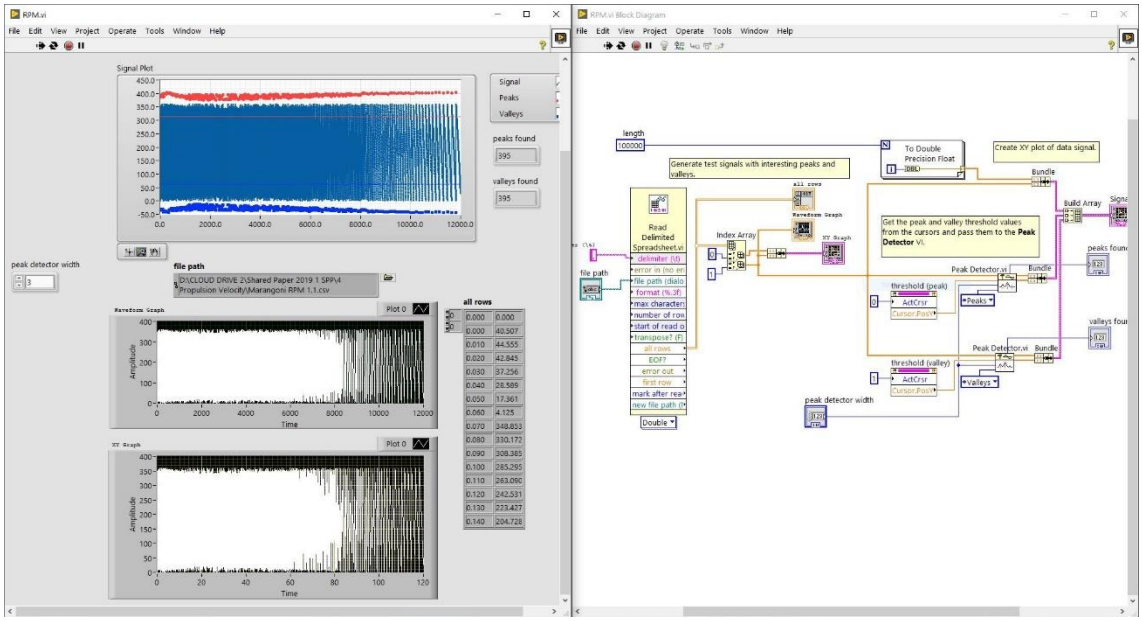

Figure 4.4: *Image of the Front Panel and Block Diagram of the LabVIEW programme which I made for calculating the RPM by counting the repeats in the angle of orientation of the SPMs. The programme simply counts the crests / troughs in a graphical data, which in this case, were the angles of orientation observed over 120 seconds of propulsion of various SPMs.*

4.3.9 Statistics

The instantaneous velocities and angular or rotational angles (Φ) of the propelling SPMs were generated once every 0.01 seconds, which was the time gap between two consecutive video frames. This gave a total of 12,000 data points for instantaneous velocity and angular position for a 120 seconds long video. These instantaneous velocities and angular positions or angles of orientation (Φ) were then plotted against time (t) to generate the instantaneous velocity decay curve and angular velocity decay

curve of each SPM. Next, the change in angular orientation (δΦ) between two consecutive video frames was plotted against the change in time (δt) between two consecutive video frames. This generated the graph showing rate of change of angular velocity or RPM (deceleration or acceleration) of each SPM. All the graphs were plotted in Origin™ 2020.

4.4 Results

The light micrographs of freshly printed catalytic and Marangoni SPMs are shown in **Figure 4.5** and **4.6**, respectively. In the catalytic SPMs, the rectangular red regions show the engine part where fibroin is doped with catalase. In the Marangoni SPMs, the rectangular red region shows the engine-equivalent part which ensures that the design of SPMs remains consistent across the catalytic and Marangoni propulsions. Several satellite droplets are also seen deposited around the SPMs which get away once the SPMs are removed from the silicon wafer substrate.

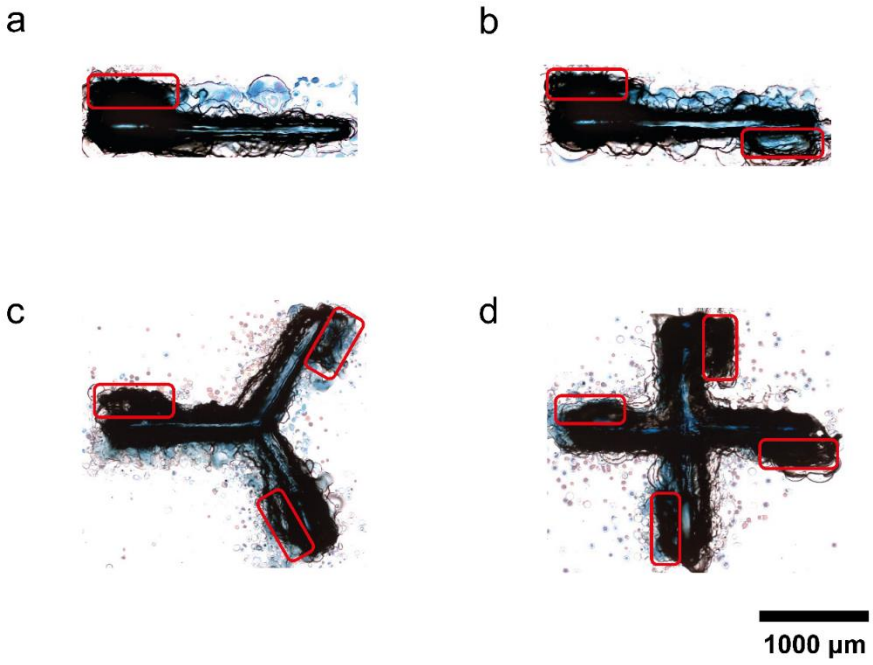

Figure 4.5: *Light micrograph of freshly fabricated catalytic SPMs with catalytic* ***(a)*** *1-engine,* ***(b)*** *2-engine,* ***(c)*** *3-engine,* ***(d)*** *4-engine, shown in red box.*

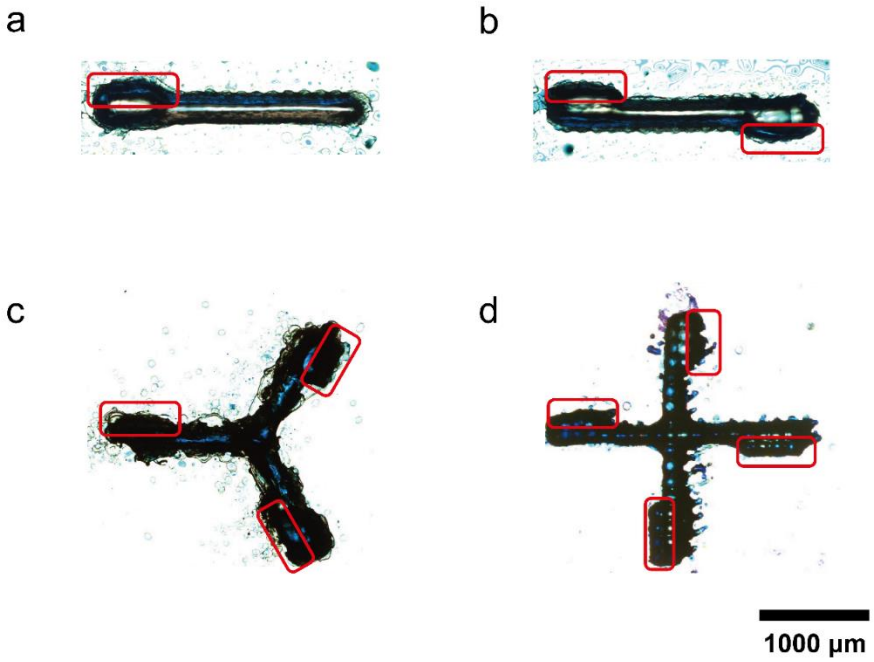

Figure 4.6: *Light micrograph of freshly fabricated Marangoni SPMs with* ***(a)*** *1-engine equivalent,* ***(b)*** *2-engine equivalent,* ***(c)*** *3-engine equivalent,* ***(d)*** *4-engine equivalent regions shown in red box.*

The schematic illustration in **Figure 4.7** shows the propulsion mechanism of catalytic and Marangoni SPMs by taking a 1-engine SPM and a 1-engine equivalent SPM as examples. In a catalytic SPM, the hydrogen peroxide present in the surrounding medium gets decomposed into water and oxygen at the engine site. The oxygen molecules, thus produced, assemble and form bubbles which eventually burst and produce the thrust needed to propel the SPM in the opposite direction. In a Marangoni SPM, the leaching of PEG_{400} occurs throughout the SPM body with the main concentration at the engine-equivalent bulging part. As mentioned previously, the bulging design of the engine and engine-equivalent part also provides an asymmetry which causes rotational motion.

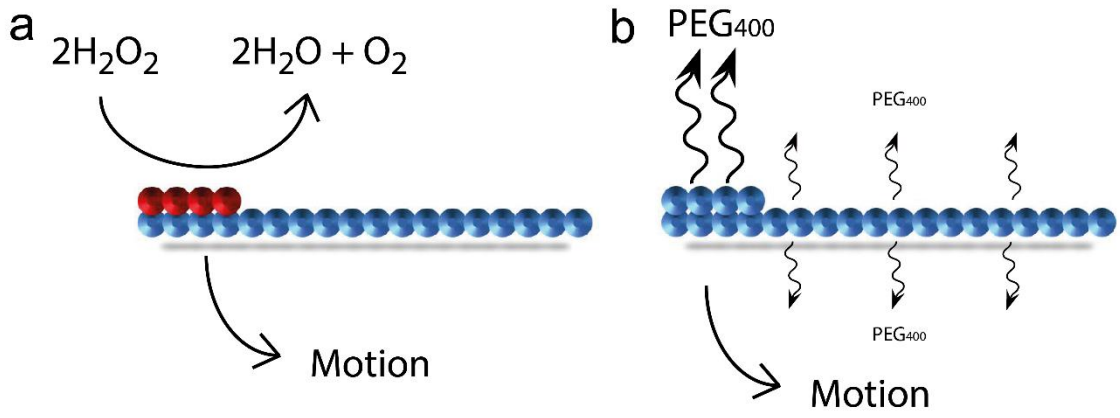

Figure 4.7: *Illustration of the two types of propulsion mechanisms analysed in this study.* ***(a)*** *Catalytic propulsion, which is a physical mechanism caused by the thrust produced from the bursting oxygen bubbles. It shows the catalytic breakdown of hydrogen peroxide into water and oxygen by catalase embedded in the SPMS's scaffold at desired location (shown in red).* ***(b)*** *Surface tension driven propulsion originating from concentration gradient caused by the continuous leaching of a surface-active agent* PEG_{400}*.*

High magnification images of the SPMs were obtained using a scanning electron microscope to analyse the topography of the catalytic and Marangoni SPMs both before as well as after their propulsion. As evident in **Figure 4.8 a – b**, the engine part of the catalytic SPM showed smooth texture before propulsion and a rough and punctured texture after propulsion. The punctures indicate the site of catalytic reaction and oxygen bubble formation. On the other hand, the engine-equivalent part of the Marangoni SPMs showed visibly smooth textures both before as well as after propulsion as shown in **Figure 4.8 c – d**. This is because of the smooth and continuous leaching of PEG_{400} molecules which are significantly smaller than the oxygen bubble produced vigorously at certain weak points on the catalytic SPM surface. The irregularly sized punctures at the reaction sites on the catalytic SPMs also indicated the lack of regularity in bubble production which in turn resulted in irregular or jerky motion as observed during the real time propulsion.

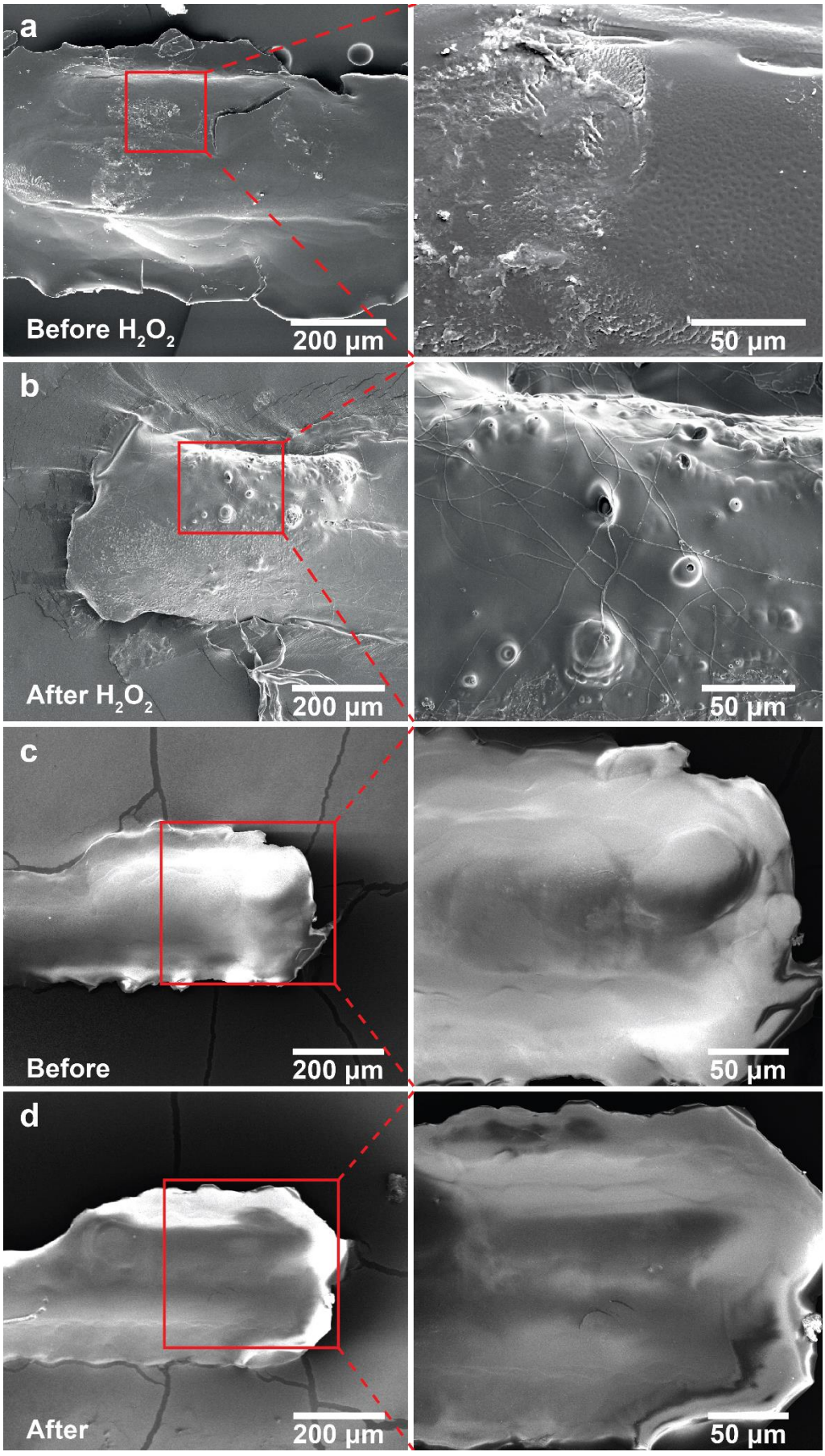
a
Before H_2O_2
200 µm
50 µm
b
After H_2O_2
200 µm
50 µm
c
Before
200 µm
50 µm
d
After
200 µm
50 µm

Figure 4.8: (a – b) *SEM images of the main body and catalase engine part of a catalytic SPM.* ***(a)*** *Catalytic SPM before exposure to 5% w/v H_2O_2 fuel solution.* ***(b)*** *Catalytic SPM after exposure to 5% w/v H_2O_2 fuel solution. Pores can be clearly seen on the engine surface in the SEM images of the SPMs originating from the oxygen bubble release. Images on the right are enlargements of the red boxed regions.* ***(c – d)*** *SEM images of the main body and engine-equivalent part of a Marangoni SPM.* ***(c)*** *Marangoni SPM before exposure to DI water* ***(d)*** *Marangoni SPM after exposure to DI water. No significant differences are observed in the morphology or surface features between the pre-propulsion and post-propulsion images.*

For tracking the motion of the SPMs, two extreme points, as indicated by green 'X' symbol in **Figure 4.9**, were manually selected on each SPM after importing their propulsion videos in the LabVIEW tracking software. These points continuously tracked the SPM displacement frame-by-frame and traced the overall path as red and green lines as seen in the time-lapse images in **Figure 4.10**, **4.12** and **4.13**. The linear displacement shown in purple arrow helped in automated calculation of the instantaneous velocity by dividing the displacement by time taken between two frames. The change in angle of orientation ϕ over time was measured to obtain data on rotations per minute.

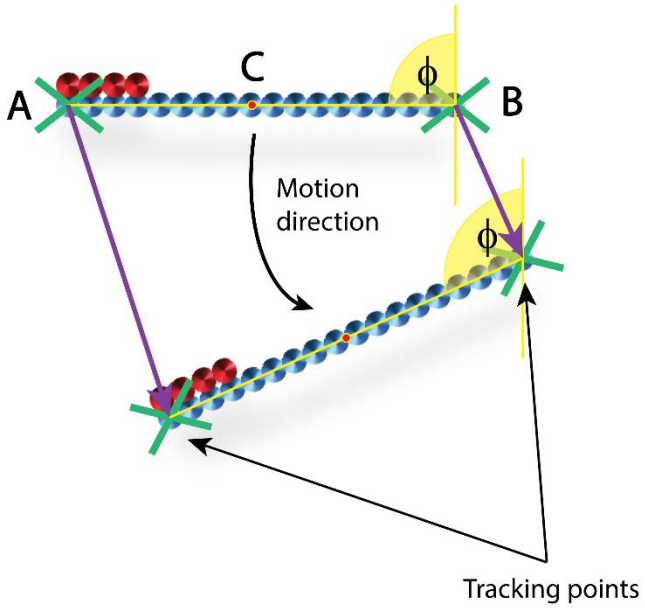

Figure 4.9: *Schematic representation of SPM tracking over two consecutive frames. 'A' and 'B' indicate tracking points and C indicates the centre of mass. The symbol ϕ indicates the angle of orientation. SPM trajectory direction is indicated by the curved black arrow.*

Before comparing the effects of geometry and propulsion mechanism on SPM motion, two different layers of thickness in SPM fabrication were compared for catalytic SPMs as a trial model. To analyse this effect of mass difference on SPM propulsion, 100 layers thick catalytic 1-engine SPM was compared against the 200 layers thick one. **Figure 4.10** shows the selected frames from the extracted image sequence of the propulsion video of the two SPMs. **Figure 4.11** shows the angle of orientation of the two SPMs over a period of 30 seconds and showing clearly that the more catalase content in 200 layered SPM allowed higher RPM.

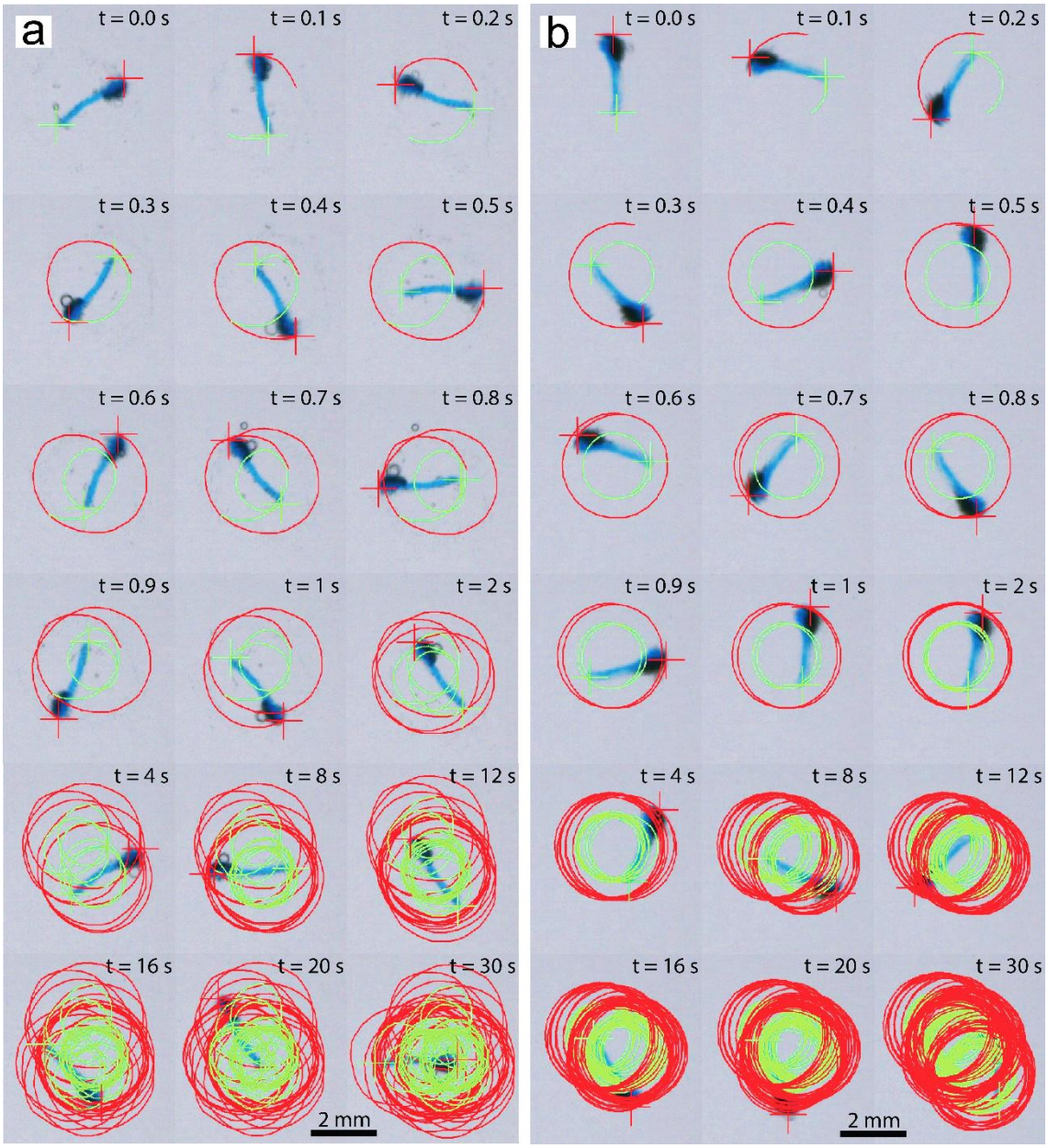

Figure 4.10: *Select video frames of two 1-engine catalytic SPMs propelling in 5% H_2O_2 aqueous solution showing the trajectory over time at select timestamps up to 30 seconds.* ***(a)*** *100-layer SPM;* ***(b)*** *200-layer SPM. Here, the droplet ejection frequency was 4 droplets per jetting, thus giving 4 times thicker layers compared to the later experiments where bubble and Marangoni SPMs were printed at 1 droplet per jetting.*

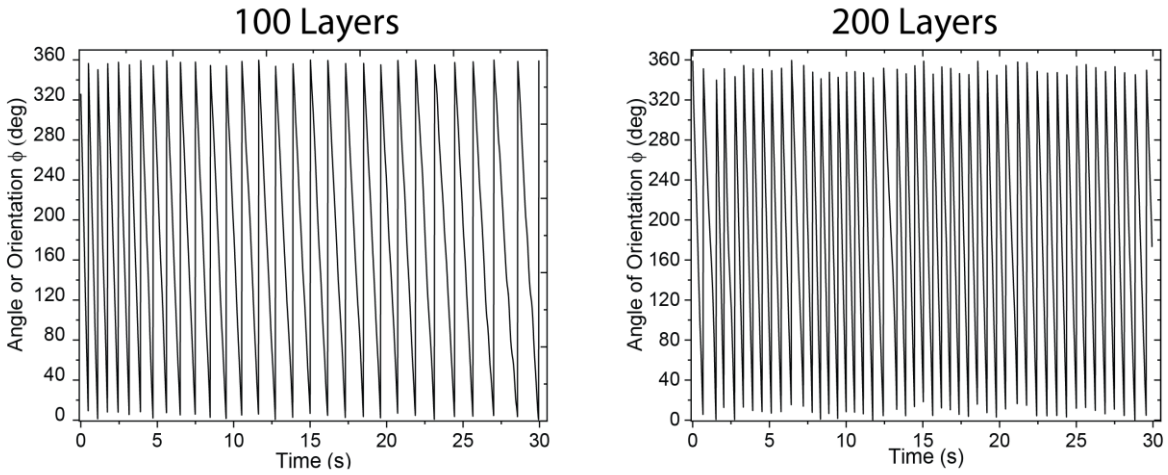

Figure 4.11: *Comparison of angle of orientation (ϕ) for 100-layer (60 ± 6 rpm) and 200-layer (100 ± 10 rpm) catalytic 1-engine SPM.*

As mentioned previously, for the comparison between geometry and propulsion mechanisms, all SPM samples were fabricated in 100 layers. The select video frames from the propulsion of catalytic and Marangoni SPMs are shown in **Figure 4.12** and **4.13**. As clearly visible from the edgy red and green tracking lines, all four geometric shapes of the catalytic SPMs showed jerky motion in comparison to their Marangoni counterparts, which showed smoother and circular tracking lines. Visual inspection of the extent and density of the tracking lines in the frames also showed that the Marangoni SPMs were able to propel over much larger areas in comparison to the catalytic SPMs. **Figure 4.14** compares the instantaneous velocity decays of one representative SPM belonging to each of the four geometric shapes and each of the two propulsion mechanisms. Here, it can be deduced that the 1-engine equivalent Marangoni SPM showed the smoothest deceleration or change in instantaneous velocity.

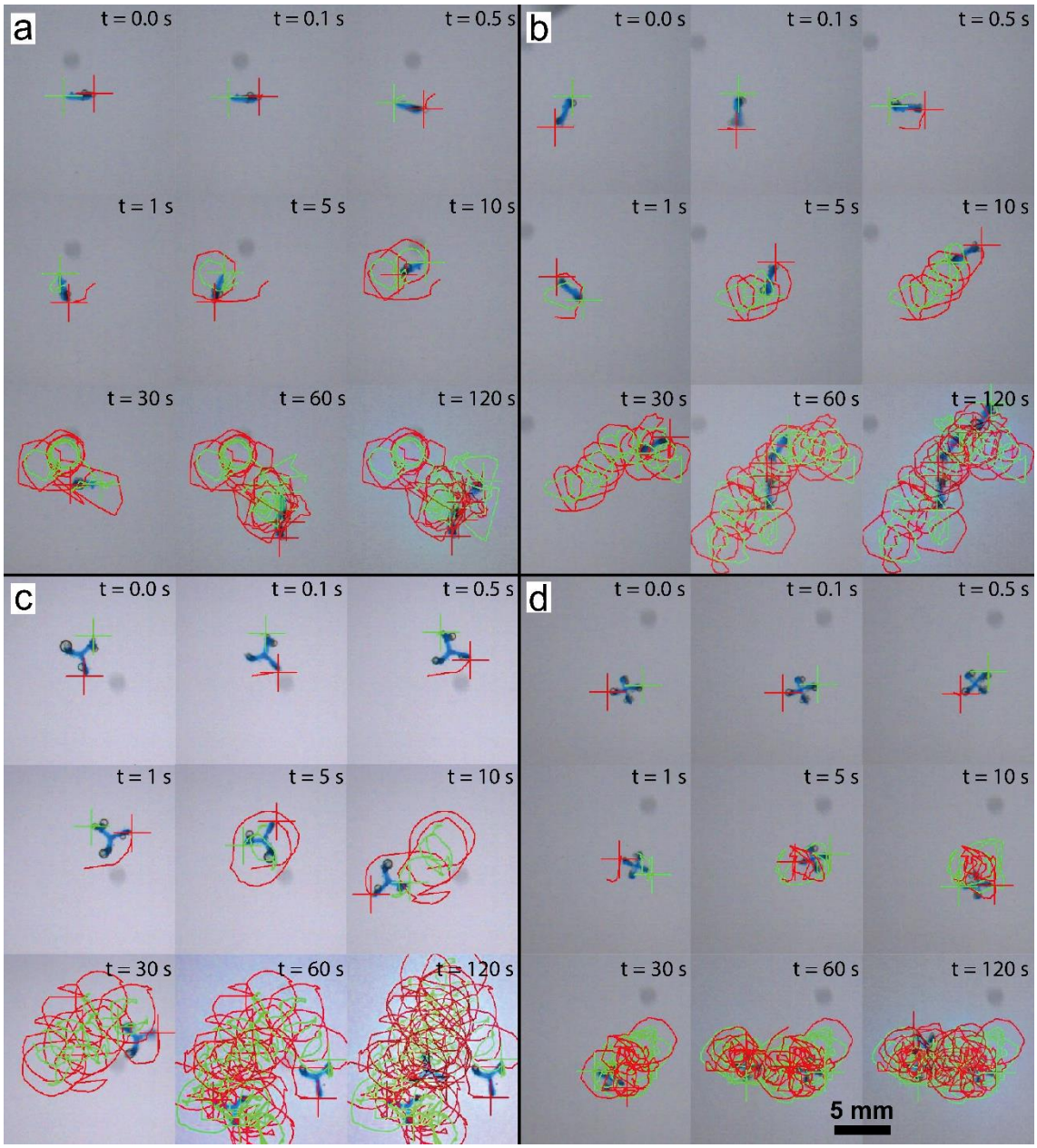

Figure 4.12: *Select video frames of catalytic SPMs propelling in 5% H_2O_2 fuel solution showing the trajectory over time at select timestamps up to 120 seconds.* ***(a)*** *1-engine,* ***(b)*** *2-engine,* ***(c)*** *3-engine, and* ***(d)*** *4-engine. Here, the droplet ejection frequency was 1 droplet per jetting so that the SPMs don't become too thick and dampen propulsion too early due to the excessive quantity of enzyme.*

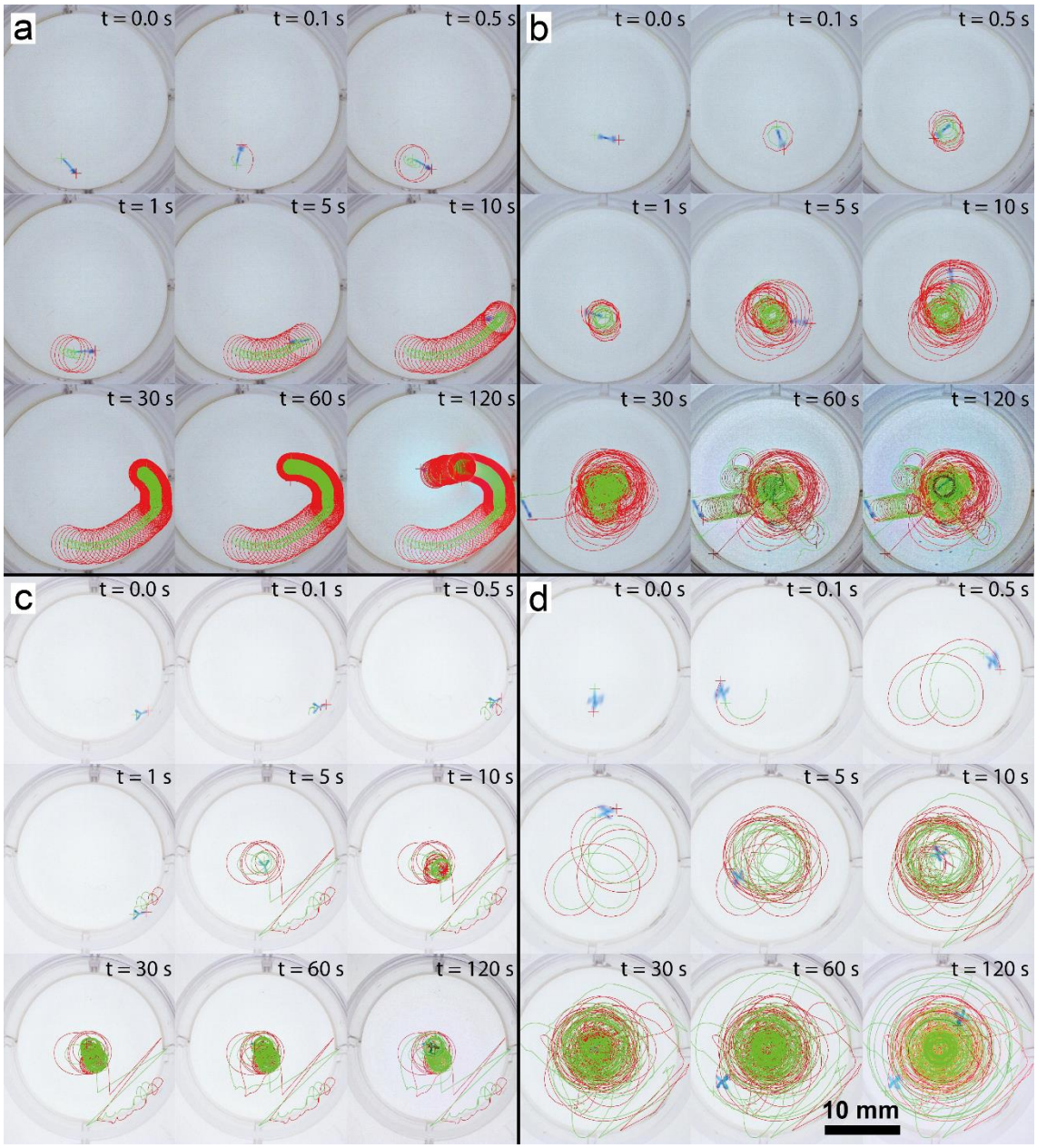

Figure 4.13: *Select video frames of Marangoni SPMs propelling in DI-water showing the trajectory over time at select timestamps up to 120 seconds.* ***(a)*** *1-engine equivalent,* ***(b)*** *2-engine equivalent,* ***(c)*** *3-engine equivalent, and* ***(d)*** *4-engine equivalent. Here, the droplet ejection frequency was 1 droplet per jetting so that the SPMs don't become too thick and dampen propulsion too early due to saturation of interface with surface active agent.*

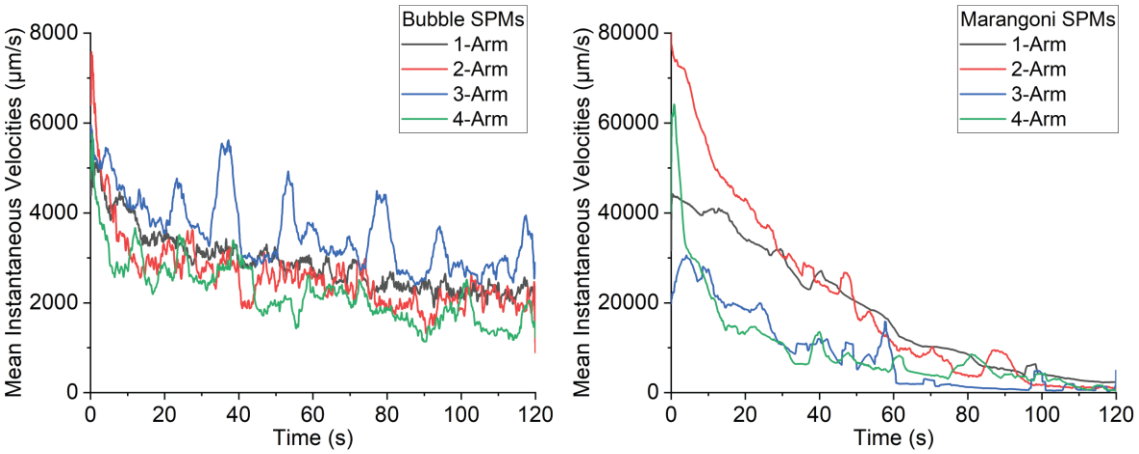

Figure 4.14: *Instantaneous velocity deceleration of a representative SPM for the four catalytic SPMs and the four Marangoni SPMs.*

The total number of RPMs of one representative SPM from each of the four geometric shapes and each of the two propulsion mechanisms are shown in **Figure 4.15** and **4.16**. The RPMs are shown as the number of changes in the angle of orientation over the 120 second period. It is clearly evident that the Marangoni SPMs undergo a rapid change in angle of orientation which is several times higher than that of the catalytic SPMs. Within catalytic propulsion, the 3- and 4- engine SPMs showed relatively smoother propulsion in comparison to the 1- and 2- engine SPMs. This might have happened as the higher number of catalase-doped sites in 3- and 4- engine SPMs would assure that more bubbles were formed and available for propelling the SPM and thus leading to lesser periods of rest when no bubble burst. Within Marangoni propulsion, the 1- and 2- engine equivalent SPMs showed relatively smoother and longer sustained propulsion in comparison to the 3- and 4- engine equivalent SPMs. This could be attributed to the simpler geometry and relatively slower and consistent rates of surfactant leaching from the 1- and 2- engine equivalent SPMs.

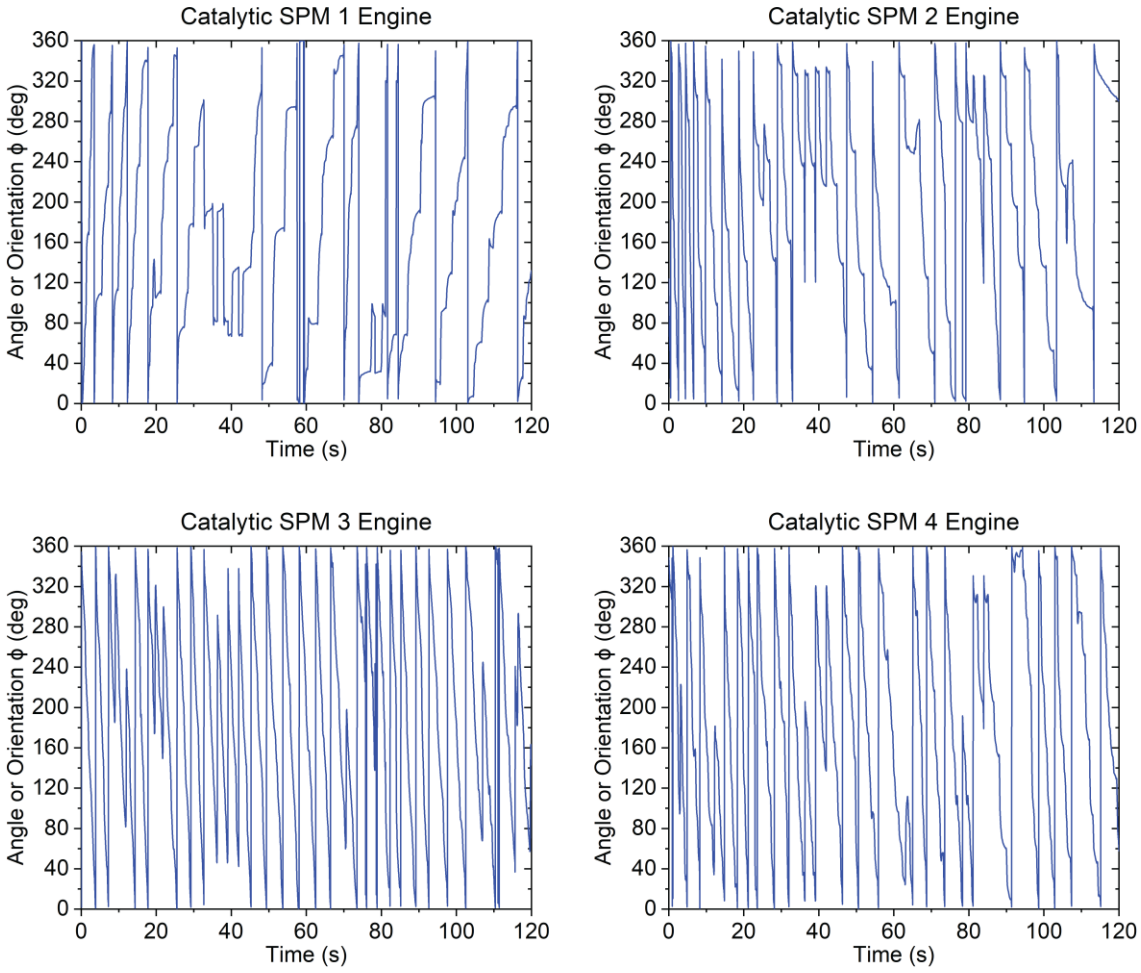

Figure 4.15: *Angle of orientation of representative catalytic SPMs of the four geometric shapes over the propulsion period of 120 seconds.*

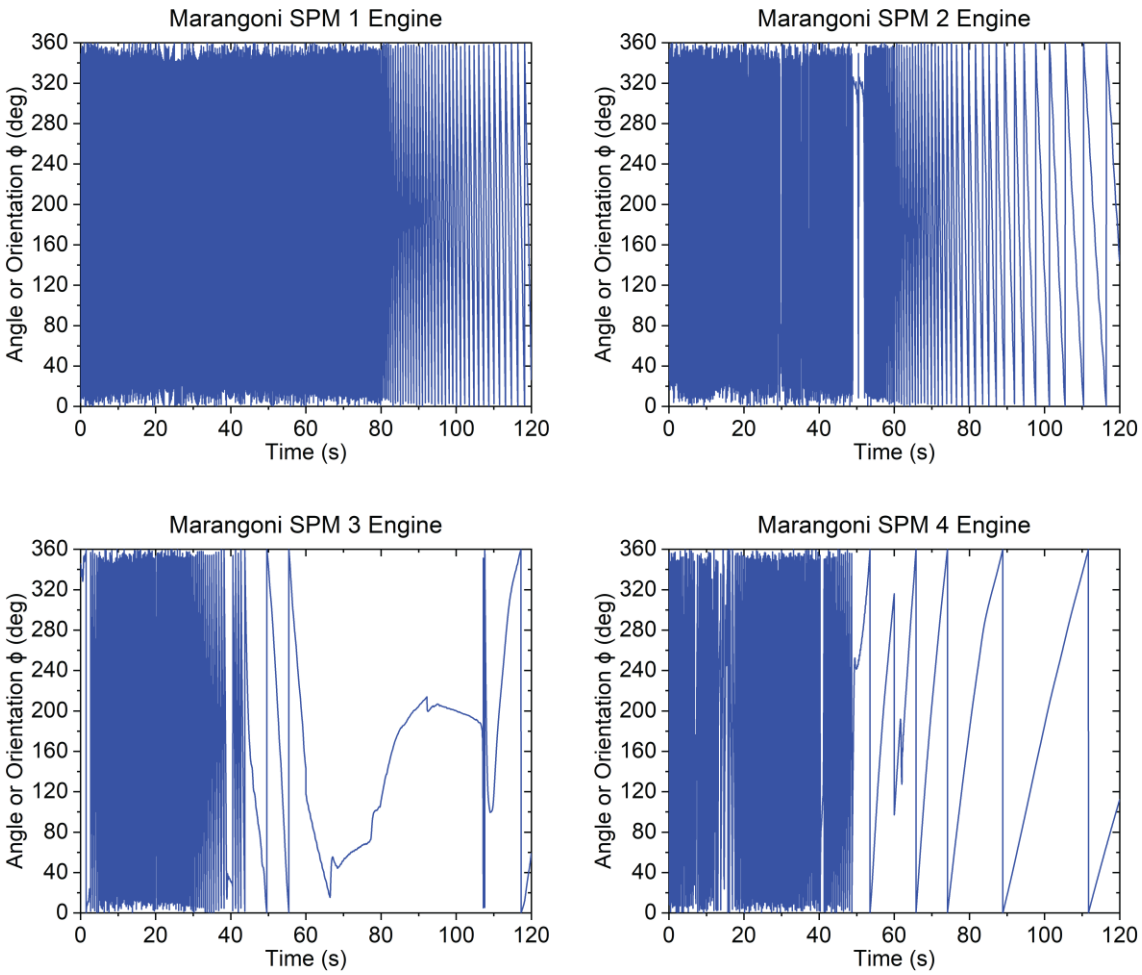

Figure 4.16: *Angle of orientation of representative Marangoni SPMs of the four geometric shapes over the propulsion period of 120 seconds.*

The mean RPM of each type of SPM within both propulsion mechanisms were calculated from the data on angle of orientation using the LabVIEW RPM counter programme and are presented in **Figure 4.17**. Overall, the RPMs of Marangoni SPMs were found to be around ten times more than the catalytic SPMs. Within Marangoni propulsion, the 1- and 2- engine equivalent SPMs showed much higher RPM averaged throughout the 120 seconds of observation time.

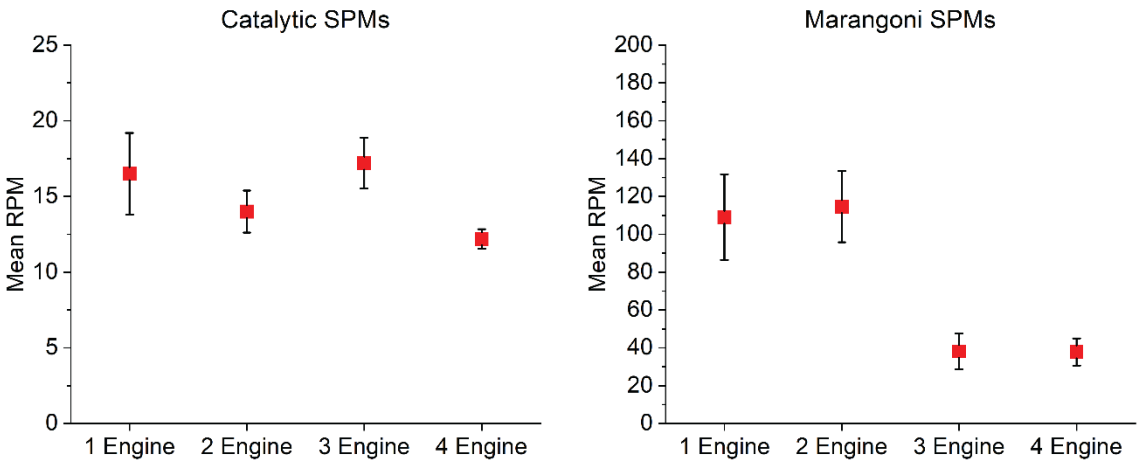

Figure 4.17: *Mean RPM with standard deviations of mean of catalytic and Marangoni SPMs.*

From the data on angle of orientation and mean RPM, it is difficult to decipher whether the RPM of the SPMs decelerated evenly or showed high degree of fluctuations throughout the observation period of 120 seconds. Accordingly, the rate of change of RPM of representative SPMs were plotted against time as shown in **Figure 4.18**. Similar to the data in angle of orientation and mean RPM, the Marangoni SPMs showed around ten times higher degree of fluctuation in the rate of change or deceleration of RPM. However, the 1-engine equivalent Marangoni SPM showed the least fluctuation.

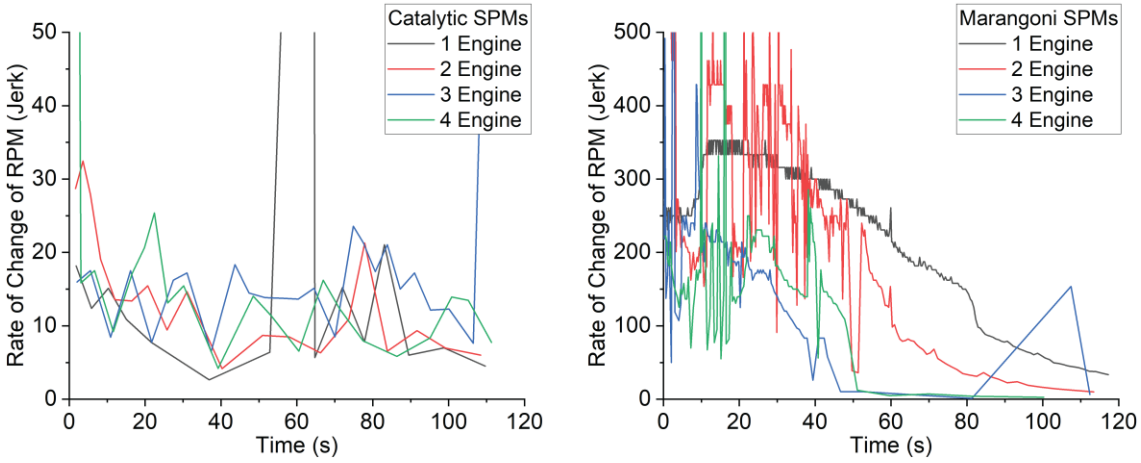

Figure 4.18: *Fluctuation in RPM of catalytic SPMs (left) and Marangoni SPMs (right) over 120 seconds of observation time period. One representative sample from each of the four geometries is shown here.*

4.5 Discussion

At a fluid interface, any particle moves if it has forces, such as thrust and concentration gradient, acting on it. On the other hand, forces, such as the viscous force, oppose particle propulsion by imparting drag. Additionally, the opposing forces of buoyancy and gravity also affect propulsion. In this study, in catalytic SPMs, the bulging regions contain the enzyme catalase causing the catalysis of hydrogen peroxide and oxygen bubble production in these regions. The bubbles, on bursting, create a thrust and push the SPMs in the opposite direction leading to propulsion. Additionally, the core PEG is supposed to make the SPP structure more porous after getting washed out, allowing easier interaction of catalase and H_2O_2 and bubble burst [10]. In Marangoni SPMs, change in concentration gradient causes change in surface tension and subsequent propulsion. During propulsion, the SPM position remains parallel to the fluid surface and as the SPMs are much larger than 100 microns, their propulsion is not affected by Brownian motion. Owing to the design of the SPMs, there is an uneven mass distribution, with more mass on the bulging end. The bulging end of arms of SPMs was designed to keep the geometry same for both the propulsion mechanisms and to provide an asymmetry in mass distribution with an intent to cause an uneven drag on the SPMs which manifested as rotation as the primary form of propulsion as the SPMs were pushed by bubbles or surface tension gradient.

4.5.1 Effect of Geometry

In the catalytic SPMs, no distinguishing difference was observed among the four shapes in their mean instantaneous velocity decay, mean RPM and rate of change of RPM. In the total RPM, however, different SPMs showed different results. In the Marangoni SPMs, 1-engine and 2-engine equivalent SPMs showed motion throughout the 120 seconds period whereas the 3-engine and 4-engine equivalent SPMs showed drastic reduction in motion after 40–50 seconds. This could be attributed to the increasing

complexity of geometry which interfered with the free and smooth rotational motion and also to the relatively larger amounts of leaching surfactant causing the quicker dampening of surface tension gradient. However, the mean RPMs of both 1-engine and 2-engine equivalent SPMs have higher standard deviation than those of the 3-engine and 4-engine equivalent SPMs. Even though both 1-engine and 2-engine equivalent Marangoni SPMs showed a higher mean RPM and a larger total number of RPMs, the 1-engine equivalent SPM showed considerably less jerk and a smooth deceleration or decay of instantaneous velocity over time than the 2-engine equivalent SPM. Short propulsion life and relatively uneven propulsion of complex geometries favour a simpler design, such as a straight line of the 1-engine equivalent Marangoni SPMs.

4.5.2 Effect of Propulsion Mechanism

In catalytic SPMs, bubbling is not smooth and causes uneven periods of rest and motion throughout the propulsion. The irregular pattern of bursting of bubbles also poses a problem in providing accuracy in predicting the motion. In Marangoni SPMs, fibroin scaffold causes PEG to release slowly, continuously and consistently over long periods of time, rather than leaching out all at once, resulting in smoother motion and deceleration. Though around 10 times slower in the instantaneous velocities measured at same time intervals, the propulsions of catalytic SPMs last as long as those of the Marangoni SPMs and also surpass in case of 3-engine and 4-engine SPMs after 40–50 second mark. This is because the decomposition of hydrogen peroxide by catalase is a first-order reaction with respect to either reactant and is affected only by the concentration of hydrogen peroxide which is available in plenty. From the image sequence of the video frames, it is clear that the spatial extents over time are much larger in all Marangoni SPMs in comparison to their catalytic counterparts. Due to their faster propulsion velocities, smoother velocity decay, and usability in virtually any neutral fluid medium, the Marangoni SPMs are preferred over the catalytic ones for microstirring

applications. Unpredictable and slower motion and the limitation in fluid choice in catalytic propulsion favours the surface tension driven propulsion, such as the PEG_{400} powered Marangoni SPMs.

4.6 Conclusion

Even though nano and micro scale self-propelled motors or particles have been extensively studied, very little research has been conducted on macroscopic millimetre-sized SPMs [205]. In this study, two propulsion mechanisms were compared in four geometric shapes of millimetre-scale self-propelled motors fabricated from silk fibroin using 3D inkjet printing technology. Up to 120 seconds of propulsion and tracking data were obtained for each sample. The data were obtained from the mean of values of 5 samples for each type of SPM, whereas, instantaneous velocity decay over time and angular velocity or RPM fluctuation and deceleration over time were shown for one representative SPM from each sample type. The results obtained in this study reveals that the surface tension driven propulsion of SPMs with simple geometry shows smooth deceleration and sustains propulsion for extended periods of time, observed and measured up to 120 seconds, and is, therefore, most suitable for micro-stirring applications in biomedical assays, such as for inducing fluid flow in diffusion rate limited assays [204]. Additionally, surface tension driven particles can be applied in almost any fluid media as long as the leaching surface active agent is chemically neutral with the fluid. The study in this chapter helped establish the ground for the study conducted in Chapters 5 in which a surface tension driven SPM, with an even weight distribution in design, has been used as a sensor to indicate minute changes in surface tension and act as a generic marker for dissolved contaminant level in wastewater samples.

Chapter 5: 3D PRINTABLE SELF-PROPELLING SENSORS FOR DETECTION OF WATER QUALITY VIA SURFACE TENSION

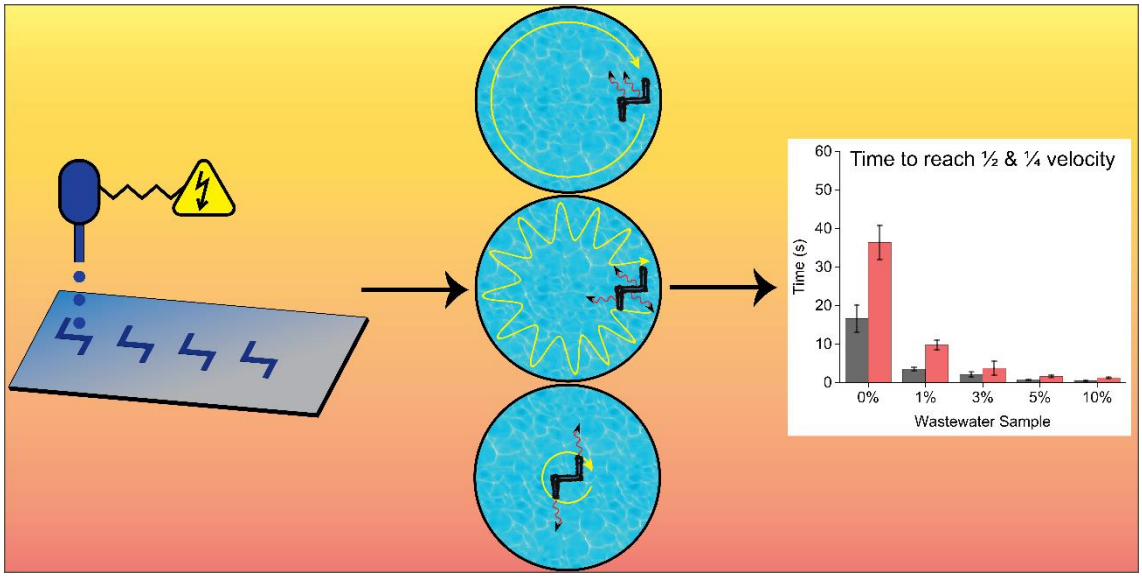

5.1 Abstract

In this chapter, I report the potential of using printable propelling sensors as quantitative indicators of soluble organic pollutant concentration in water samples containing different dilutions of sewage wastewater. I, for the first time in my knowledge, utilized 3D reactive inkjet printing technology for fabricating self-propelling sensors which can quickly determine the contaminant level by indicating the probable surface tension value of a water sample. The sensors were fabricated from regenerated silk fibroin which is an environmentally neutral and biodegradable material. Inkjet printing has the advantage of high resolution and precise deposition of materials and it thus helps in the fabrication of small millimetre-sized sensors doped with PEG_{400}, which acts as the 'fuel' to drive the sensors on the water surface through the surface tension gradient, a phenomenon which is called the Marangoni effect. The results showed that the sensor's propulsion velocity decay rate is an excellent metric to determine the surface tension which in turn indicates the water quality. Precise quantification of this data by a hand-held image analysis system in the future will provide an excellent method to quickly assess, in less than a minute, the water quality in the field.

5.2 Introduction

This study concerns with the use of propelling sensors to determine water quality through surface tension detection. Water pollution has been a major challenge to the global sustainable development as it adversely impacts the environment and poses a threat to the survival of various species including humans in the long term. World over, the sources of fresh or potable water, such as groundwater, are becoming scarce due to much higher rates of anthropogenic depletion than the rate of natural recharge [206-209]. The human population living under water scarcity has increased from around 14% of global population to around 58% of global population in the 2000s [210]. Moreover, many fresh water sources are becoming increasingly polluted and require increasing treatment to be suitable for drinking and cooking [211-215]. In many areas simple field tests could be valuable to determine the quality of a water resource for potable use, for example with respect to ground water resources. This is even more important if the reclaimed water is targeted for recharging tanks, wells and groundwater in arid geographical areas and remote human settlements where water scarcity and/or lack of water treatment plants forces the local population to depend on any available water source [216]. In remote areas, access to simple pollution indicator test could be a valuable tool to improve water safety. Such tests could also be used to check efficiency of water treatment systems that are in place. Simple field friendly water quality tests to determine inflow of wastewater discharge into rivers in the field could also be useful to determine if combined sewer overflows near urban areas are spilling at a higher frequency than permitted [217]. Likewise simple water quality indicator tests could be useful for emergency responses in natural disaster areas where there can be an acute need to indicate cross contamination between wastewater and potable water resources [218].

Current available field methods for assessment of water quality often relies on chemical sensors which requires a source of power and are relatively costly in procurement.

Alternatively, samples are collected for detection of markers of pollution. Moreover, there are a number of factors or incidents which can cause an unintended ingress of municipal wastewater into a natural water body, including sanitary sewer overflows, and misconnections in separate sewer systems where home appliances are mistakenly connected to the storm sewer rather than to the sanitary sewer [219, 220]. The misconnections put a significant pollutant load onto natural water bodies [220]. These are usually infrequent and localised events and the *in situ* pollutant detection is therefore difficult to conduct. The detection methods rely on a number of marker compounds that would only be present in household discharge. These markers can be either chemical or biological and vary in difficulty of detection, with only a few being detectable rapidly and *in situ* [219, 221-223].

Different regulations in different countries require the detection of different biological and physicochemical pollutants as indicators of water quality [224]. In the past, several studies have been conducted to detect different pollutants in fresh water. For example, using spectroscopic techniques and LIDAR (light detection and ranging), it is possible to remotely detect minute quantities of oil pollutants at levels substantially below that in oil slick [225]. Another study found that the presence and density of coliphage viruses can be used as an indicator of the faecal pollution level in contaminated natural waters, such as rivers. This is because coliphages are consistently detected in all contaminated water samples in comparison to other viruses [226]. Another study was conducted to detect the hydrogen sulphide levels in drinking water as an indicator of levels of the hydrogen sulphide producing coliform bacteria [227]. UV-Vis spectrometry is also a simple yet accurate analytical method to quantify various pollutant indicators, such as turbidity, chemical oxygen demand and biological oxygen demand [224]. Even though these studies provide new techniques with significant results, none of them seems plausible to be deployed on the field for a quick and generic quantification of water quality to detect whether a seemingly clean water sample is actually pollutant free or not owing to the requirement of sophisticated equipment and chemical tests.

Many kinds of soluble pollutants are present in effluents coming out from domestic and industrial sewage [228]. Such impurities have a potential to act as indicators of the presence and level of contamination or pollution. Direct detection of soluble pollutants requires sophisticated laboratory equipment [228], however one of the effects of soluble contaminants, in most cases, is lowering of the surface tension of water. In such a situation, it would be beneficial if a cheap, simple and fast field-test exists that could detect water purity level on a preliminary basis. A rapid *in situ* detection of surface tension could therefore be an important first indicator of wastewater ingress in a water system. Such a test will be specifically useful for screening drinking water supplies in rural, remote and arid areas and in those urban areas where there is a limit of resources, such as, laboratory facilities, skilled manpower and ample amount of time [227].

Sewage wastewater is a complex mixture of water, dissolved and particulate matter, micro-organisms and pollutants, such as heavy metals, micro-plastics and detergents [229]. Any simple or complex mixture of soluble contaminants in a water sample acts as a solute in a solvent. As stated previously, the presence of a solutes, surfactants and other miscible compounds affects the surface tension of a liquid or solvent depending on their surface excess or surface concentration [230-232]. Thus, several of the impurities or contaminants present in wastewater also cause a decrease in its surface tension. Here, we exploited this phenomenon to devise printable and surface tension gradient driven self-propelling sensors with millimetre-scale dimensions whose motion properties reflect surface tension values, and thus, can act as a generic indicator for the overall impurity level in the water sample for simple detection of water quality in the field. The silk fibroin sensors, that we investigate here for this application, continuously leach a soluble surface-active compound, poly (ethylene glycol) (MW = 400) (PEG_{400}), to create a surface tension gradient. This causes motion at the air-water interface via the Marangoni effect [12]. In previous studies by Zhang et al. [12] and Gregory et al. [11], it has been demonstrated that it is possible to control the propulsion behaviour of these, and other related devices, by varying their composition and structure during manufacture

via reactive inkjet printing. It was also described that the propulsion behaviour of the Marangoni effect driven stirrers propelling in varying concentrations of an aqueous anionic surfactant, sodium dodecyl sulphate (SDS), correlated with the solutions' surface tension. Specifically, the stirrers' number of revolutions per minute (RPM) during rotational propulsion was found to decrease as the concentration of SDS increased from 0.3 mM to 1.0 mM [12]. The aim of the present work is to determine whether this propulsion system can consequently be utilised to distinguish between wastewater samples of different surface tensions, with sufficient resolution so that it can indicate their quality differences by, ideally, only requiring observation of the sensors' motion by eye without any further complicated analysis of propulsion behaviour.

5.3 Experimental Methods

5.3.1 Materials

The materials required for the fabrication of fibroin self-propelled sensors are described in **Chapter 2, section 2.1**.

5.3.2 Collection of Wastewater

Urban wastewater (WW) containing a mixture of domestic and industrial wastewater was used in the experiments as it is a highly contaminated source of water and can be diluted down to represent any natural and artificial water source, such as rivers, ponds and urban supply water. The wastewater was collected from the inlet of a large wastewater treatment works serving about 185000 PE. The wastewater was inlet wastewater collected from a sewage treatment plant (Woodhouse Mills Wastewater Treatment Plant in Sheffield, UK) after it had been passed through coarse and fine screening to remove large debris and grit, but before any chemical or biological treatment had been done. The sewage was collected in 500 mL bottles and stored at 2 °C for use in the experiments.

5.3.3 Wastewater Sample Preparation

The collected wastewater was diluted down to four different concentrations of 10%, 5%, 3% and 1% for the experiments by adding different amounts of deionised water. In addition, 100% pure deionised water (henceforth called wastewater-0% or WW-0%) was also used for comparison and to understand how soluble contaminants affect water's physical properties in terms of its chemical oxygen demand and surface tension.

5.3.4 Characterization of Wastewater: Chemical Oxygen Demand

The chemical oxygen demand of wastewater samples was measured by the COD cuvette test (LCK 514, Hach Lange Ltd, UK) using a COD spectrophotometer (Hach Lange Ltd, UK). For each reading, 2 mL of the wastewater samples were used in each analysis following the manufacturer's instructions. A reaction with 2 mL of deionized water was used as blank. The cuvettes were then heated to 148 °C for 2 hours in a thermostat. The spectrophotometer was calibrated using COD standards with concentrations of 0, 100, 200, 300 and 400 mg/L COD.

5.3.5 Characterization of Wastewater: Surface Tension

The detailed process of surface tension measurement is described in **Chapter 2, Section 2.8, Sub-section 2.8.1**. Briefly, the surface tensions of the different wastewater samples were measured by a tensiometer (KRÜSS GmbH) with a standard platinum plate probe measuring 19.9 x 10 x 0.2 mm in dimensions and having an immersion depth of 2 mm in the sample. Five measurements were taken for each WW sample to obtain the mean values along with their standard deviation of mean. 10 mL of sample was taken for each measurement conducted at an ambient temperature of around 20 °C. Each measurement was run for 50 minutes generating 3000 readings, of which, the last 10 readings were averaged automatically by the tensiometer to give the final reading of the surface tension of the sample.

5.3.6 Sensor Fabrication by 3D Inkjet Printing

The process of 3D reactive inkjet printing is described in **Chapter 2, Section 2.11 – 2.12**. The water quality detecting sensors were fabricated in a shape similar to the letter 'Z'. The propelling sensors were fabricated from regenerated silk fibroin (RSF) solution, which was prepared using the process described in **Chapter 2, Section 2.2 – 2.7**. In this study, the concentrations of RSF and PEG_{400} were kept at 40 mg/mL and 20 mg/mL, respectively. The raw materials, RSF and PEG_{400} used for fabrication, are easily accessible and safe to use, thereby keeping the cost of fabrication minimal and having no risk of environmental hazard. PEG_{400} acts as the fuel to propel the sensors as it leaches out from them into the water, thus, causing a local decrease in the surface tension which causes propulsion due to the Marangoni effect [11, 12]. During fabrication, 150 layers of primary ink was printed on a silicon wafer substrate to yield one batch of Z-shaped sensors. Each layer of the primary ink was cured with a layer of methanol mixed with Coomassie brilliant blue dye to provide contrasting blue colour to the sensors for better visibility. The dimensions of the mid-section and the two arms of the Z-shaped sensors were, respectively, set to be approximately 2.0 mm and 0.5 mm. **Figure 5.1** schematically illustrates the process of RIJ printing alongside a representative light micrograph of a freshly printed sensors.

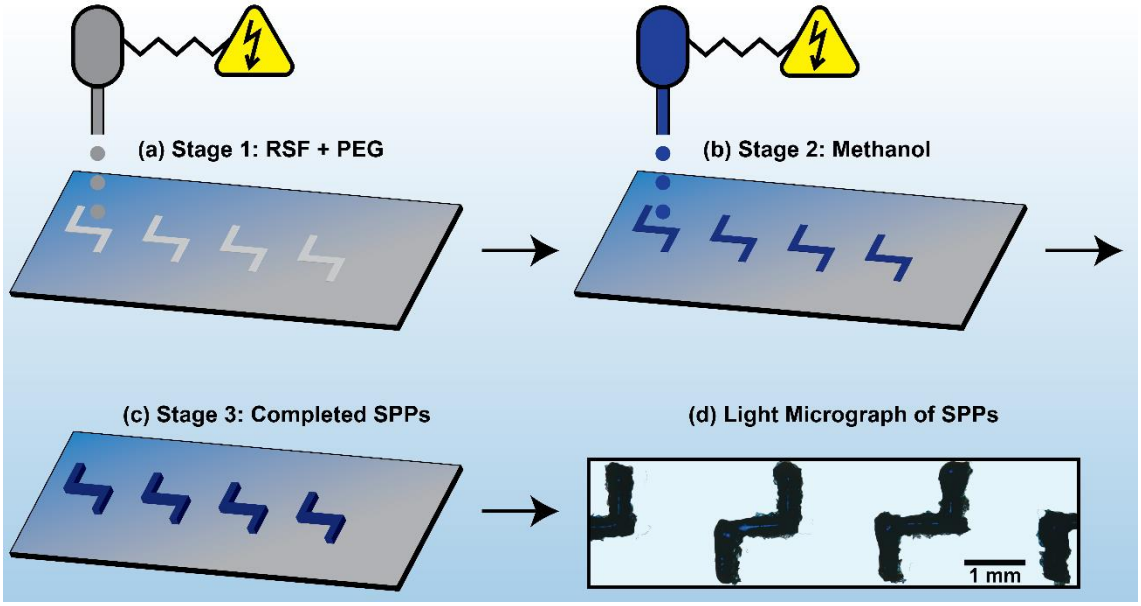

Figure 5.1: *Schematic illustration of the layer-by-layer process of reactive inkjet (RIJ) printing of Z-shaped sensors from regenerated silk fibroin (RSF) / PEG_{400} (primary ink) and methanol (curing ink).* ***(a)*** *Stage 1 is the deposition of the primary ink to form the body of the indicators.* ***(b)*** *Stage 2 is the deposition of the curing ink to transform the soluble random coil proteins of silk fibroin into the insoluble β-sheet structure. Additionally, this stage provides visibility to the otherwise transparent sensors due to the deposition of Coomassie brilliant blue dye mixed in the curing ink.* ***(c)*** *Stage 3 is the final fabricated 3D structures formed after 150 consecutive repetitions of the stages 1 and 2.* ***(d)*** *Image-adjusted light micrograph of a section of the silicon wafer with freshly printed sensors.*

5.3.7 Sensor Propulsion in Wastewater

After the printing was over, the individual sensors were taken off of the silicon wafer substrate very carefully using a fine needle, making sure that no physical damage or distortion occurs. The PEG_{400}-doped sensors were then placed on the surface of pure or deionized water having a conductivity of < 1 µS/cm (wastewater-0% or WW-0%) and the four previously diluted concentrations of the sewage wastewater (WW-1%, WW-3%, WW-5%, and WW-10 %) for the propulsion test. Each printed sensor was used for a single propulsion test after which it was discarded. This was repeated 5 times for each of the wastewater concentrations. For each experiment, 4 mL of the appropriate liquid sample was placed in a 3 cm diameter well of a 12-well plate. The sensor propulsion was video-recorded at 100 frames per second (fps) for 60 seconds, totalling to 6000 frames,

using a PixeLink™ CCD colour camera [model: PL-D732CU-T] fitted with Navitar™ macro zoom lens [model: 1-60135 zoom tube lens with 1-6010 camera coupler attachment]. After recording, ImageJ was used to generate image sequence from the video frames for all the sensors.

5.3.8 Propulsion Trajectory Tracking and Analysis

The process of propulsion recording, tracking and data analysis was similar to the process described in **Chapter 4, Section 4.3, Sub-section 4.3.6 – 4.3.7**. The propulsion trajectory was tracked using an in-house built tracking programme based on LabVIEW™ (National Instruments Corporation, USA). After importing the video in the tracking software, the two edges of a sensor were pinpointed for tracking which were eventually traced throughout the video frame-by-frame to generate the propulsion path of the sensor. The software also calculated the instantaneous velocities (v_{inst}) at the edges and the centres of each of the sensors in each frame, which were analyzed for determining the rate of decay of propulsion velocity of a sensor over the observation time of 60 seconds. The v_{inst} was obtained as micrometres per second for each of the frame, thus, totalling to 6000 data points, which were then smoothed by adjacent averaging in Origin™ and plotted as velocity–time graph to observe v_{inst} decay over the 60 second period.

5.3.9 Statistics

The process of statistical analyses was similar to the process described in **Chapter 4, Section 4.3, Sub-section 4.3.9**. The data from measurements of chemical oxygen demand and surface tension were plotted in Origin. The instantaneous velocities of the propelling sensors were generated once every 0.01 seconds, which was the time gap between two consecutive video frames. This gave a total of 6,000 data points for instantaneous velocity for a 60 seconds long video. These instantaneous velocities were

then plotted against time (t) to generate the instantaneous velocity decay curve of each sensor. Next, the time taken by the sensors to reach half and quarter of their initial instantaneous velocities was calculated and averaged for all the samples for plotting as a bar chart along with respective standard deviation of mean. All the graphs were plotted in Origin™ 2020.

5.4 Results

It is important to know the amounts of dissolved organic pollutants in the wastewater used in this experiment and relate it to its surface tension. For this, the chemical oxygen demand (COD), a measure of the organic matter content, of the collected wastewater was used. Triplicate samples were analysed for COD and the average was 370 mg/L ±6 mg/L. This COD is relatively low for this wastewater treatment works, where more typical dry weather COD values would be between 600 and 700 mg/L, indicating a slight rain impact on the samples, but still a significant content of domestic wastewater in the samples. The wastewater samples used in the surface tension experiments was diluted to contain, 0%, 1%, 3%, 5% and 10% of this wastewater meaning that the samples would have had COD values of 0, 3.7, 11.1, 18.5 and 37 mg/L, respectively, as shown in **Figure 5.2 (a)**.

Next, I considered crucially if the level of contaminants in the wastewater in different samples corresponded to a change in surface tension, which is the key link required to enable our proposed sensing method. **Figure 5.2 (b)** shows the surface tension (ST) values of the 5 different water samples calculated using a tensiometer (KRÜSS GmbH). The ST values of the wastewater diluted to the concentrations of 0%, 1%, 3%, 5%, and 10%, respectively, are 72.4 ±0.14, 71.3 ±0.11, 69.2 ±0.07, 64.4 ±0.25, and 59.4 ±0.24 mN/m (here, 0% means deionised or pure water). The surface tension changes from 0% to 3% WW are slight, becoming become more significant above WW-3%. The observation that the surface tension does not simply follow the dilution series suggests

some complex phenomena are present in these solutions, which would require more sophisticated chemical analysis to fully understand. Nevertheless, this data establishes the required link between the amount of wastewater in the sample and its surface tension.

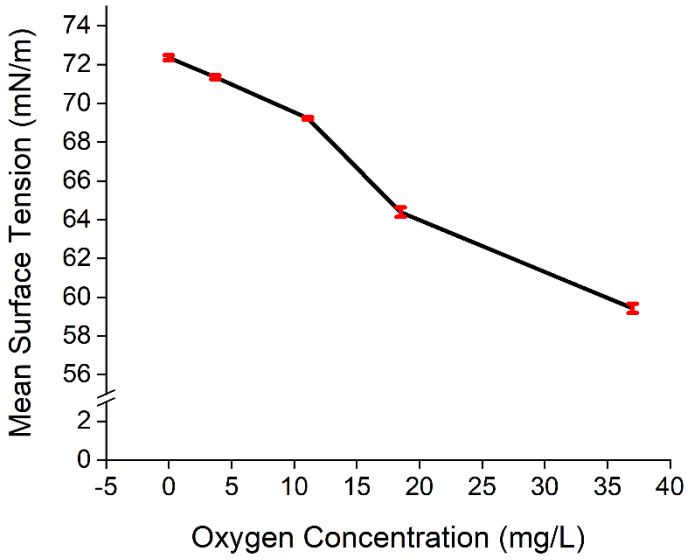

Figure 5.2: *Correlation between the amount of contaminant, measured as Chemical Oxygen Demand (COD), and surface tension of different dilutions of the wastewater. COD was estimated from the absorbance values measured in absorbance units (au) in a spectrophotometer. The oxygen concentrations of WW-0%, WW-1%, WW-3%, WW-5% and WW-10% were measured to be 0, 3.7, 11.1, 18.5 and 37 mg/L, respectively, and their mean surface tension values were measured to be 72.35, 71.34, 69.22, 64.38 and 59.42 mN/m, respectively. Standard deviation of mean is shown as error bars in red.*

Having established this link, we proceeded to investigate the motion of the propelling sensors in each waste water dilution. **Figure 5.3 (a – e)** shows the selected time sequence frames of propulsion trajectory of one representative sensor from each wastewater concentration. After observing all the propulsion behaviours from all wastewater samples, we have systematised and classified the propulsion behaviour of the sensors into three main patterns, which are revolution, zig-zag and rotation as illustrated in **Figure 5.3 (f – h)**. We define these patterns as follows: (1) Revolution is the smooth circular motion of a sensor along the periphery and around the centre of the well;

(2) Zig-zag is the to-and-fro motion of a sensor between the central region and the periphery with an overall circular motion around the centre of the well; (3) Rotation is the circular motion of a sensor roughly around its own centre of axis. For the WW-0% sample, the propulsion trajectory clearly followed one or more of the three main patterns as shown in **Figure 5.3 (a)**. In addition, the motion remained smoothly decelerating throughout the 60 seconds of the observation period. On increasing wastewater concentration, even though the three motion patterns were observed, the propulsion deceleration became less and less smooth, such as in **Figure 5.3 (c – d)**. As the wastewater concentration is increased even further, the three patterns became less evident, with the sensor propelling in WW-10% moving only with a momentary jerk and coming to an almost halt in less than 5 seconds in all samples. These differences in the observed sensor propulsion patterns suggest that the decreased surface tension confirmed for higher concentration wastewater samples may be disrupting the Marangoni effect driven motion, and decrease the time up to which the sensor can keep propelling. This is in line with the previous reports of loss of rotation rate as surface tension was reduced in simple water-surfactant solutions [11, 12]. However, without further analysis, it is not possible to unambiguously link all of the observed motion changes with surface tension, as other chemical compositional changes or changes in the sample's fluid properties may also interfere with propulsion, albeit to a lesser degree. **Figure 5.3 (i – n)** shows the SEM images of a sensor before and after propulsion with little morphological difference observed in the magnified images, similar to a previous study [12]. This suggests that the rigid structure of the sensor is porous enough to allow PEG_{400} molecules to simply diffuse out without causing excessive micrometre-scale structural changes or damages to the sensor morphology.

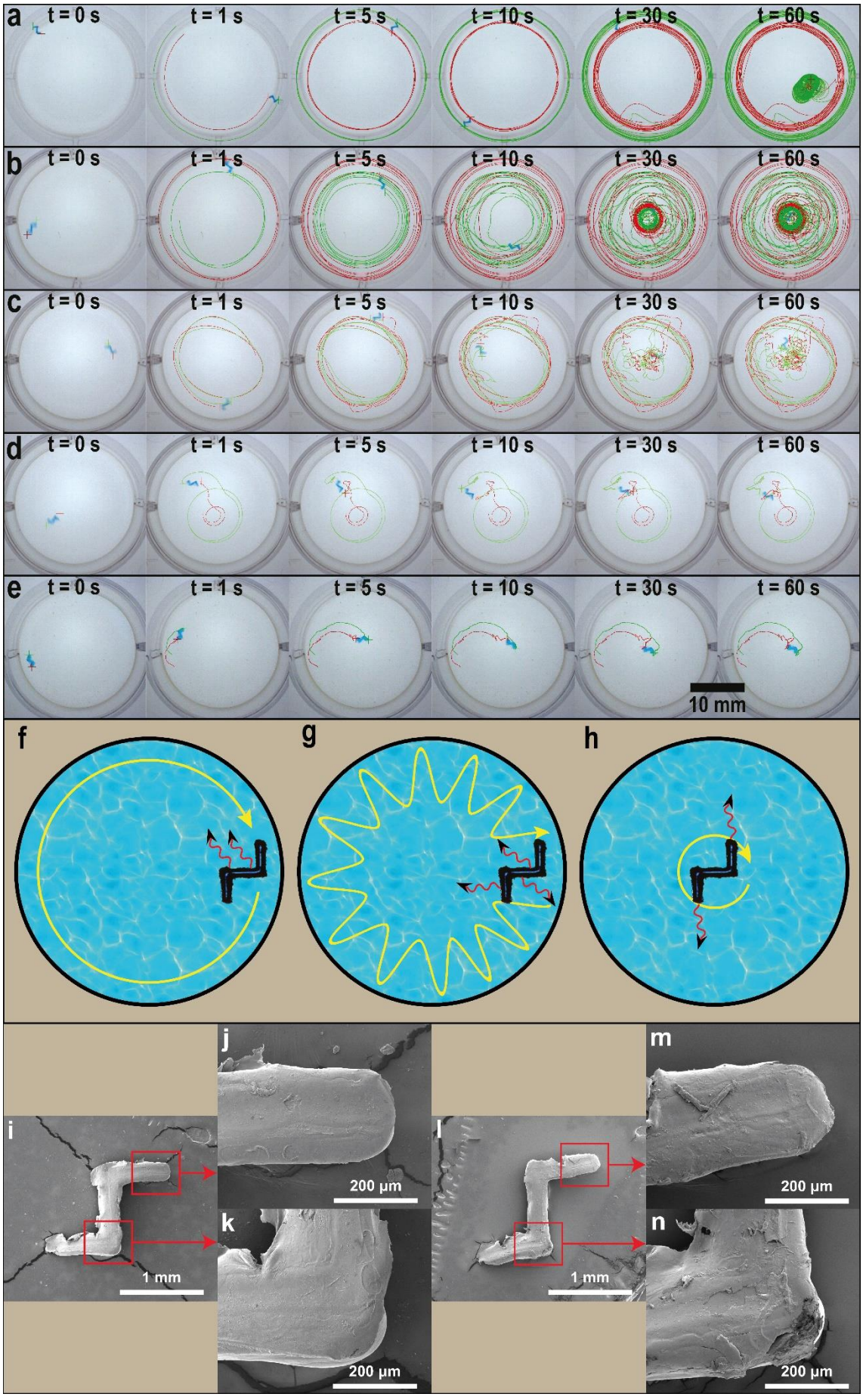
a
b
c
d
e
t = 0 s
t = 1 s
t = 5 s
t = 10 s
t = 30 s
t = 60 s
10 mm
f
g
h
i
j
k
l
m
n
1 mm
200 µm

Figure 5.3: *Time sequence of sensors with PEG400 propelling in wastewater samples at concentrations (v/v %) of* ***(a)*** *0%* ***(b)*** *1%* ***(c)*** *3%* ***(d)*** *5%* ***(e)*** *10%. One small blue coloured sensor can be seen propelling in each well, with the propulsion trajectory marked by red and green coloured lines positioned at the two edges of each sensor.* ***(f – h)*** *Illustration of the three main types of propulsion behaviour shown by the surface-tension-driven sensors. The red-black arrows indicate supposed direction of leaching of PEG400.* ***(f)*** *Revolution along the periphery of the well;* ***(g)*** *Zig-zag or see-saw motion between centre and periphery of the well;* ***(h)*** *Rotation along its own centre of mass.* ***(i – n)*** *SEM images of the sensors* ***(i)*** *before propulsion,* ***(j – k)*** *with magnification;* ***(l)*** *after propulsion,* ***(m – n)*** *with magnification. The post-propulsion SEM images show mild erosion of the surface topography.*

The time of occurrence and duration of a specific pattern of motion could not be successfully predicted. Thus, it can be said that the type of sensor propulsion pattern is not indicative of the water quality or the contaminant concentration and the resultant ST. This makes it difficult to estimate the surface tension or contaminant level of the given water sample just by visually observing a sensor's propulsion pattern. However, both quantitative and qualitative consistent changes in motion can still be distinguished, regardless of the overall pattern of motion. In particular, the rate of decay of velocity of the sensors was found to be a useful metric, as described below.

The frame-by-frame v_{inst} data is used to determine how much time the sensors take to reduce to half and quarter values of their initial propulsion velocities. **Figure 5.4 (a – b)** shows the mean times taken by five sensors per wastewater concentration to reach the half and quarter values of their initial velocities. The mean values are plotted as bar graph with error bars representing the respective standard deviation of mean. The data in the graphs show that there are significant differences between the v_{inst} decay half-life and quarter-life of the sensors propelling in WW-0%, WW-1% and WW-3%. The difference, however, becomes insignificant between WW-5% and WW-10%, suggesting that the technique employed in this study is readily applicable to detecting very low levels of impurities, which cause very little difference in surface tension values. This reflects the high sensitivity of the propulsion mechanism to surface tension. **Figure 5.4 (c – d)** shows the actual instantaneous velocity (v_{inst}) decay rates of one representative sensor

propelling in each of the 5 wastewater concentration samples. The v_{inst} values are plotted as line graph against time, thereby showing their gradual deceleration or decay over time. Similar with the half-life and quarter-life data, the representative v_{inst} decay rates also show significant differences among the v_{inst} of sensors propelling in WW-0%, WW-1% and WW-3% but not between WW-5% and WW-10%. One important feature to notice is that the v_{inst} decay rate is not dependant on the initial velocity of the sensors. For instance, as observed in **Figure 5.4 (c – d)**, the initial velocity of the sensors in WW-0% is much less in comparison to those of the sensors in WW-1% and WW-3%. However, the v_{inst} decay rate is much lower for the sensors propelling in WW-0% than the sensors propelling in all other samples. Selected videos frames of the representative sensors are also depicted as image sequences in **Figure 5.3 (a – e)**.

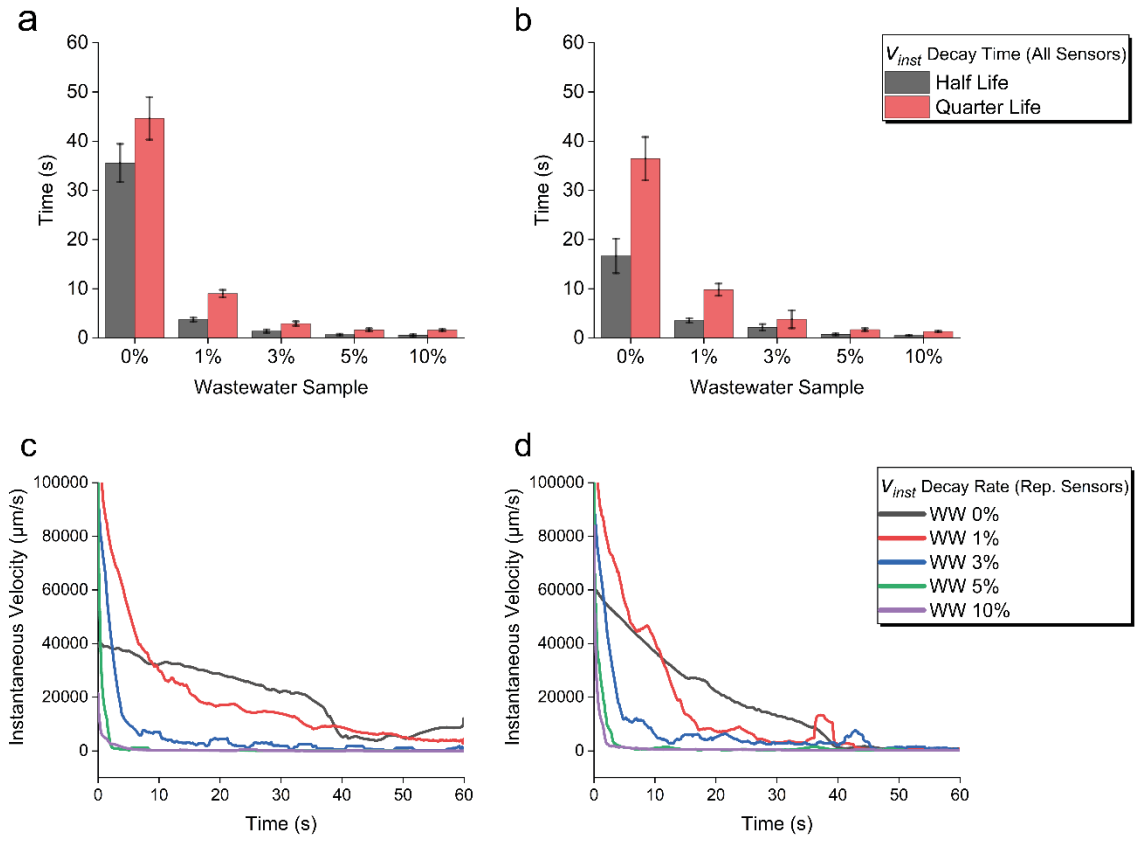

Figure 5.4: (a – b) *Mean instantaneous velocity (mean v_{inst}) decay times of the PEG_{400} containing sensors propelling in different wastewater samples. The decay is assessed as the time taken for the mean vinst to reach half and quarter of its initial value.* ***(c – d)*** *Instantaneous velocity (v_{inst})*

decay rates of one representative sensor over a period of 60 seconds. Each line in the graphs is taken from the one representative sensor which has its v_{inst} half-life and quarter-life values closest to the mean half-life and mean quarter-life values shown in the bar graphs in 'a' and 'b'.

Note that also, during the sensor propulsion, the v_{inst} decay rates show minor deviations in the form of minute crests and troughs as can be seen in the line graphs in **Figure 5.4 (c – d)**. In the primary ink, silk fibroin and PEG_{400} are completely miscible with each other which makes the primary ink a very homogeneous mixture. However, as the RIJ printing technique has millimetre-scale resolution, the formation of the rigid and insoluble silk fibroin β-sheets within the sensors remains uneven at molecular level. This causes an uneven distribution of PEG_{400} throughout the three-dimensional structure of the sensors as they get fabricated layer-by-layer during RIJ printing, leading to an unpredictable rate and direction of leaching of PEG_{400} out of different regions of the sensor at the air-water interface, that could account for these variations, and also explain the different motion patterns described above. Similar observation have also been reported in other studies using silk fibroin–PEG_{400} sensors [12] and water soluble camphor [233] propelling at the air-water interface through the Marangoni effect.

5.5 Discussion

Having concluded that the instantaneous velocity decay is the best way to tell the difference between water samples irrespective of which of the 3 main propulsion patterns occurs, I considered potential practical deployments of the sensors for testing. In this regard, the best readout method was to use a timer and observe the total propulsion time or the time the sensor takes to reach to a halt, which as explained earlier, was notably different among the different concentrations of the wastewater sample. From there, the surface tension of a wastewater sample could be roughly estimated. As the ultimate objective of this study was to be able to visually distinguish the differences in propulsion behaviour in order to readily diagnose a water sample, it was important to focus on those

results which hugely differ from each other (WW-0% vs. all other, WW-1% vs. all other, WW-3% vs. all other) instead of those which marginally or insignificantly differ from each other (WW-5% vs. WW-10%). On visual inspection of the sensor propulsion, it could be deduced that between the 0% and 5% samples or 1% and 10% samples the difference in propulsion velocity and v_{inst} decay times were significant enough to be detectable and viably discernible by human eye. This difference was relatively too subtle between the 3% and 5% or 5% and 10% samples to be detectable by eye. For that, in the future, an image analysis based detection system could be developed which could use a mobile phone's camera to continuously scan and capture the sensor propulsion on the field and match it online against a video library of calibrated sensor propulsion data to roughly estimate the surface tension and, thus, obtain the miscible waste or contaminant concentration values in a water sample. Thus, a better resolution in this quantitative analysis based approach could be envisaged. Afterwards, if a sample is found to contain a large amount of contaminants, then it can be sent from the field to a laboratory for further investigation so that the water sample source can be treated to prevent widespread contamination.

The fact that this technique was able to detect very low concentrations of pollutants makes it a very attractive technique because it could be seen that sensor propulsion behaviour shows marked difference between WW-0%, WW-1% and WW-3% whereas the tensiometer data may not be precise enough at such small differences in the miscible contaminant or impurity levels. The advantage of the technique used in this study is not just the ease of reproducibility of the sensor's precise geometry and composition, but also the sensor's ability to quantify the generic contaminant or impurity level at very low concentrations in a water sample.

5.6 Conclusion

In this study, I succeeded in propelling the millimetre-sized sensors through the dynamic alteration in surface tension gradient at the air-water interface. I also showed that the propulsion behaviour of the printable sensors was strongly dependent on miscible pollutant (solute) concentration which in turn could act as a diagnostic tool for the detection of pollutant level in a given water sample. The decay rate, half-life and quarter-life of the sensors' instantaneous velocities in different samples showed a strong correlation between the wastewater dilution factor, its surface tension and the propulsion pattern of the sensors, which could be recorded as well as visually inspected and analyzed to form of a predictable trend.

Chapter 6: CONCLUSION AND FUTURE PROSPECTS

3D inkjet bioprinting has become a common technology for use in both research and industry. It is used for a variety of applications for fabricating structures with a bottom-up approach, which is very cost-effective and consumes much less resources and raw materials in comparison to the more common and conventional top-down material fabrication technologies. In this thesis, we have seen the versatility of 3D inkjet bioprinting and inkjet printed 3D fibroin structures in different areas of research. I have presented and discussed the results which I obtained on applying 3D inkjet bioprinting of silk fibroin to 3 different areas.

The first area is biomedical science where I use printed silk fibroin scaffolds for cultivating neuronal PC12 and SH-SY5Y cells on them. The fibroin scaffolds were used as cell carriers for 3D culture and proliferation to develop a 3D cell culture model and to present this model as a potential 3D nerve guidance conduit. Such 3D culture environments help cells maintain their native and physiologically relevant spherical shape. Different shapes of the cell carriers also help differentiate nerve cells in desired patterns. In this study, though the PC12 cells showed adherence, the SH-SY5Y cells failed to show significant adherence on the scaffolds. This makes the study open ended with significant scope for improvement and integration of material engineering to develop better methods of formulating a more cell adhesive fibroin which is more supportive of cell growth for use as cell carrier and nerve guidance conduit both *in vitro* and *in vivo*.

The second area is the exploration of physics of differently shaped and differently propelled millimetre-scale self-propelled motors to compare their different propulsion behaviour and determine the best motor to act as micro-mixing devices in biomedical applications. The results showed significantly smoother and predictable motion in case of the SPMs with simpler geometric design and surface tension driven propulsion compared to relatively more complex designs and catalytic propulsion.

The third area is environmental science where I utilised the surface tension driven millimetre-scale self-propelled sensors as a tool to decipher the approximate surface tension of a given water sample, thereby acting as an indicator of the water quality. Different dilutions of real-world wastewater sample were used in this study and the results showed a significant correlation between the surface tension of water sample, which was determined by its pollutant concentration, and the velocity deceleration of the sensor propelling in the sample.

3D inkjet bioprinting is a fast-evolving tool with continuous additions of technological advancements in it design and process. With respect of silk fibroin, there is a huge scope for further improvements and efforts will be made to print fibroin along with a wider range of other materials to print hybrid products. Multi-nozzle printhead systems of various sizes, integrated into an inkjet bioprinter and their independent dispensing of multiple biomaterials is also a hugely promising approach to print highly scalable multi-material structures at high speeds.

In recent years, 4D inkjet bioprinting has attracted increasing attention, and is believed to be the next generation of biofabrication technique. 4D inkjet bioprinting is capable of fabricating dynamic 3D biological constructs that can be stimulated to change behaviours by using stimuli-responsive materials [234]. The inks for use with 4D inkjet bioprinting, or smart inks, containing biomaterials, cells, growth factors, and other physical and chemical agents, can be dynamically controlled, for example, through targeted protein folding, DNA origami, and anisotropic biomaterials, to carry out required activities with the printed structures. Additionally, integration of different printing techniques can be a promising avenue to overcome current technical bottlenecks of 3D inkjet bioprinting. For instance, extrusion bioprinting, which suffers from low resolution while possessing high printing speed, can be combined with high resolution inkjet printing to fabricate large volumetric tissues. Several research groups and companies have, over the years, developed different types of inkjet bioprinting tools and methodologies which would require a convergent evolution in the future along with the establishment of broad

universal principles which would dictate the application of 3D inkjet bioprinting in different cases and with minimal drawbacks. The continuous optimization of printing parameters, evolution of the printing equipment, and adjustment of ink formulations are attempts to make inkjet bioprinting more accurate, advanced and relevant to the specific requirements. Such ongoing studies will help eliminate the current disadvantages, such as lack of commercial scalability which is posing as a roadblock to a much wider acceptance of the inkjet bioprinting technology.

Chapter 7: REFERENCES

[1] H. Kodama, Automatic method for fabricating a three-dimensional plastic model with photo-hardening polymer, Review of Scientific Instruments 52(11) (1981) 1770-1773.

[2] C.W. Hull, Apparatus for production of three-dimensional objects by stereolithography, United States Patent, Appl., No. 638905, Filed (1984).

[3] S.C. Joshi, A.A. Sheikh, 3D printing in aerospace and its long-term sustainability, Virtual and Physical Prototyping 10(4) (2015) 175-185.

[4] P. Rokicki, B. Kozik, G. Budzik, T. Dziubek, J. Bernaczek, L. Przeszlowski, O. Markowska, B. Sobolewski, A. Rzucidlo, Manufacturing of aircraft engine transmission gear with SLS (DMLS) method, Aircraft Engineering and Aerospace Technology: An International Journal 88(3) (2016) 397-403.

[5] J.H. Martin, B.D. Yahata, J.M. Hundley, J.A. Mayer, T.A. Schaedler, T.M. Pollock, 3D printing of high-strength aluminium alloys, Nature 549(7672) (2017) 365-369.

[6] M. Savastano, C. Amendola, D. Fabrizio, E. Massaroni, 3-D printing in the spare parts supply chain: an explorative study in the automotive industry, Digitally supported innovation, Springer2016, pp. 153-170.

[7] S.R. Shin, R. Farzad, A. Tamayol, V. Manoharan, P. Mostafalu, Y.S. Zhang, M. Akbari, S.M. Jung, D. Kim, M. Comotto, A bioactive carbon nanotube-based ink for printing 2D and 3D flexible electronics, Advanced materials 28(17) (2016) 3280-3289.

[8] A.D. Valentine, T.A. Busbee, J.W. Boley, J.R. Raney, A. Chortos, A. Kotikian, J.D. Berrigan, M.F. Durstock, J.A. Lewis, Hybrid 3D printing of soft electronics, Advanced materials 29(40) (2017) 1703817.

[9] L.Y. Zhou, J.Z. Fu, Q. Gao, P. Zhao, Y. He, All-Printed Flexible and Stretchable Electronics with Pressing or Freezing Activatable Liquid-Metal-Silicone Inks, Adv Funct Mater 30(3) (2020) 1906683.

[10] D.A. Gregory, Y. Zhang, P.J. Smith, X. Zhao, S.J. Ebbens, Reactive Inkjet Printing of Biocompatible Enzyme Powered Silk Micro-Rockets, Small 12(30) (2016) 4048-4055.

[11] D.A. Gregory, P. Kumar, A. Jimenez-Franco, Y. Zhang, Y. Zhang, S.J. Ebbens, X.B. Zhao, Reactive Inkjet Printing and Propulsion Analysis of Silk-based Self-propelled Micro-stirrers, Jove-J Vis Exp (146) (2019).

[12] Y. Zhang, D.A. Gregory, Y. Zhang, P.J. Smith, S.J. Ebbens, X. Zhao, Reactive Inkjet Printing of Functional Silk Stirrers for Enhanced Mixing and Sensing, Small 15(1) (2019) e1804213.

[13] Y. Zhang, C. Tse, D. Rouholamin, P. Smith, Scaffolds for tissue engineering produced by inkjet printing, Central European Journal of Engineering 2(3) (2012) 325-335.

[14] C.M.B. Ho, A. Mishra, P.T.P. Lin, S.H. Ng, W.Y. Yeong, Y.J. Kim, Y.J. Yoon, 3D printed polycaprolactone carbon nanotube composite scaffolds for cardiac tissue engineering, Macromolecular Bioscience 17(4) (2017) 1600250.

[15] X. Yang, Z. Lu, H. Wu, W. Li, L. Zheng, J. Zhao, Collagen-alginate as bioink for three-dimensional (3D) cell printing based cartilage tissue engineering, Materials Science and Engineering: C 83 (2018) 195-201.

[16] A. De Mori, M. Peña Fernández, G. Blunn, G. Tozzi, M. Roldo, 3D printing and electrospinning of composite hydrogels for cartilage and bone tissue engineering, Polymers 10(3) (2018) 285.

[17] S. You, J. Li, W. Zhu, C. Yu, D. Mei, S. Chen, Nanoscale 3D printing of hydrogels for cellular tissue engineering, Journal of Materials Chemistry B 6(15) (2018) 2187-2197.

[18] X. Du, D. Wei, L. Huang, M. Zhu, Y. Zhang, Y. Zhu, 3D printing of mesoporous bioactive glass/silk fibroin composite scaffolds for bone tissue engineering, Materials Science and Engineering: C 103 (2019) 109731.

[19] Z.J. Wang, R. Abdulla, B. Parker, R. Samanipour, S. Ghosh, K. Kim, A simple and high-resolution stereolithography-based 3D bioprinting system using visible light crosslinkable bioinks, Biofabrication 7(4) (2015).

[20] X. Liu, S. Michael, K. Bharti, M. Ferrer, M.J. Song, A biofabricated vascularized skin model of atopic dermatitis for preclinical studies, Biofabrication 12(3) (2020) 035002.

[21] S. Yu, S. Xiaolei, F. Kevin, F. Yongcong, Z. Ting, S. Wei, Engineering of brain-like tissue constructs via 3D cell-printing technology, Biofabrication (2020).

[22] G. Brunello, S. Sivolella, R. Meneghello, L. Ferroni, C. Gardin, A. Piattelli, B. Zavan, E. Bressan, Powder-based 3D printing for bone tissue engineering, Biotechnol Adv 34(5) (2016) 740-753.

[23] R. Lozano, L. Stevens, B.C. Thompson, K.J. Gilmore, R. Gorkin, E.M. Stewart, M.I.H. Panhuis, M. Romero-Ortega, G.G. Wallace, 3D printing of layered brain-like structures using peptide modified gellan gum substrates, Biomaterials 67 (2015) 264-273.

[24] A.K. Gaharwar, A. Arpanaei, T.L. Andresen, A. Dolatshahi-Pirouz, 3D biomaterial microarrays for regenerative medicine: current state-of-the-art, emerging directions and future trends, Advanced materials 28(4) (2016) 771-781.

[25] S. Vijayavenkataraman, W.C. Yan, W.F. Lu, C.H. Wang, J.Y.H. Fuh, 3D bioprinting of tissues and organs for regenerative medicine, Advanced Drug Delivery Reviews 132 (2018) 296-332.

[26] J.I. Lipton, M. Cutler, F. Nigl, D. Cohen, H. Lipson, Additive manufacturing for the food industry, Trends in Food Science & Technology 43(1) (2015) 114-123.

[27] F.C. Godoi, S. Prakash, B.R. Bhandari, 3d printing technologies applied for food design: Status and prospects, Journal of Food Engineering 179 (2016) 44-54.

[28] Z. Liu, M. Zhang, B. Bhandari, Y. Wang, 3D printing: Printing precision and application in food sector, Trends in Food Science & Technology 69 (2017) 83-94.

[29] J. Goole, K. Amighi, 3D printing in pharmaceutics: A new tool for designing customized drug delivery systems, International Journal of Pharmaceutics 499(1-2) (2016) 376-394.

[30] A. Goyanes, U. Det-Amornrat, J. Wang, A.W. Basit, S. Gaisford, 3D scanning and 3D printing as innovative technologies for fabricating personalized topical drug delivery systems, Journal of Controlled Release 234 (2016) 41-48.

[31] A. Maroni, A. Melocchi, F. Parietti, A. Foppoli, L. Zema, A. Gazzaniga, 3D printed multi-compartment capsular devices for two-pulse oral drug delivery, Journal of controlled release : official journal of the Controlled Release Society 268 (2017) 10-18.

[32] L.K. Prasad, H. Smyth, 3D Printing technologies for drug delivery: a review, Drug development and industrial pharmacy 42(7) (2016) 1019-31.

[33] W. Zhu, B. Holmes, R.I. Glazer, L.G. Zhang, 3D printed nanocomposite matrix for the study of breast cancer bone metastasis, Nanomedicine: Nanotechnology, Biology and Medicine 12(1) (2016) 69-79.

[34] J.C. Lindegaard, M.L. Madsen, A. Traberg, B. Meisner, S.K. Nielsen, K. Tanderup, H. Spejlborg, L.U. Fokdal, O. Nørrevang, Individualised 3D printed vaginal template for MRI guided brachytherapy in locally advanced cervical cancer, Radiotherapy and Oncology 118(1) (2016) 173-175.

[35] S. Knowlton, S. Onal, C.H. Yu, J.J. Zhao, S. Tasoglu, Bioprinting for cancer research, Trends in Biotechnology 33(9) (2015) 504-513.

[36] Y. Li, T. Zhang, Y. Pang, L. Li, Z.-N. Chen, W. Sun, 3D bioprinting of hepatoma cells and application with microfluidics for pharmacodynamic test of Metuzumab, Biofabrication 11(3) (2019) 034102.

[37] S. Swaminathan, Q. Hamid, W. Sun, A.M. Clyne, Bioprinting of 3D breast epithelial spheroids for human cancer models, Biofabrication 11(2) (2019) 025003.

[38] H. Tseng, J.A. Gage, W.L. Haisler, S.K. Neeley, T. Shen, C. Hebel, H.G. Barthlow, M. Wagoner, G.R. Souza, A high-throughput in vitro ring assay for vasoactivity using magnetic 3D bioprinting, Scientific Reports 6 (2016) 30640.

[39] Y.R. Liang, L.N. Zhu, J. Gao, H.X. Zhao, Y. Zhu, S. Ye, Q. Fang, 3D-printed high-density droplet array chip for miniaturized protein crystallization screening under vapor diffusion mode, ACS Applied Materials and Interfaces 9(13) (2017) 11837-11845.

[40] E.A. Roth, T. Xu, M. Das, C. Gregory, J.J. Hickman, T. Boland, Inkjet printing for high-throughput cell patterning, Biomaterials 25(17) (2004) 3707-3715.

[41] M. Mohammed, A. Fitzpatrick, S. Malyala, I. Gibson, Customised design and development of patient specific 3D printed whole mandible implant, Proceedings of the 27th Annual International Solid Freeform Fabrication Symposium, 2016, pp. 1708-1717.

[42] D.C. Ackland, D. Robinson, M. Redhead, P.V.S. Lee, A. Moskaljuk, G. Dimitroulis, A personalized 3D-printed prosthetic joint replacement for the human temporomandibular joint: From implant design to implantation, Journal of The Mechanical Behavior of Biomedical Materials 69 (2017) 404-411.

[43] S. Arabnejad, B. Johnston, M. Tanzer, D. Pasini, Fully porous 3D printed titanium femoral stem to reduce stress-shielding following total hip arthroplasty, Journal of Orthopaedic Research 35(8) (2017) 1774-1783.

[44] K. Murugesan, P.A. Anandapandian, S.K. Sharma, M. Vasantha Kumar, Comparative evaluation of dimension and surface detail accuracy of models produced by three different rapid prototype techniques, Journal of Indian Prosthodontic Society 12(1) (2012) 16-20.

[45] M.A. Rendón-Medina, L. Andrade-Delgado, J.E. Telich-Tarriba, A. Fuente-del-Campo, C.A. Altamirano-Arcos, Dimensional error in rapid prototyping with open source software and low-cost 3D-printer, Plastic and Reconstructive Surgery Global Open 6(1) (2018).

[46] C. Cvetkovic, R. Raman, V. Chan, B.J. Williams, M. Tolish, P. Bajaj, M.S. Sakar, H.H. Asada, M.T. Saif, R. Bashir, Three-dimensionally printed biological machines powered by skeletal muscle, Proc Natl Acad Sci U S A 111(28) (2014) 10125-30.

[47] F. Guillemot, V. Mironov, M. Nakamura, Bioprinting is coming of age: report from the International Conference on Bioprinting and Biofabrication in Bordeaux (3B'09), Biofabrication 2(1) (2010) 010201.

[48] J. Groll, T. Boland, T. Blunk, J.A. Burdick, D.-W. Cho, P.D. Dalton, B. Derby, G. Forgacs, Q. Li, V.A. Mironov, L. Moroni, M. Nakamura, W. Shu, S. Takeuchi, G. Vozzi,

T.B.F. Woodfield, T. Xu, J.J. Yoo, J. Malda, Biofabrication: reappraising the definition of an evolving field, Biofabrication 8(1) (2016) 013001.

[49] L. Moroni, T. Boland, J.A. Burdick, C. De Maria, B. Derby, G. Forgacs, J. Groll, Q. Li, J. Malda, V.A. Mironov, C. Mota, M. Nakamura, W. Shu, S. Takeuchi, T.B.F. Woodfield, T. Xu, J.J. Yoo, G. Vozzi, Biofabrication: A Guide to Technology and Terminology, Trends in Biotechnology 36(4) (2018) 384-402.

[50] A.M. Compaan, K. Christensen, Y. Huang, Inkjet Bioprinting of 3D Silk Fibroin Cellular Constructs Using Sacrificial Alginate, ACS Biomaterials Science & Engineering 3(8) (2017) 1519-1526.

[51] G. Gao, T. Yonezawa, K. Hubbell, G. Dai, X. Cui, Inkjet-bioprinted acrylated peptides and PEG hydrogel with human mesenchymal stem cells promote robust bone and cartilage formation with minimal printhead clogging, Biotechnology Journal 10(10) (2015) 1568-1577.

[52] S.V. Murphy, A. Atala, 3D bioprinting of tissues and organs, Nature biotechnology 32(8) (2014) 773-85.

[53] A. Lee, A. Hudson, D. Shiwarski, J. Tashman, T. Hinton, S. Yerneni, J. Bliley, P. Campbell, A. Feinberg, 3D bioprinting of collagen to rebuild components of the human heart, Science 365(6452) (2019) 482-487.

[54] A. Isaacson, S. Swioklo, C.J. Connon, 3D bioprinting of a corneal stroma equivalent, Experimental Eye Research 173 (2018) 188-193.

[55] W.L. Ng, J.T.Z. Qi, W.Y. Yeong, M.W. Naing, Proof-of-concept: 3D bioprinting of pigmented human skin constructs, Biofabrication 10(2) (2018) 025005.

[56] T. Xu, J. Jin, C. Gregory, J.J. Hickman, T. Boland, Inkjet printing of viable mammalian cells, Biomaterials 26(1) (2005) 93-99.

[57] T. Xu, K.W. Binder, M.Z. Albanna, D. Dice, W. Zhao, J.J. Yoo, A. Atala, Hybrid printing of mechanically and biologically improved constructs for cartilage tissue engineering applications, Biofabrication 5(1) (2012) 015001.

[58] X. Zhou, H. Cui, M. Nowicki, S. Miao, S.-J. Lee, F. Masood, B.T. Harris, L.G. Zhang, Three-dimensional-bioprinted dopamine-based matrix for promoting neural regeneration, ACS Applied Materials and Interfaces 10(10) (2018) 8993-9001.

[59] H. Gudapati, M. Dey, I. Ozbolat, A comprehensive review on droplet-based bioprinting: Past, present and future, Biomaterials 102 (2016) 20-42.

[60] J.A. Phillippi, E. Miller, L. Weiss, J. Huard, A. Waggoner, P. Campbell, Microenvironments Engineered by Inkjet Bioprinting Spatially Direct Adult Stem Cells Toward Muscle- and Bone-Like Subpopulations, Stem Cells 26(1) (2008) 127-134.

[61] D.J. Hayes, W.R. Cox, D.B. Wallace, Printing systems for MEMS packaging, Micromachining and Microfabrication, SPIE, 2001, p. 9.

[62] M.T. Inc., Microdispensing. http://www.microfab.com/biomedical/microdispensing.

[63] X. Li, B. Liu, B. Pei, J. Chen, D. Zhou, J. Peng, X. Zhang, W. Jia, T. Xu, Inkjet Bioprinting of Biomaterials, Chemical Reviews 120(19) (2020) 10793-10833.

[64] J. Alaman, R. Alicante, J.I. Pena, C. Sanchez-Somolinos, Inkjet Printing of Functional Materials for Optical and Photonic Applications, Materials 9(11) (2016).

[65] P. Calvert, Printing cells, Science 318(5848) (2007) 208-209.

[66] C. Mandrycky, Z. Wang, K. Kim, D.H. Kim, 3D bioprinting for engineering complex tissues, Biotechnol Adv 34(4) (2016) 422-434.

[67] J. Li, F. Rossignol, J. Macdonald, Inkjet printing for biosensor fabrication: combining chemistry and technology for advanced manufacturing, Lab on a chip 15(12) (2015) 2538-58.

[68] L. Gonzalez-Macia, A.J. Killard, Screen printing and other scalable point of care (POC) biosensor processing technologies, Woodh Publ Ser Biom 118 (2017) 69-98.

[69] T.G. Henares, K. Yamada, K. Suzuki, D. Citterio, Inkjet printing of biomolecules for biorecognition, Design of Polymeric Platforms for Selective Biorecognition, Springer2015, pp. 197-235.

[70] K. Holzl, S.M. Lin, L. Tytgat, S. Van Vlierberghe, L.X. Gu, A. Ovsianikov, Bioink properties before, during and after 3D bioprinting, Biofabrication 8(3) (2016).

[71] B. Derby, Inkjet Printing of Functional and Structural Materials: Fluid Property Requirements, Feature Stability, and Resolution, Annu Rev Mater Res 40 (2010) 395-414.

[72] R.E. Saunders, B. Derby, Inkjet printing biomaterials for tissue engineering: bioprinting, Int Mater Rev 59(8) (2014) 430-448.

[73] M.Y. Teo, L. Stuart, K. Aw, J. Stringer, Micro-Reactive Inkjet Printing of Polyaniline, NIP & Digital Fabrication Conference 2018 (2018) 16-20.

[74] M.Y. Teo, L. Stuart, H. Devaraj, C.Y. Liu, K.C. Aw, J. Stringer, The in situ synthesis of conductive polyaniline patterns using micro-reactive inkjet printing, Journal of Materials Chemistry C 7(8) (2019) 2219-2224.

[75] J. Groll, J.A. Burdick, D.W. Cho, B. Derby, M. Gelinsky, S.C. Heilshorn, T. Jüngst, J. Malda, V.A. Mironov, K. Nakayama, A. Ovsianikov, W. Sun, S. Takeuchi, J.J. Yoo, T.B.F. Woodfield, A definition of bioinks and their distinction from biomaterial inks, Biofabrication 11(1) (2018) 013001.

[76] H.J. Hong, W.S. Koom, W.G. Koh, Cell Microarray Technologies for High-Throughput Cell-Based Biosensors, Sensors 17(6) (2017) 1293.

[77] O.I. Berthuy, S.K. Muldur, F. Rossi, P. Colpo, L.J. Blum, C.A. Marquette, Multiplex cell microarrays for high-throughput screening, Lab on a chip 16(22) (2016) 4248-4262.

[78] R. Jonczyk, T. Kurth, A. Lavrentieva, J.G. Walter, T. Scheper, F. Stahl, Living Cell Microarrays: An Overview of Concepts, Microarrays 5(2) (2016) 11.

[79] R. Jonczyk, S. Timur, T. Scheper, F. Stahl, Development of living cell microarrays using non-contact micropipette printing, J Biotechnol 217 (2016) 109-111.

[80] M.L. Yarmush, K.R. King, Living-cell microarrays, Annual review of biomedical engineering 11 (2009) 235-57.

[81] A. Yusof, H. Keegan, C.D. Spillane, O.M. Sheils, C.M. Martin, J.J. O'Leary, R. Zengerle, P. Koltay, Inkjet-like printing of single-cells, Lab on a chip 11(14) (2011) 2447-54.

[82] R. The, S. Yamaguchi, A. Ueno, Y. Akiyama, K. Morishima, Piezoelectric Inkjet-based One Cell per One Droplet Automatic Printing by Image Processing, Ieee Int C Int Robot (2013) 502-507.

[83] A.R. Liberski, J.T. Delaney, Jr., U.S. Schubert, "One cell-one well": a new approach to inkjet printing single cell microarrays, ACS combinatorial science 13(2) (2011) 190-5.

[84] T.M. Park, D. Kang, I. Jang, W.S. Yun, J.H. Shim, Y.H. Jeong, J.Y. Kwak, S. Yoon, S. Jin, Fabrication of In Vitro Cancer Microtissue Array on Fibroblast-Layered Nanofibrous Membrane by Inkjet Printing, Int J Mol Sci 18(11) (2017) 2348.

[85] S. Mi, S. Yang, T. Liu, Z. Du, Y. Xu, B. Li, W. Sun, A Novel Controllable Cell Array Printing Technique on Microfluidic Chips, IEEE transactions on bio-medical engineering 66(9) (2019) 2512-2520.

[86] A. Martinez-Rivas, G.K. Gonzalez-Quijano, S. Proa-Coronado, C. Severac, E. Dague, Methods of Micropatterning and Manipulation of Cells for Biomedical Applications, Micromachines 8(12) (2017) 347.

[87] M. Thery, A. Jimenez-Dalmaroni, V. Racine, M. Bornens, F. Julicher, Experimental and theoretical study of mitotic spindle orientation, Nature 447(7143) (2007) 493-6.

[88] G. Letort, A.Z. Politi, H. Ennomani, M. Thery, F. Nedelec, L. Blanchoin, Geometrical and mechanical properties control actin filament organization, PLoS computational biology 11(5) (2015) e1004245.

[89] R.J. Klebe, Cytoscribing: a method for micropositioning cells and the construction of two- and three-dimensional synthetic tissues, Experimental cell research 179(2) (1988) 362-73.

[90] V. Mironov, T. Boland, T. Trusk, G. Forgacs, R.R. Markwald, Organ printing: computer-aided jet-based 3D tissue engineering, Trends in Biotechnology 21(4) (2003) 157-161.

[91] T. Xu, C.A. Gregory, P. Molnar, X. Cui, S. Jalota, S.B. Bhaduri, T. Boland, Viability and electrophysiology of neural cell structures generated by the inkjet printing method, Biomaterials 27(19) (2006) 3580-3588.

[92] N. Antill-O'Brien, J. Bourke, C.D. O'Connell, Layer-By-Layer: The Case for 3D Bioprinting Neurons to Create Patient-Specific Epilepsy Models, Materials 12(19) (2019) 3218.

[93] J.A. Park, S. Yoon, J. Kwon, H. Now, Y.K. Kim, W.J. Kim, J.Y. Yoo, S. Jung, Freeform micropatterning of living cells into cell culture medium using direct inkjet printing, Sci Rep 7(1) (2017) 14610.

[94] M. Matsusaki, K. Sakaue, K. Kadowaki, M. Akashi, Three-Dimensional Human Tissue Chips Fabricated by Rapid and Automatic Inkjet Cell Printing, Advanced Healthcare Materials 2(4) (2013) 534-539.

[95] X.F. Cui, T. Boland, Human microvasculature fabrication using thermal inkjet printing technology, Biomaterials 30(31) (2009) 6221-6227.

[96] T. Xu, W. Zhao, J.-M. Zhu, M.Z. Albanna, J.J. Yoo, A. Atala, Complex heterogeneous tissue constructs containing multiple cell types prepared by inkjet printing technology, Biomaterials 34(1) (2013) 130-139.

[97] S. Hewes, A.D. Wong, P.C. Searson, Bioprinting microvessels using an inkjet printer, Bioprinting 7 (2017) 14-18.

[98] J.A. Park, H.R. Lee, S.Y. Park, S. Jung, Self-Organization of Fibroblast-Laden 3D Collagen Microstructures from Inkjet-Printed Cell Patterns, Advanced biosystems 4(5) (2020) e1900280.

[99] S. Yoon, J.A. Park, H.R. Lee, W.H. Yoon, D.S. Hwang, S. Jung, Inkjet–spray hybrid printing for 3D freeform fabrication of multilayered hydrogel structures, Advanced Healthcare Materials 7(14) (2018) 1800050.

[100] B.S. Kim, J.S. Lee, G. Gao, D.W. Cho, Direct 3D cell-printing of human skin with functional transwell system, Biofabrication 9(2) (2017) 025034.

[101] A. Negro, T. Cherbuin, M.P. Lutolf, 3D Inkjet Printing of Complex, Cell-Laden Hydrogel Structures, Sci Rep 8(1) (2018) 17099.

[102] S.V. Murphy, P. De Coppi, A. Atala, Opportunities and challenges of translational 3D bioprinting, Nature biomedical engineering 4(4) (2020) 370-380.

[103] S. Dixit, D.R. Baganizi, R. Sahu, E. Dosunmu, A. Chaudhari, K. Vig, S.R. Pillai, S.R. Singh, V.A. Dennis, Immunological challenges associated with artificial skin grafts: available solutions and stem cells in future design of synthetic skin, Journal of biological engineering 11 (2017) 49.

[104] M. Albanna, K.W. Binder, S.V. Murphy, J. Kim, S.A. Qasem, W. Zhao, J. Tan, I.B. El-Amin, D.D. Dice, J. Marco, J. Green, T. Xu, A. Skardal, J.H. Holmes, J.D. Jackson, A. Atala, J.J. Yoo, In Situ Bioprinting of Autologous Skin Cells Accelerates Wound Healing of Extensive Excisional Full-Thickness Wounds, Scientific Reports 9(1) (2019) 1856.

[105] J. Lipskas, K. Deep, W. Yao, Robotic-Assisted 3D Bio-printing for Repairing Bone and Cartilage Defects through a Minimally Invasive Approach, Scientific Reports 9 (2019).

[106] V. Mironov, G. Prestwich, G. Forgacs, Bioprinting living structures, Journal of Materials Chemistry 17(20) (2007) 2054-2060.

[107] T. Xu, J. Rohozinski, W.X. Zhao, E.C. Moorefield, A. Atala, J.J. Yoo, Inkjet-Mediated Gene Transfection into Living Cells Combined with Targeted Delivery, Tissue Eng Pt A 15(1) (2009) 95-101.

[108] T. Goldmann, J.S. Gonzalez, DNA-printing: utilization of a standard inkjet printer for the transfer of nucleic acids to solid supports, Journal of Biochemical and Biophysical Methods 42(3) (2000) 105-110.

[109] K.M. Singh, L.L. Brott, J.G. Grote, R.R. Naik, Inkjet Printing of DNA for Use in Bioelectronic Applications, 2008 IEEE National Aerospace and Electronics Conference, 2008, pp. 107-109.

[110] G.M. Nishioka, A.A. Markey, C.K. Holloway, Protein Damage in Drop-on-Demand Printers, Journal of the American Chemical Society 126(50) (2004) 16320-16321.

[111] L. Setti, A. Fraleoni-Morgera, B. Ballarin, A. Filippini, D. Frascaro, C. Piana, An amperometric glucose biosensor prototype fabricated by thermal inkjet printing, Biosensors and Bioelectronics 20(10) (2005) 2019-2026.

[112] S. Di Risio, N. Yan, Piezoelectric Ink-Jet Printing of Horseradish Peroxidase: Effect of Ink Viscosity Modifiers on Activity, Macromolecular rapid communications 28(18-19) (2007) 1934-1940.

[113] B. Derby, Bioprinting: inkjet printing proteins and hybrid cell-containing materials and structures, Journal of Materials Chemistry 18(47) (2008) 5717-5721.

[114] C. Li, A. Faulkner-Jones, A.R. Dun, J. Jin, P. Chen, Y. Xing, Z. Yang, Z. Li, W. Shu, D. Liu, R.R. Duncan, Rapid formation of a supramolecular polypeptide-DNA hydrogel for in situ three-dimensional multilayer bioprinting, Angewandte Chemie 54(13) (2015) 3957-61.

[115] S. Ilkhanizadeh, A.I. Teixeira, O. Hermanson, Inkjet printing of macromolecules on hydrogels to steer neural stem cell differentiation, Biomaterials 28(27) (2007) 3936-3943.

[116] B.M. Wu, S.W. Borland, R.A. Giordano, L.G. Cima, E.M. Sachs, M.J. Cima, Solid free-form fabrication of drug delivery devices, Journal of Controlled Release 40(1) (1996) 77-87.

[117] C.W. Rowe, W.E. Katstra, R.D. Palazzolo, B. Giritlioglu, P. Teung, M.J. Cima, Multimechanism oral dosage forms fabricated by three dimensional printing™, Journal of Controlled Release 66(1) (2000) 11-17.

[118] D. Radulescu, N. Schwade, D. Wawro, Uniform Paclitaxel-Loaded Biodegradable Microspheres Manufactured by Ink-Jet Technology, 2003.

[119] R.D. Boehm, P.R. Miller, J. Daniels, S. Stafslien, R.J. Narayan, Inkjet printing for pharmaceutical applications, Materials Today 17(5) (2014) 247-252.

[120] P.J. Tarcha, D. Verlee, H.W. Hui, J. Setesak, B. Antohe, D. Radulescu, D. Wallace, The Application of Ink-Jet Technology for the Coating and Loading of Drug-Eluting Stents, Ann Biomed Eng 35(10) (2007) 1791-1799.

[121] W. Wu, Q. Zheng, X. Guo, J. Sun, Y. Liu, A programmed release multi-drug implant fabricated by three-dimensional printing technology for bone tuberculosis therapy, Biomedical Materials 4(6) (2009) 065005.

[122] T. Li, J. Li, K.I. Morozov, Z. Wu, T. Xu, I. Rozen, A.M. Leshansky, L. Li, J. Wang, Highly Efficient Freestyle Magnetic Nanoswimmer, Nano Letters 17(8) (2017) 5092-5098.

[123] A. Barbot, D. Decanini, G. Hwang, Controllable Roll-to-Swim motion transition of helical nanoswimmers, 2014 IEEE/RSJ International Conference on Intelligent Robots and Systems, 2014, pp. 4662-4667.

[124] W. Gao, X. Feng, A. Pei, Y. Gu, J. Li, J. Wang, Seawater-driven magnesium based Janus micromotors for environmental remediation, Nanoscale 5(11) (2013) 4696-4700.

[125] J. Li, V.V. Singh, S. Sattayasamitsathit, J. Orozco, K. Kaufmann, R. Dong, W. Gao, B. Jurado-Sanchez, Y. Fedorak, J. Wang, Water-Driven Micromotors for Rapid Photocatalytic Degradation of Biological and Chemical Warfare Agents, ACS Nano 8(11) (2014) 11118-11125.

[126] O. Hartman, C. Zhang, E.L. Adams, M.C. Farach-Carson, N.J. Petrelli, B.D. Chase, J.F. Rabolt, Microfabricated Electrospun Collagen Membranes for 3-D Cancer Models and Drug Screening Applications, Biomacromolecules 10(8) (2009) 2019-2032.

[127] K. Sisson, C. Zhang, M.C. Farach-Carson, D.B. Chase, J.F. Rabolt, Evaluation of Cross-Linking Methods for Electrospun Gelatin on Cell Growth and Viability, Biomacromolecules 10(7) (2009) 1675-1680.

[128] A.-V. Do, B. Khorsand, S.M. Geary, A.K. Salem, 3D Printing of Scaffolds for Tissue Regeneration Applications, Advanced Healthcare Materials 4(12) (2015) 1742-1762.

[129] Q. Lu, X. Hu, X. Wang, J.A. Kluge, S. Lu, P. Cebe, D.L. Kaplan, Water-Insoluble Silk Films with Silk I Structure, Acta biomaterialia 6(4) (2010) 1380-1387.

[130] D. Wilson, R. Valluzzi, D. Kaplan, Conformational Transitions in Model Silk Peptides, Biophysical Journal 78(5) (2000) 2690-2701.

[131] L.-D. Koh, Y. Cheng, C.-P. Teng, Y.-W. Khin, X.-J. Loh, S.-Y. Tee, M. Low, E. Ye, H.-D. Yu, Y.-W. Zhang, M.-Y. Han, Structures, mechanical properties and applications of silk fibroin materials, Progress in Polymer Science 46 (2015) 86-110.

[132] T.D. Fink, R.H. Zha, Silk and Silk-Like Supramolecular Materials, Macromolecular rapid communications 39(17) (2018) e1700834.

[133] D. Jao, X. Mou, X. Hu, Tissue Regeneration: A Silk Road, Journal of functional biomaterials 7(3) (2016).

[134] B.B. Mandal, A. Grinberg, E.S. Gil, B. Panilaitis, D.L. Kaplan, High-strength silk protein scaffolds for bone repair, Proc Natl Acad Sci U S A 109(20) (2012) 7699-704.

[135] B. Kundu, R. Rajkhowa, S.C. Kundu, X. Wang, Silk fibroin biomaterials for tissue regenerations, Adv Drug Deliv Rev 65(4) (2013) 457-70.

[136] H.J. Jin, J. Park, V. Karageorgiou, U.J. Kim, R. Valluzzi, P. Cebe, D.L. Kaplan, Water-Stable Silk Films with Reduced β-Sheet Content, Adv Funct Mater 15(8) (2005) 1241-1247.

[137] D.N. Rockwood, R.C. Preda, T. Yucel, X. Wang, M.L. Lovett, D.L. Kaplan, Materials fabrication from Bombyx mori silk fibroin, Nature protocols 6(10) (2011) 1612-31.

[138] P.H. Chao, S. Yodmuang, X. Wang, L. Sun, D.L. Kaplan, G. Vunjak-Novakovic, Silk hydrogel for cartilage tissue engineering, Journal of biomedical materials research. Part B, Applied biomaterials 95(1) (2010) 84-90.

[139] D.M. Sah, K. Pramanik, Regenerated Silk Fibroin from B. mori Silk Cocoon for Tissue Engineering Applications, International Journal of Environmental Science and Development 1 (2010) 404-408.

[140] M.R. Sommer, M. Schaffner, D. Carnelli, A.R. Studart, 3D Printing of Hierarchical Silk Fibroin Structures, ACS applied materials & interfaces 8(50) (2016) 34677-34685.

[141] Z. Zheng, J. Wu, M. Liu, H. Wang, C. Li, M.J. Rodriguez, G. Li, X. Wang, D.L. Kaplan, 3D Bioprinting of Self-Standing Silk-Based Bioink, Adv Healthc Mater 7(6) (2018) e1701026.

[142] K. Cai, K. Yao, S. Lin, Z. Yang, X. Li, H. Xie, T. Qing, L. Gao, Poly(d,l-lactic acid) surfaces modified by silk fibroin: effects on the culture of osteoblast in vitro, Biomaterials 23(4) (2002) 1153-1160.

[143] Y. Gotoh, M. Tsukada, N. Minoura, Y. Imai, Synthesis of poly(ethylene glycol)-silk fibroin conjugates and surface interaction between L-929 cells and the conjugates, Biomaterials 18(3) (1997) 267-271.

[144] Y. Wang, D.J. Blasioli, H.-J. Kim, H.S. Kim, D.L. Kaplan, Cartilage tissue engineering with silk scaffolds and human articular chondrocytes, Biomaterials 27(25) (2006) 4434-4442.

[145] G.H. Altman, R.L. Horan, H.H. Lu, J. Moreau, I. Martin, J.C. Richmond, D.L. Kaplan, Silk matrix for tissue engineered anterior cruciate ligaments, Biomaterials 23(20) (2002) 4131-4141.

[146] H.J. Kim, U.-J. Kim, G.G. Leisk, C. Bayan, I. Georgakoudi, D.L. Kaplan, Bone Regeneration on Macroporous Aqueous-Derived Silk 3-D Scaffolds, Macromolecular Bioscience 7(5) (2007) 643-655.

[147] M. Lovett, C. Cannizzaro, L. Daheron, B. Messmer, G. Vunjak-Novakovic, D.L. Kaplan, Silk fibroin microtubes for blood vessel engineering, Biomaterials 28(35) (2007) 5271-5279.

[148] C. Kirker-Head, V. Karageorgiou, S. Hofmann, R. Fajardo, O. Betz, H.P. Merkle, M. Hilbe, B. von Rechenberg, J. McCool, L. Abrahamsen, A. Nazarian, E. Cory, M. Curtis, D. Kaplan, L. Meinel, BMP-silk composite matrices heal critically sized femoral defects, Bone 41(2) (2007) 247-255.

[149] U. Hersel, C. Dahmen, H. Kessler, RGD modified polymers: biomaterials for stimulated cell adhesion and beyond, Biomaterials 24(24) (2003) 4385-4415.

[150] X. Wang, E. Wenk, A. Matsumoto, L. Meinel, C. Li, D.L. Kaplan, Silk microspheres for encapsulation and controlled release, Journal of Controlled Release 117(3) (2007) 360-370.

[151] X. Wang, X. Hu, A. Daley, O. Rabotyagova, P. Cebe, D.L. Kaplan, Nanolayer biomaterial coatings of silk fibroin for controlled release, Journal of Controlled Release 121(3) (2007) 190-199.

[152] S.H. Kim, Y.K. Yeon, J.M. Lee, J.R. Chao, Y.J. Lee, Y.B. Seo, M.T. Sultan, O.J. Lee, J.S. Lee, S.I. Yoon, I.S. Hong, G. Khang, S.J. Lee, J.J. Yoo, C.H. Park, Precisely printable and biocompatible silk fibroin bioink for digital light processing 3D printing, Nat Commun 9(1) (2018) 1620.

[153] P.M. Rider, I.M. Brook, P.J. Smith, C.A. Miller, Reactive Inkjet Printing of Regenerated Silk Fibroin Films for Use as Dental Barrier Membranes, Micromachines 9(2) (2018).

[154] M.J. Rodriguez, T.A. Dixon, E. Cohen, W. Huang, F.G. Omenetto, D.L. Kaplan, 3D freeform printing of silk fibroin, Acta Biomater 71 (2018) 379-387.

[155] P.C. Bessa, E.R. Balmayor, H.S. Azevedo, S. Nürnberger, M. Casal, M. van Griensven, R.L. Reis, H. Redl, Silk fibroin microparticles as carriers for delivery of human recombinant BMPs. Physical characterization and drug release, Journal of Tissue Engineering and Regenerative Medicine 4(5) (2010) 349-355.

[156] K. Tsioris, W.K. Raja, E.M. Pritchard, B. Panilaitis, D.L. Kaplan, F.G. Omenetto, Fabrication of Silk Microneedles for Controlled-Release Drug Delivery, Adv Funct Mater 22(2) (2012) 330-335.

[157] S.S. Silva, A. Motta, M.T. Rodrigues, A.F. Pinheiro, M.E. Gomes, J.F. Mano, R.L. Reis, C. Migliaresi, Novel genipin-cross-linked chitosan/silk fibroin sponges for cartilage engineering strategies, Biomacromolecules 9(10) (2008) 2764-74.

[158] X. Chen, Y.-Y. Qi, L.-L. Wang, Z. Yin, G.-L. Yin, X.-H. Zou, H.-W. Ouyang, Ligament regeneration using a knitted silk scaffold combined with collagen matrix, Biomaterials 29(27) (2008) 3683-3692.

[159] S. Wang, Y. Zhang, G. Yin, H. Wang, Z. Dong, Electrospun polylactide/silk fibroin–gelatin composite tubular scaffolds for small-diameter tissue engineering blood vessels, Journal of Applied Polymer Science 113(4) (2009) 2675-2682.

[160] A. Ajisawa, Dissolution of silk fibroin with calciumchloride/ethanol aqueous solution, Journal of Sericultural Science of Japan 67(2) (1998) 91-94.

[161] G. KRÜSS GmbH, Wilhelmy plate method, 2013. https://www.kruss-scientific.com/en/know-how/glossary/wilhelmy-plate-method.

[162] M.T. Inc., A Basic Ink-Jet Setup, 2012. http://www.microfab.com/a-basic-ink-jet-microdispensing-setup.

[163] M.T. Inc., JetServer, 2012. http://www.microfab.com/electronics/jetserver.

[164] M. Tsukada, Y. Gotoh, M. Nagura, N. Minoura, N. Kasai, G. Freddi, Structural changes of silk fibroin membranes induced by immersion in methanol aqueous solutions, Journal of Polymer Science Part B: Polymer Physics 32(5) (1994) 961-968.

[165] L. Bruslind, General Microbiology, Oregon State University2017.

[166] H. Lodish, Darnell, J., Berk, A., Zipursky, L. S., Matsudaira, P., & Baltimore, D., Integrating Cells into Tissues, Molecular Cell Biology, W. H. Freeman, New York, 2000.

[167] K. Von Der Mark, V. Gauss, H. Von Der Mark, P. MÜLler, Relationship between cell shape and type of collagen synthesised as chondrocytes lose their cartilage phenotype in culture, Nature 267(5611) (1977) 531-532.

[168] O.W. Petersen, L. Rønnov-Jessen, A.R. Howlett, M.J. Bissell, Interaction with basement membrane serves to rapidly distinguish growth and differentiation pattern of normal and malignant human breast epithelial cells, Proceedings of the National Academy of Sciences of the United States of America 89(19) (1992) 9064-9068.

[169] K.M. Yamada, E. Cukierman, Modeling Tissue Morphogenesis and Cancer in 3D, Cell 130(4) (2007) 601-610.

[170] A. Birgersdotter, R. Sandberg, I. Ernberg, Gene expression perturbation in vitro—A growing case for three-dimensional (3D) culture systems, Seminars in Cancer Biology 15(5) (2005) 405-412.

[171] C. Li, M. Kato, L. Shiue, J.E. Shively, M. Ares, R.-J. Lin, Cell Type and Culture Condition–Dependent Alternative Splicing in Human Breast Cancer Cells Revealed by Splicing-Sensitive Microarrays, Cancer Research 66(4) (2006) 1990.

[172] S. Ghosh, G.C. Spagnoli, I. Martin, S. Ploegert, P. Demougin, M. Heberer, A. Reschner, Three-dimensional culture of melanoma cells profoundly affects gene

expression profile: A high density oligonucleotide array study, Journal of Cellular Physiology 204(2) (2005) 522-531.

[173] E. Knight, S. Przyborski, Advances in 3D cell culture technologies enabling tissue-like structures to be created in vitro, Journal of Anatomy 227(6) (2015) 746-756.

[174] S. Khetan, J.A. Burdick, Patterning network structure to spatially control cellular remodeling and stem cell fate within 3-dimensional hydrogels, Biomaterials 31(32) (2010) 8228-8234.

[175] W. Mueller-Klieser, Multicellular spheroids, Journal of Cancer Research and Clinical Oncology 113(2) (1987) 101-122.

[176] H.B. Frieboes, X. Zheng, C.-H. Sun, B. Tromberg, R. Gatenby, V. Cristini, An Integrated Computational/Experimental Model of Tumor Invasion, Cancer Research 66(3) (2006) 1597.

[177] D.A. Gregory, A.I. Campbell, S.J. Ebbens, Effect of Catalyst Distribution on Spherical Bubble Swimmer Trajectories, The Journal of Physical Chemistry C 119(27) (2015) 15339-15348.

[178] W.F. Paxton, K.C. Kistler, C.C. Olmeda, A. Sen, S.K. St. Angelo, Y. Cao, T.E. Mallouk, P.E. Lammert, V.H. Crespi, Catalytic Nanomotors: Autonomous Movement of Striped Nanorods, Journal of the American Chemical Society 126(41) (2004) 13424-13431.

[179] R.F. Ismagilov, A. Schwartz, N. Bowden, G.M. Whitesides, Autonomous Movement and Self-Assembly, Angewandte Chemie International Edition 41(4) (2002) 652-654.

[180] M. Xuan, Z. Wu, J. Shao, L. Dai, T. Si, Q. He, Near Infrared Light-Powered Janus Mesoporous Silica Nanoparticle Motors, J Am Chem Soc 138(20) (2016) 6492-7.

[181] V. Garcia-Gradilla, J. Orozco, S. Sattayasamitsathit, F. Soto, F. Kuralay, A. Pourazary, A. Katzenberg, W. Gao, Y. Shen, J. Wang, Functionalized ultrasound-propelled magnetically guided nanomotors: toward practical biomedical applications, ACS Nano 7(10) (2013) 9232-40.

[182] C. Tomlinson, XLVII. On the motions of camphor on the surface of water, The London, Edinburgh, and Dublin Philosophical Magazine and Journal of Science 38(257) (1869) 409-424.

[183] S. Nakata, Y. Iguchi, S. Ose, M. Kuboyama, T. Ishii, K. Yoshikawa, Self-Rotation of a Camphor Scraping on Water: New Insight into the Old Problem, Langmuir 13(16) (1997) 4454-4458.

[184] Definition of Surface Tension. http://web.mit.edu/nnf/education/wettability/definition.html.

[185] C.N. Baroud, Marangoni Convection, in: D. Li (Ed.), Encyclopedia of Microfluidics and Nanofluidics, Springer US, Boston, MA, 2013, pp. 1-8.

[186] L. Meggs, The Marangoni Effect: A Fluid Phenom, 2011. https://www.nasa.gov/mission_pages/station/research/news/marangoni.html.

[187] Y. Wu, T. Si, J. Shao, Z. Wu, Q. He, Near-infrared light-driven Janus capsule motors: Fabrication, propulsion, and simulation, Nano Research 9(12) (2016) 3747-3756.

[188] L. Baraban, D. Makarov, R. Streubel, I. Mönch, D. Grimm, S. Sanchez, O.G. Schmidt, Catalytic Janus Motors on Microfluidic Chip: Deterministic Motion for Targeted Cargo Delivery, ACS Nano 6(4) (2012) 3383-3389.

[189] O.D. Velev, K.H. Bhatt, On-chip micromanipulation and assembly of colloidal particles by electric fields, Soft matter 2(9) (2006) 738-750.

[190] D. Pantarotto, W.R. Browne, B.L. Feringa, Autonomous propulsion of carbon nanotubes powered by a multienzyme ensemble, Chemical communications (13) (2008) 1533-5.

[191] X. Ma, A.C. Hortelao, A. Miguel-Lopez, S. Sanchez, Bubble-Free Propulsion of Ultrasmall Tubular Nanojets Powered by Biocatalytic Reactions, J Am Chem Soc 138(42) (2016) 13782-13785.

[192] S.J. Ebbens, J.R. Howse, Direct observation of the direction of motion for spherical catalytic swimmers, Langmuir 27(20) (2011) 12293-6.

[193] W.F. Paxton, A. Sen, T.E. Mallouk, Motility of catalytic nanoparticles through self-generated forces, Chemistry 11(22) (2005) 6462-70.

[194] W. Duan, R. Liu, A. Sen, Transition between Collective Behaviors of Micromotors in Response to Different Stimuli, Journal of the American Chemical Society 135(4) (2013) 1280-1283.

[195] Z. Ghalanbor, S.-A. Marashi, B. Ranjbar, Nanotechnology helps medicine: Nanoscale swimmers and their future applications, Medical Hypotheses 65(1) (2005) 198-199.

[196] E. Lauga, A.M.J. Davis, Viscous Marangoni propulsion, Journal of Fluid Mechanics 705 (2011) 120-133.

[197] P. Chelikani, I. Fita, P.C. Loewen, Diversity of structures and properties among catalases, Cellular and Molecular Life Sciences CMLS 61(2) (2004) 192-208.

[198] C.D. Putnam, A.S. Arvai, Y. Bourne, J.A. Tainer, Active and inhibited human catalase structures: ligand and NADPH binding and catalytic mechanism11Edited by R. Huber, Journal of Molecular Biology 296(1) (2000) 295-309.

[199] U. Technologies, What is the pH of H2O2 solutions?, 2009. http://www.h2o2.com/faqs/FaqDetail.aspx?fId=26.

[200] M. Ghadermarzi, A.A. Moosavi-Movahedi, The effects of temperature and pH on the kinetics of reactions between catalase and its suicide substrate hydrogen peroxide, The Italian journal of biochemistry 46(4) (1997) 197-205.

[201] S. Lu, X. Wang, Q. Lu, X. Hu, N. Uppal, F.G. Omenetto, D.L. Kaplan, Stabilization of enzymes in silk films, Biomacromolecules 10(5) (2009) 1032-42.

[202] H. Hu, R.G. Larson, Marangoni effect reverses coffee-ring depositions, The journal of physical chemistry. B 110(14) (2006) 7090-4.

[203] I. COMSOL, The Marangoni Effect, 2017. https://www.comsol.com/multiphysics/marangoni-effect.

[204] Q. Hu, Y. Ren, W. Liu, Y. Tao, H. Jiang, Simulation Analysis of Improving Microfluidic Heterogeneous Immunoassay Using Induced Charge Electroosmosis on a Floating Gate, Micromachines 8(7) (2017).

[205] G. Zhao, M. Pumera, Macroscopic Self-Propelled Objects, Chemistry – An Asian Journal 7(9) (2012) 1994-2002.

[206] J.J. Gurdak, Climate-induced pumping, Nature Geoscience 10(2) (2017) 71-71.

[207] J.S. Famiglietti, The global groundwater crisis, Nature Climate Change 4(11) (2014) 945-948.

[208] B. Ashraf, A. AghaKouchak, A. Alizadeh, M. Mousavi Baygi, H. R. Moftakhari, A. Mirchi, H. Anjileli, K. Madani, Quantifying Anthropogenic Stress on Groundwater Resources, Scientific Reports 7(1) (2017) 12910.

[209] V. Srinivasan, E.F. Lambin, S.M. Gorelick, B.H. Thompson, S. Rozelle, The nature and causes of the global water crisis: Syndromes from a meta-analysis of coupled human-water studies, Water Resources Research 48(10) (2012).

[210] M. Kummu, J.H.A. Guillaume, H. de Moel, S. Eisner, M. Flörke, M. Porkka, S. Siebert, T.I.E. Veldkamp, P.J. Ward, The world's road to water scarcity: shortage and stress in the 20th century and pathways towards sustainability, Scientific Reports 6(1) (2016) 38495.

[211] Z. Xu, J. Xu, H. Yin, W. Jin, H. Li, Z. He, Urban river pollution control in developing countries, Nature Sustainability 2(3) (2019) 158-160.

[212] Y. Wen, G. Schoups, N. van de Giesen, Organic pollution of rivers: Combined threats of urbanization, livestock farming and global climate change, Scientific Reports 7(1) (2017) 43289.

[213] H.-M. Chen, M.-T. Wu, Residential exposure to chlorinated hydrocarbons from groundwater contamination and the impairment of renal function-An ecological study, Scientific Reports 7(1) (2017) 40283.

[214] P. Höhener, D. Werner, C. Balsiger, G. Pasteris, Worldwide Occurrence and Fate of Chlorofluorocarbons in Groundwater, Critical Reviews in Environmental Science and Technology 33(1) (2003) 1-29.

[215] T. Kistemann, J. Hundhausen, S. Herbst, T. Claßen, H. Färber, Assessment of a groundwater contamination with vinyl chloride (VC) and precursor volatile organic compounds (VOC) by use of a geographical information system (GIS), International Journal of Hygiene and Environmental Health 211(3) (2008) 308-317.

[216] L.A. Schaider, K.M. Rodgers, R.A. Rudel, Review of Organic Wastewater Compound Concentrations and Removal in Onsite Wastewater Treatment Systems, Environmental Science & Technology 51(13) (2017) 7304-7317.

[217] Z. Wang, D. Shao, P. Westerhoff, Wastewater discharge impact on drinking water sources along the Yangtze River (China), Science of The Total Environment 599-600 (2017) 1399-1407.

[218] I. Keenum, M.C. Medina, E. Garner, K.J. Pieper, M.F. Blair, E. Milligan, A. Pruden, G. Ramirez-Toro, W.J. Rhoads, Source-to-Tap Assessment of Microbiological Water Quality in Small Rural Drinking Water Systems in Puerto Rico Six Months After Hurricane Maria, Environmental Science & Technology 55(6) (2021) 3775-3785.

[219] N.H. Tran, M. Reinhard, E. Khan, H. Chen, V.T. Nguyen, Y. Li, S.G. Goh, Q.B. Nguyen, N. Saeidi, K.Y.-H. Gin, Emerging contaminants in wastewater, stormwater runoff, and surface water: Application as chemical markers for diffuse sources, Science of The Total Environment 676 (2019) 252-267.

[220] D.M. Revitt, J.B. Ellis, Urban surface water pollution problems arising from misconnections, Science of The Total Environment 551-552 (2016) 163-174.

[221] H. Yin, M. Xie, L. Zhang, J. Huang, Z. Xu, H. Li, R. Jiang, R. Wang, X. Zeng, Identification of sewage markers to indicate sources of contamination: Low cost options for misconnected non-stormwater source tracking in stormwater systems, Science of The Total Environment 648 (2019) 125-134.

[222] Y.O.O. Hu, N. Ndegwa, J. Alneberg, S. Johansson, J.B. Logue, M. Huss, M. Käller, J. Lundeberg, J. Fagerberg, A.F. Andersson, Stationary and portable sequencing-based approaches for tracing wastewater contamination in urban stormwater systems, Scientific Reports 8(1) (2018) 11907.

[223] D.M. Chandler, D.N. Lerner, A low cost method to detect polluted surface water outfalls and misconnected drainage, Water and Environment Journal 29(2) (2015) 202-206.

[224] E. Carre, J. Perot, V. Jauzein, L. Lin, M. Lopez-Ferber, Estimation of water quality by UV/Vis spectrometry in the framework of treated wastewater reuse, Water science and technology : a journal of the International Association on Water Pollution Research 76(3-4) (2017) 633-641.

[225] A.E. Dudeizak, S.M. Babichenko, L.V. Poryvkina, K.J. Saar, Total luminescent spectroscopy for remote laser diagnostics of natural water conditions, Applied optics 30(4) (1991) 453-8.

[226] M.A. Morinigo, D. Wheeler, C. Berry, C. Jones, M.A. Munoz, R. Cornax, J.J. Borrego, Evaluation of Different Bacteriophage Groups as Fecal Indicators in Contaminated Natural-Waters in Southern England, Water Res 26(3) (1992) 267-271.

[227] K.S. Manja, M.S. Maurya, K.M. Rao, A simple field test for the detection of faecal pollution in drinking water, Bulletin of the World Health Organization 60(5) (1982) 797-801.

[228] F. Robert-Peillard, A.D. Syakti, B. Coulomb, P. Doumenq, L. Malleret, L. Asia, J.L. Boudenne, Occurrence and fate of selected surfactants in seawater at the outfall of the Marseille urban sewerage system, International Journal of Environmental Science and Technology 12(5) (2015) 1527-1538.

[229] C. Warwick, A. Guerreiro, A. Soares, Sensing and analysis of soluble phosphates in environmental samples: A review, Biosensors and Bioelectronics 41 (2013) 1-11.

[230] L. Martínez-Balbuena, A. Arteaga-Jiménez, E. Hernández-Zapata, C. Márquez-Beltrán, Applicability of the Gibbs Adsorption Isotherm to the analysis of experimental

surface-tension data for ionic and nonionic surfactants, Advances in Colloid and Interface Science 247 (2017) 178-184.

[231] C. Wang, X. Wang, F. Liu, Z. Jiang, X. Lin, Surface concentration or surface excess, which one dominates the surface tension of multicomponent mixtures?, Colloid and Polymer Science 296(1) (2018) 89-93.

[232] A. Mitropoulos, What is a surface excess?, Journal of Engineering Science and Technology Review 1 (2008).

[233] N.J. Suematsu, T. Sasaki, S. Nakata, H. Kitahata, Quantitative estimation of the parameters for self-motion driven by difference in surface tension, Langmuir 30(27) (2014) 8101-8.

[234] Y.-C. Li, Y.S. Zhang, A. Akpek, S.R. Shin, A. Khademhosseini, 4D bioprinting: the next-generation technology for biofabrication enabled by stimuli-responsive materials, Biofabrication 9(1) (2016) 012001.